# The role of neuronal dystonin in sensory neuron survival

Anisha Lynch-Godrei

Thesis submitted to the Faculty of Graduate and Postdoctoral Studies
in partial fulfillment of the requirements for the Ph.D. degree in Neuroscience

Department of Cellular and Molecular Medicine

Faculty of Medicine

University of Ottawa

**Abstract**

The mouse dystonin gene (*Dst;* previously *Bpag1*) yields three tissue specific isoforms of a giant cytoskeletal linker protein, namely the skin isoform dystonin-e, neuronal isoform dystonin-a, and muscle isoform dystonin-b. Through alternative splicing events at the 5' end of neuronal and muscle transcripts, three further isoforms with unique N-termini are produced (dystonin-a/b1, -a/b2, and -a/b3). Though dystonin-e has long since been known to be the autoantigen responsible for the human skin blistering disease bullous pemphigoid, mutations affecting the neuronal isoforms have emerged as the major determinant in the murine sensory neuropathy *dystonia musculorum* ($Dst^{dt}$), and more recently the human disease Hereditary sensory and autonomic neuropathy type VI (HSAN-VI). Here we report an upregulation in autophagy within sensory neurons from two $Dst^{dt}$ alleles: $Dst^{dt\text{-}27J}$ mice that are dystonin-a null, and $Dst^{dt\text{-}Tg4}$ mice that lack dystonin-a1 and -a2 but retain dystonin-a3. Whether this upregulation is protective or pathogenic has yet to be determined. It was initially believed that insufficient trafficking of autophagic vesicles to their final site of degradation in lysosomes was impaired, however extensive evaluation of the levels of motor proteins responsible for autophagosome and lysosome trafficking were found to be in appropriate quantities. Interestingly, investigation of microtubule stability as a possible cause for these changes in autophagy showed that defective microtubule stability is not a common pathology of the $Dst^{dt}$ disorder. Only $Dst^{dt\text{-}27J}$ mice have reduced microtubule acetylation, which may help explain their shorter lifespan and symptom severity. In $Dst^{dt\text{-}Tg4}$ sensory neurons, the maintenance of microtubule stability was associated with a 3-4 fold increase in dystonin-a3 transcript expression. Subsequent knockdown of this isoform in $Dst^{dt\text{-}Tg4}$ sensory neurons produced a reduction in microtubule acetylation, suggesting that dystonin isoforms may be capable of taking on novel roles to compensate for the loss of other isoforms.

Additionally, we also identify gastrointestinal abnormalities including gas accumulation, slowed motility, and reduced microbial richness/evenness in *Dst*$^{dt}$ mice, which occur independently of enteric nervous system defects. Rather, these gastrointestinal symptoms are most likely linked to an imbalance in sympathetic and parasympathetic input onto the gut. Collectively these findings help shed light on the heterogeneity of the human HSAN-VI disorder, and identify potential targets for therapeutics and symptom relief.

**TABLE OF CONTENTS**

## List of Tables

## List of Figures

### Chapter 1: General Introduction



### Chapter 2: Disruption in the autophagic process underlies the sensory neuropathy in *dystonia musculorum* mice



### Chapter 3: Dystonin-a3 upregulation is responsible for maintenance of tubulin acetylation in a less severe *dystonia musculorum* mouse model for hereditary sensory and autonomic neuropathy type VI

**Chapter 4: Elucidating the causes of increased autophagy in *dystonia musculorum* sensory neurons**



**Chapter 5: Characterization of gastrointestinal pathologies in the *dystonia musculorum* mouse model for hereditary sensory and autonomic neuropathy type VI**

**Appendix A.1: Cytoskeletal Linker Protein Dystonin Is Not Critical to Terminal Oligodendrocyte Differentiation or CNS Myelination**

## List of Abbreviations

ABD - actin binding domain
AdV - adenovirus
Ac - acetylated
ANOVA - analysis of variance
*Atp6v1* - cytosolic $V_1$ domain of ATPase protein
BPAG1 - bullous pemphigoid antigen 1
BSA - bovine serum albumin
CASP3/CC3 - cleaved caspase 3
CLEAR - coordinated lysosome expression and regulation
*Ctsb* - cathepsin b
Dctn1 - dynactin 1/P150$^{Glued}$
Detyr - detyrosinated
DMC - dynein/dynactin motor complex
DMEM - Dulbecco's Modified Eagle Medium
DNAIC1 - dynein axonemal intermediate chain 1
DRG - dorsal root ganglia
Dst - dystonin
*Dst$^{dt}$* - *dystonia musculorum*
Dync1i1 - dynein cytoplasmic 1 intermediate chain 1
ECL - enhanced chemiluminescence
EM - electron microscopy
FBS - fetal bovine serum
GI - gastrointestinal
GIT - gastrointestinal tract
*Hexa* - hexosaminidase A
HBSS - Hank's Balanced Salt Solution
HSAN-VI - hereditary sensory and autonomic neuropathy type VI
IPAN - intrinsic primary afferent neuron
Kif5c - kinesin heavy chain 5c
Klc1 - kinesin light chain 1
Klc2 - kinesin light chain 2
LAMP1 - lysosomal-associated membrane protein 1
LC3 - microtubule-associated protein 1A/1B-light chain 3
LN2 - laminin
*Lyz2* - lysozyme 2
MACF1 - microtubule- actin crosslinking factor 1
MAG - myelin associate glycoprotein
MAP1B - microtubule-associated protein 1B
MAP1LC3/LC3 - microtubule associated-protein 1 light chain 3
MBP - myelin basic protein
MOI - multiplicity of infection
MT - microtubule
MTBD - microtubule binding domain
myr - myristoylation motif

OL - oligodendrocyte
OPC - oligodendrocyte precursor cell
P - postnatal day
PBS - phosphate buffered saline
PCR - polymerase chain reaction
PFA - paraformaldehyde
PNS - parasympathetic nervous system
PrP - prion protein promoter
*Psap* - prosaposin
Rab5 - ras-related protein 5
Rab7 - ras-related protein 7
RT-qPCR - reverse transcriptase quantitative polymerase chain reaction
SDS-PAGE - sodium dodecyl sulfate-polyacrylamide gel electrophoresis
SNS - sympathetic nervous system
SQTSM1/p62 - sequestosome 1
TBS - tris-buffered saline
TCA - trichloroacetic acid
TMD - transmembrane domain
TUBB3 - tubulin b 3 class III
WT - wild type
α-tub - alpha-tubulin

**Authorizations**

## Acknowledgements

There are many people that I wish to thank, as I feel that this achievement would not have been possible without the help and support of family, friends, and peers. First off I would like to thank my mom, Barbara Lynch, for always being there for me and encouraging me to pursue higher education. She has been the most important role model in my life, and has always inspired me to go after my goals.

I would also like to thank my supervisor Dr. Rashmi Kothary, who has been absolutely essential to my success in graduate studies. He has offered me valuable guidance and advice, though most importantly he allowed me to learn from my mistakes, giving me the skills necessary to be an independent researcher. For this I will always be grateful.

To my labmates, past and present, thank you all for being great colleagues and for making my time at the lab enjoyable. And of course to my mentor Samantha Kornfeld, you stepped up and taught me the fundamentals of working in a laboratory, and if it weren't for you I'm certain I would have had a much harder time getting to this point. I appreciate everything you've done for me, thank you so much.

I'd like to thank my friends, in particular my Ottawa crew (Stewart, JPizz, and Lalice), for being tremendously supportive of my graduate studies, and also for keeping me sane throughout it. Especially to Stewart, for having edited just about every paper (including this thesis), even though he was unable to understand it. Thanks man - you're the best.

I also wish to thank the members of my thesis advisory committee, Drs. Steffany Bennett, Christopher Kennedy, and Johnny Ngsee, for their valuable guidance and recommendations. Their input has been greatly appreciated, and has certainly directed the success of these projects.

Lastly, I am also grateful to the following agencies for funding me throughout my graduate studies: Canadian Institutes of Health Research, Ontario Graduate Scholarship, and the University of Ottawa.

# Chapter 1:

# General Introduction

**Dystonin/BPAG1 isoform diversity and structure**

The bullous pemphigoid antigen 1 (BPAG1) protein was first identified in epithelia as the autoantigen in the human skin blistering disease known as bullous pemphigoid (Mueller et al., 1989). This skin protein now referred to as BPAG1-e/dystonin-e (Dst-e), functions by tethering keratin intermediate filaments to hemidesmosomes within keratinocytes, thus playing an important role in maintaining structural integrity of the cell (Mutasim et al., 1985; Hopkinson and Jones, 2000). Since the discovery of Dst-e, several other isoforms with differential tissue expression and alternative splicing patterns have emerged (Leung et al., 2001). These include the muscle isoforms (BPAG1-b/dystonin-b or Dst-b) and neuronal isoforms (BPAG1-a/dystonin-a or Dst-a).

Historically, the intermediate filament-interacting neuronal isoform variants were described first: BPAG1n1, BPAG1n2, BPAG1n3. However, whether these are true prominent isoforms and their importance is not entirely clear. Subsequently, the spectraplakin dystonin isoforms were described (BPAG1-a1, -a2, -a3 also known as dystonin-a1, -a2, and -a3 — hereon referred to as dystonin to easily distinguish between neuronal isoforms). These latter isoforms are the predominant forms (Leung et al., 2001). The neuronal dystonin isoforms are cytoskeletal linker proteins with crucial roles in maintaining cellular shape and function. Each of the BPAG1n isoforms are believed to be derived from the same N-termini exons as the dystonin isoforms (Figure 1.1) (Suozzi et al., 2012). BPAG1n1 and dystonin-a1 have an N-terminus actin-binding domain composed of two calponin homology repeats (Jefferson et al., 2006). BPAG1n2 and dystonin-a2 also possess this actin-binding domain, but dystonin-a2's N-terminus is unique in that it is preceded by a transmembrane domain (Young et al., 2006). Finally, the N-terminus of BPAG1n3 and dystonin-a3 isoforms have a myristoylation motif that lies upstream from a single

calponin homology repeat (Figure 1.1) (Jefferson et al., 2006). Although all isoforms have a plakin domain just downstream from the calponin homology repeats, the main difference between the BPAG1n and the dystonin isoforms lies in the composition of their C-terminus. BPAG1n isoforms have a coiled-coil rod domain (also known as the plectin repeat domain), followed by a plakin repeat domain (Figure 1.1A). It is this plakin repeat domain that confers the ability of BPAG1n isoforms to interact with intermediate filaments (Yang et al., 1996). Dystonin isoforms on the other hand have a large spectrin repeat domain downstream from the plakin domain (Figure 1.1B). This domain is believed to act as a spacer to separate the different functional domains of the N- and C-termini (Suozzi et al., 2012). The C-terminus of dystonin has a microtubule-binding domain (MTBD) made up of two EF-hand motifs and a growth-arrest specific 2 protein-related region (GAR) (Figure 1.1B) (Leung et al., 2001).

The neuronal dystonin isoforms are predominantly expressed in sensory neurons and have important roles in cytoskeletal organization, organelle integrity, and intracellular transport (Dalpé et al., 1998; Liu et al., 2003; Ryan et al., 2012a; Ryan et al., 2012c). Dystonin loss-of-function in mice results in a mutant phenotype known as *dystonia musculorum* (*Dst*$^{dt}$, previously *dt*). This is a movement disorder characterized by rapid sensory neuron degeneration and death occurring around 3 weeks of age (Duchen et al., 1963, 1964; Duchen, 1976). Similarly, in humans, mutations in the BPAG1 gene (now predominantly referred to as dystonin gene; *DST*) result in a sensory neuropathy known as hereditary sensory and autonomic neuropathy type VI (HSAN-VI). Since the recent discovery of HSAN-VI in 2012 (Edvardson et al., 2012), there has been an increased drive to elucidate the unique roles of the neuronal dystonin isoforms, which should provide novel insight into the etiology of the human disease.

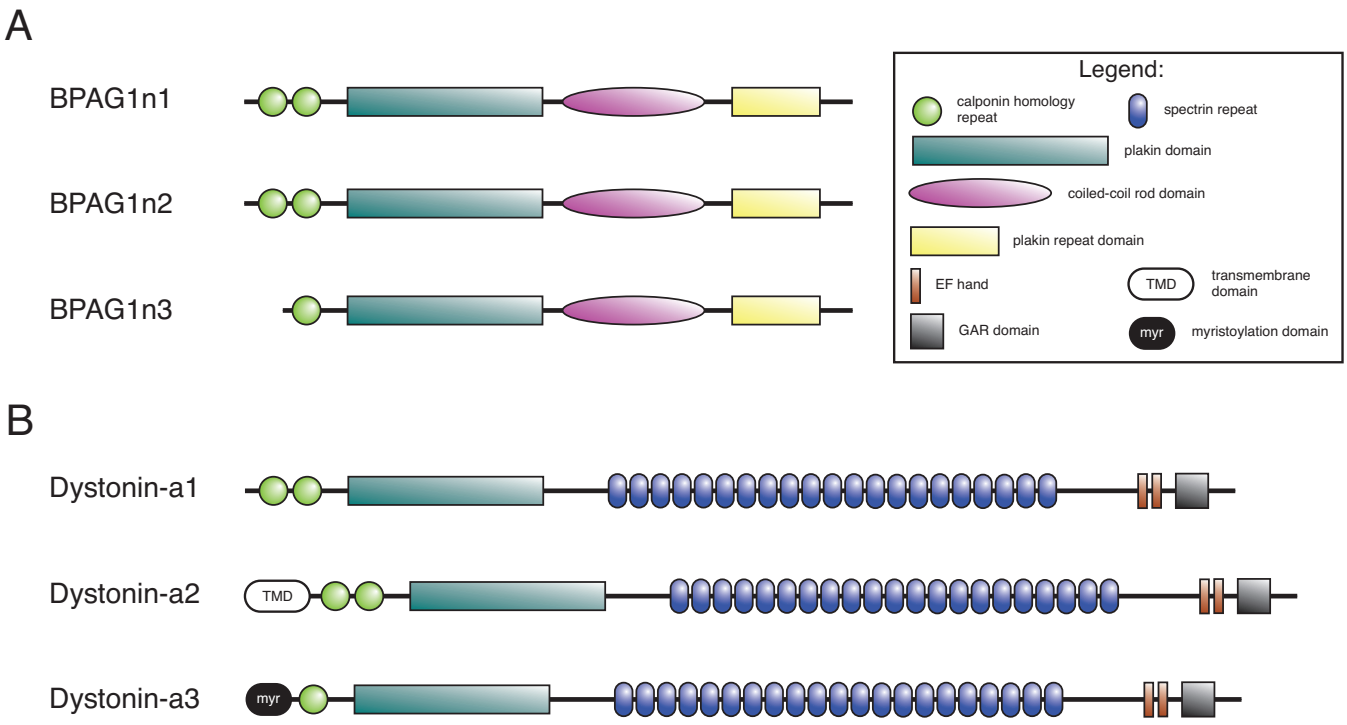


**Figure 1.1.** Schematic representation of the BPAG1 and dystonin neuronal isoforms. **(A)** The putative neuronal BPAG1 plakin proteins consist of BPAG1n1, BPAG1n2, and BPAG1n3. BPAG1n1 and BPAG1n2 were identified as having actin-binding domains consisting of two calponin homology repeats at the N-terminus. All three isoforms were suggested to have a plakin repeat domain at their C-terminus, which permits intermediate filament binding. **(B)** The neuronal BPAG1 spectraplakin proteins are the more prominent isoforms. They are much larger in size compared to the BPAG1n isoforms and consist of dystonin-a1, dystonin-a2, and dystonin-a3. The neuronal dystonin proteins also differ from the BPAG1n isoforms in that they possess a functional microtubule-binding domain at their C-termini. Like BPAG1n1, dystonin-a1 has an actin-binding domain consisting of two calponin homology repeats. Dystonin-a2, however, has a transmembrane domain (TMD) that precedes its actin-binding domain, which allows it to localize to the perinuclear membranes. Unique to dystonin-a3 is an N-terminus myristoylation motif (myr), which is believed to permit localization to the plasma membrane.

### *Dst*$^{dt}$ mice

The murine disease *dystonia musculorum* (*Dst*$^{dt}$) is a result of autosomal recessive mutations in the *Dst* gene. Many of the *Dst* mutations have arisen by spontaneous events, which is not surprising given the large size of the gene. Others have come about by transgene insertion, chemical induction, gene knockout, and gene trapping (Table 1.1). Of these, only four have been characterized at the molecular level (*Dst*$^{dt\text{-}Tg4}$, *Dst*$^{dt\text{-}Alb}$, *Dst* $^{Gt(E182H05)Wrst}$, and *Dst*$^{tm1EFu}$). In our laboratory, the primary mutant alleles used to study neuronal dystonin isoforms are *Dst*$^{dt\text{-}Tg4}$ and *Dst*$^{dt\text{-}27J}$. *Dst*$^{dt\text{-}Tg4}$ (previously referred to as *dt*$^{Tg4}$) arose due to the insertion of a multicopy *hsp68-LacZ* transgene at the 5' end of *Dst*, interrupting expression of dystonin-a1 and -a2 (Kothary et al., 1988; Brown et al., 1994; Brown et al., 1995b; Brown et al., 1995a). In contrast, the exact genetic mutation underlying the *Dst*$^{dt\text{-}27J}$ (previously referred to as *dt*$^{27J}$) allele is unknown. However, evidence suggests that this mutation results in the disruption of all neuronal dystonin isoforms in this mouse (Bernier et al., 1995; Pool et al., 2005).

Initially, *Dst*$^{dt}$ mice do not show any overt phenotype and are indistinguishable from their wild type and heterozygous littermates. Between postnatal days 7–10, *Dst*$^{dt}$ mice begin to display symptoms such as hindlimb clasping when picked up by the tail. Phenotype rapidly becomes more apparent as *Dst*$^{dt}$ mice typically remain smaller in size, and exhibit symptoms such as uncoordinated movements, writhing and twisting of the trunk, as well as hyperflexion and pronation of the paws. Average lifespan of *Dst*$^{dt}$ mice is about 3 weeks, however some differences in lifespan are observed between the different alleles. *Dst*$^{dt\text{-}27J}$ mice display a more severe phenotype and have a shorter lifespan (live to about postnatal day 18; P18) than other strains of *Dst*$^{dt}$ mice (Lynch-Godrei et al., 2018).

**Table 1.1.** The various *Dst*$^{dt}$ alleles

| Mutation Type | Allele |
|---|---|
| Spontaneous mutation | *Dst*$^{dt\text{-}22J}$, *Dst*$^{dt\text{-}23J}$, *Dst*$^{dt\text{-}23Rbrc}$, *Dst*$^{dt\text{-}24J}$, *Dst*$^{dt\text{-}25J}$, *Dst*$^{dt\text{-}26J}$, *Dst*$^{dt\text{-}27J}$ (*dt*$^{27J}$), *Dst*$^{dt\text{-}29J}$, *Dst*$^{dt\text{-}30J}$, *Dst*$^{dt\text{-}31J}$, *Dst*$^{dt\text{-}32J}$, *Dst*$^{dt\text{-}35J}$, *Dst*$^{dt\text{-}39J}$, *Dst*$^{dt\text{-}Alb}$ (*dt*$^{Alb}$), *Dst*$^{dt\text{-}J}$, and *Dst*$^{dt}$ |
| Chemically induced mutation | *Dst*$^{dt\text{-}33J}$, *Dst*$^{dt\text{-}36J}$, *Dst*$^{dt\text{-}37J}$, *Dst*$^{dt\text{-}38J}$, *Dst*$^{m1Btlr}$, *Dst*$^{m2Btlr}$, and *Dst*$^{m3Btlr}$ |
| Targeted mutation | *Dst*$^{tm1EFu}$ (*dt*$^{tm1EFu}$, BPAG1 null), *Dst*$^{tm1a(EUCOMM)Wtsi}$ and *Dst*$^{tm1b(EUCOMM)Wtsi}$ |
| Transgene insertion | *Dst*$^{dt\text{-}Tg4}$ (*dt*$^{Tg4}$) |
| Endonuclease mediated | *Dst*$^{em13Dcr}$, and *Dst*$^{em14Dcr}$ |
| Gene trapped | *Dst*$^{Gt(E182H05)Wrst}$* |

Information obtained from (Bult et al., 2019).

*Only gene trapped allele to be characterized, though 272 other gene trapped alleles exist

**Hereditary sensory and autonomic neuropathy type VI**

In 2012, a frameshift mutation in the human dystonin gene (*DST*) was discovered in three infants and one fetus (Edvardson et al., 2012). These individuals presented with a disease similar to murine $Dst^{dt}$, having symptoms such as joint contractures, problems eating and breathing, poor psychomotor development, autonomic irregularities, and a shortened lifespan (all succumbed to the disease by the age of 2). The human disease was termed hereditary sensory and autonomic neuropathy type VI (HSAN-VI), making it the most severe disease within this class of peripheral nervous system disorders (Rotthier et al., 2012).

In the years to come, a number of different *DST* mutations would be identified in adolescent and adult patients, indicating that the HSAN-VI disease presents on a spectrum and is not always lethal in childhood (Cappuccio et al., 2017; Manganelli et al., 2017; Fortugno et al., 2018). The adult patients present with a much milder form of the disease, though insensitivity to pain, joint problems, and autonomic irregularities remain universal among HSAN-VI patients. The major difference between the infants first described and the subsequent cases lies in the nature of their mutations and the number of neuronal dystonin isoforms affected. The infants described by Edvardson and colleagues possessed a frameshift mutation that disrupted the expression of the C-termini MTBD, common to all neuronal dystonin isoforms (Edvardson et al., 2012). Conversely, the adult patients contain various compound heterozygous mutations, all of which led to disrupted expression of at least the dystonin-a2 isoform. This provides further evidence from what we have already known (from $Dst^{dt}$ experiments) about the unique and vital role of dystonin-a2.

**Dystonin and microtubule stability**

As dystonin-a has roles in integrating the various components of the cytoskeleton, a lack of dystonin would result in disorganization of the cytoskeletal network. This is indeed observed in the more severe *Dst*$^{dt\text{-}27J}$ allele, as multiple studies have reported microtubule disorganization and instability in *Dst*$^{dt\text{-}27J}$ dorsal root ganglia (DRG) and sciatic nerves (Dalpé et al., 1998; De Repentigny et al., 2003; Ryan et al., 2012b). Electron microscopy analysis of *Dst*$^{dt\text{-}27J}$ DRGs and sciatic nerves reveal that microtubules and neurofilaments are highly fragmented. Unlike wild type microtubules that are well organized in parallel along the axon, *Dst*$^{dt\text{-}27J}$ microtubules are not oriented in any specific direction (Young et al., 2006; Ferrier et al., 2013).

Stability of the microtubule network also seems to be a factor in *Dst*$^{dt}$ sensory neuron pathology. One study found that levels of acetylated α-tubulin, a common marker of microtubule stability, were significantly reduced in both *Dst*$^{dt\text{-}27J}$ primary sensory neurons and DRG tissue (Ryan et al., 2012b). Knockdown experiments in human embryonic kidney (HEK) 293T cells further show that dystonin-a2 is the major isoform responsible for maintaining α-tubulin acetylation. Given this, we would expect for *Dst*$^{dt\text{-}Tg4}$ sensory neurons to also show a similar defect in microtubule stability considering their lack of the dystonin-a2 isoform.

**Dystonin and intracellular transport**

One of the hallmark pathologies of *Dst*$^{dt}$ mice is the presence of axonal swellings within the peripheral and central nervous systems (Duchen et al., 1964; Janota, 1972; Bernier et al., 1995). These axonal swellings are made up of accumulated neurofilaments, microtubules, organelles, and vesicles. This accumulation is indicative of defects in axonal transport. In 2003, De Repentigny and colleagues first identified anterograde and retrograde trafficking defects

within the sciatic nerve of *Dst*$^{dt\text{-}27J}$ mice (De Repentigny et al., 2003). These defects were also confirmed within *Dst*$^{dt\text{-}27J}$ primary sensory neurons, although it was noted that retrograde trafficking appeared to be more persistently impaired compared to anterograde trafficking (Liu et al., 2003). This observation was attributed to dystonin-a's interaction with the p150$^{Glued}$/Dctn1 subunit of the dynactin complex. As the dynactin complex is an activator for the dynein motor protein, a mediator of retrograde transport, interruption of this relationship is likely to have a negative effect on cargo movement in the retrograde direction (Liu et al., 2003). Further evaluation went on to identify an endosomal transmembrane protein termed retrolinkin as an interacting partner of BPAG1n4 (dystonin-a) (Liu et al., 2007; Ferrier et al., 2013). Considering the nature of these two interacting partners, it was proposed that the trafficking defects observed in *Dst*$^{dt\text{-}27J}$ sensory neurons was due to the uncoupling of endosomes and endosome-related vesicles from dynein motors.

Dystonin-a2 has also been suggested to have a role in intracellular trafficking. Knockdown of this isoform in HEK 293T cells leads to defects in the secretory flux pathway (Ryan et al., 2012b). This however was suggested to be a result of a more indirect role of dystonin-a2 on intracellular trafficking, via the maintenance of microtubule acetylation (as previously discussed). Albeit this indirect mechanism is the only one that has been characterized so far, and the possibility of a more direct role in intracellular trafficking may also exist.

**Autophagy and the endolysosomal pathway**

The intracellular process of autophagy is an essential mechanism for degrading and recycling old or damaged cellular material. This is particularly important in times of starvation to allow for the production of new functional cell components, but is also an essential process in

non-dividing cells like neurons, to maintain homeostasis and prevent accumulation of dysfunctional material. There are three main types of autophagy: microautophagy, chaperone-mediated autophagy, and macroautophagy. Both microautophagy and chaperone-mediated autophagy involve the direct transfer of cargo to the lysosome for degradation (Parzych and Klionsky, 2014). However, macroautophagy (herein referred to as simply autophagy) is much more complex in that it involves the formation of a double membraned vesicle around the cargo that is to be degraded. In neurons, which are highly polarized cell types, autophagosome biogenesis is most prevalent at the distal axon process (Maday et al., 2012; Maday and Holzbaur, 2014). Upon formation, autophagosomes appear to have bidirectional movement, which is restricted to the neurite tip. However upon exit from the axon tip, this switches to a robust retrograde movement. This form of movement is orchestrated by the dynein motor protein and its associated activators (e.g. $p150^{Glued}$/Dctn1). Recently it was discovered that the means by which dynein is recruited to autophagic vacuoles is through fusion with late endosomes that are already primed with dynein motors (Cheng et al., 2015a, b). Fusion of these two vesicle types results in the formation of a vesicle known as an amphisome. The amphisome exits the neurite tip with primarily retrograde movement, and will mature as it is transported along the axon towards the soma (Maday et al., 2012). The end stages of autophagy involve the formation of the autolysosome, whereby the amphisome fuses with mature acidic lysosomes located around the soma. Release of the lysosome's digestive enzymes will result in degradation of the luminal contents, and eventual recycling of the broken down biological matter.

**The gastrointestinal tract of *Dst*$^{dt}$ mice**

Through rigorous evaluation of *Dst*$^{dt}$ mouse organ systems, it was noted that striking differences exist between gut gross morphology of wild type and *Dst*$^{dt}$ mice. This varies to a certain degree between *Dst*$^{dt\text{-}27J}$ and *Dst*$^{dt\text{-}Tg4}$ mice, however they both present with gastrointestinal irregularities such as: large bloated sections of the intestine, pockets filled with gas, bubbles along the length of the gastrointestinal tract (GIT), and an occasional greenish-brown colouration of the GIT. Furthermore, with the recent identification of adult HSAN-VI patients we learned that GIT symptoms (such as abdominal pain and chronic diarrhea) also present with the disease.

As the enteric nervous system is composed of about 22 different kinds of neurons, many of which are sensory subtype (known as the intrinsic primary afferent neurons, or IPANs) (Furness et al., 2014), we speculate that these neurons may also be vulnerable to dystonin loss-of-function akin to DRG sensory neurons. Enteric neurodegeneration could be linked to defective gut morphology and impaired GIT function, and possibly even account for the gastrointestinal symptoms experienced by HSAN-VI patients.

## Hypothesis

We hypothesize that: 1) neuronal dystonin is necessary for efficient intracellular transport in sensory neurons, and that the defects observed in *Dst*$^{dt}$ sensory neurons are linked to microtubule instability and insufficient motor protein availability; and 2) degeneration of the enteric nervous system is linked to defective structure and function of the gastrointestinal tract in *Dst*$^{dt}$ mice.

## Objectives

1) Characterize microtubule stability in *Dst*$^{dt}$ sensory neurons
2) Evaluate motor protein expression profiles, and the endolysosomal pathway in dystonin deficient cells
3) Examine the structure and function of the gastrointestinal tract and enteric nervous system of *Dst*$^{dt}$ mice

# Chapter 2:

# Disruption in the autophagic process underlies the sensory neuropathy in *dystonia musculorum* mice

# Disruption in the autophagic process underlies the sensory neuropathy in *dystonia musculorum* mice

Andrew Ferrier[1,2,#], Yves De Repentigny[1,#], Anisha Lynch-Godrei[1,2], Sabrina Gibeault[1], Walaa Eid[1,3], Daniel Kuo[1], Xiaohui Zha[1,3,4], and Rashmi Kothary[1,2,4,5,*]

[1]Regenerative Medicine Program, Ottawa Hospital Research Institute, Ottawa, K1H 8L6, Canada

[2]Department of Cellular and Molecular Medicine, University of Ottawa, Ottawa, K1H 8M5, Canada

[3]Department of Biochemistry, Microbiology, and Immunology, University of Ottawa, Ottawa, K1H 8M5, Canada

[4] Department of Medicine, University of Ottawa, Ottawa, K1H 8M5, Canada

[5]Centre for Neuromuscular Disease, University of Ottawa, K1H 8M5, Canada

*To whom correspondence should be addressed at: Ottawa Hospital, 501 Smyth Road, ORCC 4406a, Ottawa, Ontario, K1H 8L6, Canada; Tel: (613) 737-8707; Fax: (613) 737-8803; Email: rkothary@ohri.ca

[#] These authors contributed equally to this work

***Published in Autophagy 2015, 11(7): 1025-1036***

**Author Contributions:**

AF (figures 2.1, 2.3, 2.4, 2.5A & B, 2.6A-C, 2.7A & B, and supplemental figures S2.1, S2.2A) and YDR (figures 2.2, 2.5C-E, and supplemental figures S2.2B-D) performed the research assisted by ALG (figure 2.6A, 2.7C), WE (figure 2.6A), DK, and SG. Study designed by AF, data analyzed by AF, YDR, ALG, and the paper was written by AF and ALG with assistance and supervision from RK.

**Abstract**

A homozygous mutation in the *DST* (dystonin) gene causes a newly identified lethal form of hereditary sensory and autonomic neuropathy in humans (HSAN-VI). *Dst* loss of function similarly leads to sensory neuron degeneration and severe ataxia in dystonia musculorum ($Dst^{dt}$) mice. Dst is involved in maintaining cytoskeletal integrity and intracellular transport. As autophagy is highly reliant upon stable microtubules and motor proteins, we assessed the influence of Dst loss of function on autophagy using the $Dst^{dt\text{-}Tg4}$ mouse model. Electron microscopy (EM) revealed an accumulation of autophagosomes in sensory neurons from these mice. Furthermore, we demonstrated that the autophagic flux was impaired. Levels of LC3-II, a marker of autophagosomes, were elevated. Consequently, $Dst^{dt\text{-}Tg4}$ sensory neurons displayed impaired protein turnover of autophagosome substrate SQTSM1/p62 and of polyubiquitinated proteins. Interestingly, in a previously described $Dst^{dt\text{-}Tg4}$ mouse model that is partially rescued by neuronal specific expression of the *Dst-a2* isoform, autophagosomes, autolysosomes, and damaged organelles were reduced when compared to $Dst^{dt\text{-}Tg4}$ mutant mice. LC3-II, SQTSM1, polyubiquitinated proteins and autophagic flux were also restored to wild-type levels in the rescued mice. Finally, a significant decrease in Dnaic1 (dynein, axonemal, intermediate chain 1; the mouse ortholog of human DNAI1), a member of the DMC (dynein/dynactin motor complex), was noted in $Dst^{dt\text{-}Tg4}$ dorsal root ganglia and sensory neurons. Thus, *Dst-a2* loss of function perturbs late stages of autophagy, and dysfunctional autophagy at least partially underlies $Dst^{dt}$ pathogenesis. We therefore conclude that the Dst-a2 isoform normally facilitates autophagy within sensory neurons to maintain cellular homeostasis.

## Introduction

DST is a large cytoskeletal linker protein whose loss of function in both humans and mice results in lethal peripheral neuropathies, namely HSAN-VI and $Dst^{dt,}$ respectively (Brown et al., 1995b; Edvardson et al., 2012). In mice, homozygous recessive mutations in the *Dst* gene cause a severe sensory neuropathy, characterized by overt ataxic and dystonic movements, rapid sensory neuron degeneration, and ultimately death at approximately 3 wk of age (Duchen et al., 1964; Duchen, 1976). The *Dst* gene gives rise to 3 tissue-specific Dst isoforms expressed in neurons, muscle, and epithelial cells (Sawamura et al., 1991; Brown et al., 1995a; Leung et al., 2001; Okumura et al., 2002). Moreover, through alternative splicing of the first 50 exons, 3 major neuronal isoforms are produced, namely Dst-a1, Dst-a2, and Dst-a3. The overall domain architecture of each Dst isoform is similar, comprising of an N-terminal actin binding domain, an extensive coiled-coil region, and a C-terminal microtubule (MT)-binding domain. However, each contains unique N-terminal regions that differentiate them and consequently determine their subcellular localization and biological functions (Ferrier et al., 2013). Loss of *Dst-a1* and *Dst-a2* is the cause of the $Dst^{dt\text{-}Tg4}$ disorder (Pool et al., 2005). The $Dst^{dt\text{-}27J}$ mutant allele, in contrast, precludes the expression of all *Dst* isoforms, exhibits a more severe phenotype, and is allelic to $Dst^{dt\text{-}Tg4}$ mice and do not complement (Pool et al., 2005; Ferrier et al., 2013).

Autophagy is essential in the maintenance of neuronal homeostasis (Hara et al., 2006; Komatsu et al., 2006), and is implicated in various neurodegenerative diseases (Wong and Cuervo, 2010). Within peripheral nerves, the transport of autophagosomes is highly reliant upon the neuronal cytoskeleton and its constituent parts, particularly MTs and motor proteins (Jahreiss et al., 2008; Kimura et al., 2008; Monastyrska et al., 2009). This dependence on the cytoskeleton is because autophagosomes form distally in the axon and are transported in a retrograde manner

toward the soma in order to fuse with lysosomes (Maday et al., 2012). Indeed, perturbing the stability of MTs or motor protein function disrupts autophagic flux (Aplin et al., 1992; Ravikumar et al., 2005; Köchl et al., 2006), which in turn can lead to the demise of the cell.

A number of studies suggest that a lack of Dst isoforms might negatively influence autophagy, most likely through impairments in motor protein trafficking and/or MT dynamics (Dalpé et al., 1998; Liu et al., 2003; Liu et al., 2007; Bhanot et al., 2011; Ryan et al., 2012b). Stable MTs in neurons are required for the recruitment of motor proteins and proper trafficking (Reed et al., 2006; Dompierre et al., 2007). Moreover, the biogenesis and fusion of autophagosomes with lysosomes relies upon stabilized MTs (Geeraert et al., 2010; Xie et al., 2010), therefore implicating Dst in multiple aspects of autophagy.

Here we demonstrate that sensory neurons from presymptomatic $Dst^{dt\text{-}Tg4}$ mice have increased levels of the autophagosome marker LC3-II as compared to wild type (WT). Electron microscopy further confirmed an increase in autophagosome number in $Dst^{dt\text{-}Tg4}$ sensory neurons, as well as an increase in autolysosomes and aberrant mitochondria. We also find that while autophagic flux proceeds normally in primary $Dst^{dt\text{-}Tg4}$ cortical neurons, it is impaired in sensory neurons from presymptomatic $Dst^{dt\text{-}Tg4}$ mice, suggesting Dst loss of function imparts a cell-specific impairment on autophagy. Consequently, impairments in autophagic flux within presymptomatic $Dst^{dt\text{-}Tg4}$ sensory neurons lead to impaired protein turnover, resulting in accumulated autophagic substrates SQTSM1/p62 and polyubiquitinated proteins. Similarly, we observed a decrease in Dnaic1 protein levels in sensory neurons but not cortical neurons of $Dst^{dt\text{-}Tg4}$ mice.

Interestingly, $Dst^{dt\text{-}Tg4}$ sensory neurons expressing *Dst-a2* exogenously show reversion of these aforementioned autophagic defects. We conclude that less stable MTs and reduced

retrograde motor protein expression underlie the defects observed in autophagy in the *Dst*$^{dt\text{-}Tg4}$ mouse. Collectively, this work establishes the importance of Dst in the autophagic process, and further highlights that impairments in autophagic homeostasis contribute to the dysfunction and death of sensory neurons in *Dst*$^{dt}$ mice.

## Results

### $Dst^{dt\text{-}Tg4}$ sensory neurons exhibit autophagosome accumulation

Dst plays an important role in integrating the various cytoskeletal components, which is necessary for the maintenance of MT organization and stability (Dalpé et al., 1998; Ryan et al., 2012b). As the process of autophagy is highly dependent on the MT network for efficient trafficking of autophagosomes to lysosomes, we hypothesized that the disorganized MT network due to Dst loss of function in $Dst^{dt}$ mice would impede transport of autophagosomes within neurons.

Autophagosomes are transient structures, undergoing rounds of maturation and degradation in lysosomes. Impairment in autophagic activity through diminished trafficking, for instance, could be reflected by a buildup of autophagosomes. To address whether this occurs in $Dst^{dt\text{-}Tg4}$ sensory neurons, we examined the levels of LC3-II. Total dorsal root ganglia (DRGs) were collected from symptomatic (P17: postnatal day 17) and presymptomatic (P10) WT and $Dst^{dt\text{-}Tg4}$ mice. Compared to P17 WT DRGs, $Dst^{dt\text{-}Tg4}$ DRGs displayed a significant increase in LC3-II protein levels (Figure 2.1A). P10 $Dst^{dt\text{-}Tg4}$ DRGs also displayed an increase in LC3-II protein levels compared to WT (Figure 2.1B). In addition, DRGs from a second allele ($Dst^{dt\text{-}27J}$) also displayed increased LC3-II protein levels compared to WT littermates, suggesting that this is a common pathological signature of $Dst^{dt}$ DRGs (Figure S2.1).

To determine if the increase in LC3-II protein level reflects accumulation in autophagosomes and not accelerated LC3-I processing, we conducted transmission EM on P5 (presymptomatic) WT and $Dst^{dt\text{-}Tg4}$ primary sensory neurons that were cultured in nutrient-rich media for 5 d. Our qualitative analysis suggested that WT sensory neurons were largely devoid of autophagosomes (Figure 2.2A & A'), while $Dst^{dt\text{-}Tg4}$ sensory neurons were replete with

double-membrane autophagosomes, damaged mitochondria (Figure 2.2B & B'), and enlarged autolysosomes (Figure 2.2C & C').

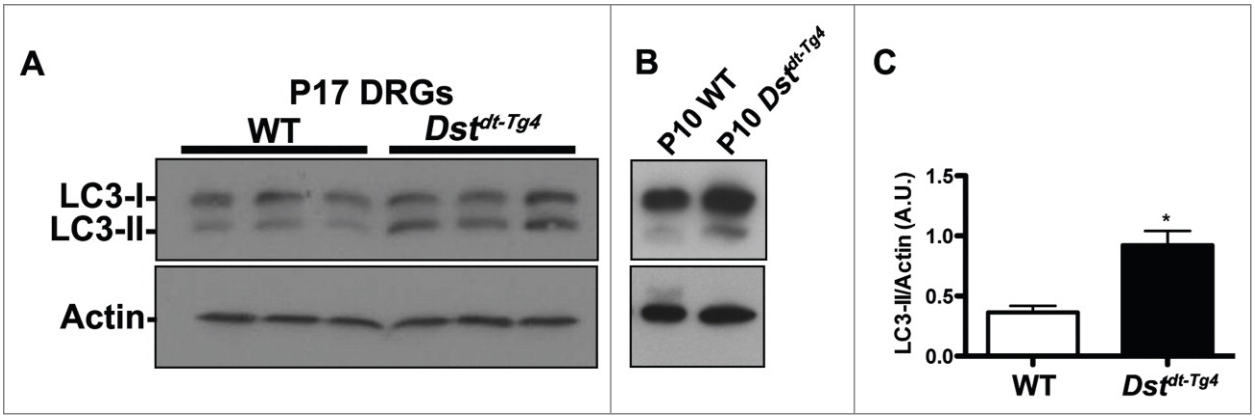


**Figure 2.1** Sensory neurons from symptomatic and presymptomatic *Dst*$^{dt\text{-}Tg4}$ mice display increased LC3-II protein levels. **(A)** DRG protein lysates from P17 WT and symptomatic *Dst*$^{dt\text{-}Tg4}$mice were analyzed by western blot for LC3-II protein levels. A significant induction of LC3-II was observed in P17 *Dst*$^{dt\text{-}Tg4}$ DRGs. LC3-I represents a soluble form and LC3-II a lipidated and membrane-bound form of LC3 (a key autophagy marker). Each lane represents 20 μg of DRG protein collected from a single mouse. **(B)** Induction of LC3-II is also evident in DRGs of presymptomatic (P10) *Dst*$^{dt\text{-}Tg4}$ mice. **(C)** Quantification by densitometry of the blot in **(A)**. LC3-II levels are normalized to total actin levels. Student's *t*-test; error bars represented as SEM (**P* < 0.05).

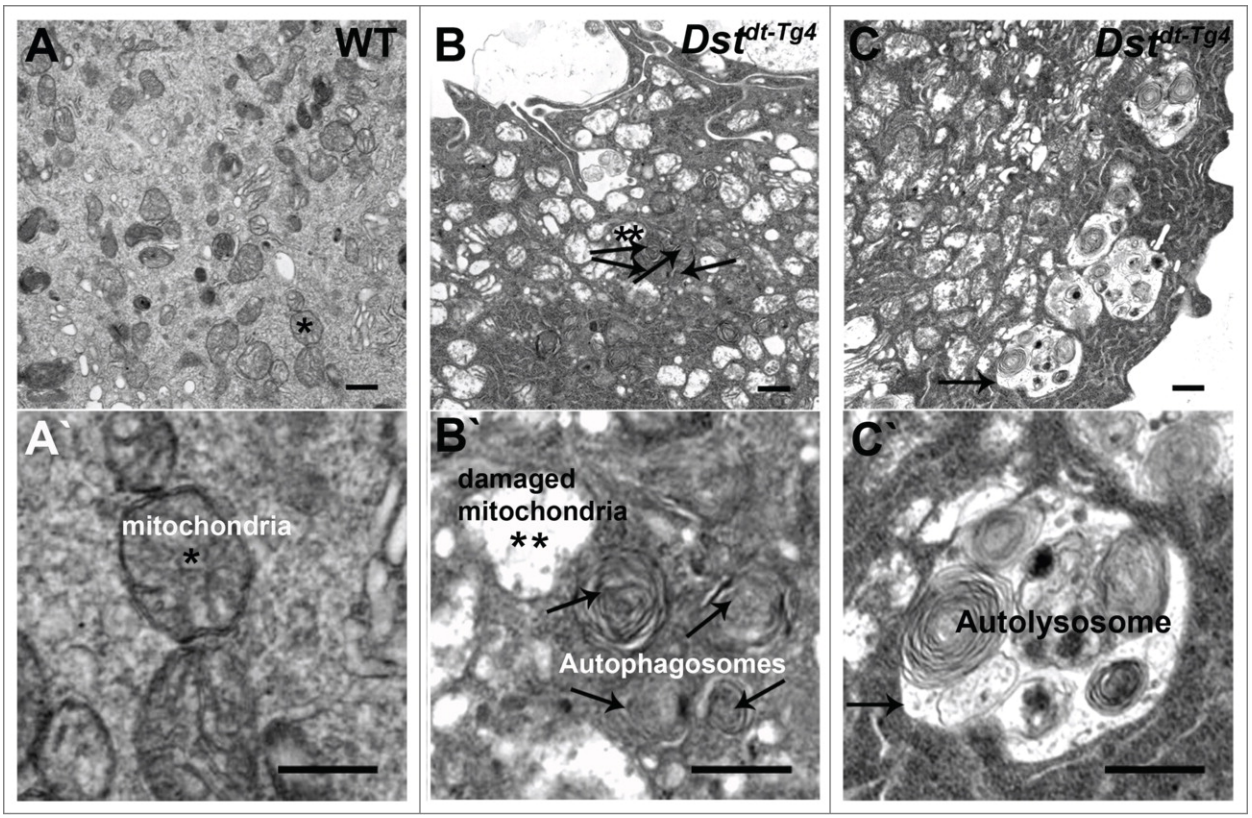


**Figure 2.2** Ultrastructural analysis of sensory neurons derived from P5 WT and *Dst*$^{dt\text{-}Tg4}$ mice. **(A, A')** WT sensory neurons cultured for 5 d did not display any autophagosomes, autolysosomes, and damaged mitochondria. **(B, B')** Damaged mitochondria (asterisks) and accumulating double-membrane autophagosomes (arrows) were evident in *Dst*$^{dt\text{-}Tg4}$ sensory neurons. **(C, C')** Single-membrane autolysosome vacuoles with electron-dense sequestered material (arrows) were also present in *Dst*$^{dt\text{-}Tg4}$ sensory neurons. Magnification and scale bars for **A)**, **B)**, and **C)** (20,000X, scale bar: 500 nm), and **A')**, **B')**, and **C')** (60,000X, scale bar: 500 nm).

Autophagic flux is compromised in *Dst*$^{dt\text{-}Tg4}$ sensory neurons but not in cortical neurons

The increased expression of LC3-II coupled with the pathologies observed in our EM analysis suggests that autophagy initiation is normal or even upregulated but fails to proceed to completion in *Dst*$^{dt\text{-}Tg4}$ sensory neurons. Indeed, increased LC3- II protein levels, accumulating autophagosomes, autolysosomes, and damaged mitochondria are all indicative of impairments in the latter stages of the autophagy pathway (Levine and Kroemer, 2008; Xie et al., 2011). To address whether autophagy proceeds normally in *Dst*$^{dt\text{-}Tg4}$ neurons, we assessed autophagic flux. Autophagic flux encompasses the maturation of autophagosomes to the trafficking, fusion and degradation of autophagic material in lysosomes (Yang and Klionsky, 2010). We made use of a well-established cortical neuron culture system to assess autophagic flux, with the expectation that *Dst*$^{dt\text{-}Tg4}$ cortical neurons would mirror the autophagy impairments observed in *Dst*$^{dt\text{-}Tg4}$ sensory neurons. Cortical neurons are amenable to autophagic flux conditions, easy to culture, and like sensory neurons, express Dst (Bernier et al., 1995). Cortices from P0 mice were dissociated and cultured for 7 d in nutrient-rich conditions in the presence of serum supplement B27 and mitotic inhibitors to reduce contaminating cells. As anticipated, prior to assessing autophagic flux, both WT and *Dst*$^{dt\text{-}Tg4}$ cortical neurons produced extensive branching, as assessed by anti-tubulin, b 3 class III (TUBB3) staining (Figure 2.3A), and anti-glial fibrillary acidic protein immunostaining showed few, if any, contaminating astrocytes present within the cultures (data not shown). Furthermore, RT-PCR analyses of WT cortical neurons indicated that both *Dst-a1* and *Dst-a2* transcripts were expressed (Figure 2.3B).

Following 7 d in culture, autophagic flux was assessed in WT and *Dst*$^{dt\text{-}Tg4}$ cortical neurons. Neurons were treated with 500 nM rapamycin for 2 h to induce autophagy. In some instances neurons were also treated with 30 mM chloroquine for 2 h to block autophagosome

degradation. The controls included untreated neurons, and neurons treated with chloroquine alone. Surprisingly, we found that WT and *Dst*$^{dt\text{-}Tg4}$ cortical neurons showed a similar autophagic flux profile (Figure 2.3C & D). Untreated conditions for both WT and *Dst*$^{dt\text{-}Tg4}$ cortical neurons were marked by low basal levels of LC3-II, while neurons treated with the autophagy inducing agent rapamycin showed slight increases in LC3-II protein levels compared to untreated samples. As expected, blocking lysosomal activity with chloroquine produced even greater amounts of LC3-II protein compared to rapamycin and untreated conditions. Similarly, we saw increased LC3-II protein levels when cortical neurons were treated with both rapamycin and chloroquine. Coupled with this, we performed immunocytochemical quantitative analyses of LC3-II puncta in both the cell soma and axons following autophagic induction with 500 nM rapamycin for 2 h (Figure 2.3E–H). Neurons displayed a striking LC3-II puncta distribution, consistent with prominent autophagosome formation. The average number of LC3-II puncta within cell soma and axons was equivalent between WT and *Dst*$^{dt\text{-}Tg4}$ cortical neurons (n = 3). Thus, autophagy is apparently normal in cortical neurons, despite the absence of both Dst-a1 and Dst-a2.

To assess whether Dst loss of function specifically impacts autophagic activity in *Dst*$^{dt\text{-}Tg4}$ sensory neurons, we performed similar flux assays. Presymptomatic (P5) WT and *Dst*$^{dt\text{-}Tg4}$ primary sensory neurons were cultured for 5 d in nutrient-rich sensory neuron media and challenged in the aforementioned flux conditions. Due to low yields in cell number, each autophagic flux condition, that is each lane of the western blot, represented total sensory neurons from a single mouse. Both P5 WT and *Dst*$^{dt\text{-}Tg4}$ primary sensory neurons exhibited extensive neurite outgrowth and were devoid of any dying sensory neurons after 5 d in culture as assessed by antigenic labeling of TUBB3 and CASP3 (caspase 3, apoptosis-related cysteine peptidase), respectively (Figure 2.4A & B).

As expected, WT primary sensory neurons displayed a typical autophagic flux profile (Figure 2.4C), akin to what was observed with cortical neurons. In contrast, presymptomatic $Dst^{dt\text{-}Tg4}$ sensory neurons had persistently high levels of LC3-II, and were completely insensitive to rapamycin and chloroquine treatment (Figure 2.4D). Even untreated $Dst^{dt\text{-}Tg4}$ sensory neurons displayed high LC3-II protein levels. Indeed, LC3-II protein levels in untreated $Dst^{dt\text{-}Tg4}$ sensory neurons were comparable to those in the other 3 $Dst^{dt\text{-}Tg4}$ flux conditions. This suggests that autophagy is already upregulated in $Dst^{dt\text{-}Tg4}$ sensory neurons, and that autophagosomes are not being turned over adequately or at all. Taken together, we conclude that loss of Dst disrupts autophagic flux in $Dst^{dt\text{-}Tg4}$ sensory neurons, but not in cortical neurons.

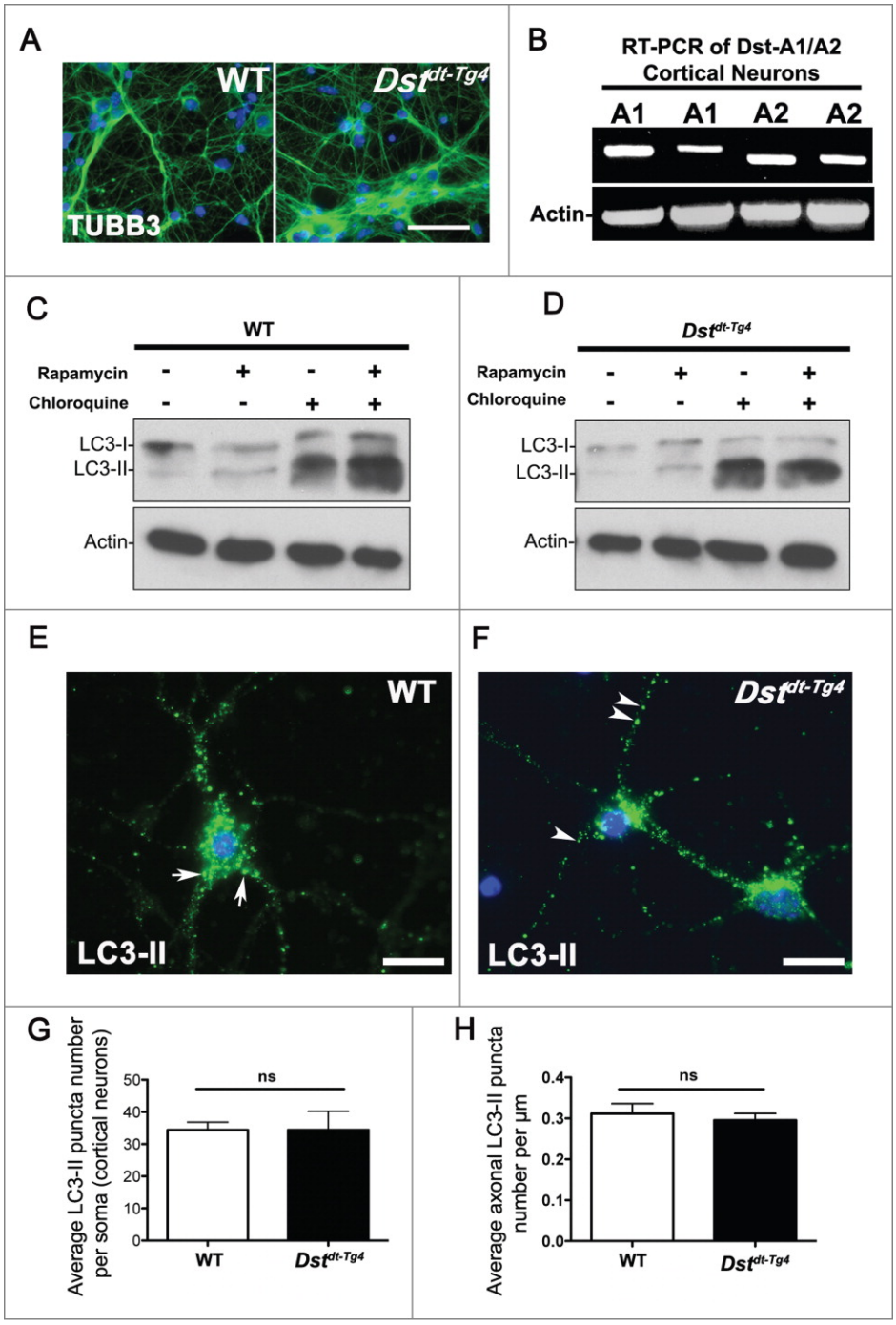


**Figure 2.3** Autophagic flux proceeds normally in cortical neurons derived from *Dst*$^{dt\text{-}Tg4}$ mice. **(A)** P0 primary cortical neurons from WT or *Dst*$^{dt\text{-}Tg4}$ mice were cultured for 7 d and antigenically labeled for TUBB3. Both genotypes exhibit extensive neurite branching and

viability (scale bar: 20 μm). **(B)** *Dst-a1* and *Dst-a2* transcripts are present in WT cortical neurons as assessed by RT-PCR. **(C and D)** Both WT **(C)** and $Dst^{dt\text{-}Tg4}$ **(D)** cortical neurons display similar autophagic flux profiles (n = 2). Where indicated, neurons were treated with autophagy-inducing agents (500 nM rapamycin), or autophagy blocking agents (30 μM chloroquine) for 2 h. Each lane represents a cortical neuron lysate derived from a single mouse. Cultures were lysed, total proteins (10 μg per lane) were separated by SDS-PAGE, and endogenous LC3 was recognized by antigenic labeling with anti-LC3B antibody. Actin served as a loading control. **(E and F)** Representative immunocytochemical images of cortical neurons from WT **(E)** and $Dst^{dt\text{-}Tg4}$ **(F)** mice stained with anti-LC3B (scale bar: 10 μm). Arrows and arrowheads exemplify LC3-II puncta within the neuronal soma or axons, respectively. **(G)** Average number of LC3-II puncta per WT (34.39 ± 2.442) and $Dst^{dt\text{-}Tg4}$ (34.45 ± 5.774) soma showed no significant difference (Student's *t* test, $P = 0.99$; n = 3, with 40 cells analyzed per n). **(H)** Average number of axonal LC3-II puncta per μm length showed no significant difference between WT (0.3114 ± 0.02426) and $Dst^{dt\text{-}Tg4}$ (0.2955 ± 0.01625) neurons (Student's *t* test, $P = 0.71$; n = 3 with 40 cells analyzed per n).

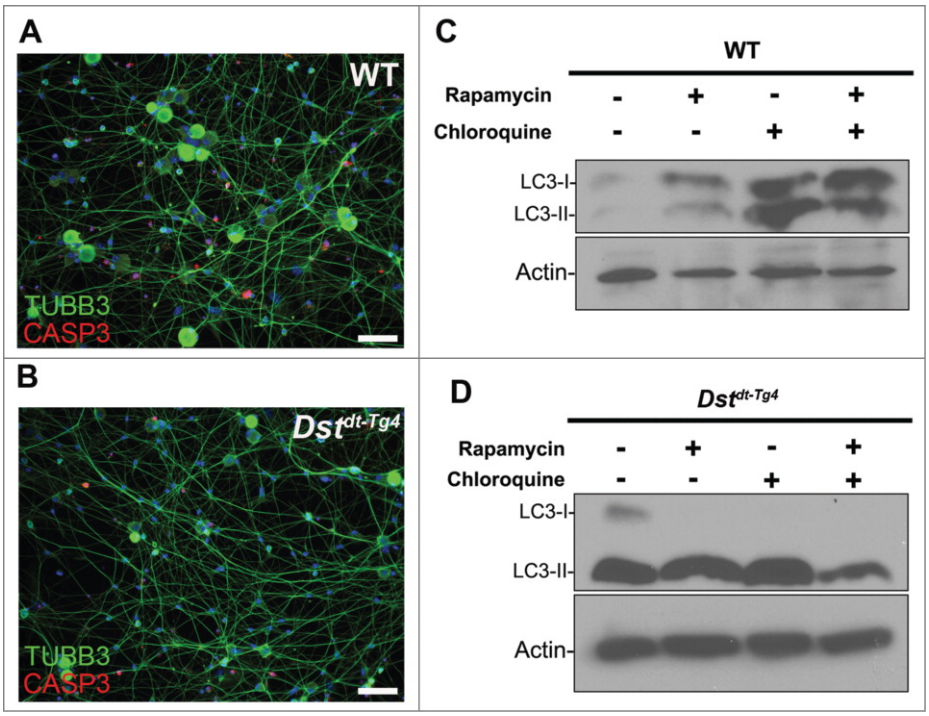


**Figure 2.4** Abnormal autophagic flux in sensory neurons derived from *Dst*$^{dt\text{-}Tg4}$ mice. **(A** and **B)** P5 primary sensory neurons from WT **(A)** or *Dst*$^{dt\text{-}Tg4}$ **(B)** mice were cultured for 5 d and antigenically labeled for TUBB3 and CASP3. Both genotypes exhibit extensive neurite branching and are devoid of CASP3-positive neurons (scale bar: 20 µm). **(C** and **D)** WT **(C)** and *Dst*$^{dt\text{-}Tg4}$ **(D)** display dissimilar autophagic flux profiles (n = 2). Where indicated, neurons were treated with autophagy inducing agents (500 nM rapamycin), or autophagy blocking agents (30 µM chloroquine) for 2 h. Note the high levels of LC3-II proteins within each lane of the *Dst*$^{dt\text{-}Tg4}$ sensory neuron flux assay. Each lane represents a sensory lysate derived from a single mouse. Cultures were lysed, total proteins (10 µg per lane) were separated by SDS-PAGE, and LC3-I and LC3-II were recognized by antigenic labeling with anti-LC3B antibody. Actin served as a loading control.

Restoring *Dst-a2* expression in *Dst*$^{dt\text{-}Tg4}$ sensory neurons ameliorates defects in autophagic flux

Recently, loss of Dst-a2 has been determined as a principal initiator of neuronal degeneration in *Dst*$^{dt}$ mice (Ryan et al., 2012b; Ryan et al., 2012c; Ferrier et al., 2014). To determine if loss of Dst-a2 underlies the autophagic defects observed in *Dst*$^{dt\text{-}Tg4}$ sensory neurons, we employed the *PrP-Dst-A2/PrP-Dst-A2*;*Dst*$^{dt\text{-}Tg4}$ transgenic mouse model (Ferrier et al., 2014). These transgenic mice express exogenous *Dst-a2* under the control of the neuronal prion protein promoter *(PrP-Dst-a2*) on the *Dst*$^{dt\text{-}Tg4}$ background. They robustly express *Dst-a2* throughout the nervous system, and particularly in sensory neurons (Ferrier et al., 2014), and would be expected to exhibit a restoration or "rescue" of responses toward the WT phenotype. For simplicity, these mice will henceforth be termed *PrP/Dst*$^{dt\text{-}Tg4}$ in the manuscript.

P5 PrP/*Dst*$^{dt\text{-}Tg4}$ sensory neurons cultured for 5 d were viable, displayed extensive axonal branching, and were devoid of dying sensory neurons (Figure 2.5A). Unlike P5 *Dst*$^{dt\text{-}Tg4}$ sensory neurons (Figure 2.4D), P5 *PrP/Dst*$^{dt\text{-}Tg4}$ sensory neurons exhibited a normal LC3-II flux profile (Figure 2.5B). Furthermore, EM micrographs of P5 *PrP/Dst*$^{dt\text{-}Tg4}$ sensory neurons cultured for 5 d also showed a reduction in the number of autophagosomes, autolysosomes, and abnormal mitochondria (Figure 2.5D) compared to *Dst*$^{dt\text{-}Tg4}$ sensory neurons (Figures 2.2B & C, and 2.5E).

As one of the consequences of the autophagic pathway is degradation of long-lived proteins, we assessed protein turnover by radiolabeling with [$^{14}$C]-L-valine. There was a significant decrease in the rate of protein degradation in *Dst*$^{dt\text{-}Tg4}$ sensory neurons compared to WT sensory neurons (Figure 2.6A). Transgenic expression of *Dst-a2*, as in *PrP/Dst*$^{dt\text{-}Tg4}$ sensory neurons, effectively restored protein degradation by autophagy to WT levels (Figure 2.6A).

In numerous *in vitro* and *in vivo* neurodegenerative models, impairment in autophagy results in the accumulation of autophagosome substrates SQTSM1 and ubiquitin-containing

aggregates (Bjorkoy et al., 2005; Pankiv et al., 2007; Johansen and Lamark, 2011). As such, defects in protein turnover within $Dst^{dt\text{-}Tg4}$ sensory neurons observed above should also lead to an increase in SQTSM1 and polyubiquitinated proteins. Indeed, P5 $Dst^{dt\text{-}Tg4}$ primary sensory neurons cultured for 5 d exhibited significant increases in both LC3-II and SQTSM1 protein levels compared to WT samples (Figure 2.6B). Once again, LC3-II and SQTSM1 protein levels were reduced to WT levels in P5 $PrP/Dst^{dt\text{-}Tg4}$ sensory neurons (Figure 2.6B). Also in agreement with these results, WT and $PrP/Dst^{dt\text{-}Tg4}$ sensory neurons displayed fewer polyubiquitinated proteins compared to $Dst^{dt\text{-}Tg4}$ sensory neurons (Figure 2.6C). Taken together, these results show that autophagic-mediated protein degradation is impaired in $Dst^{dt\text{-}Tg4}$ sensory neurons, and Dst-a2 is necessary for the optimal functioning of autophagy in sensory neurons.

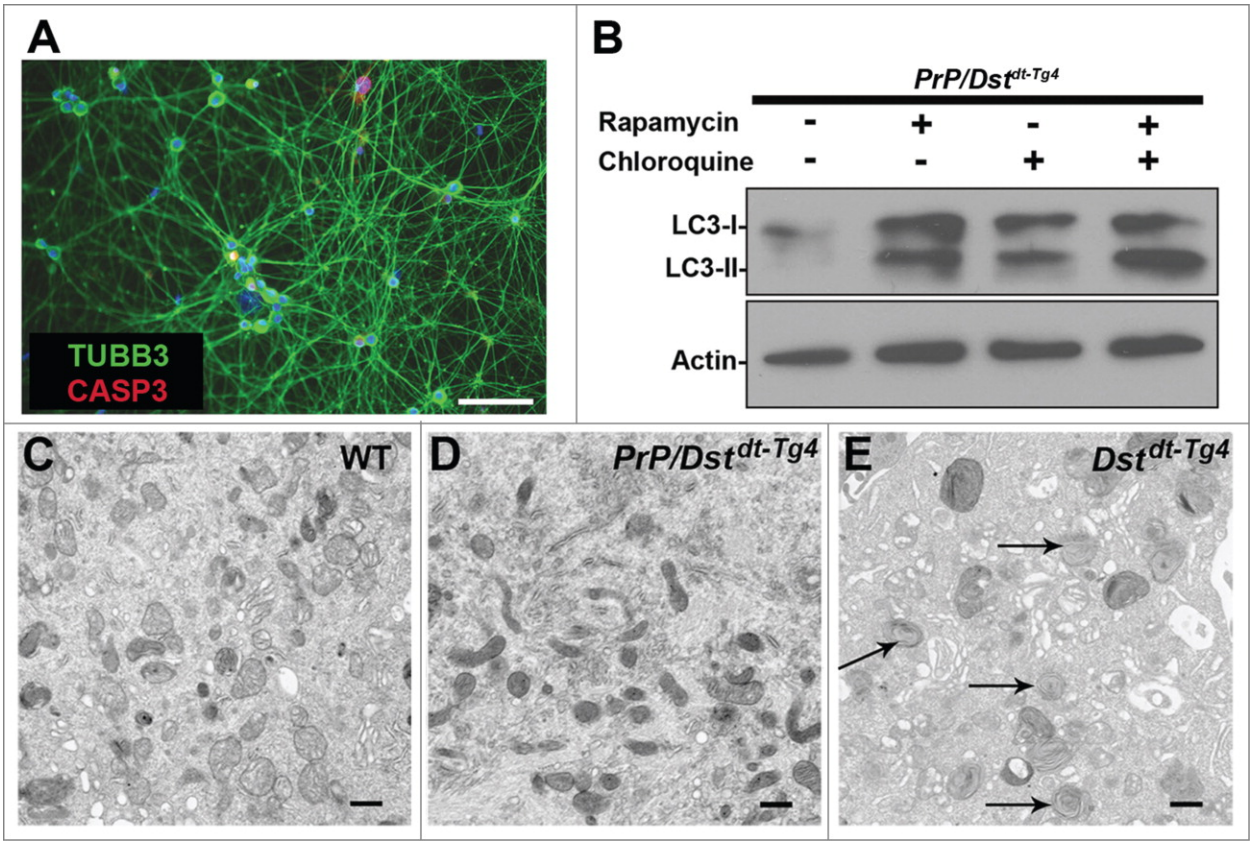


**Figure 2.5** Exogenous *Dst-a2* expression in sensory neurons of *PrP/Dst*$^{dt\text{-}Tg4}$ mice ameliorates autophagic defects. **(A)** Antigenic labeling for TUBB3 and CASP3 indicates presymptomatic (P5) *PrP/Dst*$^{dt\text{-}Tg4}$ sensory neurons are mature, forming extensive neurites, and do not undergo apoptosis (scale bar: 50 μm). **(B)** Autophagic flux in P5 *PrP/Dst*$^{dt\text{-}Tg4}$ sensory neurons proceeds normally. Representative EM micrographs of P5 WT **(C)**, *PrP/Dst*$^{dt\text{-}Tg4}$ **(D)**, and *Dst*$^{dt\text{-}Tg4}$ **(E)** sensory neurons. WT and *PrP/Dst*$^{dt\text{-}Tg4}$ micrographs are free of accumulating autophagosomes, single-membrane autolysosomes, and damaged mitochondria. *Dst*$^{dt\text{-}Tg4}$ sensory neurons, on the other hand, are replete with double-membrane autophagosomes (arrows). (Magnification 20,000X, scale bar: 500 nm).

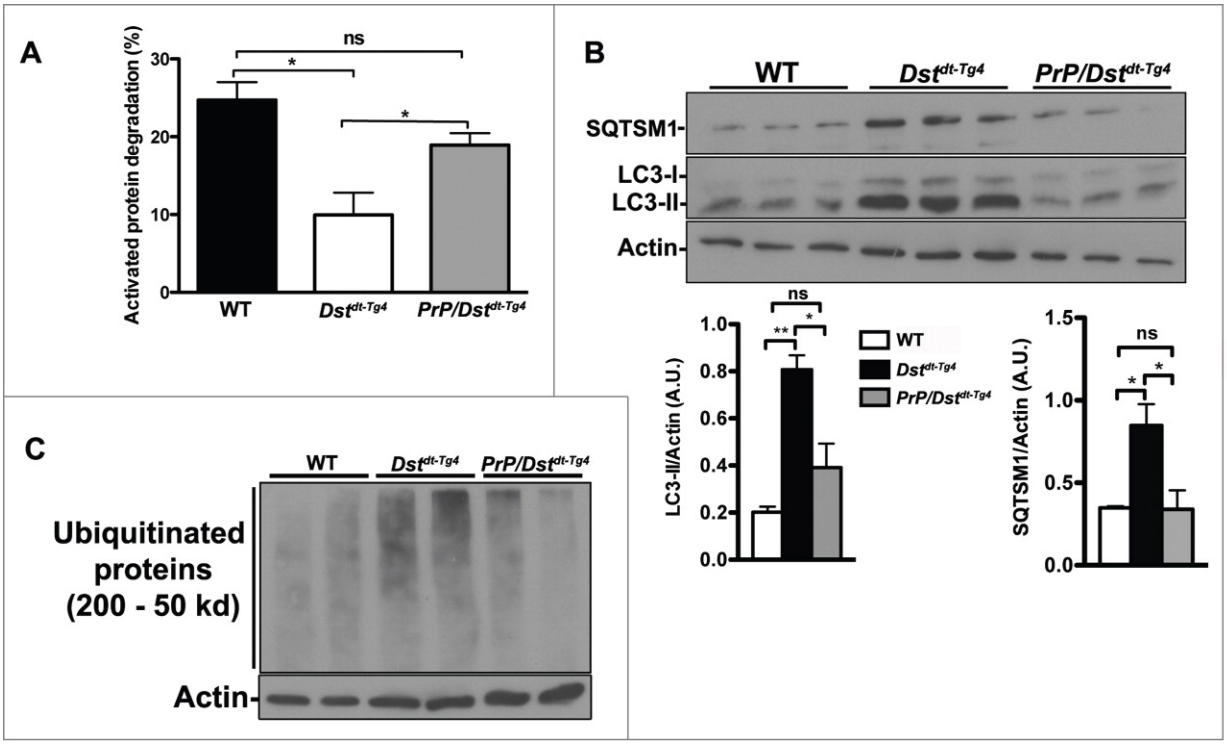


**Figure 2.6** Sensory neurons from presymptomatic (P5) *PrP/Dst*$^{dt\text{-}Tg4}$ mice, but not from *Dst*$^{dt\text{-}Tg4}$ mice, efficiently degrade the autophagosome substrate SQTSM1 and ubiquitinated proteins. **(A)** The rate of turnover of [$^{14}$C]-L-valine-labeled long-lived proteins was measured in cells incubated in complete media. Experiments were performed in presence or absence of 30 μM chloroquine. Data are expressed as the percent of cellular protein degraded in 4 h. A significant difference in protein degradation exists between WT (n = 6) and *Dst*$^{dt\text{-}Tg4}$ ($P < 0.05$), and between *Dst*$^{dt\text{-}Tg4}$ (n = 5) and *PrP/Dst*$^{dt\text{-}Tg4}$ (n = 6) ($P < 0.05$). Values reported are the mean ± SD **(B)** P5 WT, *Dst*$^{dt\text{-}Tg4}$, and *PrP/Dst*$^{dt\text{-}Tg4}$ sensory neuron lysates were analyzed by western blot for SQTSM1 and LC3-II protein levels. *Dst*$^{dt\text{-}Tg4}$ sensory neurons show significantly increased protein levels of LC3-II compared to WT ($P < 0.01$, n = 3) and *PrP/Dst*$^{dt\text{-}Tg4}$ sensory neurons ($P < 0.05$, n = 3). *Dst*$^{dt\text{-}Tg4}$ sensory neurons also exhibit significant increases in SQTSM1 protein levels compared to WT and *PrP/Dst*$^{dt\text{-}Tg4}$ sensory neurons ($P < 0.05$, n = 3). No significant

difference in LC3-II or SQTSM1 protein levels was found between WT and *PrP/Dst*$^{dt\text{-}Tg4}$ sensory neurons. Quantification by densitometry and normalized to actin standard; ANOVA, post-hoc Dunnett *t*-test; error bars represented as SEM. **(C)** Qualitative western blot analysis indicates an increase in polyubiquitinated proteins between 200 and 50 kDa in P5 *Dst*$^{dt\text{-}Tg4}$ sensory neurons.

Microtubule instability may be responsible for impeding autophagy in *Dst*$^{dt}$ sensory neurons

We next investigated microtubule integrity as a possible mechanism for the observed autophagic defects within *Dst*$^{dt\text{-}Tg4}$ sensory neurons. We have previously reported MT disorganization and instability via deacetylation of α-tubulin in the *Dst*$^{dt\text{-}27J}$ mouse (Ryan et al., 2012b). Here, we treated WT sensory neurons with the MT destabilizing agent vinblastine, and subsequently assessed autophagosome levels. Western blot analysis revealed increased levels of LC3-II after treatment with 10 mM vinblastine (Figure S2.2A). The accumulation of autophagosomes was also confirmed by EM (Figure S2.2B–D). These results are similar to those we observed in *Dst*$^{dt\text{-}Tg4}$ sensory neurons, suggesting that MT instability is likely an underlying cause of these autophagic defects.

Dst-a2 partially rescues autophagic defects in *Dst*$^{dt\text{-}Tg4}$ mice through restoration of Dnaic1 expression

Since autophagosomes are cargos of the DMC and play a crucial role in the turnover of several organelles and proteins, it is likely that disrupting the DMC through loss of Dst would perturb the transport of autophagosomes within neurons and contribute to the degeneration of *Dst*$^{dt\text{-}Tg4}$ sensory neurons. To assess the influence that Dst loss of function imparts on the DMC, we assessed protein levels of Dnaic1, a critical subunit of the DMC involved in binding cellular cargo in particular autophagosomes (Batlevi et al., 2010). While we did not observe a significant change in the levels of Dnaic1 between P15 WT and *Dst*$^{dt\text{-}Tg4}$ brains (Figure 2.7A), we did find levels to be markedly reduced in P15 *Dst*$^{dt\text{-}Tg4}$ DRGs compared to WT controls (Figure 2.7B). Given this observation, we next examined whether restoring *Dst-A2* expression in *Dst*$^{dt\text{-}Tg4}$ sensory neurons improves Dnaic1 levels. Once again, we observed a significant difference in

Dnaic1 levels between WT and *Dst*$^{dt\text{-}Tg4}$ sensory neurons (Figure 2.7C and D). Interestingly, Dnaic1 protein levels were partially restored in the *PrP/Dst*$^{dt\text{-}Tg4}$ sensory neurons, but not to WT levels (Figure 2.7D).

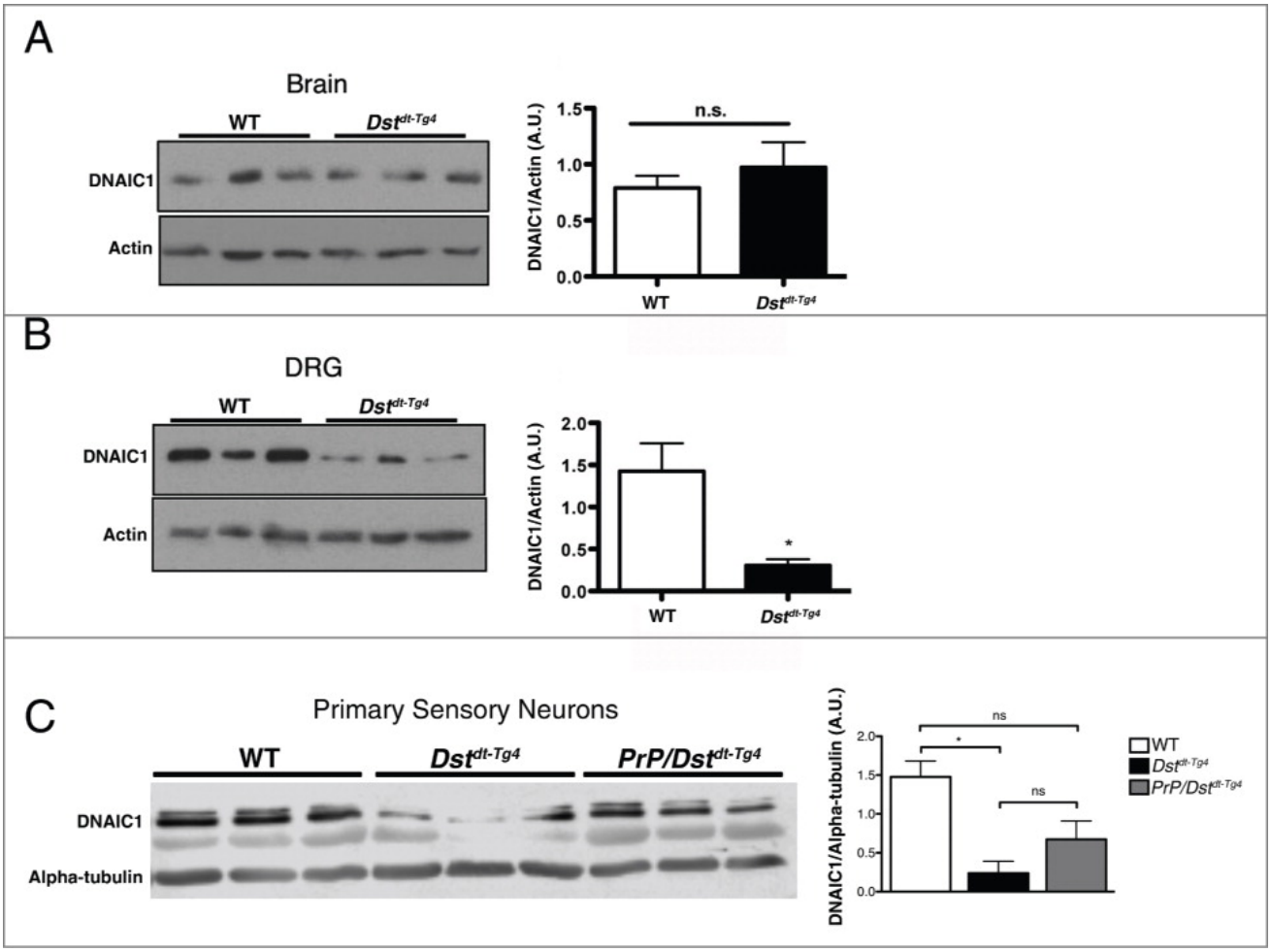


**Figure 2.7** Exogenous *Dst-Aa2* expression in sensory neurons from *PrP/Dst*$^{dt\text{-}Tg4}$ mice partially restores Dnaic1 levels. Dst loss of function has a cell-specific impact on the DMC. **(A)** Immunoblot analyses of WT and *Dst*$^{dt\text{-}Tg4}$ P15 brain (cortical) lysates indicate no significant changes in Dnaic1 protein levels ($P > 0.05$, n = 3). **(B)** P15 *Dst*$^{dt\text{-}Tg4}$ DRG lysates show a significant decrease in Dnaic1 protein levels ($P < 0.05$, n = 3) compared to P15 WT DRGs. Student's *t*-test, error bars indicate SEM (* $P < 0.05$). Graphs represent densitometric analysis of membranes, normalized to actin standard. **(C)** P5 fluorescence immunoblot analysis of Dnaic1 in sensory neurons derived from WT, *Dst*$^{dt\text{-}Tg4}$, and *PrP/Dst*$^{dt\text{-}Tg4}$ mice. A significant difference in Dnaic1 levels exists between WT and *Dst*$^{dt\text{-}Tg4}$ ($P < 0.05$), but not between *PrP/Dst*$^{dt\text{-}Tg4}$ and WT

($P > 0.05$), and *PrP/Dst*$^{dt\text{-}Tg4}$ and *Dst*$^{dt\text{-}Tg4}$ ($P > 0.05$; n = 3). This indicates a partial rescue in Dnaic1 levels when Dst-a2 is restored. Quantification of blot in **(C)** with an Odyssey imaging system, and normalized to the α-tubulin standard. ANOVA, post-hoc Dunnett *t*-test; error bars represented as SEM (*$P < 0.05$).

## Discussion

In this study, we demonstrate that $Dst^{dt\text{-}Tg4}$ sensory neurons have impairments in the autophagy pathway. Presymptomatic $Dst^{dt\text{-}Tg4}$ sensory neurons exhibit increased LC3-II protein levels coupled with accumulation of autophagosomes, autolysosomes, and damaged organelles. In addition to these pathologies, there are deficiencies in protein turnover, including of the autophagic substrate SQTSM1 and of polyubiquitinated proteins. Collectively, we attribute these aforementioned abnormalities in $Dst^{dt\text{-}Tg4}$ sensory neurons to compromised autophagic flux. Surprisingly, similar defects in autophagic flux and Dnaic1 were not observed in $Dst^{dt\text{-}Tg4}$ cortical neurons, suggesting Dst loss of function has a cell-specific influence on the autophagy pathway. Cortical neurons may be spared due to the relatively high expression of Macf1 (microtubule-actin crosslinking factor 1), a protein with similar function to Dst, but which is only expressed in sensory neurons at very low levels (Ferrier et al., 2013). Macf1 could compensate for the loss of Dst-a1 and Dst-a2 in $Dst^{dt\text{-}Tg4}$ cortical neurons, but fails to do so in $Dst^{dt\text{-}Tg4}$ sensory neurons. Interestingly, autophagic activity in $PrP/Dst^{dt\text{-}Tg4}$ sensory neurons was partially rescued, though only expression of *Dst-a2* is restored in this model. The molecular mechanism underlying this improvement is likely mediated, at least in part, by restoration of Dnaic1 levels. Taken together, our study reveals autophagy as an impaired pathway in the $Dst^{dt}$ disorder, and proposes Dst-a2 as a critical variant underlying this aberration.

### How does Dst affect autophagy?

It is difficult to elucidate the exact cause of autophagy impairment in $Dst^{dt\text{-}Tg4}$ sensory neurons as Dst has such a wide range of functions and interacting partners. Both Dst-a1 and Dst-a2 isoforms are absent in $Dst^{dt\text{-}Tg4}$ mice (Pool et al., 2005). As such, loss of both variants can

individually influence autophagy. For example, Dst-a1 interacts with Dctn1/p150$^{Glued}$, a critical component of the DMC, and regulates retrograde transport in sensory neurons (Liu et al., 2003). Dst-a1 also recruits and anchors TMEM108/retrolinkin, an endosomal vesicle protein, to the DMC and ensures proper transport of endosomal vesicles (Liu et al., 2007). Coupled with the fact that dynactin loss of function alters autophagosome trafficking and induces neurodegeneration (Ikenaka et al., 2013), the fusion of endosomes and autophagosomes (forming amphisomes), and subsequent trafficking to lysosomes for degradation could be compromised in *Dst*$^{dt\text{-}Tg4}$ sensory neurons. As well, newly synthesized precursors of lysosomal hydrolases are transported via endosomes through the trans-Golgi network to acidic late endosomes for maturation into lysosomes (Mizushima, 2007). It is interesting to note that our EM analyses of *Dst*$^{dt\text{-}Tg4}$ sensory neurons display autolysosomes filled with undigested amorphous cytoplasmic material, which are reminiscent of the autolysosomes seen in WT sensory neurons when treated with the lysosomal deacidifying agent chloroquine. Taken together, Dst-a1 loss of function could disrupt retrograde transport of autophagic and endosomal vesicles, which, in turn, could disrupt the degradative and maturation capacity of the autophagy-lysosomal system.

In addition to Dst-a1, we now show that Dst-a2 also contributes to the autophagy pathway. Restoring *Dst-a2* expression in presymptomatic primary *Dst*$^{dt\text{-}Tg4}$ sensory neurons restored autophagic flux, reduced the number of autophagosomes, autolysosomes, and damaged organelles, and normalized the protein levels of LC3-II, SQTSM1, and polyubiquitinated proteins. Dst-a2 interacts with Map1B (microtubule-associated protein 1B) (Bhanot et al., 2011; Ryan et al., 2012b). Map1B is also implicated in aspects of autophagy. It interacts with LC3-II (Wang et al., 2006), mediates the degradation of mitochondria (Xie et al., 2011) and, through interactions with the autophagic substrate Nbr1 (neighbor of BRCA1 gene 1), aids in the

degradation of ubiquitinated aggregate proteins (Marchbank et al., 2012). The Dst-a2-Map1B interaction in neurons maintains perinuclear MT acetylation (Ryan et al., 2012b). MT acetylation is necessary for the fusion between mature autophagosomes and lysosomes, and plays a major role in starvation-induced autophagy (Geeraert et al., 2010; Xie et al., 2010). Furthermore, Dst-a2 was also ascribed a role in sustaining and modifying endoplasmic reticulum morphology (Young and Kothary, 2008; Ryan et al., 2012c). Collectively, the current experimental evidence supports Dst-a2 as an important regulator of the endomembrane system (Ryan et al., 2012a) and therefore as a putative component of the autophagy pathway. Thus, the loss of both Dst-a1 and Dst-a2, such as in $Dst^{dt\text{-}Tg4}$ mice, has severe consequences for autophagy.

Impaired autophagy — a novel pathogenic mechanism of $Dst^{dt}$ sensory neurons

Autophagosome accumulation in presymptomatic $Dst^{dt\text{-}Tg4}$ sensory neurons could be due to enhanced autophagic activities in order to meet elevated cellular demands, or impaired autophagosome clearance. The former is conceivable, as increases in SQTSM1, polyubiquitinated proteins, and damaged mitochondria are all known to enhance autophagy in degenerative settings (Pankiv et al., 2007; Wang and Klionsky, 2011). Furthermore, the endoplasmic reticulum-stress pathway, a known inducer of the autophagy pathway (Yorimitsu et al., 2006), is activated in $Dst^{dt}$ sensory neurons (Ryan et al., 2012c), suggesting $Dst^{dt}$ sensory neurons employ a canonical response during pathogenic conditions (Hoyer-Hansen and Jaattela, 2007). However, impaired autophagy is more likely responsible for the persistent pathologies in these neurons. Various studies indicate that changes in the properties of the cellular cytoskeleton (Monastyrska et al., 2009), motor proteins, or degradation compartments (i.e., endosomes and lysosomes) alter autophagosome clearance (He and Klionsky, 2009). As Dst has been ascribed a

role in all of these cellular properties (Ferrier et al., 2013), impaired autophagosome clearance is a logical explanation for the accumulating autophagosomes.

In conclusion, we demonstrate that depletion of Dst-a2, in $Dst^{dt\text{-}Tg4}$ sensory neurons is responsible for the autophagic pathology. This pathology likely arises through impaired clearance of autophagic vacuoles. Therapeutic modulation of autophagy in $Dst^{dt\text{-}Tg4}$ sensory neurons may, therefore, require specific targeting of late steps in the autophagic pathway.

## Materials and Methods

### Ethics statement

All experimental protocols for mice were approved by the Animal Care Committee of the University of Ottawa. Care and use of experimental mice followed the guidelines of the Canadian Council on Animal Care.

### Animal models

The *Dst*$^{dt\text{-}27J}$, *Dst*$^{dt\text{-}Tg4}$, and *PrP-Dst-a2/PrP-Dst-a2;Dst*$^{dt\text{-}Tg4}$ rescue mice (referred to as *PrP/Dst*$^{dt\text{-}Tg4}$ mice in the text) were used at presymptomatic (P3 to 5, P10) and symptomatic (P15 to P17) stages. The derivation of *Dst*$^{dt\text{-}27J}$, *Dst*$^{dt\text{-}Tg4}$, *PrP/Dst*$^{dt\text{-}Tg4}$ transgenic lines and characterization of mutations were described previously (Kothary et al., 1988; Brown et al., 1995a; Ferrier et al., 2014). The onset of symptoms was generally assessed by the appearance of clasping of hind limbs after the mice were picked up by the tails. *Dst*$^{dt\text{-}27J}$ and *Dst*$^{dt\text{-}Tg4}$ mice were genotyped by polymerase chain reaction (PCR) amplification of genomic tail DNA as previously described (Pool et al., 2005).

### Primary culture of sensory neurons

Sensory neurons were collected from WT, *Dst*$^{dt\text{-}Tg4}$, and *PrP/ Dst*$^{dt\text{-}Tg4}$ mice at P3 to 5. Spinal columns were removed and transferred to a dissection microscope. Approximately 40 DRGs were isolated per mouse and subsequently digested for 10 min with papain (Worthington, LS003126), and 10 min with collagenase A (Roche, 10103586001). DRG neurons were dissociated with flame-polished glass Pasteur pipettes and seeded onto 12-mm laminin (LN2) (Millipore, CC085) coated coverslips at a density of 50,000 in DMEM (Wisent, 319–005-CL)

with 10% fetal bovine serum (FBS; Gibco, 12484–028) and 1% penicillin/ streptomycin (Gibco, 15140–122). Cells were placed in a 37°C tissue culture incubator under 8.5% $CO_2$. The following day, the media was changed to neuronal maintenance media (DMEM base [Wisent, 319–005-CL], 0.5% FBS [Gibco, 12484–028], 1% penicillin/streptomycin [Gibco, 15140–122], 2% B27 supplement [Gibco, 17504–044], 1% GlutaMax [Gibco, 35050– 061], 16 mg/ml putrescine [Sigma-Aldrich, P7505], 400 mg/ml thyroxine [Sigma-Aldrich, T2501], 400 mg/ml triiodothyronine [Sigma-Aldrich, T6397], 6.2 ng/ml progesterone [Sigma- Aldrich, P8783], 5 ng/ml sodium selenite [Sigma-Aldrich, S5261], 100 mg/ml bovine serum albumin [Sigma-Aldrich, A4503], 5 mg/ml bovine insulin [Sigma-Aldrich, I6634], 50 mg/ ml holo-transferrin [Sigma-Aldrich, T0665] supplemented with 1 mM 5-fluoro-20 -deoxyuridine (Sigma-Aldrich, F0503). A three-fourths media change was performed every other day, up until d 5 of culture, when autophagy flux, pulse-chase assays, or western blot analyses were performed.

Primary culture of cortical neurons

Cortical brain samples were dissected from P0 WT and $Dst^{dt\text{-}Tg4}$ mice. Brains were kept in cold Hank's balanced salt solution (Gibco, 14170–112), 10 mM HEPES (Gibco, 15630– 080), and 1% penicillin/streptomycin (Gibco, 15140–122) during meninges removal. Post meninges separation, the brain cortices were diced and rinsed with prewarmed Hank's balanced salt solution (Gibco, 14170–112) at 37°C prior to digestion. The digestion of unwanted cortical tissues was done with 0.5 mg/mL trypsin (ATCC, 30–2101) and 0.1 mg/mL DNaseI (Roche, 10104159001), incubating for 20 min with agitation. Further, digested samples were triturated to achieve single-cell suspension with 10% FBS (Gibco, 12484–028) in Neurobasal Media (Gibco, 21103–049), centrifuged and resuspended in neuron media composed of neural basal media, 1X

B27 supplement (Gibco, 17504–044), 1X Sato's supplement, 0.5 mM GlutaMax (Gibco, 35050–061), 1X $N_2$ supplement (Gibco, 17502–048), and 1:1000 gentamycin (Gibco, 15710–064). Resuspended cells were allowed to rest for the settling of cell debris, and upper-layer, single-cell neurons were seeded on LN2 (Millipore, CC085) plus 1 mg/ml poly-D-lysine (Millipore, A-003-E) coated cover slips at 5.0 X $10^4$ cells/well and 2.5 X $10^5$ cells/well in 24-well and 6-well plates, respectively. Gentamycin was removed after 24 h incubation after sufficient neuronal growth selection.

Cortical neuron cell soma and axonal autophagosome counts

Autophagosomes were visualized with anti-LC3B antibody (1:1000; Abcam, ab48394) using epifluorescence, and photomicrographs captured using a Zeiss Axiovert 200M microscope (Göttingen, Germany) equipped with AxiovisionLEV 4.8.0.0. Prior to counting, each sample coverslip was individually examined for the minimal signal intensity appropriate to resolve between distinct autophagosomal puncta. The determined minima were set as the standard intensities and remain unchanged for the corresponding coverslip between autophagosome counts of individual cells. Signal intensity differences between cover slips were kept to a range to minimize counting bias due to intensity, and visually ambiguous cells were excluded from the results. Somatic autophagosome counts were recorded as average number autophagosomes/cell soma at n = 3 with 40 cells analyzed per n. Axonal autophagosomes were counted as average number autophagosomes/mm length of all axons at n = 3 with 40 cells analyzed per n. Axonal counts were restricted to linear extensions of axons for accuracy of length determination. All counts were done blindly by 2 individuals to compare reproducibility, and highly differing counts of the same coverslip were discarded to avoid ambiguity and bias.

Autophagy flux assay

Primary cortical neurons (P0) or sensory neurons (P5) were cultured (as outlined above) from each genotype in a 6-well culture vessel for 7 or 5 d, respectively. Neurons were washed 3 times with 1X phosphate-buffered saline (PBS; 8 mg/mL sodium chloride [Fisher Scientific, S271–3], 0.2 mg/mL potassium chloride [Sigma-Aldrich, P9541], 2.74 mg/mL sodium phosphate dibasic heptahydrate [Sigma-Aldrich, S9390], and 0.24 mg/mL potassium phosphate [Anachemia, AC-7718]) and challenged by different flux conditions for 2 h thereafter. Flux conditions included: untreated (DMEM C 10% FBS), induction of autophagy (DMEM + 10% FBS + 500 nM rapamycin [Sigma-Aldrich, R8781]), blockage of autophagy (DMEM + 10% FBS + 30 mM chloroquine [Sigma-Aldrich, C6628]), and a combination treatment of inducing and blocking autophagy (DMEM + 10% FBS + 500 nM rapamycin + 30 mM chloroquine). Neurons were harvested from each condition and LC3-II protein levels examined thereafter via western blot analysis. A single 6-well vessel represented total sensory neurons from 1 mouse. Each flux assay was conducted twice for each genotype.

Long-lived protein degradation assay

Following the standard method (Ogier-Denis et al., 1996; Pattingre et al., 2004), long-lived protein degradation assay was performed. In brief, cells were incubated for 2 d at 37°C with 0.2 μCi/ml [$^{14}$C]-L-valine (PerkinElmer, NEC291EU050UC). The cells are then washed with 1X PBS to remove unincorporated radioisotope, then supplemented and incubated for 60 min with fresh medium containing 0.1% bovine serum albumin (Sigma-Aldrich, A4503) and cold 10 mM valine (Sigma-Aldrich, V0500) to allow the short-lived proteins to be degraded. The medium was then removed and replaced with fresh medium containing 10% FBS and incubation

resumed for 4 h. The medium was then collected and precipitated with 10% trichloroacetic acid (TCA; Sigma-Aldrich, T6399) at 4°C, and TCA-soluble radioactivity was measured using a scintillation counter. The precipitate was washed with 10% TCA and dissolved using 0.5 ml of 0.2 M sodium hydroxide (Sigma-Aldrich, S8045) and radioactivity was measured by liquid scintillation counting. The rate of protein degradation was calculated from the ratio of radioactivity in the TCA-precipitated medium to the cell fraction.

Parallel cell samples were treated with autophagic suppressive reagent (30 mM chloroquine [Sigma-Aldrich, C6628]) to distinguish the autophagic versus non-autophagic protein degradation, and the values obtained were then subtracted from the total (Klionsky et al., 2008).

Cell preparation for transmission EM and morphometric analysis

P3 to 5 primary sensory neurons were cultured as described above, washed with 1X PBS and trypsinized (0.25% trypsin, 0.53 mM EDTA [ATCC, 30–2101]) for 5 min at 37°C. To obtain a suitable sized pellet of sensory neurons, an n = 3 was collected and combined for each genotype (WT, $Dst^{dt\text{-}Tg4}$, and $PrP/Dst^{dt\text{-}Tg4}$). Cells were centrifuged at 300 X g for 5 min and the supernatant fraction removed. Neurons were fixed for 1 h at room temperature in Karnovsky's fixative (4% paraformaldehyde, 2% glutaraldehyde [Sigma-Aldrich, G6257], and 0.1 M cacodylate [Electron Microscopy Sciences, 11652] in 1X PBS) and subsequently washed twice in 0.1 M cacodylate buffer. Neurons were postfixed with 1% osmium tetroxide (Electron Microscopy Sciences, RT19100) in 0.1 M cacodylate buffer for 1 h at room temperature, followed by 3 5-min washes in water. Cells were dehydrated twice for 20 min for each step in a graded series of ethanol (Commercial Alcohols, P016EAAN) from water through 30%, 50%,

70%, 85%, and 95% ethanol, and twice for 30 min in 100% ethanol (molecular sieves were used to dehydrate ethanol), followed by two 15-min washes in 50% ethanol and 50% acetone (Fisher Scientific, A18SK) and washed twice for 15 min in 100% acetone. Neurons were infiltrated in 30% Spurr epoxy resin (DER 736 Epoxy resin; Electron Microscopy Sciences, 13000) in acetone for 15 h (overnight), then in 50% Spurr resin/acetone for 6 h, and in fresh 100% Spurr epoxy resin, NSA (Electron Microscopy Sciences, 19050), DMAE (Electron Microscopy Sciences, 13300), and ERL (Electron Microscopy Sciences, 15004) overnight. The Spurr resin was changed twice daily for 3 d at room temperature. All infiltration steps were performed on a rotator. Neurons were embedded in fresh liquid Spurr epoxy resin and polymerized overnight at 70°C. Ultrathin sections (80 nm) of cells were collected onto a 200-mesh copper grid and allowed to dry overnight. Grids were stained with 2% aqueous uranyl acetate (Electron Microscopy Sciences, 22400) and with Reynold lead citrate (sodium citrate [Electron Microscopy Sciences, 21140], and lead nitrate [Electron Microscopy Sciences, 17900]). Sections were observed under a transmission electron microscope (Hitachi 7100; Chiyoda, Tokyo, Japan).

Approximately 100 EM micrographs were examined per genotype. For our qualitative analysis, we identified autophagosomes as double-membrane compartments of 0.5 mm in diameter or larger, whereas autolysosomes were defined as single-membrane vesicles with densely compacted amorphous or multi-lamellar contents. Mitochondria were considered damaged if they exhibited absent or abnormal cristae.

RT-PCR analysis

For reverse transcription-polymerase chain reaction (RT-PCR) analysis, RNA was isolated from transgenic P0 cortical tissues of WT mice. To synthesize cDNA, equal amounts of

RNA were reverse-transcribed in a standard reaction with MuLV reverse transcriptase (Invitrogen, N8080018). From these samples, cDNAs encoding *Dst* isoforms were PCR amplified using primer pairs targeting Dst-a1 (accession number NM_134448.3) and Dst-a2 (accession number NM_001276764) transcripts as previously described (Pool et al., 2005).

Western blot analysis

Protein lysates were collected from symptomatic or presymptomatic stage DRGs, or from primary sensory neuron cultures as previously described (Ryan et al., 2012b). Proteins were isolated in RIPA buffer (10 mM PBS, 1% NP-40 [Sigma-Aldrich, I3021], 0.5% sodium deoxycholate [Sigma-Aldrich, D6750], 0.1% sodium dodecyl sulfate [Fisher Scientific, BP166], 30 ml/ml aprotinin [Sigma- Aldrich, A1153], 10 mM sodium orthovanadate [Sigma-Aldrich, S6508], 6 ml/ml phenyl methyl sulfonyl fluoride [Sigma-Aldrich, P7626]). Protein samples (10 mg) were separated by SDS-PAGE under reducing conditions. Western blot analyses were performed using the following primary antibodies: rabbit polyclonal anti-LC3B antibody (1:1000; Abcam, ab48394), mouse monoclonal anti-SQTSM1/p62 (1:2000; Abcam, ab56416), mouse anti-ubiquitin (1:2000; Biolegend, 646302), rabbit monoclonal anti-TUBA1A/a-tubulin (1:50,000; Millipore, 04–1117), mouse monoclonal anti-Dnaic1 (1:5000; Abcam, ab23905), and mouse monoclonal anti-pan-actin (1:5000; Fitzgerald Industries International, 10R-A106a).

Secondary antibodies used for enhanced chemiluminescence processing were horseradish peroxidase-conjugated anti-mouse IgG (IgG, 1:2000; Bio-Rad, 170–6516) and horseradish peroxidase-conjugated anti-rabbit IgG (1:2000; Bio-Rad, 172– 1019). Immunoreactive bands were visualized using SuperSignal West Pico (MJS BioLynx, Brockville, ON Canada). Quantification of protein expression levels was performed by densitometric analysis of

individual bands using ImageJ analysis software (National Institutes of Health, Bethesda, MD USA). At least 3 western blots from different experiments were evaluated by densitometry and normalized to a protein standard (actin, or α-tubulin) for all western blots depicted.

For infrared fluorescent western blots, the secondary antibodies used were infrared dye conjugated (IRDye®) goat anti-rabbit 800CW (IgG, 1:10,000; LI-COR, 926–32211), goat anti-rabbit 680RD (IgG, 1:10,000; LI-COR, 926–68071), goat anti-mouse 800CW (IgG, 1:10,000; LI-COR, 926–32210), and goat anti- mouse 680RD (IgG, 1:10,000; LI-COR, 926–68070). Bands were visualized and quantified using the Odyssey® CLx infrared imaging system (LI-COR Biosciences, Lincoln, NB USA).

Statistical analysis

Data were analyzed using the Student's *t*-test or factorial analysis of variance (ANOVA) as applicable using InStat, version 3.0 (GraphPad Software, La Jolla, CA USA). Following detection of a statistically significant difference in a given series of treatments by ANOVA, post-hoc Dunnett *t*-tests or Tukey tests were performed where appropriate. $P < 0.05$ was considered statistically significant (shown as either *); $P < 0.01$ was considered highly statistically significant (shown as **).

**Acknowledgements**

We would like to thank the Kothary laboratory for valuable discussions and Samantha Kornfeld for careful reading of the manuscript.

**Supplementary Material**

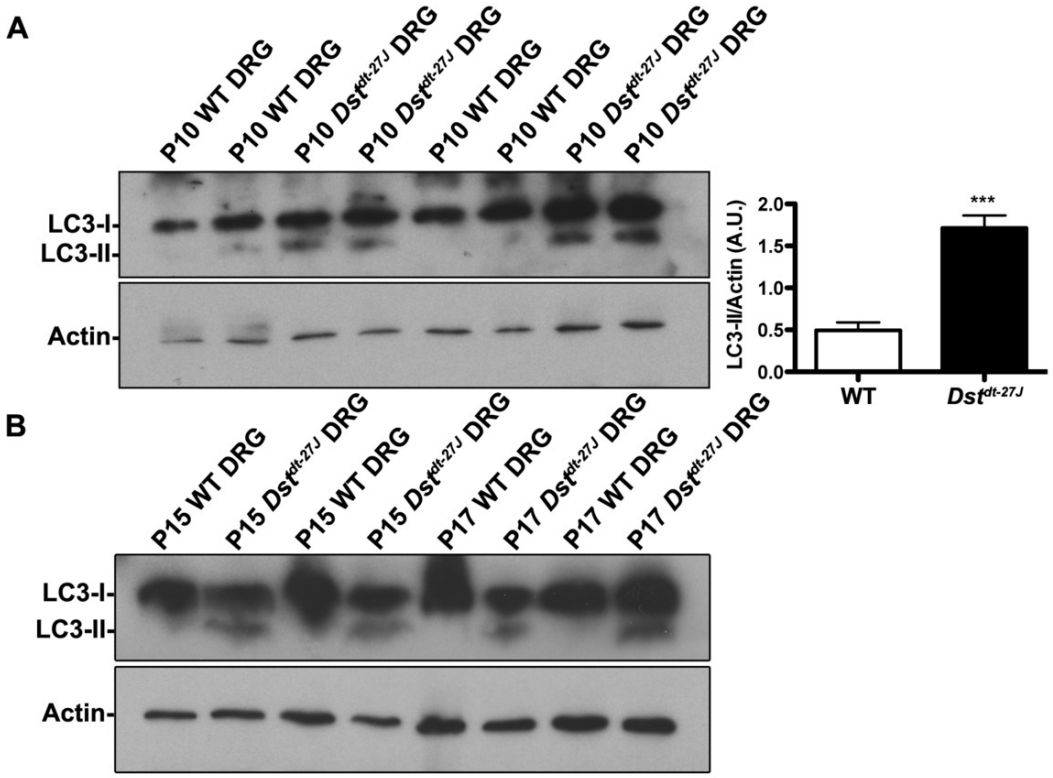


**Figure S2.1** Symptomatic and pre-symptomatic *Dst*$^{dt\text{-}27J}$ sensory neurons display increased LC3-II protein levels. **(A)** Western blot analysis of pre-symptomatic stage (P10) *Dst*$^{dt\text{-}27J}$ DRG protein lysates antigenically labelled for LC3B display a significant increase in LC3-II compared to WT ($P < 0.001$, n = 4). Quantification by densitometry and normalized to actin standard; Student's *t*-test; error bars represented as SEM. **(B)** LC3-II protein levels are increased in symptomatic stage (P15, P17) *Dst*$^{dt\text{-}27J}$ DRGs.

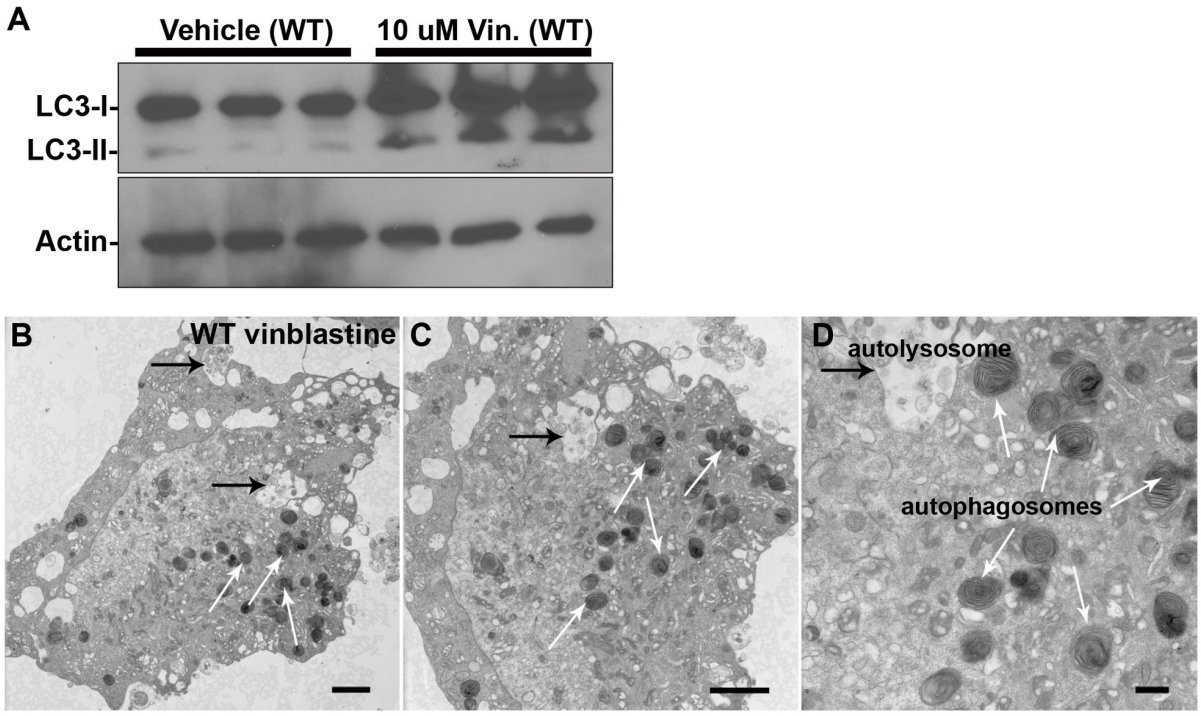


**Figure S2.2** Treatment of WT sensory neurons with microtubule destabilizer vinblastine invokes autophagy defects similar to those observed in sensory neurons from *Dst*$^{dt\text{-}Tg4}$ mice. **(A)** P5 WT sensory neuron cultures were treated with 10 μM vinblastine in DMSO for 6 h. Protein lysates were analyzed by immunoblot. An increase in LC3-II levels was noted after vinblastine exposure. **(B-D)** EM micrographs of WT sensory neurons after treatment with vinblastine for 6 h. Accumulation of single membrane autolysosomes (black arrows) and autophagosomes (white arrows) is present within these treated sensory neurons. Magnification and scale bars for **(B)** (6,000X & 2 μm), **(C)** (9,000X & 2 μm), and **(D)** (20,000X & 500 nm).

# Chapter 3:

# Dystonin-A3 upregulation is responsible for maintenance of tubulin acetylation in a less severe *dystonia musculorum* mouse model for hereditary sensory and autonomic neuropathy type VI

# Dystonin-A3 upregulation is responsible for maintenance of tubulin acetylation in a less severe *dystonia musculorum* mouse model for hereditary sensory and autonomic neuropathy type VI

Anisha Lynch-Godrei[1,2], Yves De Repentigny[1], Sabrina Gagnon[1], My Tran Trung[1] and Rashmi Kothary[1,2,3,4,*]

[1]Regenerative Medicine Program, Ottawa Hospital Research Institute, Ottawa, K1H 8L6, Canada

[2]Department of Cellular and Molecular Medicine, University of Ottawa, Ottawa, K1H 8M5, Canada

[3]Department of Medicine, University of Ottawa, Ottawa, K1H 8M5, Canada

[4]Centre for Neuromuscular Disease, University of Ottawa, K1H 8M5, Canada

*To whom correspondence should be addressed at: Ottawa Hospital, 501 Smyth Road, ORCC 4406a, Ottawa, Ontario, K1H 8L6, Canada; Tel: (613) 737-8707; Fax: (613) 737-8803; Email: rkothary@ohri.ca

***Published in Human Molecular Genetics 2018, 27(20): 3598–3611***

## Author Contributions

ALG performed the research (figures 3.1, 3.2, 3.3A-D, 3.4, 3.6, 3.7A-B, 3.8A-K, 3.9, and supplementary figures 3.1, 3.2, 3.4, and 3.5), assisted by YDR (figures 3.3E, 3.5, 3.7C, and supplementary figure 3.3), SG (figure 3.8L) and MTT. ALG designed the research study, analyzed the data, and wrote the paper with assistance and supervision from RK.

**Abstract**

Hereditary sensory and autonomic neuropathy type VI (HSAN-VI) is a recessive human disease that arises from mutations in the dystonin gene (*DST*; also known as Bullous pemphigoid antigen 1 gene). A milder form of HSAN-VI was recently described, resulting from loss of a single dystonin isoform (DST-a2). Similarly, mutations in the mouse dystonin gene (*Dst*) result in severe sensory neuropathy, *dystonia musculorum* ($Dst^{dt}$). Two $Dst^{dt}$ alleles, $Dst^{dt\text{-}Tg4}$ and $Dst^{dt\text{-}27J}$, differ in the severity of disease. The less severe $Dst^{dt\text{-}Tg4}$ mice have disrupted expression of *Dst-a1* and *-a2* isoforms, while the more severe $Dst^{dt\text{-}27J}$ allele affects *Dst-a1*, *-a2* and *-a3* isoforms. As dystonin is a cytoskeletal-linker protein, we evaluated microtubule network integrity within sensory neurons from $Dst^{dt\text{-}Tg4}$ and $Dst^{dt\text{-}27J}$ mice. There is a significant reduction in tubulin acetylation in $Dst^{dt\text{-}27J}$ indicative of microtubule instability and severe microtubule disorganization within sensory axons. However, $Dst^{dt\text{-}Tg4}$ mice have no change in tubulin acetylation, and microtubule organization was only mildly impaired. Thus, microtubule instability is not central to initiation of $Dst^{dt}$ pathogenesis, though it may contribute to disease severity. Maintenance of microtubule stability in $Dst^{dt\text{-}Tg4}$ dorsal root ganglia could be attributed to an upregulation in *Dst-a3* expression as a compensation for the absence of Dst-a1 and -a2 in $Dst^{dt\text{-}Tg4}$ sensory neurons. Indeed, knockdown of Dst-a3 in these neurons resulted in a decrease in tubulin acetylation. These findings shed light on the possible compensatory role of dystonin isoforms within HSAN-VI, which might explain the heterogeneity in symptoms within the reported forms of the disease.

## Introduction

Dystonin (Dst), also known as bullous pemphigoid antigen 1 (Bpag1), is a massive cytoskeletal-linker protein (>600 kDa) belonging to the spectraplakin family of proteins (Roper et al., 2002; Jefferson et al., 2007; Atai et al., 2012; Suozzi et al., 2012). Differential expression of Dst isoforms occurs in neuronal, muscular and epithelial tissues. Furthermore, alternative splicing of 5′ exons yields 3 major neuronal isoforms: Dst-a1, Dst-a2 and Dst-a3 (Leung et al., 2001; Ferrier et al., 2013). While all three isoforms possess central plakin and spectrin repeat domains and a C-terminus microtubule binding domain (MTBD), they are unique in the organization of their N-termini. Dst-a1 possesses two calponin homology repeats that make up a functional actin-binding domain (ABD) (Brown et al., 1995b; Jefferson et al., 2006). This allows Dst-a1 to participate in crosslinking of actin micro laments with microtubules (Young et al., 2006). Dst-a2 also possesses an ABD, which is preceded by a transmembrane domain (TMD) (Young et al., 2006). This unique N-terminus localizes Dst-a2 to perinuclear membranes and surrounding microfilaments (Yang et al., 1999; Young et al., 2006; Ferrier et al., 2014). Though it has a specific intracellular localization, Dst-a2 is involved in many different cellular roles, including microtubule stability, organelle integrity and intracellular transport (De Repentigny et al., 2003; Young and Kothary, 2008; Ryan et al., 2012b; Ryan et al., 2012c; Ferrier et al., 2015). Finally, Dst-a3 possesses a putative myristoylation motif (myr) followed by a single calponin homology domain, which dramatically reduces its affinity for actin (Yang et al., 1999; Jefferson et al., 2006; Ferrier et al., 2013). It is thought that myristoylation of Dst-a3 allows localization to the plasma membrane, though its specific function remains unknown (Jefferson et al., 2006).

Hereditary sensory and autonomic neuropathy type VI (HSAN-VI) is the recessive human disease that results from mutations in the *DST* gene. The disease was first classified in

2012 when three Ashkenazi infants presented with joint contractures, dysautonomias and severe psychomotor retardation, which ultimately led to death before the age of two (Edvardson et al., 2012). It was discovered that these individuals possessed a homozygous frameshift mutation that disrupted the C-terminal MTBD, which is common to all three DST isoforms. More recently, two different compound heterozygous mutations have also been found to result in a non-lethal form of HSAN-VI. All three affected siblings presented with joint deformities, reduced pain and tactile sensation and an array of autonomic irregularities including hypohidrosis, chronic diarrhea and sexual dysfunction. It was determined that their novel mutations only affected the expression of DST-a2 (Manganelli et al., 2017), suggesting the importance of DST-a1 and DST-a3 isoforms.

Similarly, a murine disease known as *dystonia musculorum* (*Dst*$^{dt}$) also arises due to mutations in the *Dst* gene. *Dst*$^{dt}$ mice first present with uncoordinated movements at postnatal day 10. Phenotype then rapidly worsens to include severe ataxia, writhing and twisting of the trunk and eventually death by about 3 weeks of age (Duchen et al., 1964; Duchen, 1976). In accordance with this, the major cell types affected in *Dst*$^{dt}$ mice are the dorsal root ganglion (DRG) neurons involved in proprioception. They exhibit axonal swellings, a hallmark of *Dst*$^{dt}$, and undergo rapid neurodegeneration (Sotelo and Guenet, 1988; al-Ali and al-Zuhair, 1989; Bernier and Kothary, 1998; Ryan et al., 2012c; Ferrier et al., 2014). Of the numerous *Dst*$^{dt}$ alleles, *Dst*$^{dt\text{-}Tg4}$ and *Dst*$^{dt\text{-}27J}$ are among the best studied. *Dst*$^{dt\text{-}27J}$ first arose by spontaneous mutation at The Jackson Laboratory and lacks all three neuronal Dst isoforms (Figure 3.1) (Pool et al., 2005; Ryan et al., 2012a). These mice present with pronounced ataxia and severe dystonic postures, with death occurring around postnatal day 17–18. Conversely, *Dst*$^{dt\text{-}Tg4}$ mice arose by a transgene insertion–deletion event that disrupted expression of Dst-a1 and -a2, but left Dst-a3

intact (Figure 3.1) (Kothary et al., 1988; Brown et al., 1995b; Ferrier et al., 2013). They exhibit a milder phenotype and generally live a few days longer than $Dst^{dt\text{-}27J}$ mice.

Previous studies have described massive disorganization of the cytoskeleton in the neurons of *Dst* deficient mice, with the microtubule network showing substantial defects (Dalpé et al., 1998; Yang et al., 1999; De Repentigny et al., 2003; Tseng et al., 2011). Work done in our laboratory has also characterized a significant reduction in microtubule stability within $Dst^{dt\text{-}27J}$ sensory neurons, with evidence pointing towards Dst-a2 as the major isoform responsible for this (Ryan et al., 2012b). Here we sought to validate these results in $Dst^{dt\text{-}Tg4}$ sensory neurons, as Dst-a2 is also lacking in these mice. Surprisingly we did not observe any obvious changes in microtubule stability in $Dst^{dt\text{-}Tg4}$ primary sensory neurons or DRGs at either the pre-phenotype or phenotype stages. Further analysis of dorsal root axons revealed cervical and thoracic level $Dst^{dt\text{-}Tg4}$ DRGs to have milder defects in microtubule organization compared to $Dst^{dt\text{-}27J}$. Although both alleles are present on different genetic backgrounds, the major difference between the two is the retention of *Dst-a3* in $Dst^{dt\text{-}Tg4}$ mice. Through evaluation of *Dst-a3* transcript levels in $Dst^{dt\text{-}Tg4}$ neural tissues, we determined that upregulation is most dramatic in tissues that exhibit major defects due to loss of *Dst*. We also observed that the retention of tubulin acetylation in $Dst^{dt\text{-}Tg4}$ sensory neurons is specifically a result of this increase in *Dst-a3* transcript levels. These results are consistent with Dst-a3 taking on a compensatory role when Dst-a1 and -a2 are lost. Collectively, these findings suggest that microtubule instability is not central to initiation of $Dst^{dt}$ pathogenesis though it may contribute to disease severity and that Dst-a3 upregulation compensates for the loss of other Dst isoforms.

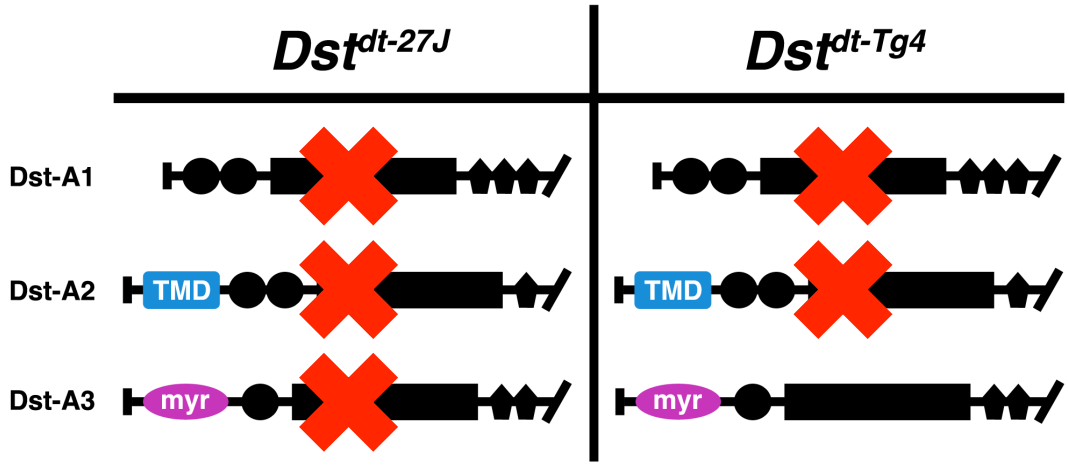


**Figure 3.1.** Schematic of the neuronal Dst isoforms expressed in *Dst*$^{dt\text{-}27J}$ and *Dst*$^{dt\text{-}Tg4}$ mice. The more severe *Dst*$^{dt\text{-}27J}$ mice lack expression of all three neuronal Dst isoforms. The *Dst*$^{dt\text{-}Tg4}$ mice possess a mutation that affects only Dst-a1 and Dst-a2 expression, with Dst-a3 remaining intact. They also have a milder disease presentation and a slightly longer lifespan.

## Results

*Dst*$^{dt}$ pathogenesis is not driven by microtubule instability

Tubulin acetylation (Ac) can be used as an indicator for microtubule stability. This post-translational modification of tubulin occurs on lysine 40 of the alpha-tubulin subunit and marks stability of polymerized microtubules as indicated by their resistance to colchicine and nocodazole treatment (Hammond et al., 2008; Janke and Kneussel, 2010; Wloga and Gaertig, 2010). Previous work on *Dst*$^{dt\text{-}27J}$ DRGs reported a reduction in the ratio of Ac-tubulin to total alpha tubulin at the pre-phenotype stage (P4) and phenotype stage (P15) as assessed by enhanced chemiluminescence immunoblot (Ryan et al., 2012b). We first set out to validate these findings using more quantitative fluorescent immunoblotting techniques. We observed a significant reduction in the ratio of Ac-tubulin to alpha-tubulin in phenotype stage (P15) *Dst*$^{dt\text{-}27J}$ DRG tissue (Figure 3.2A). This reduction was further confirmed in a homogenous population of P5 primary sensory neurons grown in culture, suggesting that this pathology precedes disease onset (Figure 3.2B).

To determine whether *Dst*$^{dt\text{-}Tg4}$ sensory neurons also had impaired tubulin acetylation, we evaluated both pre-phenotype (P5) and phenotype (P15) stage primary sensory neurons and DRG tissue by fluorescence immunoblot. Surprisingly, regardless of *in vivo* or *in vitro* analysis at either P5 or P15 developmental stages, we did not observe any changes in the ratio of Ac-tubulin to overall alpha-tubulin between wild type (WT) and *Dst*$^{dt\text{-}Tg4}$ samples (Figure 3.3A–D). Additionally, immunofluorescent staining of Ac-tubulin in P15 *Dst*$^{dt\text{-}Tg4}$ DRG tissue showed no difference in signal intensity compared to WT DRGs (Figure 3.3E).

As tubulin acetylation in *Dst*$^{dt\text{-}Tg4}$ sensory neurons is unaffected, we decided to assess a second marker for microtubule stability. Tubulin detyrosination had previously been reported to

be unaltered in *Dst*$^{dt\text{-}27J}$ DRGs (Ryan et al., 2012b), which we have also confirmed here in P15 *Dst*$^{dt\text{-}27J}$ DRG tissue (Figure S3.1). However, tubulin detyrosination had yet to be assessed in *Dst*$^{dt\text{-}Tg4}$ sensory neurons. This post-translational modification involves the proteolytic removal of the C-terminal tyrosine residue on alpha-tubulin subunits within polymerized microtubules (Fukushima et al., 2009; Janke and Kneussel, 2010). Using the same experimental setup as we did for tubulin acetylation, we assessed the ratio of detyrosinated-tubulin to overall alpha-tubulin. Both P5 and P15 *Dst*$^{dt\text{-}Tg4}$ DRGs and sensory neurons had similar detyrosinated-tubulin to alpha-tubulin ratios as WT littermates (Figure 3.4A–D). Taken with the normal tubulin acetylation also found, these data suggest that *Dst*$^{dt\text{-}Tg4}$ sensory neurons do not have impaired microtubule stability. This is in contrast to *Dst*$^{dt\text{-}27J}$ sensory neuron microtubules, which do exhibit reduced microtubule stability even before the onset of phenotype (Ryan et al., 2012b).

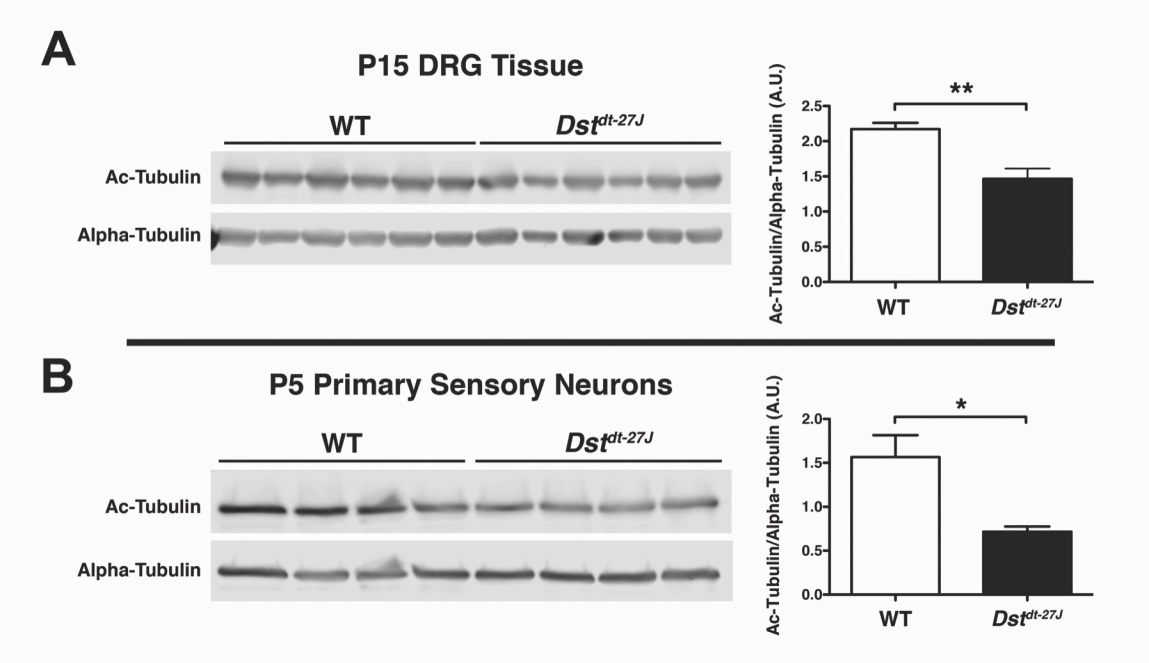


**Figure 3.2.** *Dst*$^{dt\text{-}27J}$ sensory neurons have reduced levels of Ac-tubulin. **(A)** Fluorescence immunoblot of Ac-tubulin and alpha-tubulin loading control for P15 *Dst*$^{dt\text{-}27J}$ DRG tissue, quantification of Ac-tubulin:alpha-tubulin ratio shown on the right (n = 6; $**P$-value < 0.01). **(B)** Fluorescence immunoblot of Ac-tubulin and alpha-tubulin loading control for P5 *Dst*$^{dt\text{-}27J}$ primary sensory neurons grown in culture, quantification of Ac-tubulin:alpha-tubulin ratio shown on the right (n = 4; $*$ $P$-value < 0.05). All lanes in immunoblot represent DRGs from a single mouse, 10 μg of total protein per lane. Graphical data represented as mean ± SEM, statistical analysis by two-tailed Student's *t*-test.

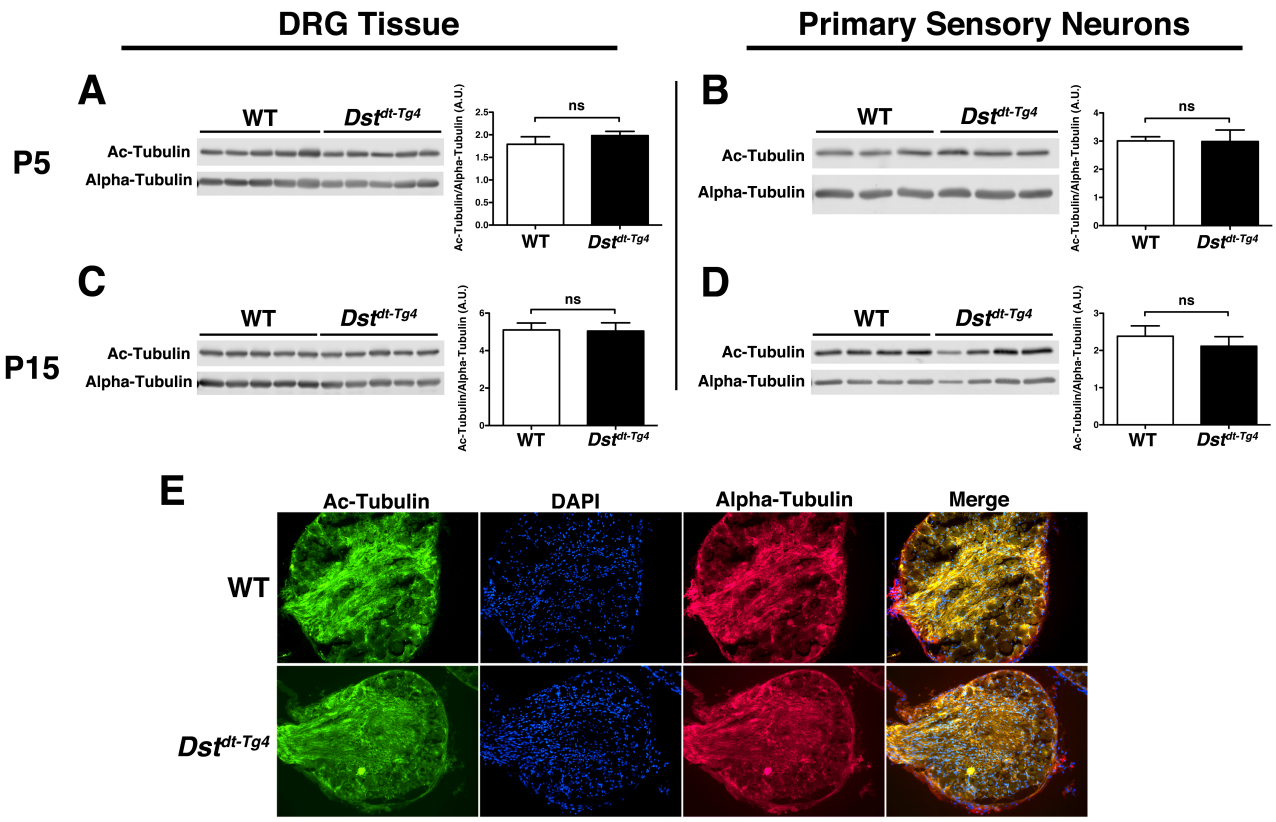


**Figure 3.3.** Tubulin-acetylation is not altered in *Dst*$^{dt\text{-}Tg4}$ sensory neurons. Fluorescence immunoblot analysis of Ac-tubulin and alpha-tubulin loading control for **(A)** P5 *Dst*$^{dt\text{-}Tg4}$ DRGs (n = 5), **(B)** P5 *Dst*$^{dt\text{-}Tg4}$ primary sensory neurons grown in culture (n = 3), **(C)** P15 *Dst*$^{dt\text{-}Tg4}$ DRGs (n = 5) and **(D)** P15 *Dst*$^{dt\text{-}Tg4}$ primary sensory neurons grown in culture (n = 4). Corresponding quantification for each Ac-tubulin:alpha-tubulin ratio is shown on the right of each immunoblot. All lanes of immunoblots represent DRG lysates from a single mouse, 10 µg of protein per lane. Graphical data represented as mean ± SEM, all comparisons were non-significant as assessed by two-tailed Student's *t*-test (*P*-value > 0.05). **(E)** Immunofluorescence micrographs of P15 WT and *Dst*$^{dt\text{-}Tg4}$ DRG tissue stained positive for Ac-tubulin (green) and alpha-tubulin (red; Micrographs at 20X magnification).

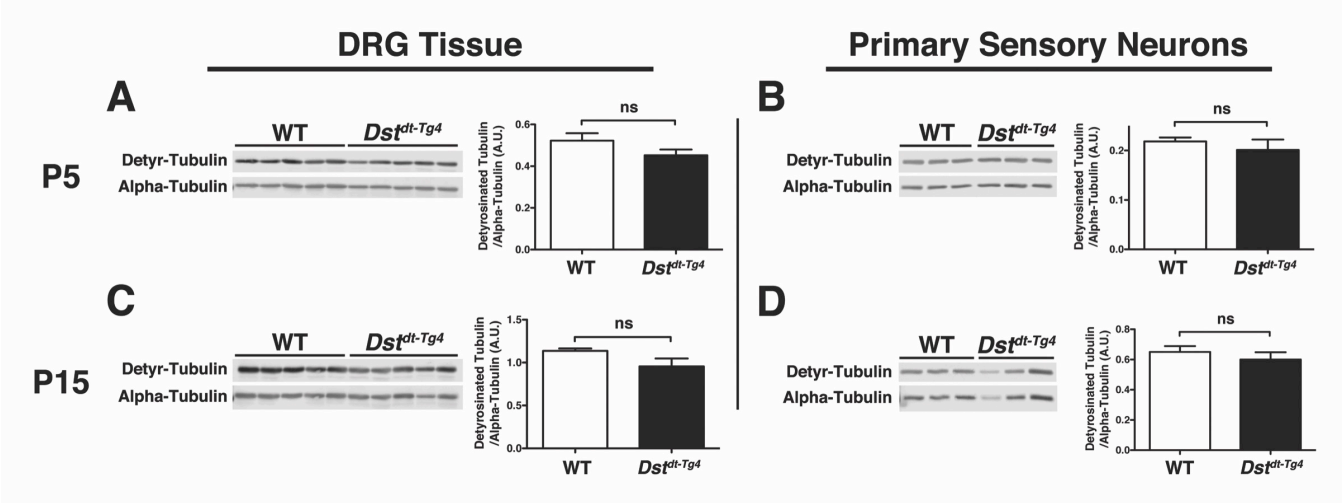


**Figure 3.4.** Detyrosinated-tubulin levels are not altered in *Dst*$^{dt\text{-}Tg4}$ sensory neurons. Fluorescence immunoblot analysis of detyrosinated-tubulin and alpha-tubulin loading control for **(A)** P5 *Dst*$^{dt\text{-}Tg4}$ DRGs (n = 5), **(B)** P5 *Dst*$^{dt\text{-}Tg4}$ primary sensory neurons grown in culture (n = 3), **(C)** P15 *Dst*$^{dt\text{-}Tg4}$ DRGs (n = 5) and **(D)** P15 *Dst*$^{dt\text{-}Tg4}$ primary sensory neurons grown in culture (n = 3). Corresponding quantification for each detyrosinated-tubulin:alpha-tubulin ratio is shown on the right of each immunoblot. All lanes of immunoblots represent DRG lysates from a single mouse, 10 µg of protein per lane. Graphical data represented as mean ± SEM, all comparisons were non-significant as assessed by two-tailed Student's *t*-test (*P*-value > 0.05).

*Dst*$^{dt-27J}$ and *Dst*$^{dt-Tg4}$ mice show disparate patterns of microtubule disorganization in dorsal root axons

As there were no significant changes in microtubule stability of *Dst*$^{dt-Tg4}$ DRGs, we wanted to assess if microtubule organization was also unaffected. Using electron microscopy, we assessed the cytoskeletal organization within dorsal root axons from P15 WT, *Dst*$^{dt-Tg4}$ and *Dst*$^{dt-27J}$ mice (Figure 3.5). As expected, *Dst*$^{dt-27J}$ axons showed massive disorganization of the microtubule network at the cervical, thoracic and lumbar levels. This was marked by short randomly oriented microtubules (white arrows) and areas completely devoid of microtubules (black arrows). *Dst*$^{dt-Tg4}$ axons showed only mild defects at the cervical and thoracic levels, particularly in polarization along the length of the axon. However, their axons at the lumbar region appeared to be just as impaired as in *Dst*$^{dt-27J}$.

Considering the severe lumbar defects in microtubule organization in *Dst*$^{dt-Tg4}$ mice, we wanted to assess whether restoration of the *Dst-a2* isoform could improve these impairments. To test this we used the *PrP-Dst-a2/PrP-Dst-a2*;*Dst*$^{dt-Tg4}$ transgenic mouse model. *PrP-Dst-a2/PrP-Dst-a2*;*Dst*$^{dt-Tg4}$ mice (herein referred to as *PrP*;*Dst*$^{dt-Tg4}$) are *Dst*$^{dt-Tg4}$ mice in which there is transgenic expression of full-length *Dst-a2* cDNA under the neuronal prion protein promoter (PrP) (Ferrier et al., 2014). Interestingly, we did not observe any major differences between *PrP*;*Dst*$^{dt-Tg4}$ and *Dst*$^{dt-Tg4}$ axons (Figure 3.5). The lack of any discernable difference could be due to the fact that Dst-a1 is still absent or possibly due to the low levels of the *Dst-a2* transgene expressed in DRG tissue (Ferrier et al., 2014). It may even be that differential expression of the transgene in DRGs along the length of the spinal cord contributes to the lumbar defects that persist in *PrP*;*Dst*$^{dt-Tg4}$ mice. In order to address this concern we evaluated *Dst-a2* expression within cervical, thoracic and lumbar level DRGs from WT and *PrP*;*Dst*$^{dt-Tg4}$ mice (Figure S3.2).

We however did not see a significant difference in transgene expression at any of the spinal levels from *PrP*;*Dst*$^{dt\text{-}Tg4}$ mice, suggesting that *Dst-A2* is uniformly expressed in DRGs at all levels.

Curiously, the observed patterns of microtubule disorganization mirror the way in which both *Dst*$^{dt\text{-}Tg4}$ and *Dst*$^{dt\text{-}27J}$ mice present their phenotype. By P15, *Dst*$^{dt\text{-}27J}$ mice have lost all fore-limb and hindlimb movement coordination and exhibit dystonic postures (Figure 3.6A left panel), in accordance with defects observed along the full length of the spinal cord. Conversely *Dst*$^{dt\text{-}Tg4}$ mice are not as severely affected at this age as they can still support themselves and coordinate movement with their forelimbs and do not adopt dystonic postures. However, in parallel with lumbar spinal cord defects, their hindlimbs do exhibit impaired movement coordination (Figure 3.6A right panel). *PrP;Dst*$^{dt\text{-}Tg4}$ mice also exhibit a phenotype similar to *Dst*$^{dt\text{-}Tg4}$, although onset is delayed. They retain forelimb control, but hindlimb coordination is impaired, in line with the impairments in microtubule disorganization observed.

Results from horizontal ladder test confirm that *Dst*$^{dt\text{-}27J}$ forelimb and hindlimb coordination is more severely affected compared to WT littermates and *Dst*$^{dt\text{-}Tg4}$ mice. Defects are observed as early as P10, and coordination of both limb pairs continues to worsen until death (Figure 3.6B and C). *Dst*$^{dt\text{-}Tg4}$ mice show some impairment in forelimb coordination, though this level of impairment is maintained at a relatively steady state from P10 until death (Figure 3.6B). *Dst*$^{dt\text{-}Tg4}$ hindlimb coordination however appears to gradually decline over the testing period (Figure 3.6C). Although no significant difference was detectable between *Dst*$^{dt\text{-}Tg4}$ forelimb and hindlimb coordination by horizontal ladder test, qualitative assessment of these mice suggests a greater impairment in hindlimb function and coordination. As *Dst*$^{dt\text{-}Tg4}$ mice tend to drag their

hindlimbs behind them when they walk, the severity of their hindlimb defect would not be detectable by this test.

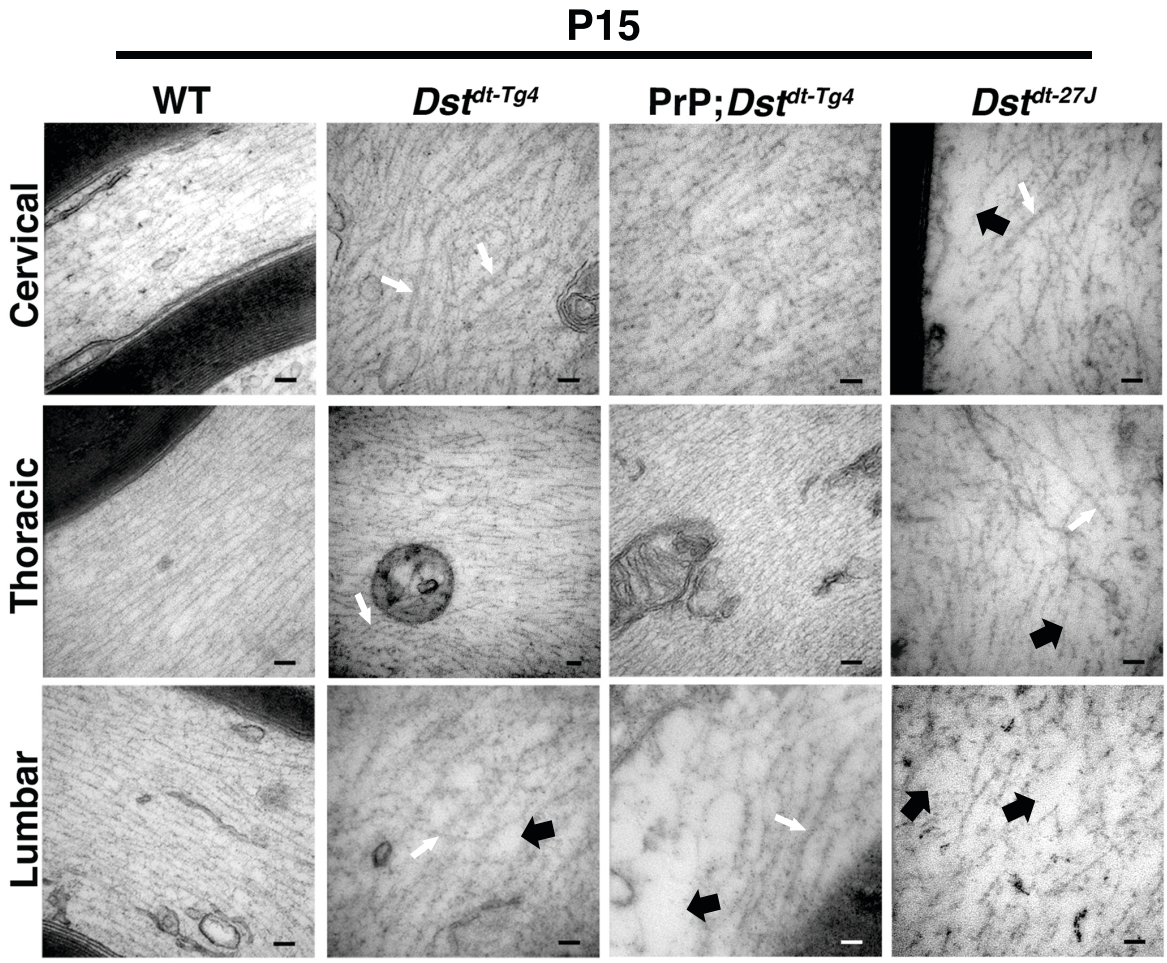


**Figure 3.5.** Microtubule organization in *Dst*$^{dt\text{-}Tg4}$ dorsal root axons shows milder defects compared to *Dst*$^{dt\text{-}27J}$. Electron micrographs of P15 WT, *Dst*$^{dt\text{-}Tg4}$,*PrP*;*Dst*$^{dt\text{-}Tg4}$ and *Dst*$^{dt\text{-}27J}$ dorsal root axons from cervical, thoracic and lumbar levels. At all levels *Dst*$^{dt\text{-}27J}$ appears to have major defects in microtubule network organization. Conversely, *Dst*$^{dt\text{-}Tg4}$ and *PrP*;*Dst*$^{dt\text{-}Tg4}$ dorsal root axons at the cervical and thoracic levels show much milder defects. However, their lumbar level dorsal root axons appear to have microtubule defects similar to those seen in *Dst*$^{dt\text{-}27J}$. Black arrows indicate areas devoid of microtubules, white arrows indicate disorganized microtubules (scale bars = 100 nm).

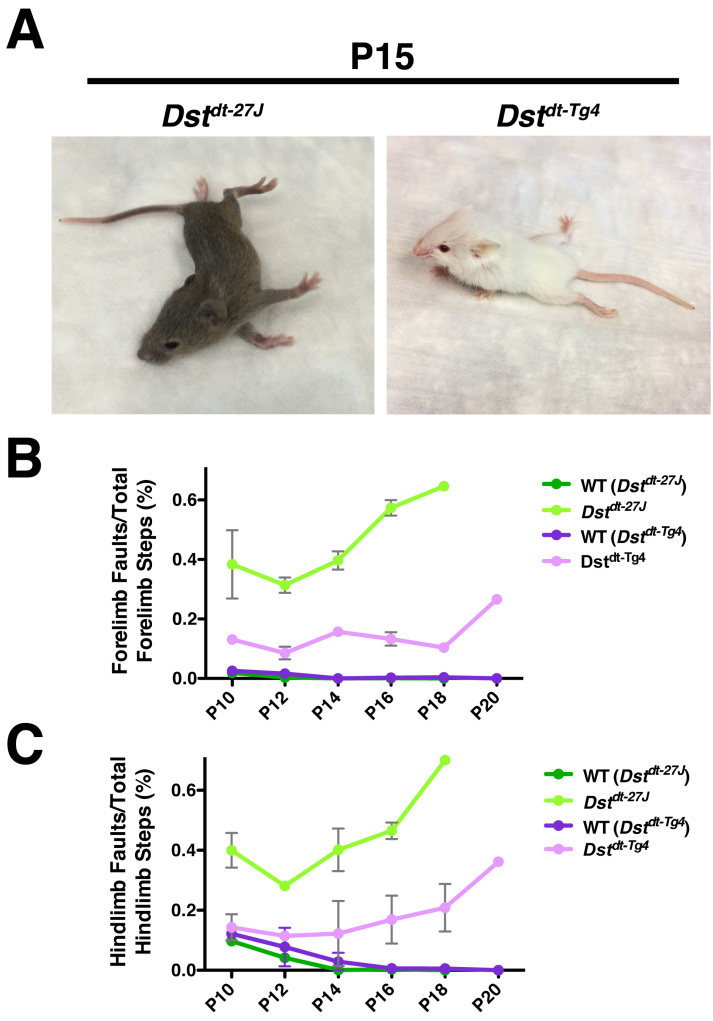


**Figure 3.6.** *Dst*$^{dt\text{-}Tg4}$ mice have a milder phenotype than *Dst*$^{dt\text{-}27J}$. **(A)** Phenotype stage (P15) *Dst*$^{dt\text{-}27J}$ mouse (left) and *Dst*$^{dt\text{-}Tg4}$ mouse (right). *Dst*$^{dt\text{-}27J}$ has lost all limb coordination and shows writhing and twisting of the trunk. The *Dst*$^{dt\text{-}Tg4}$ mouse does not have dystonic postures. They can support themselves and direct movement with their forelimbs, however their hindlimbs often exhibit poor coordination and drag behind them when they walk. **(B–C)** Results from the horizontal ladder test shows that forelimb and hindlimb coordination simultaneously decline early (P10–12) in *Dst*$^{dt\text{-}27J}$ mice (n = 7 for WT, and n = 3 for *Dst*$^{dt\text{-}27J}$ though only one mouse survived to P18 time point). Conversely, *Dst*$^{dt\text{-}Tg4}$ mice exhibit a milder impairment in forelimb

coordination compared to $Dst^{dt\text{-}27J}$. Hindlimb defects are also less severe compared to $Dst^{dt\text{-}27J}$. The frequency of detectable hindlimb faults appears to gradually increase over time in $Dst^{dt\text{-}Tg4}$ mice (n = 3, though for $Dst^{dt\text{-}Tg4}$ only one mouse survived to P20 time point). It should however be noted that hindlimb dragging, a common $Dst^{dt\text{-}Tg4}$ phenotype, could not be measured by this test (∗ *P*-value < 0.05, ∗∗ *P*-value < 0.005, ∗∗∗*P*-value < 0.0005 comparison between $Dst^{dt\text{-}27J}$ and $Dst^{dt\text{-}Tg4}$; # *P*-value < 0.05, ## *P*-value < 0.005 comparison between $Dst^{dt\text{-}27J}$ and their WT littermates; $ *P*-value < 0.05, $$ *P*-value < 0.005 comparison between $Dst^{dt\text{-}Tg4}$ and their WT littermates).

Microtubule stability and organization remain unchanged in late-stage *Dst*$^{dt\text{-}Tg4}$ DRGs

Considering *Dst*$^{dt\text{-}Tg4}$ mice live longer than *Dst*$^{dt\text{-}27J}$ (Figure 3.8L), we wanted to make certain that we were not missing any microtubule-related defects at P15, which is not necessarily 'end-stage' for *Dst*$^{dt\text{-}Tg4}$ mice. As such, ratios of Ac-tubulin and detyrosinated-tubulin to overall alpha-tubulin were determined for P21 *Dst*$^{dt\text{-}Tg4}$ and WT DRGs (Figure 3.7A and B). There were no significant differences observed for either condition. We also assessed microtubule organization in cervical, thoracic and lumbar dorsal root axons from P20 *Dst*$^{dt\text{-}Tg4}$ and *PrP*;*Dst*$^{dt\text{-}Tg4}$ mice, as well as from P40 *PrP*;*Dst*$^{dt\text{-}Tg4}$ mice (Figure 3.7C). Cervical and thoracic level microtubule organization in *Dst*$^{dt\text{-}Tg4}$ and *PrP*;*Dst*$^{dt\text{-}Tg4}$ axons was similar to that at P15. Lumbar dorsal root axons continued to display the same level of cytoskeletal disorganization. No further defects were observed in late-stage (P40) *PrP*;*Dst*$^{dt\text{-}Tg4}$ dorsal root axons. From this we find that 1) microtubule stability is unaltered in *Dst*$^{dt\text{-}Tg4}$ DRGs and 2) defects in microtubule organization are present, particularly at the lumbar level, which correlates with presentation of phenotype.

In order to address whether the observed differences between *Dst*$^{dt\text{-}27J}$ and *Dst*$^{dt\text{-}Tg4}$ mice could be due to differences in cell death, we evaluated apoptosis by TUNEL labeling, along with a cell death analysis by assessment of histological features via hematoxylin and eosin staining in phenotype stage DRGs (Figure S3.3). We did not observe any overt difference in number of TUNEL positive sensory neurons between *Dst*$^{dt\text{-}27J}$ and *Dst*$^{dt\text{-}Tg4}$ at any spinal level. We do however see that there is an abundance of TUNEL positive glial cells in *Dst*$^{dt\text{-}27J}$ and *Dst*$^{dt\text{-}Tg4}$ sections, these can primarily be seen at cervical and thoracic levels. Histological analysis reveals that there may be fewer sensory neurons present within *Dst*$^{dt\text{-}27J}$ when compared to *Dst*$^{dt\text{-}Tg4}$ mice, however this may be due to the somewhat smaller size of the mice and their DRGs. Further

quantitative analysis of sensory neuron number over multiple time points is necessary to determine whether this is a result of cell death or other factors.

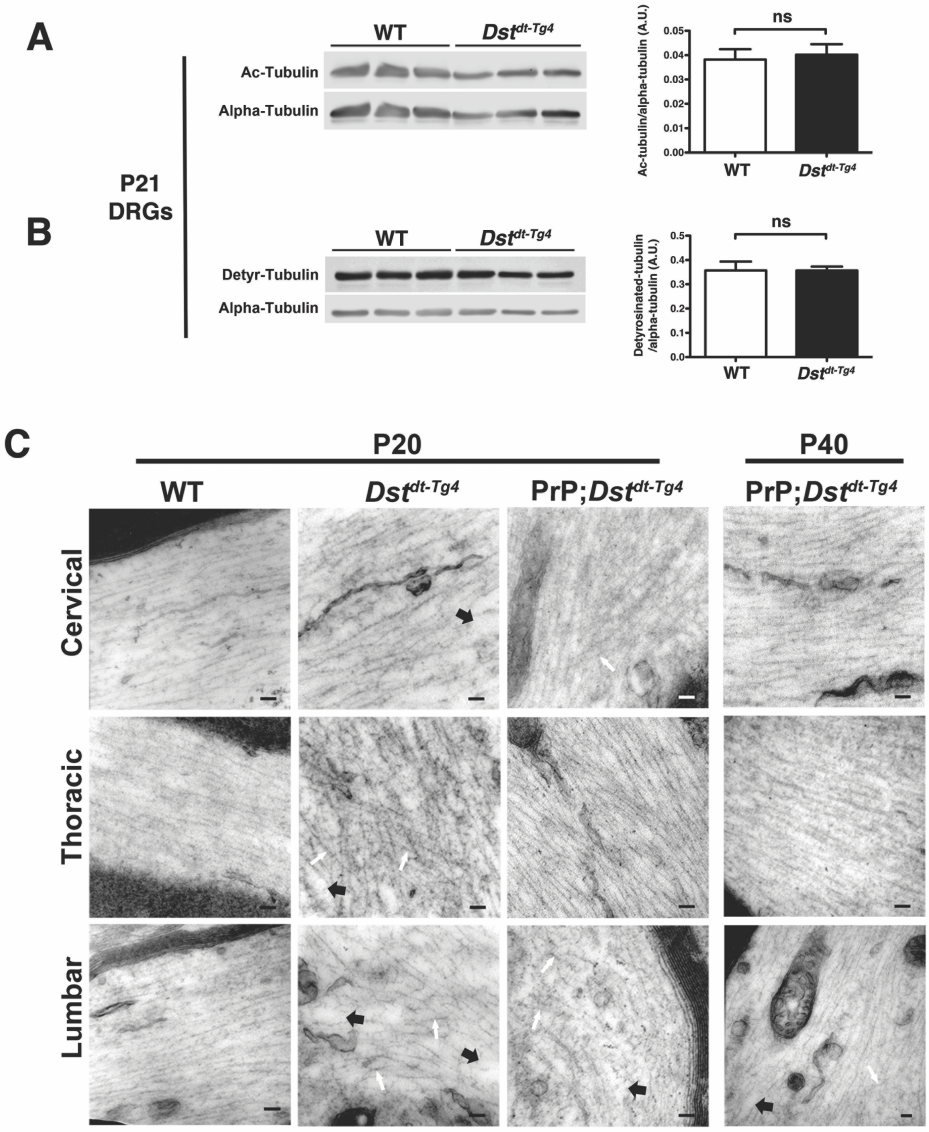


**Figure 3.7.** Late stage *Dst*$^{dt\text{-}Tg4}$ DRGs show no further changes to microtubule network organization. **(A)** Fluorescence immunoblot analysis of Ac-tubulin and alpha-tubulin loading control for P21 *Dst*$^{dt\text{-}Tg4}$ DRGs, quantification of Ac-tubulin:alpha-tubulin ratio shown on the right (n = 3, ns *P*-value > 0.05). **(B)** Fluorescence immunoblot analysis of detyrosinated-tubulin and alpha-tubulin loading control for P21 *Dst*$^{dt\text{-}Tg4}$ DRGs, quantification of detyrosinated-tubulin:alpha-tubulin ratio shown on the right (n = 3, ns *P*-value > 0.05). **(C)** Electron micrographs of P20 WT, *Dst*$^{dt\text{-}Tg4}$ and *PrP*;*Dst*$^{dt\text{-}Tg4}$ dorsal root axons, and P40 *PrP*;*Dst*$^{dt\text{-}Tg4}$

dorsal root axons from cervical, thoracic and lumbar levels. No further changes are observed from P15 electron micrographs. Black arrows indicate areas devoid of microtubules, white arrows indicate disorganized microtubules (scale bars = 100 nm).

*Dst-a3* is upregulated in *Dst*$^{dt\text{-}Tg4}$ DRGs and spinal cord

As we were surprised to find that microtubule stability was unimpaired in *Dst*$^{dt\text{-}Tg4}$ sensory neurons, we considered possibilities for why this pathology is not shared by the different *Dst* alleles. Although *Dst*$^{dt\text{-}27J}$ and *Dst*$^{dt\text{-}Tg4}$ mice are on different genetic backgrounds, C57BL6 and CD1, respectively, the major difference between them is that *Dst*$^{dt\text{-}Tg4}$ retains Dst-a3 expression. Perhaps this isoform has a role in maintaining microtubule stability when the other neuronal isoforms are lost. To evaluate this, we assessed *Dst-a3* gene expression in WT and *Dst*$^{dt\text{-}Tg4}$ DRGs by real-time quantitative reverse transcription-polymerase chain reaction (RT-qPCR). Interestingly, we observed an ~4-fold increase in *Dst-a3* transcript levels in P5 *Dst*$^{dt\text{-}Tg4}$ DRGs (Figure 3.8A), while P15 *Dst*$^{dt\text{-}Tg4}$ DRGs showed an ~3-fold increase in transcript levels (Figure 3.8B). This pattern of upregulation suggests that Dst-a3 may have a compensatory role.

To rule out the possibility that the inserted *hsp68-LacZ* transgene of the *Dst*$^{dt\text{-}Tg4}$ allele is responsible for *Dst-a3* upregulation, we assessed *Dst-a3* transcript levels in P15 heterozygous *Dst*$^{dt\text{-}Tg4}$/+ DRGs and in P15 *PrP*;*Dst*$^{dt\text{-}Tg4}$ DRGs. As *Dst*$^{dt\text{-}Tg4}$/+ DRGs have a 50% reduction in *Dst-a1* and *-a2* expression, and yet *Dst*-a3 transcript levels remain unchanged from WT, this indicates that the *hsp68-LacZ* transgene alone is not capable of increasing *Dst-a3* expression (Figure 3.8C and D). *PrP*;*Dst*$^{dt\text{-}Tg4}$ DRGs on the other hand continue to overexpress *Dst-a3* at a level similar to *Dst*$^{dt\text{-}Tg4}$ DRGs (Figure 2.8C and D). This could be because *Dst-a2* levels in *PrP*;*Dst*$^{dt\text{-}Tg4}$ DRGs are not restored to WT levels (Ferrier et al., 2014) or perhaps Dst-A3 is compensating for a role normally performed by *Dst-a1*.

We also examined *Dst-a3* transcript levels in other neuronal tissues, such as the spinal cord and cerebral cortex, to determine whether this was simply a global effect driven by loss of

*Dst-a1* and *-a2*. $Dst^{dt\text{-}Tg4}$ spinal cord exhibited only an ~50% increase in *Dst-A3* gene expression compared to WT (Figure 3.8E and F), while $Dst^{dt\text{-}Tg4}$ cortex did not show any significant difference (Figure 3.8G and H). Interestingly, when we collectively look at the *Dst-a3* patterns of expression in $Dst^{dt\text{-}Tg4}$ tissues, it appears to occur in a manner that reflects the necessity of Dst for that specific tissue, i.e. *Dst-a3* overexpression is greatest in DRGs, the tissue where loss of Dst has the most severe impact. Milder pathologies are also observed in the spinal cord, where we find *Dst-a3* to be moderately upregulated, and no changes are present in the cerebral cortex where loss of Dst has no significant impact. These results are consistent with Dst-a3 taking on a compensatory role in tissues where Dst is needed, when *Dst-a1* and *-a2* are lost.

To put this in perspective, we assessed the relative levels of *Dst-a3* expression normally present in P15 WT neural tissues (Figure 3.8I and J). Unexpectedly, highest levels were observed in the spinal cord, being roughly 12-fold higher than in cerebral cortex or DRGs. This might be indicative of a unique/novel role for Dst-a3 in the spinal cord. In any case, these results help us to gauge the impact of a 50% increase in spinal cord, and a 3–4-fold increase in DRGs as it relates to *Dst-a3* expression in $Dst^{dt\text{-}Tg4}$ mice. Furthermore, evaluation of the three neuronal *Dst* isoforms in P15 WT DRGs reveals that *Dst-a3* is expressed at extremely low levels compared to both *Dst-a1* and *-a2* (Figure S3.4A and B). This suggests that Dst-a3 may typically not be as important as the other two isoforms in DRGs. However, upon the loss of *Dst-a1* and *-a2*, a 3–4-fold upregulation in *Dst-a3* may have a significant biological effect, further suggesting a compensatory role.

We then examined the *Dst-a3* expression profile for WT and $Dst^{dt\text{-}Tg4}$ DRGs by spinal level to determine whether Dst-a3 has a role in maintaining microtubule organization. We observed no significant differences in *Dst-a3* expression between cervical, thoracic or lumbar

*Dst*$^{dt\text{-}Tg4}$ DRGs, indicating no correlation between level of *Dst-a3* expression and degree of microtubule disorganization (Figure 3.8K). Further examination of microtubule stability in cervical, thoracic and lumbar DRGs also revealed no overt changes in the tubulin acetylation or detyrosination status of *Dst*$^{dt\text{-}Tg4}$ DRGs compared to WT (Figure S3.5A and B).

As both *Dst*$^{dt\text{-}Tg4}$ and *Dst*$^{dt\text{-}27J}$ alleles are on different genetic backgrounds (CD1 and C57BL6, respectively) we wanted to rule out the possibility that genetic factors other than *Dst* could be responsible for the differences between these two alleles. For this we assessed survival of *Dst*$^{dt}$ mice, including *Dst*$^{dt\text{-}Tg4}$ mice on a mixed CD1/C57BL6 background (Figure 3.8L). Since these mixed background *Dst*$^{dt\text{-}Tg4}$ mice have similar survival to *Dst*$^{dt\text{-}Tg4}$ on CD1 background, it is likely that the genetic background doesn't have a major effect on disease presentation.

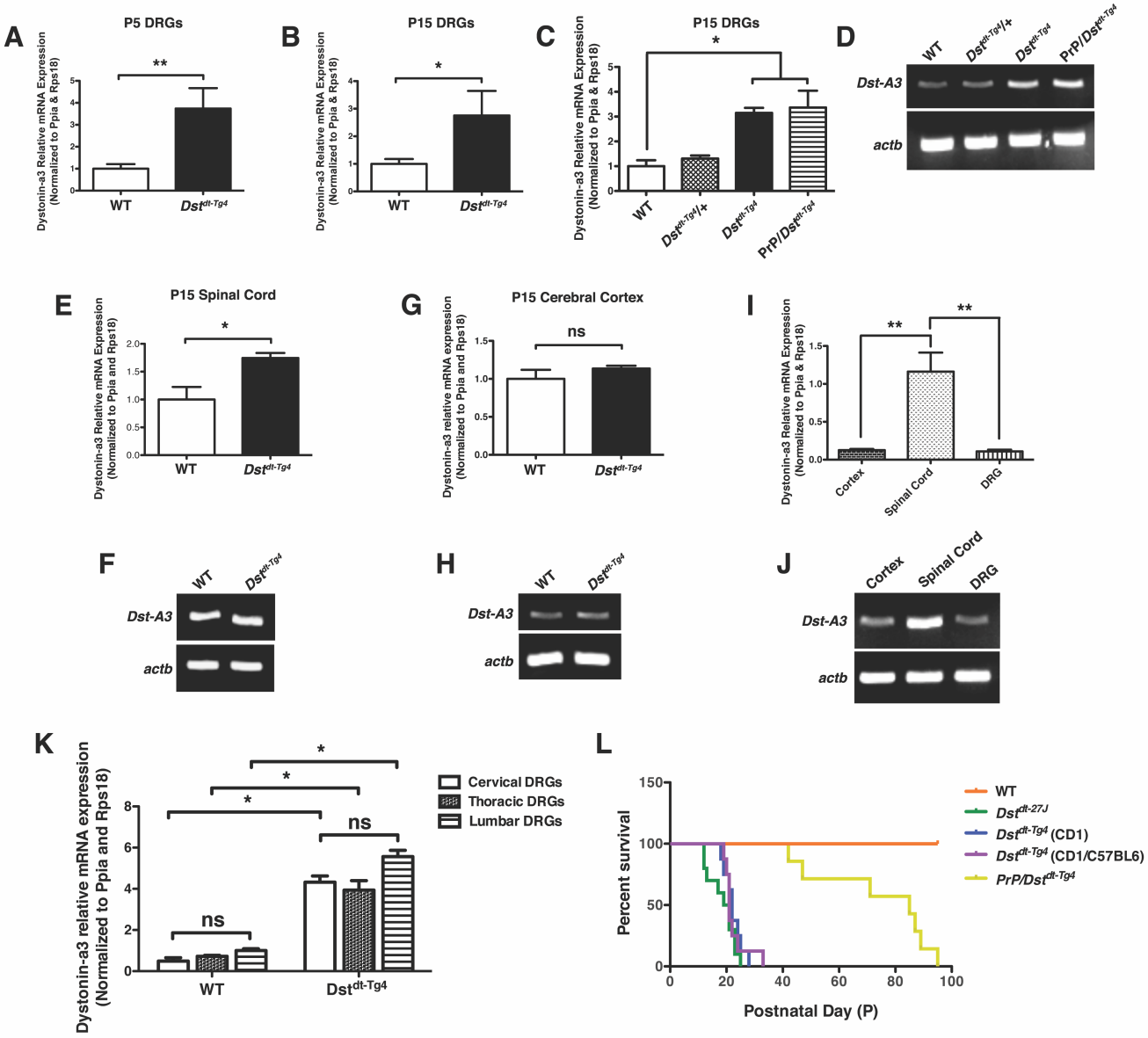


**Figure 3.8.** *Dst-A3* is upregulated in *Dst*$^{dt\text{-}Tg4}$ dorsal root ganglia and spinal cord tissue. Quantification of the relative levels of *Dst-A3* mRNA in P5 **(A)** and P15 **(B)** WT and *Dst*$^{dt\text{-}Tg4}$ DRGs (n = 4, ∗*P*-value < 0.05, ∗∗*P*-value < 0.01). Relative *Dst-A3* expression levels also assessed in P15 WT, heterozygous *Dst*$^{dt\text{-}Tg4}$/+, *Dst*$^{dt\text{-}Tg4}$ and *PrP*;*Dst*$^{dt\text{-}Tg4}$ DRGs by RT-qPCR **(C)** and RT-PCR **(D)** (n = 3, ∗*P*-value < 0.05). *Dst-A3* mRNA expression also assessed in P15 WT and *Dst*$^{dt\text{-}Tg4}$ by RT-qPCR and RT-PCR in spinal cord **(E,F)** and cerebral cortex **(G,H)** tissues (n = 3, ∗*P*-value < 0.05). **(I, J)** *Dst-A3* expression profile assessed in P15 WT cerebral cortex,

spinal cord and DRGs by RT-qPCR and RT-PCR (n = 3, $**P$-value < 0.01). Graphical data represented as mean ± SEM, statistical analysis by two-tailed Student's *t*-test or one-way ANOVA and Tukey's post hoc test, where appropriate. Actin (*actb*) used for loading control in RT-PCR analysis, while *Ppia* and *Rps18* used to normalize in RT-qPCR experiments. **(K)** Quantification of *Dst-A3* mRNA levels in P15 WT and $Dst^{dt\text{-}Tg4}$ DRGs separated by spinal level (cervical, thoracic and lumbar). No significant differences observed within DRGs from each genotype (n = 3, ns *P*-value > 0.05). *Dst-A3* expression normalized to *Ppia* and *Rps18*. Data represented as mean ± SEM, statistical analysis by one-way ANOVA and Tukey's post hoc test. **(L)** Kaplan–Meier survival curve indicates that $Dst^{dt\text{-}Tg4}$ mice, including those on the mixed CD1/C57BL6 background, live longer than $Dst^{dt\text{-}27J}$ mice.

*Dst* knockdown in *Dst*$^{dt\text{-}Tg4}$ sensory neurons results in loss of tubulin acetylation

Thus far we have shown that *Dst-a3* is upregulated in *Dst*$^{dt\text{-}Tg4}$ sensory neurons, in a manner that suggests that this isoform has a compensatory role when *Dst-a1* and *-a2* are lost. To test whether the increase in *Dst-a3* expression within *Dst*$^{dt\text{-}Tg4}$ sensory neurons is directly responsible for the preservation of microtubule stability, we assessed tubulin acetylation status after *Dst* knockdown in *Dst*$^{dt\text{-}Tg4}$ primary sensory neuron cultures. Using an adenovirus delivery system, shRNA specific for either the *Dst* mRNA or a scrambled control were introduced to sensory neuron cultures established from P15 mice. Through RT-qPCR analysis, we were able to validate that the increase in *Dst-a3* expression is specific to the *Dst*$^{dt\text{-}Tg4}$ sensory neuron, as we observed a significant difference between WT and *Dst*$^{dt\text{-}Tg4}$ scrambled groups (Figure 3.9A). In *Dst*$^{dt\text{-}Tg4}$ sensory neurons treated with Dst shRNA, *Dst-a3* was knocked down by 80% relative to scrambled control (Figure 3.9A). Interestingly, the *Dst-A3* knockdown level achieved was comparable to normal physiological levels in WT sensory neurons, thus simply mimicking a loss of the characteristic *Dst-a3* overexpression seen in *Dst*$^{dt\text{-}Tg4}$ DRGs.

To assess changes in microtubule stability with the loss of *Dst-a3* upregulation, we proceeded with immunofluorescence analysis of acetylated-tubulin within *Dst*$^{dt\text{-}Tg4}$ transduced (GFP-positive) neurons. Comparison of the Dst shRNA versus scrambled control-treated *Dst*$^{dt\text{-}Tg4}$ sensory neurons revealed a stark difference in levels of tubulin acetylation within the cell bodies. While scrambled control-treated *Dst*$^{dt\text{-}Tg4}$ neurons maintained high levels of acetylated tubulin throughout the cell body cytoplasm (Figure 3.9B left), the Dst shRNA-treated *Dst*$^{dt\text{-}Tg4}$ neurons had little or no tubulin acetylation throughout the neuron soma (Figure 3.9B right). We also observed neurons in the non-transduced (GFP-negative) Dst shRNA-treated *Dst*$^{dt\text{-}Tg4}$ group that retained a high level of acetylated-tubulin in the soma (Figure 3.9B right, white arrow). Since

*Dst*$^{dt\text{-}Tg4}$ neurons do not express *Dst-a1* or *-a2*, our results indicate *Dst-a3* upregulation is required to achieve the improved microtubule stability observed in *Dst*$^{dt\text{-}Tg4}$ sensory neurons, since returning the expression to normal physiological levels is sufficient to promote a loss of stability when the other *Dst* isoforms are not present.

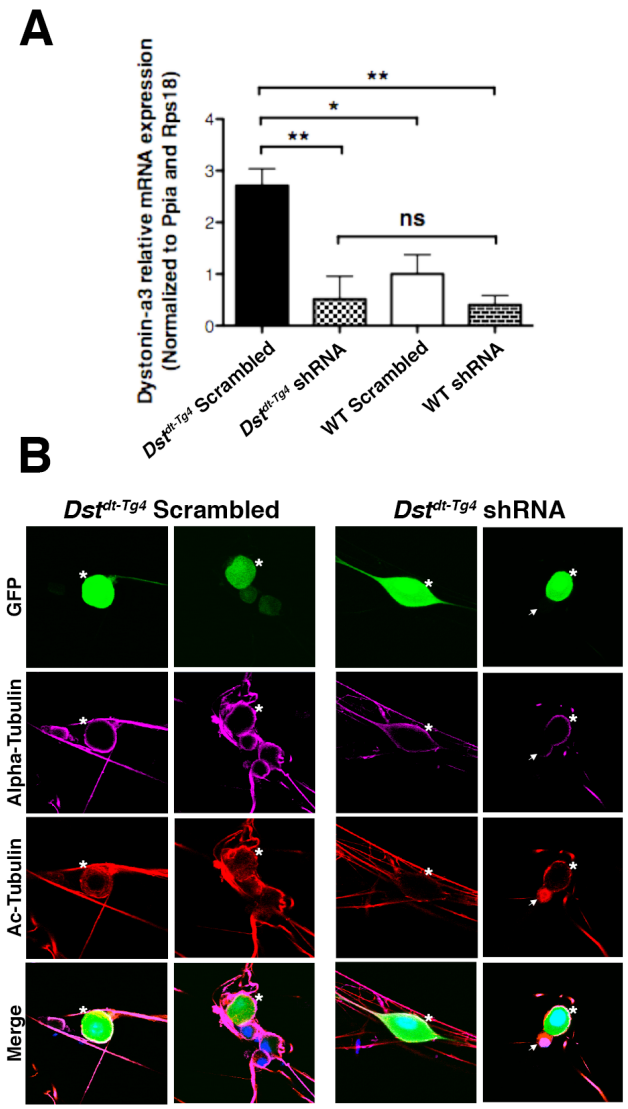


**Figure 3.9.** Knockdown of *Dst-a3* in *Dst*$^{dt\text{-}Tg4}$ primary sensory neurons results in loss of tubulin acetylation. **(A)** Quantification of the relative levels of *Dst-a3* mRNA in *Dst*$^{dt\text{-}Tg4}$ and WT sensory neurons post adenoviral transduction with either Dst shRNA or scrambled control. *Dst*$^{dt\text{-}Tg4}$ sensory neurons show a significant reduction in *Dst-a3* mRNA expression after Dst shRNA treatment compared to the scrambled control-treated sensory neurons. *Dst-a3* expression normalized to *Ppia* and *Rps18*. Data represented as mean ± SEM, statistical analysis by one-way ANOVA and Tukey's post hoc test (n = 3, ∗*P*-value < 0.05, ∗∗*P*-value < 0.01). **(B)**

Immunofluorescence micrographs of *Dst*$^{dt\text{-}Tg4}$ sensory neurons post transduction by AdV-shRNA(Scrambled)-GFP (left) or by AdV-shRNA(Dst)-GFP (right). Transduced cells expressing GFP and the scrambled control are observed to have high levels of acetylated tubulin within the neuronal cell body (indicated by an asterisk). In transduced neurons expressing GFP and Dst shRNA, we observe a reduction in acetylated-tubulin levels. We also observe a non-transduced *Dst*$^{dt\text{-}Tg4}$ sensory neuron (GFP-negative) among the *Dst* shRNA group that continues to maintain a high degree of tubulin acetylation within the cell body (indicated by white arrow). Micrographs shown at 40X magnification.

## Discussion

As Dst-a2 was thought to be the major isoform responsible for microtubule stability, we expected to find defects in tubulin acetylation in $Dst^{dt\text{-}Tg4}$ DRGs, as had previously been found in $Dst^{dt\text{-}27J}$ (Ryan et al., 2012b). Surprisingly, tubulin acetylation was unaltered in $Dst^{dt\text{-}Tg4}$ DRGs, and the organization of the microtubule network was not as severely impaired as $Dst^{dt\text{-}27J}$. Our results show that microtubule instability is not causative of the $Dst^{dt}$ disease, though it may contribute to the severity. We also report an upregulation in *Dst-a3* within $Dst^{dt\text{-}Tg4}$ DRGs, spinal cord tissues and sensory neurons in culture. We have determined that the increase in expression within sensory neurons is part of a compensatory mechanism when other neuronal Dst isoforms are lost. Though Dst-a3 may not typically have a major role in microtubule stability, its increased expression in sensory neurons is responsible for maintaining tubulin acetylation. This is likely one of the major reasons why we see milder pathologies and a longer lifespan in $Dst^{dt\text{-}Tg4}$ mice compared to $Dst^{dt\text{-}27J}$ mice.

### Differences between the $Dst^{dt\text{-}Tg4}$ and $Dst^{dt\text{-}27J}$ alleles

In studying Dst, we often attempt to corroborate our findings from one $Dst^{dt}$ allele in another $Dst^{dt}$ allele (Ferrier et al., 2015). The evidence from the present study, however, shows that this may not always be possible. For the first time, we report differences in pathology between $Dst^{dt\text{-}Tg4}$ and $Dst^{dt\text{-}27J}$ alleles, even though they both still succumb to the disease at an early age.

It had been previously thought that microtubule instability was a common pathology of $Dst^{dt}$, primarily due to the loss of *Dst-a2* expression (Ryan et al., 2012b). Decreased tubulin acetylation had been observed by immunoblot analysis in $Dst^{dt\text{-}27J}$ DRGs and by

immunofluorescence staining of $Dst^{dt\text{-}27J}$ primary sensory neurons. Through siRNA knockdown of *Dst-a1* and *Dst-a2* isoforms in HEK293T immortalized cells, it was found that loss of *Dst-a2* resulted in the most profound defects in microtubule stability and organization (Ryan et al., 2012b). Based on these results, it was believed that *Dst-a2* was the major isoform involved in maintaining microtubule stability; and since $Dst^{dt\text{-}Tg4}$ also lacked this isoform, we presumed microtubule stability would also be impaired. However, what was not accounted for in these studies was the impact of *Dst-a3* expression on microtubules, and siRNA knockdown of this isoform was not attempted in HEK293T cells. Recent work in our laboratory has determined that HEK293T cells do not express the *Dst-a3* isoform (data not shown). Thus, when *Dst-a2* was knocked down, *Dst-a3* would not have been able to compensate, resulting in a dramatic loss of tubulin acetylation.

We saw no change in $Dst^{dt\text{-}Tg4}$ DRG microtubule stability, which is the result of not only *Dst-a3* retention, but of a compensatory effect mediated by *Dst-a3* upregulation (Figure 3.3 and 3.4). This maintenance of microtubule stability may also help to explain why defects in axonal trafficking were not previously observed in $Dst^{dt\text{-}Tg4}$ primary sensory neurons (Bernier et al., 1995). Live imaging of mitochondrial movement over a very short time frame was conducted on WT and $Dst^{dt\text{-}Tg4}$ sensory neurons grown in culture. It was determined that there was no difference in number of motile mitochondria, or in their velocity along the axon. Since molecular motors such as kinesin and dynein preferentially bind and move along acetylated microtubules, this may be why no major defects in mitochondria movement were observed in $Dst^{dt\text{-}Tg4}$ sensory neurons (Reed et al., 2006; Dompierre et al., 2007; Alper et al., 2014). It also appears that the previous work describing microtubule disorganization of $Dst^{dt\text{-}Tg4}$ DRGs had only assessed DRGs of the lumbar spinal level (Bernier and Kothary, 1998). This result is in line with what we

have observed for lumbar *Dst*$^{dt\text{-}Tg4}$ DRGs, however no previous insight had been given as to the state of microtubule organization at higher spinal cord levels. We have now determined that microtubule organization is only mildly impaired at cervical and thoracic level *Dst*$^{dt\text{-}Tg4}$ dorsal root axons, while major defects are present at the lumbar level (Figure 3.5). As this correlates with the *Dst*$^{dt\text{-}Tg4}$ phenotype, we suspect that microtubule disorganization plays some role in phenotype development. It may be that *Dst-a3* overexpression protects against the rapid loss of axonal cytoskeleton disorganization, but since lumbar DRGs continue to overexpress *Dst-a3* and still succumb to extensive microtubule disorganization (Figure 3.8K), Dst-a3 alone is clearly not enough to rescue it. Lumbar DRGs may be more vulnerable to defects since they possess the longest axons (Fernyhough and Calcutt, 2010), or it might be due to another factor that has yet to be elucidated.

It should also be noted that the majority of studies that have reported defective axonal trafficking in *Dst*$^{dt}$ neurons have done so using the *Dst*$^{dt\text{-}27J}$ or *Dst*$^{tm1EFu}$ (*Dst* knockout) alleles, which both lack all *Dst* isoforms (Guo et al., 1995; Dalpé et al., 1998; De Repentigny et al., 2003; Liu et al., 2003; Liu et al., 2007; Ryan et al., 2012b). So perhaps it is a combination of microtubule instability and disorganization that contributes to impaired axonal transport. Although this is the first time we have directly compared *Dst*$^{dt\text{-}Tg4}$ and *Dst*$^{dt\text{-}27J}$ mice to discover differences in their pathologies, it is possible that more differences exist between the two alleles. Identification of these would only stand to help us understand the differences in phenotype and lifespan, and also elucidate a common mechanism of death.

Insights into the role of Dst-a3

Of the three neuronal Dst isoforms, Dst-a3 is the one we know the least about. There is only one previous study that had directly evaluated Dst-a3 (also named BPAG1a3) intracellular localization by use of Flag-tagged constructs. They reported that the Dst-a3 N-terminus contains an myr, which allows this isoform to primarily localize to the plasma membrane (Jefferson et al., 2006). However, a prior study had been conducted on the BPAG1n3 isoform (the less abundant intermediate lament binding isoform) also using Flag-tagged constructs containing the N-terminal of this isoform (Yang et al., 1999). Since both BPAG1n3 and BPAG1a3 (Dst-a3) possess the same N-terminal sequences and only vary towards the C-terminus (Suozzi et al., 2012; Ferrier et al., 2013; Kunzli et al., 2016), we believe the use of N-terminal BPAG1n3 constructs would likely yield results most relevant to Dst-a3, as it is the more predominantly expressed isoform. Their study had found that the BPAG1n3/Dst-a3 N-terminal constructs localized mainly to microtubules, and this was further validated using N-terminal specific BAPG1n3/Dst-a3 antibodies. The proposed function of this isoform on microtubules was that it conferred stability, since this interaction made microtubules more resistant to nocodazole and colchicine treatment (Yang et al., 1999).

Our results further support Dst-a3's involvement in microtubule stability since the knockdown of *Dst-aA3* in $Dst^{dt\text{-}Tg4}$ sensory neurons led to a loss of tubulin acetylation. However, this role may only be relevant when Dst-a3 is upregulated, as is the case for $Dst^{dt\text{-}Tg4}$ sensory neurons and cells transfected with BPAG1n3/Dst-a3 constructs. Under normal conditions Dst-a2 is most likely the major isoform responsible for microtubule stability (Ryan et al., 2012b), especially as *Dst-a2* is also the isoform most abundantly expressed in DRGs (Figure S3.4A and B).

Aside from its N-terminus, Dst-a3 contains the same central plakin domain and C-terminal Gas2-related domain as Dst-a1 and -a2. The plakin domain of Dst has previously been shown to interact with the microtubule stabilizing protein MAP1B (Bhanot et al., 2011). More specifically, MAP1B interaction with Dst-a2 has been shown to maintain tubulin acetylation (Ryan et al., 2012b). It could be that when Dst-a2 is lost, MAP1B preferentially binds to the upregulated Dst-a3 and preserves microtubule stability. Some degree of microtubule stability may also come from direct binding of Dst-a3's Gas2-related domain with microtubules, which has been shown to protect against depolymerization (Prokop et al., 2013).

Ultimately, overexpression of Dst-a3 is not enough to rescue the defects from loss of Dst-a1 and -a2. Therefore this isoform must have its own unique function within the cell and is not fully redundant to either Dst-a1 or -a2. It appears that Dst-a3 is involved in maintaining microtubule stability, however this may not be its predominant function under normal conditions. It would certainly be interesting to further investigate what role Dst-a3 plays within neurons, and as spinal cord seems to express the highest levels of this isoform (Figure 3.8I and J), this tissue would be a good starting point for elucidating its quintessential function within neurons.

Dst isoform compensation in HSAN-VI?

It was previously believed that HSAN-VI was a lethal disorder of childhood (Edvardson et al., 2012), however the discovery of novel compound heterozygous mutations in an Italian family in 2017 has proven otherwise (Manganelli et al., 2017). As these patients are ~40 years of age and were found to only lack the *Dst-a2* isoform, we now know that retention of all three neuronal isoforms is not critical to survival. Considering this, we may expect for HSAN-VI to present in a variety of manners, varying in severity depending on the mutation and the isoforms

affected. Our findings of *Dst-a3* upregulation in $Dst^{dt\text{-}Tg4}$ sensory neurons also lead us to believe that this same mechanism of Dst isoform upregulation is possible in HSAN-VI. This may even be one of the reasons for why a much milder disease presentation is observed in the Italian patients; *Dst-a3* and maybe even *Dst-a1* might be expressed at much higher levels than normal in attempt to offset and compensate for the lack of Dst-a2. This concept is highly exciting as it could open up a number of different therapeutic options, aimed at altering isoform expression levels opposed to the more challenging route of gene therapy.

## Conclusions

Here we have determined that the different *Dst* alleles do not always have identical pathologies. We have observed that microtubule instability is not causative of $Dst^{dt}$ pathology, however it may be one of the factors that influences how severely the disease presents. Additionally, we have also identified an upregulation of *Dst-a3* within $Dst^{dt\text{-}Tg4}$ sensory neurons, indicative of the Dst-a3 isoform taking on a compensatory role in maintenance of microtubule stability when the other neuronal isoforms are lost.

Taken together, the work presented here sheds light onto the phenotypic differences observed between different *Dst* alleles and the underlying genetics that cause them. This is highly relevant to human disease, as *DST* mutations resulting in HSAN-VI lead to a spectrum of symptoms and longevity. Prior to the discovery of the most recent set of HSAN-VI cases, it was believed that HSAN-VI was lethal before the age of two (Edvardson et al., 2012); however the more recent patients deficient in only *DST-a2* continue to live well into their forties (Manganelli et al., 2017). Given the findings we report here, we might even expect to find that *DST-a3* (and even possibly *DST-a1*) are upregulated in their neuronal tissues, potentially compensating for the

normal roles of DST-a2 resulting in milder symptoms and prolonged lifespan. As such, further investigation into the possible compensatory effects of *Dst* isoforms will be invaluable to our understanding of HSAN-VI and in developing therapies for those affected.

## Materials and Methods

### Ethics statement

All experimental protocols on mice were approved by the Animal Care Committee of the University of Ottawa. Care and use of experimental mice followed the guidelines of the Canadian Council on Animal Care and the Animals for Research Act.

### Animals

The *Dst*$^{dt\text{-}Tg4}$ mouse line arose from a transgene insertion–deletion that affected the 5′ region encoding the ABD specific to DST-a1 and DST-a2 isoforms (Kothary et al., 1988; Brown et al., 1995b; Pool et al., 2005). For these experiments, all *Dst*$^{dt\text{-}Tg4}$ mice and their WT littermates were maintained on a CD1 background (except where specifically indicated that they are on a mixed CD1/C57BL6 background). The *Dst*$^{dt\text{-}27J}$ line arose due to spontaneous mutation and was found to express very low levels of the *Dst* transcript (Pool et al., 2005). These mice, along with their WT littermates, are on a C57BL6 genetic background. Genotypes for both lines of mice were determined by PCR amplification of genomic tail DNA, as described in (Lynch-Godrei and Kothary, 2016).

The *PrP-Dst-a2/PrP-Dst-a2;Dst*$^{dt\text{-}Tg4}$ rescue mouse (referred to as *PrP*;*Dst*$^{dt\text{-}Tg4}$ mice in the text) is a transgenic mouse which exogenously expresses Dst-a2 under the control of the neuronal PrP on the *Dst*$^{dt\text{-}Tg4}$ background. These mice are maintained and bred on a mixed CD1/C57BL6 background. The derivation and characterization of these mice have been previously described in (Ferrier et al., 2014; Lynch-Godrei and Kothary, 2016).

Primary sensory neuron culture and adenovirus transduction

DRGs from P5 and P15 mice were collected following the protocol previously described in (Lynch-Godrei and Kothary, 2016). The individual 1.5 ml microfuge tubes containing DRGs in 1X Hank's Balanced Salt Solution (HBSS; Gibco) were centrifuged at 300 g for 5 min. The HBSS was removed and replaced with 300 µl of prewarmed 1.7 mg/ml papain (Worthington). Tubes were then incubated in a 37◦C water bath for 10 min and centrifuged at 300 g for 5 min. The papain solution was then removed and replaced with 300 µl of 2 mg/ml Collagenase A (Roche). Tubes were once again incubated in a 37◦C water bath for 10 min and centrifuged at 300 g for 5 min. After centrifugation, Collagenase A was carefully removed and replaced with 1 ml DRG media (10% fetal bovine serum [FBS; Gibco], 1% penicillin/streptomycin [Gibco], in a Dulbecco's Modified Eagle Medium [DMEM; Wisent] base). Tubes were centrifuged again at 300 g for 5 min. After centrifugation, the 1 ml of DRG media was removed and replaced with 1.3 ml fresh DRG media. Flame-polished glass Pasteur pipettes were then used to dissociate the DRG neurons by trituration. Tubes were centrifuged for a final time at 300 g for 5 min. Supernatant was removed, and the pellets were resuspended in 1 ml of fresh DRG media. Total DRG neurons from a single mouse were then seeded in a single well of a 6-well plate coated with 4% Laminin (LN2; Millipore). Plates were then transferred to a 37◦C tissue culture incubator at 8.5% CO2. Twelve hours later, full media change was performed by replacing DRG media with neuronal maintenance media (DMEM base [Wisent], 0.5% FBS [Gibco], 1% penicillin/streptomycin [Gibco], 2% B27 supplement [Gibco], 1% GlutaMax [Gibco], 16 mg/ml putrescine [Sigma-Aldrich], 400 mg/ml thyroxine [Sigma-Aldrich], 400 mg/ml triiodothyronine [Sigma-Aldrich], 6.2 ng/ml progesterone [Sigma-Aldrich], 5 ng/ml sodium selenite [Sigma-Aldrich], 100 mg/ml bovine serum albumin [BSA; Sigma-Aldrich], 5 mg/ml bovine insulin

[Sigma-Aldrich], 50 mg/ml holo-transferrin [Sigma-Aldrich] supplemented with 1 mm 5- uoro-2′-deoxyuridine [Sigma-Aldrich]). A two-thirds media change was performed every other day until protein or RNA collection on day five.

For adenovirus transduction experiments, P15 primary sensory neuron cultures were grown as usual until day five and then transduced with either custom-designed Ad-U6-shRNA(m*DST*)- CMV-GFP (SignaGen Laboratories) or a scrambled control Ad-U6-shRNA(Scramble)-CMV-GFP (SignaGen Laboratories) at a multiplicity of infection of 450 for both. Transduced sensory neuron cultures were maintained for 72 h, RNA was then collected or coverslips were fixed with 3% paraformaldehyde (PFA) for immunofluorescence analysis.

Immunoblotting

Protein was extracted from primary sensory neuron cultures, and from P5, P15 and P21 DRG tissue by gently homogenizing the samples with 1X RIPA buffer (Sigma-Aldrich) supplemented with 6 µl/ml phenyl methyl sulfonyl fluoride (Sigma-Aldrich). Samples were left on ice for 10 min before centrifugation at 4◦C for 10 min at 12 000 g. Supernatant was then collected, and concentrations were determined by bicinchoninic acid assay (BCA assay; Pierce). Protein samples (10 µg, except where indicated otherwise) were separated by SDS-PAGE in 10% gels. PVDF membranes were incubated overnight at 4◦C in a dilution of Odyssey® blocking buffer (LI-COR) and primary antibody. The following primary antibodies were used: mouse monoclonal anti-acetylated tubulin antibody (1:40 000; Sigma-Aldrich #T7451), rabbit polyclonal anti-detyrosinated tubulin antibody (1:25 000; Millipore #AB3201), mouse monoclonal anti-alpha tubulin antibody (1:50 000; Calbiochem CP06) and rabbit polyclonal anti-alpha tubulin antibody (1:20 000; Abcam ab18251). Membranes were then washed 3 times with

1X Tris-Buffered Saline and incubated for 1 h at RT in an Odyssey® blocking buffer (LI-COR) and secondary antibody solution. Infrared dye conjugated (IRDye®) secondary antibodies used include goat anti-rabbit 800CW (IgG, 1:10,000; LI-COR; 926–32211), goat anti- rabbit 680RD (IgG, 1:10,000; LI-COR; 926–68071), goat anti-mouse 800CW (IgG, 1:10,000; LI-COR; 926–32210) and goat anti-mouse 680RD (IgG, 1:10,000; LI-COR; 926–68070). Bands were visualized and quantified using the Odyssey® CLx infrared imaging system (LI-COR Biosciences).

Immunohistochemistry

Whole DRGs from P15 WT and $Dst^{dt\text{-}Tg4}$ mice were extracted following euthanasia and placed in Cryomolds® (Tissue-Tek®) containing O.C.T. compound (Tissue-Tek®) and snap frozen in liquid nitrogen. Sections of 7 μm thickness were made using a cryostat and mounted on glass slides for staining. Slides were then fixed in 4% PFA for 10 min and washed 3 times in 1X phosphate buffered saline (PBS), pH 7.4. Sections were permeabilized in 0.2% Triton-X (Sigma-Aldrich) in 1X PBS for 10 min and then blocked in 1% BSA (Sigma-Aldrich) in 1X PBS for 15 min. Primary antibody dilutions of anti-Ac tubulin antibody (1:1000; Sigma-Aldrich #T7451) and anti-alpha-tubulin antibody (1:1200; Millipore 04–1117) were applied to slides and incubated for 1 h at room temperature. Secondary antibodies Alexa Fluor 488 goat anti-mouse (1:1000; Invitrogen A-11001) and Alexa Fluor 555 goat anti-rabbit (1:1000; Invitrogen A-21428) applied to slides for 45 min at room temperature. Finally, DAPI (1:1000) was applied for 5 min at room temperature, and slides were then mounted in Dako fluorescence mounting medium (Dako S3023).

Immunocytochemistry

Transduced P15 primary sensory neuron cultures were fixed on coverslips in 3% PFA for 10 min, and subsequently washed 3 times with 1X PBS for 5 min. Cells were then permeabilized with 0.1% Triton-X (Sigma-Aldrich) in 1X PBS for 10 min, washed 3 times with 1X PBS and blocked for 1 h with 10% goat serum in 1X PBS. Primary antibody dilutions of anti-Ac-tubulin antibody (1:5000; Sigma-Aldrich #T7451) and anti-alpha-tubulin antibody (1:5000; Abcam ab18251) were made in 10% goat serum and left on coverslips overnight at 4°C. Coverslips were then washed 3 times in 1X PBS for 5 min and incubated with secondary antibody solution for 1 h at room temperature. The secondary antibody dilution consisted of Alexa Fluor 555 goat anti-mouse (1:200, Invitrogen A28180) and Alexa Fluor 647 goat anti-rabbit (1:200, Invitrogen A-21244). Coverslips were then counterstained with Hoechst (1:5000) and mounted in Dako fluorescence mounting medium (Dako S3023). Analysis was performed using a Zeiss LSM 510 Confocal Microscope equipped with Zen 2009 imaging software (Zeiss). An n = 3 was analyzed for WT and $Dst^{dt\text{-}Tg4}$ sensory neurons transduced with either shRNA or scrambled control. Images were taken at a magnification of 40X.

TUNEL labeling

Cervical, thoracic and lumbar DRGs were dissected from P15 WT, $Dst^{dt\text{-}27J}$ and $Dst^{dt\text{-}Tg4}$ mice. Sections were made at a thickness of 10 μm and washed in 1X PBS. Sections were fixed for 20 min in 4% PFA, followed by a 30 min wash in 1X PBS. Permeabilization was carried out using ice cold 0.1% sodium citrate/0.1% Triton X-100 for 2 min. Samples were rinsed 3 times for 5 min in 1X PBS and incubated for 1 h at 37°C with FITC-labeled dUTP in terminal deoxynucleotidyl transferase (TdT) buffer (30 mM Tris-HCl pH 7.2, 140 mm sodium cacodylate

and 1 mm cobalt chloride) and TdT according to the protocol provided by the manufacturer (Roche). Positive controls were treated with DNase I for 15 min, and negative controls included sections incubated with FITC-labeled dUTP in the absence of TdT. Cells were washed in 1X PBS, mounted in Dako fluorescent mounting media (Dako S3023) and analyzed with a Zeiss Axiovert 200 M epifluorescence microscope equipped with an AxioCam HRm digital camera and AxioVision 4.6 software (Zeiss).

Hematoxylin and Eosin staining

Whole cervical, thoracic and lumbar DRGs were extracted from P15 mice and fixed in formalin (Fisher Scientific) at 4°C for 48 h. Samples were then transferred to 70% ethanol and stored at 4°C until processing. DRG samples were processed at the University of Ottawa (Department of Pathology and Laboratory Medicine), where they were set in agarose before embedding in paraffin wax with a LOGOS microwave hybrid tissue processor. Paraffin-embedded samples were cut by microtome at a thickness of 4 μm and stained for hematoxylin and eosin using a Leica ST5010 Autostainer XL combined with Leica CV5030 Glass Coverslipper. Stained slides were scanned with a MIRAX MIDI digital slide scanner (Zeiss). Images were acquired using 3DHISTECH Panoramic Viewer 1.15.4 at 20X magnification.

RNA-isolation and RT-PCR analysis

RNA was isolated from P15 DRG, spinal cord and cortex tissues, as well as from primary sensory neuron cultures from P15 mice using the RNeasy® Mini Kit (Qiagen), as per the manufacturer's protocol. Samples were reverse-transcribed with $RT^2$ First Strand cDNA synthesis kit (Qiagen) using 1 μg total RNA. For cDNA from P15 tissues, we then further diluted

the preparation to a 1 in 5 dilution using RNase-free water (Qiagen). For each of the *Dst* transcripts, the RT-PCR reaction is made up of 10 µl SsoFastTM EvaGreen® Supermix (Bio-Rad), 5 µl diluted cDNA, 1 µl of 10 µM forward + reverse primer mix and 4 µl RNase-free water. The RT-PCR reaction for actin transcript includes 10 µl SsoFastTM EvaGreen® Supermix (Bio-Rad), 5 µl diluted cDNA, 0.2 µl of 10 µM forward + reverse primer mix and 4.8 µl RNase-free water. The cycling parameters are the same for each target: (1) denature at 95°C for 10 min; (2) denature at 95°C for 10 s; (3) anneal at 60°C for 30 s; and (4) repeat steps 2–3 for 30 cycles. The forward primers for the *Dst* isoforms are *Dst-a1* forward CTA CAT GTA CGT GGA GGA GCA, *Dst-a2* forward GAG GGC TGT GCT TCG GAT AG, *Dst-a3* forward GTC TCC AAG GAT GCA CCT AGG GAT, *Dst- a1/a2/a3* reverse CAT CGT TTG CAC CAA TGC C, β-*actin* (*actb)* forward CCG TCA GGC AGC TCA TAG CTC TTC and β-*actin* (*actb)* reverse CTG AAC CCT AAG GCC AAC CGT. Products were run in a 2% agarose gel containing RedSafe™ nucleic acid staining solution (Froggabio), and bands were visualized under UV light.

Quantitative RT-PCR

*Dst-a1/-a2/-a3* primer sets are the same as indicated above. Expression of *Dst* transcripts was normalized to *Ppia* and *Rps18* (Bio-Rad PrimePCR™ pre-optimized primers) by Ct method. These two gene products were found to have the lowest M value out of a series of different targets tested. Reaction mixtures for these are the same as for *Dst* as described above. Cycling parameters are the same for each target: (1) denature at 95°C for 10 min; (2) denature at 95°C for 10 s; (3) anneal at 60°C for 30 s; and (4) repeat steps 2–3 for 40 cycles. Runs were amplified using a Bio-Rad CFX96. Each genotype and treatment condition (*Dst* shRNA or scrambled

control) was run as three biological replicates (except where indicated), and all samples were run in technical triplicate, with only those within a range of 0.2 Cq used for analysis.

Transmission electron microscopy

Mice were anesthetized by intraperitoneal injection of tribromomethanol (Avertin) and transcardially perfused with 5 mL of 1X PBS followed by 10 mL of Karnovsky's fixative (4% paraformaldehyde, 2% glutaraldehyde [Sigma-Aldrich] and 0.1 M sodium cacodylate buffer [Electron Microscopy Sciences] in 1X PBS). Dorsal root axons were then extracted and separated according to spinal level (cervical, thoracic and lumbar) and fixed overnight at 4◦C in the same fixative. Following fixation, each root was cut into a straight 1 mm segment. Segments were subsequently washed in 0.1 M sodium cacodylate buffer (Electron Microscopy Sciences) for 1 h at room temperature, and again overnight at room temperature. Segments were post-fixed with 1% osmium tetroxide (Electron Microscopy Sciences) and 1.5% potassium ferrocyanide trihydrate (for myelin staining; Acros Organics) in 0.1 M sodium cacodylate buffer for 1 h at room temperature. Samples were then washed 3 times in 0.2 M sodium cacodylate buffer, pH 7.4, for 15 min each. A second fixation step was performed in 2% glularaldahyde and 0.2 M sodium cacodylate buffer for 1.5 h at room temperature. These were washed 3 times in distilled water for 10 min and then dehydrated twice for 20 min for each step in a graded series of ethanol (Commercial Alcohols) from 30–50–70–85–95% ethanol in water. This was followed by two 30 min washes in 100% ethanol, two 15 min washes in 50% ethanol/50% acetone and two 15 min washes in 100% acetone (Fisher Scientific). Dorsal root axon segments were infiltrated in 30% spurr resin/acetone for 20 min, and once overnight, then in 50% spurr resin/acetone for 6 h and finally in 100% spurr resin (Electron Microscopy Sciences) overnight. Segments remained in 100% spurr resin, which was changed twice a day for 3 days at room temperature. All infiltration

steps were performed on a rotator at low speed. Segments were embedded in fresh liquid spurr resin, oriented longitudinally inside the molds and then polymerized overnight at 70°C. Ultrathin sections (80 nm) were then collected onto 200 mesh copper grids and stained with 2% aqueous uranyl acetate (Electron Microscopy Sciences) and Reynold's lead citrate (sodium citrate [Electron Microscopy Sciences] and lead nitrate [Electron Microscopy Sciences]). Sections were observed under a transmission electron microscope (Hitachi 7100) at 40 000X, 70 000X and 100 000X magnifications. An n = 2–3 was used for all P15 dorsal root axon samples, while an n = 1 was used for P20 and P40 dorsal root axon samples. Approximately 50 micrographs were examined at the cervical, thoracic and lumbar levels for each n.

Horizontal ladder test

The testing apparatus was composed of a 4-sided clear box with a Sony Handycam HDR-CX210 5.3 Megapixel Camcorder placed inside, facing upwards toward a horizontal ladder placed lengthwise along the edges of the box. Pup testing began at P10, with testing occurring every second day until the death of the $Dst^{dt}$ mice. Each pup was placed in the middle of the ladder (rungs spaced 0.5 cm apart) and movements were video recorded throughout a 2 min testing period. Analysis of videos included counting total number of steps by forelimbs and by hindlimbs, as well as the total number of faults (paw falling through the rungs) per forelimb or hindlimb. The data presented is the number of faults normalized to the total number of steps taken (by forelimb or hindlimb). Statistical comparisons were made by Student's *t*-test for each time point between the following pairs: $Dst^{dt\text{-}27J}$ and $Dst^{dt\text{-}Tg4}$, $Dst^{dt\text{-}27J}$ and their WT littermates and $Dst^{dt\text{-}Tg4}$ and their WT littermates.

Statistical analysis

Prism 5.0 GraphPad software was used for all statistical analysis, with the exception of quantitative RT-PCR data. For this we used either CFX software (Bio-Rad) for two-way comparisons, and qbase+3.0 software (Biogazelle) for multiple comparison tests. All two-way comparisons were done by two-tailed Student's *t*-test. Multiple comparison tests were done by one-way Analysis of variance (ANOVA), followed by Tukey's *post hoc* test. $P$-value $< 0.05$ was considered statistically significant (shown as $*$), while $P$-value $< 0.01$ is considered highly statistically significant (shown as $**$ ).

**Acknowledgements**

We are grateful to the Kothary laboratory for helpful discussions and to Dr. Robin Parks' laboratory for generously donating AdV-mCherry for use in our optimization experiments. We thank Samantha F Kornfeld for critical reading of the manuscript. A.L.G. is supported by an Ontario Graduate Scholarship.

**Supplementary Material**

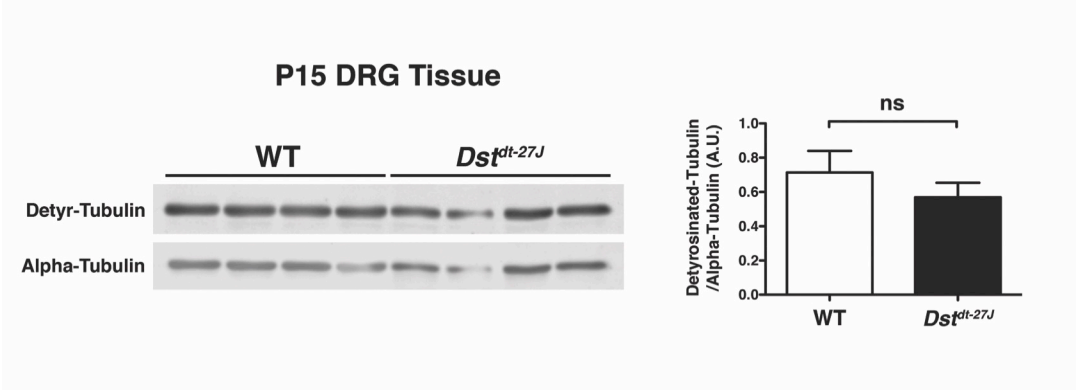


**Figure S3.1.** Tubulin detyrosination is unaltered in P15 *Dst*$^{dt\text{-}27J}$ DRGs. Fluorescence immunoblot analysis of wild type and *Dst*$^{dt\text{-}27J}$ DRG tissue (n = 4). Quantification of detyrosinated-tubulin:alpha-tubulin ratio is shown on the right. All lanes represent DRG lysates from a single mouse, 10 μg of protein per lane. Graphical data represented as mean ± SEM, all comparison was non-significant as assessed by two-tailed Student's t-test ($P > 0.05$).

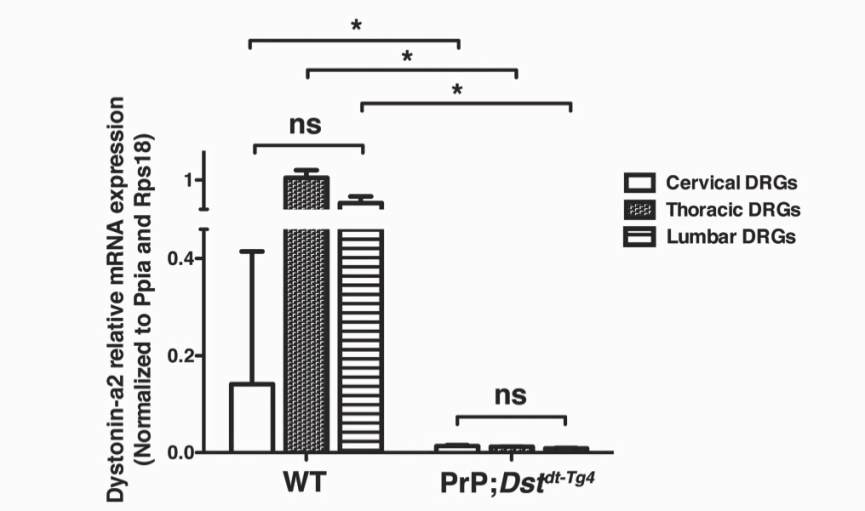


**Figure S3.2.** *Dst-A2* is uniformly expressed at very low levels in *PrP*;*Dst*$^{dt\text{-}Tg4}$ DRGs at all spinal levels. RT-qPCR analysis of *Dst-A2* in P15 wild type and *PrP*;*Dst*$^{dt\text{-}Tg4}$ DRGs (n = 3). Targets normalized to *Ppia and Rps18*. No significant differences observed within genotypes ($P > 0.05$). Graphical data represented as mean ± SEM, statistical analysis by one-way ANOVA with Tukey's post hoc test.

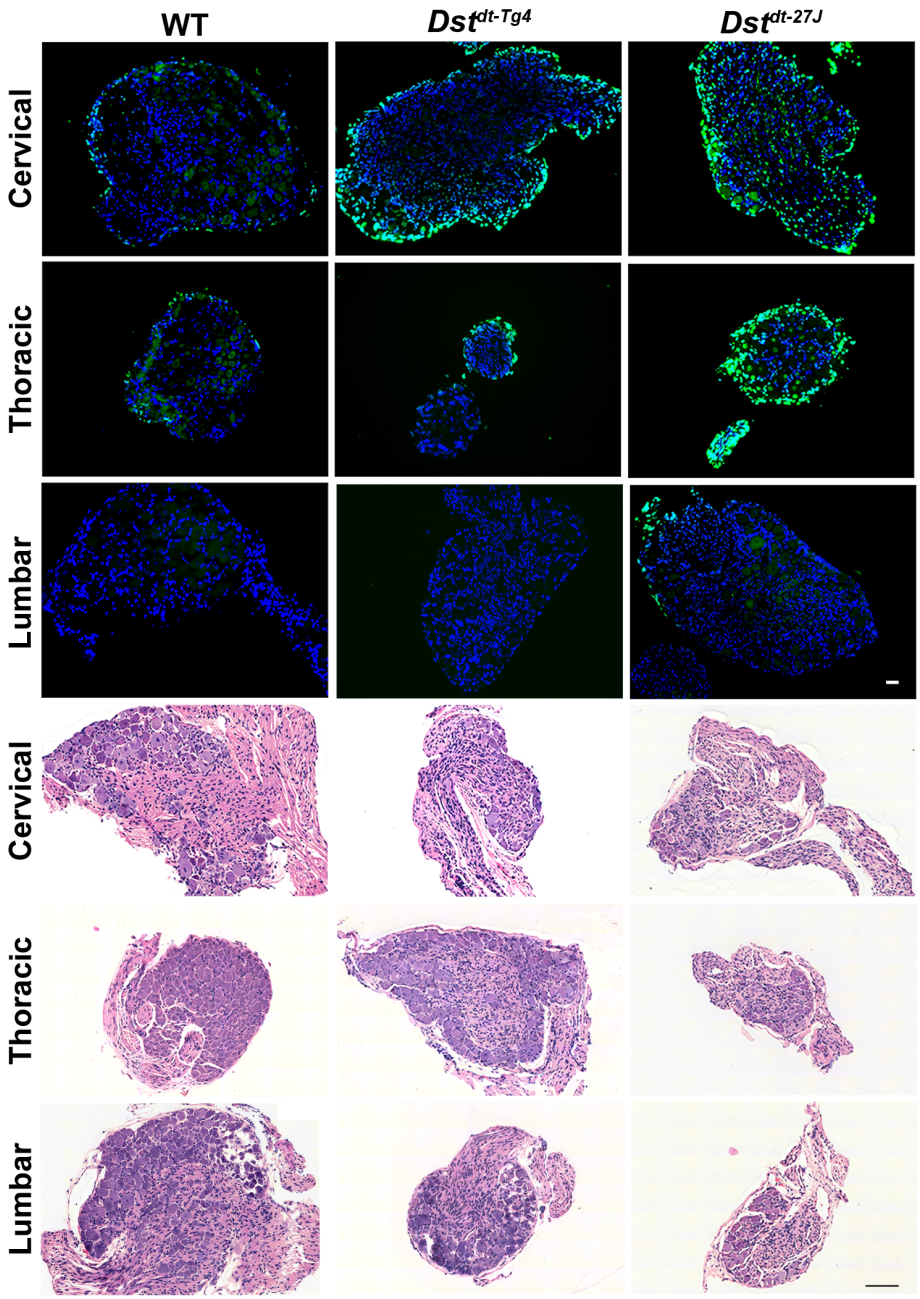


**Figure S3.3.** Viability of phenotype stage DRG neurons in *Dst*$^{dt\text{-}27J}$ and *Dst*$^{dt\text{-}Tg4}$ mice is similar. Top: Representative TUNEL labeling micrographs of P15 wild type, *Dst*$^{dt\text{-}Tg4}$, and *Dst*$^{dt\text{-}27J}$ cervical, thoracic, and lumbar levels DRGs (n = 3; scale bar = 10 μm). Bottom: Hematoxylin and eosin stained DRGs from P15 wild type, *Dst*$^{dt\text{-}Tg4}$, and *Dst*$^{dt\text{-}27J}$ cervical, thoracic, and lumbar levels DRGs (n = 1; scale bar = 100 μm).

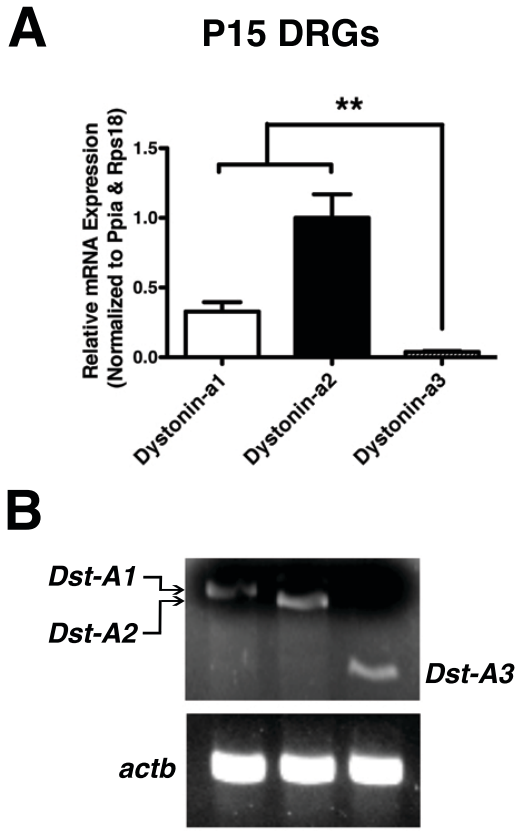


**Figure S3.4.** *Dst-A3* is normally expressed at very low levels in wild type DRGs. **(A)** RT-qPCR analysis of *Dst-A1*, *-A2*, and *-A3* in P15 wild type DRGs (n = 3, ** $P < 0.01$). Targets normalized to *Ppia* and *Rps18*. **(B)** RT-PCR products from *Dst-A1*, *-A2*, and *-A3* with *actb* loading controls from P15 wild type DRGs. Graphical data represented as mean ± SEM, statistical analysis by one-way ANOVA with Tukey's post hoc test.

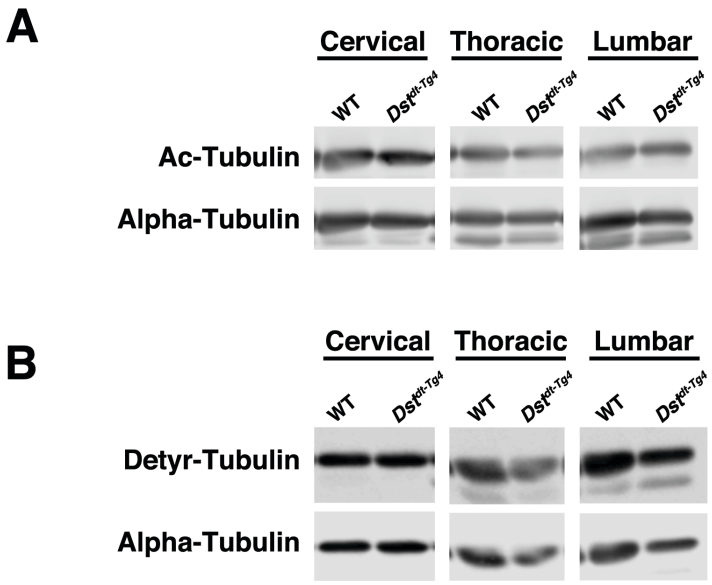


**Figure S3.5.** *Dst*$^{dt\text{-}Tg4}$ DRG microtubule stability is unaltered at all spinal levels. Fluorescence immunoblots analysis of Ac-tubulin **(A)** and detyrosinated-tubulin **(B)** in P15 wild type and *Dst*$^{dt\text{-}Tg4}$ cervical, thoracic, and lumbar level DRGs. Alpha-tubulin used as loading control (n = 1). All lanes of immunoblots represent DRG lysates from a single mouse, 10 μg of protein per lane.

# Chapter 4:

# Dystonin loss-of-function leads to impaired autophagy-endolysosomal pathway dynamics

# Dystonin loss-of-function leads to impaired autophagy-endolysosomal pathway dynamics

Anisha Lynch-Godrei[1,2], Yves De Repentigny[1], Sabrina Gagnon[1], and Rashmi Kothary[1,2,3,4,5,*]

[1] Regenerative Medicine Program, Ottawa Hospital Research Institute, Ottawa, Canada, K1H 8L6;

[2] Department of Cellular and Molecular Medicine, Faculty of Medicine, University of Ottawa, Ottawa, Canada, K1H 8M5;

[3] Department of Biochemistry, Microbiology, and Immunology, Faculty of Medicine, University of Ottawa, Ottawa, Canada, K1H 8M5;

[4] Department of Medicine, University of Ottawa, Ottawa, Canada, K1H 8M5;

[5] Centre for Neuromuscular Disease, University of Ottawa, Canada, K1H 8M5

* Correspondence to: Rashmi Kothary, Ottawa Hospital Research Institute, 501 Smyth Road, ORCC 4406a, Ottawa, Ontario, K1H 8L6; Tel: (613) 737-8707; Fax: (613) 737-8803; Email: rkothary@ohri.ca

***Manuscript submitted to Frontiers in Cellular Neuroscience.***

**Author Contributions**

ALG performed the research (figures 4.1, 4.2, 4.3, 4.4B and supplementary figure 4.1) assisted by YDR (figures 4.4) and SG. ALG designed the research study, analyzed the data, and wrote the paper with assistance and supervision from RK.

**Abstract**

The neuronal dystonin protein (DST-a, also known as Bullous pemphigoid antigen 1; BPAG1a) is a large cytoskeletal linker with numerous roles in integrating the various components of the cytoskeleton, and in mediating intracellular transport. Recessive *Dst* mutations lead to a sensory neuropathy in mice known as *dystonia musculorum* ($Dst^{dt}$). The disease is characterized by ataxia, autonomic disturbances, and ultimately death, which are associated with massive dorsal root ganglion (DRG) sensory neuron degeneration. Recent investigation of the autophagic process within $Dst^{dt}$ sensory neurons revealed an accumulation in autophagosomes and a disruption in autophagic flux. Though initially believed to be a result of insufficient motor protein availability, here we show that molecular motors are actually present in appropriate quantities. Trafficking defects may instead be attributed to defects in motor protein recruitment to vesicles.

We also identify increased levels of lysosomal marker LAMP1 in medium-large size $Dst^{dt\text{-}27J}$ sensory neurons, along with an accumulation of empty single-membraned vesicles in $Dst^{dt\text{-}27J}$ DRG tissue at late stages of disease (post natal day 15). We believe that these structures are likely to be autolysosomes, and that their presence in only late stage $Dst^{dt\text{-}27J}$ sensory neurons is suggestive of a pathological defect in autophagy. Further investigation is necessary to confirm vesicle identity, and to determine the possible role Dst-a in normal autophagic flux.

## Introduction

The dystonin protein (DST, also known as Bullous pemphigoid antigen 1 - BPAG1) is a large cytoskeletal-linker protein with differential expression in skin, muscle, and neurons (Leung et al., 2001). Alternative splicing of the neuronal isoform (DST-a) further yields three different neuronal isoforms (DST-a1, -a2, and -a3), which all have unique roles in integrating the various components of the cytoskeleton (Suozzi et al., 2012; Ferrier et al., 2013). Dystonin loss-of-function mutations in both humans and mice lead to severe peripheral neuropathies known as hereditary sensory and autonomic neuropathy type VI (HSAN-VI) and *dystonia musculorum* (*Dst*$^{dt}$), respectively. HSAN-VI presents on a spectrum that is dependent on the number of isoforms affected, with the most severe cases lacking expression of all *DST-a* isoforms and being lethal in infancy (Edvardson et al., 2012), while milder cases have been characterized in adults who have only one or two *Dst-a* isoforms affected (Cappuccio et al., 2017; Manganelli et al., 2017; Fortugno et al., 2018). It should be noted that impaired expression of *DST-a2* appears to be universal in all cases of HSAN-VI, and is likely both necessary and sufficient to cause disease. Commonalities amongst HSAN-VI patients include insensitivity to pain, joint abnormalities, heat intolerance, and autonomic disturbances. Similarly, the *Dst*$^{dt}$ murine disease arises due to homozygous recessive *Dst* mutations. Initially, newborn pups appear indistinguishable from their wild type (WT) littermates, although by postnatal day 10 (P10) *Dst*$^{dt}$ mice begin to show signs of ataxia and quickly develop severe dystonic postures, soon accompanied by death at about 3 weeks of age (Duchen et al., 1963, 1964; Duchen, 1976; Kothary et al., 1988; Guo et al., 1995; Horie et al., 2014; Lynch-Godrei et al., 2018). Unsurprisingly, as *DST-a* is most highly expressed in dorsal root ganglion (DRG) sensory neurons, these cell types are most vulnerable to dystonin loss-of-function, resulting in rapid sensory neuron degeneration.

A large breadth of evidence is in support of neuronal dystonin having major roles in mediating intracellular transport. One of the hallmark pathologies of *Dst*$^{dt}$ is the presence of axonal swellings within the peripheral and central nervous system, pointing to a defect in axonal trafficking (Duchen et al., 1964; Janota, 1972; Bernier et al., 1995). Transport within *Dst*$^{dt-27J}$ sciatic nerves and in *Bpag1* null primary sensory neurons have also been found to be significantly impaired, especially in the retrograde direction (De Repentigny et al., 2003; Liu et al., 2003). Later work also described reduced endoplasmic reticulum to Golgi vesicular trafficking upon *Dst-a2* knockdown in HEK 293T cells (Ryan et al., 2012b). Though it is clear that dystonin is involved in neuronal intracellular transport, the precise mechanisms by which it does so have yet to be elucidated. With the recent characterization of up-regulated macroautophagy (herein referred to as autophagy) in *Dst*$^{dt}$ sensory neurons, it was proposed that microtubule instability and insufficient motor protein availability were underlying causes of this autophagic dysregulation (Ferrier et al., 2015). However, as we now know that microtubule instability is not common to all *Dst*$^{dt}$ alleles, and thus not central to disease pathogenesis (Lynch-Godrei et al., 2018), this still leaves motor protein scarcity open to investigation. Considering previous mRNA microarray data finding molecular motors to be significantly down-regulated in pre-phenotype (P4) *Dst*$^{dt-27J}$ DRGs (Ryan et al., 2012b), and that autophagosomes rely on fusion with endosomes primed with motor proteins to acquire motility (Cheng et al., 2015a, b), we aim to validate motor protein expression profiles in *Dst*$^{dt}$ DRGs, and assess the dynamics of the endolysosomal pathway. Interestingly, although mRNA levels of all molecular motors assessed were significantly decreased in P5 and P15 *Dst*$^{dt-27J}$ DRGs, this difference did not translate to the protein level. Evaluation of the endolysosomal pathway also reveals increased levels of the lysosomal protein LAMP1 in P5 and P15 *Dst*$^{dt-27J}$ DRGs. Although we were unable to confirm

higher numbers of bona fide lysosomes by electron microscopy, we did observe an accumulation of single-membraned 'empty' vesicles in P15 $Dst^{dt\text{-}27J}$ sensory neurons. Given the previously characterized increase in autophagic vesicles in $Dst^{dt}$ sensory neurons, we believe these structures are likely to be autolysosomes (Ferrier et al., 2015; Arakawa et al., 2017). The lack of any of these structures at the P5 stage might also suggest that these are not simply a result of autophagy-associated cell death or coordinated apoptosis and autophagy (Denton and Kumar, 2019), but rather a result of pathologic disruption in autophagy.

## Methods

*Ethics statement:*

All experimental protocols on mice were approved by the Animal Care Committee of the University of Ottawa. Care and use of experimental mice followed the guidelines of the Canadian Council on Animal Care, and the Animals for Research Act.

*Animals:*

The *Dst*$^{dt\text{-}27J}$ line arose due to spontaneous mutation at the *Dst* locus, and are on a C57BL/6 genetic background. The *Dst*$^{dt\text{-}Tg4}$ mouse line arose from a transgene insertion-deletion that affected the expression of *Dst-a1* and *Dst-a2* isoforms (Kothary et al., 1988; Brown et al., 1995b; Pool et al., 2005). Genotypes for both lines of mice were determined by PCR amplification of genomic tail DNA, as described in (Lynch-Godrei and Kothary, 2016).

The *PrP-Dst-A2/PrP-Dst-A2;Dst*$^{dt\text{-}Tg4}$ rescue mouse (referred to as *PrP*;*Dst*$^{dt\text{-}Tg4}$ mice in the text) is a transgenic preparation expressing *Dst-a2* under the control of the neuronal prion protein promoter (PrP), on the *Dst*$^{dt\text{-}Tg4}$ background. Derivation and characterization of these mice has been previously described in (Ferrier et al., 2014; Lynch-Godrei and Kothary, 2016).

*Quantitative RT-PCR (qRT-PCR):*

RNA was isolated from P5 and P15 dorsal root ganglia (DRG) using the RNeasy® Mini Kit (Qiagen), as per the manufacturer's protocol. Samples were reverse-transcribed with RT$^2$ First Strand cDNA synthesis kit (Qiagen) using 1 µg total RNA. Bio-Rad PrimePCR™ pre-optimized primers were used to determine transcript levels of *Dctn1*, *Dync1i1*, *Klc1*, *Klc2*, *Kif5c, Atp6v1*, *Ctsb*, *Hexa*, *Lyz2*, *Psap*, and *Lamp1* by ΔΔCt method (normalized to *Rps18* and *Ppia*).

Reaction mixtures for all targets is: 10 µl SsoFast™ EvaGreen® Supermix (Bio-Rad), 5 µl of 1:5 diluted cDNA, 1 µl of 10 µM forward + reverse primer mix, and 4 µl RNase-free water. Cycling parameters are the same for each target: (1) denature at 95°C for 10 min, (2) denature at 95°C for 10 s, (3) anneal at 60°C for 30 s, and (4) repeat steps 2–3 for 40 cycles. Runs were amplified using a Bio-Rad CFX96. Each genotype was run as four biological replicates, and all samples were run in technical triplicate, with only those within a range of 0.2 Cq used for analysis.

*Immunoblotting:*

Protein was extracted from P5 and P15 DRG tissue by gently homogenizing the samples with 1X RIPA buffer (Sigma-Aldrich) supplemented with 6 µl/ml phenyl methyl sulfonyl fluoride (Sigma-Aldrich). Samples were left on ice for 10 min, before centrifugation at 4°C for 10 min at 12,000 g. Supernatant was then collected, and concentrations were determined by bicinchoninic acid assay (BCA assay; Pierce). Protein samples were separated by SDS-PAGE in 8-10% gels (10 µg per lane, except where indicated otherwise). PVDF membranes were incubated overnight at 4°C in a dilution of Odyssey® blocking buffer (LI-COR) and primary antibody. The following primary antibodies were used: mouse monoclonal anti-DIC1 (1:5000; Abcam ab23905), goat polyclonal anti-P150$^{Glued}$/DCTN1 (1:1000; Novus Biologicals NB100-1110), rabbit polyclonal anti-KLC1 (1:400; Santa Cruz Biotechnology sc-25735), rabbit polyclonal anti-KLC2 (1:400; Abcam ab103064), rabbit monoclonal anti-KIF5C (1:5000, Abcam ab193352), rabbit polyclonal anti-Rab5 (1:1000; Abcam ab18211), mouse monoclonal anti-Rab7 (1:4400; Abcam ab50533), rabbit polyclonal anti-LAMP1 (1:500; Abcam ab24170), mouse monoclonal anti-alpha tubulin (1:50,000; Calbiochem CP06), and rabbit polyclonal anti-alpha tubulin (1:20,000; Abcam ab18251). Membranes were washed 3 times with 1X tris-

buffered saline (TBS), and incubated for 1 h at room temperature in an Odyssey® blocking buffer (LI-COR) and secondary antibody solution. Infrared dye conjugated (IRDye®) secondary antibodies used include: goat anti-rabbit 800CW (IgG, 1:10,000; LI-COR; 926–32211), goat anti-rabbit 680RD (IgG, 1:10,000; LI-COR; 926–68071), goat anti-mouse 800CW (IgG, 1:10,000; LI-COR; 926–32210), goat anti-mouse 680RD (IgG, 1:10,000; LI-COR; 926–68070), donkey anti-goat 680RD (IgG; 1:10,000, LI-COR; 926-68074) and donkey anti-rabbit 800CW (IgG; 1:10,000; LI-COR; 926-32213). Bands were visualized and quantified using the Odyssey® CLx infrared imaging system (LI-COR Biosciences).

*Immunocytochemistry*:

P5 primary sensory neuron cultures were established as described in (Lynch-Godrei and Kothary, 2016). Cells were fixed on coverslips in 3% PFA for 10 min, and subsequently washed three times with 1X PBS for 5 min. Cells were then permeabilized with 0.1% triton-X (Sigma-Aldrich) in 1X PBS for 10 min, washed three times with 1X PBS, and blocked for 1 h with 10% goat serum in 1X PBS. Primary antibody dilutions of anti-LAMP1 antibody (1:1000; Abcam ab24170) and anti-neurofilament heavy chain (NF-200; 1:1000; Novus Biologicals NBP1-05210) were made in 10% goat serum and left on coverslips overnight at 4°C. Coverslips were washed three times in 1X PBS for 5 min, and incubated with secondary antibody solution for 1 h at room temperature. The secondary antibody dilution consisted of Alexa Fluor 488 goat anti-mouse (1:200, Invitrogen A11001) and Alexa Fluor 647 goat anti-rabbit (1:200, Invitrogen A21244). Coverslips were then counterstained with hoechst (1:5000) and mounted in Dako fluorescence mounting medium (Dako S3023). Micrographs were obtained using a Zeiss LSM 510 confocal microscope equipped with Zen 2009 imaging software (Zeiss). An n = 3 was

analyzed for WT and *Dst*$^{dt\text{-}27J}$ sensory neurons, with 20 neurons per n quantified using Fiji image processing software.

*Transmission electron microscopy:*

Mice were anaesthetized by intraperitoneal injection of tribromomethanol (Avertin) and transcardially perfused with 5 mL of 1X PBS followed by 10 mL of Karnovsky's fixative (4% paraformaldehyde, 2% glutaraldehyde [Sigma-Aldrich] and 0.1 M sodium cacodylate buffer [Electron Microscopy Sciences] in 1X PBS). DRGs were then extracted and separated according to spinal level (cervical, thoracic, and lumbar), and fixed overnight at 4°C in the same fixative. Following fixation, each root was cut into a straight 1 mm segment. Segments were subsequently washed in 0.1 M sodium cacodylate buffer (Electron Microscopy Sciences) for 1 h at room temperature, and again overnight at room temperature. Segments were post-fixed with 1% osmium tetroxide (Electron Microscopy Sciences) in 0.1 M sodium cacodylate buffer for 1 h at room temperature. Samples were then washed 3 times in 0.2 M sodium cacodylate buffer, pH 7.4, for 15 min each. A second fixation step was performed in 2% glutaraldehyde and 0.2 M sodium cacodylate buffer for 1.5 h at room temperature. The samples were washed 3 times in distilled water for 10 min, and then dehydrated twice for 20 min for each step in a graded series of ethanol (Commercial Alcohols) from 30%-50%-70%-85%-95% ethanol in water. This was followed by two 30 min washes in 100% ethanol, two 15 min washes in 50% ethanol/50% acetone, and two 15 min washes in 100% acetone (Fisher Scientific). DRGs were infiltrated in 30% spurr resin/acetone for 20 min, and once overnight, then in 50% spurr resin/acetone for 6 h, and finally in 100% spurr resin (Electron Microscopy Sciences) overnight. Segments remained in 100% spurr resin, which was changed twice a day for three days at room temperature. All infiltration steps were performed on a rotator at low speed. Segments were embedded in fresh

liquid spurr resin and then polymerized overnight at 70$^{o}$C. Ultrathin sections (80 nm) were then collected onto 200-mesh copper grids and stained with 2% aqueous uranyl acetate (Electron Microscopy Sciences) and Reynold's lead citrate (sodium citrate [Electron Microscopy Sciences] and lead nitrate [Electron Microscopy Sciences]). Sections were observed under a transmission electron microscope (Hitachi 7100) at 40,000X, 70,000X, and 100,000X magnifications. An n = 2 was used for all P15 DRG samples, while an n = 1 was used for P5 DRG samples. Approximately 10 neurons were evaluated at the cervical, thoracic, and lumbar levels for each n.

*Statistical analysis:*

Prism 5.0 GraphPad software was used for all statistical analysis, with the exception of qRT-PCR data. For this we used CFX software (Bio-Rad) for two-way comparisons. All two-way comparisons were done by two-tailed Student's *t*-test. Multiple comparison tests were done by one-way ANOVA, followed by Tukey's *post hoc* test. $P < 0.05$ was considered statistically significant (shown as *), while $P < 0.01$, $P < 0.001$, and $P < 0.0001$ are considered highly statistically significant (shown as **, ***, and **** respectively).

**Results**

Decrease in transcript levels of molecular motors in *Dst*$^{dt-27J}$ DRGs with no change in protein levels

As previous mRNA microarray data had found transport to be the most significantly down-regulated biological process within DRGs from P4 *Dst*$^{dt-27J}$ mice (which lack all *Dst-a* isoforms) (Ryan et al., 2012b), we validated some of these targets by qRT-PCR. Retrograde motors such as dynein intermediate chain 1 (*Dync1i1*) and P150$^{Glued}$/Dynactin 1 (*Dctn1*), along with anterograde motors such as kinesin light chain 1 (*Klc1*), kinesin light chain 2 (*Klc2*), and kinesin heavy chain 5c (*Kif5c*) were selected due to their major involvement in the autophagosome-endolysosomal pathway (Maday et al., 2012). In pre-phenotype (P5) *Dst*$^{dt-27J}$ DRGs, we observed a significant decrease in transcript levels for all molecular motors (Figure 4.1A), which further declined by the phenotype stage (P15; Figure 4.1B). Transcript levels were also evaluated in the *Dst*$^{dt-Tg4}$ allele (lacking only *Dst-a1* and *-a2*), as well as in the *PrP-Dst-a2/PrP-Dst-a2*;*Dst*$^{dt-Tg4}$ rescue mouse model, which are *Dst*$^{dt-Tg4}$ mice exogenously expressing *Dst-a2* under the neuronal prion protein promoter (henceforth referred to as *PrP;Dst*$^{dt-Tg4}$) (Ferrier et al., 2014). In this case we only observed significant decreases in *Dync1i1*, *Dctn1*, and *Klc2* at the phenotype stage (P15) for both *Dst*$^{dt-Tg4}$ and *PrP;Dst*$^{dt-Tg4}$, which can likely be attributed to a failure of the normal up-regulation that occurs from P5 to P15 (Figure S4.1).

Although we had noted a decrease in the transcript levels, analysis of molecular motors at the protein level did not show significant changes between *Dst*$^{dt-27J}$ and wild type DRGs at either the P5 or P15 stage (Figure 4.2A-I).

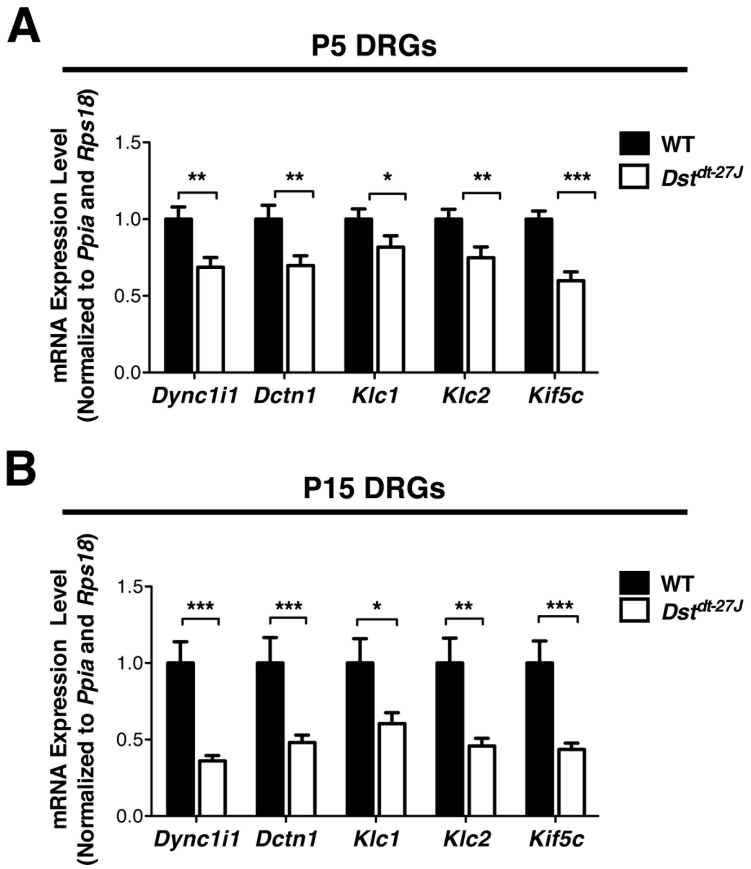


**Figure 4.1 Transcript levels of retrograde and anterograde motor proteins are significantly reduced in pre-phenotype (P5) and phenotype (P15) *Dst*$^{dt\text{-}27J}$ DRGs.** Evaluation of retrograde motors *Dctn1* (P150$^{Glued}$), and *Dync1i1* (dynein intermediate chain 1), and anterograde motors *Klc1* (kinesin light chain 1), *Klc2* (kinesin light chain 2), and *Kif5c* (kinesin heavy chain 5c) in P5 **(A)** and P15 **(B)** WT and *Dst*$^{dt\text{-}27J}$ DRGs. A significant decrease in the transcripts of all targets is observed in *Dst*$^{dt\text{-}27J}$ DRGs at both time points (n = 4; * $P < 0.05$, ** $P < 0.01$, *** $P < 0.001$).

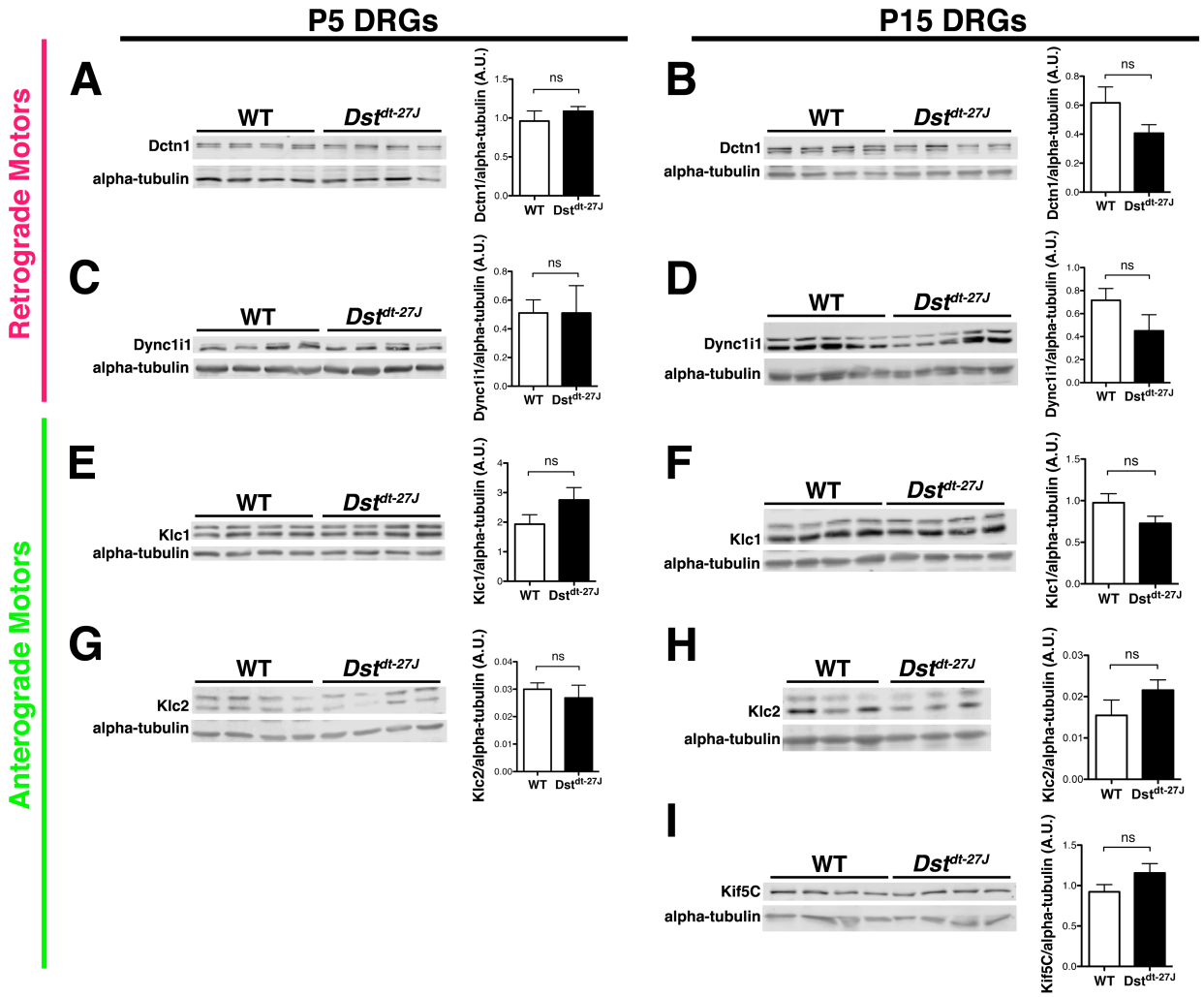


**Figure 4.2 *Dst*$^{dt\text{-}27J}$ DRG motor protein levels are similar to wild type at both pre-phenotype (P5) and phenotype (P15) stages.** Fluorescence immunoblot analysis of WT and *Dst*$^{dt\text{-}27J}$ DRGs at P5 and P15. No significant differences in levels of retrograde motor dynactin 1/P150$^{Glued}$ (Dctn1), or dynein cytoplasmic 1 intermediate chain 1 (Dync1i1) are observed between WT and *Dst*$^{dt\text{-}27J}$ at either stage **(A-D)**. Analysis of anterograde motors kinesin light chain 1 (Klc1), and kinesin light chain 2 (Klc2) show similar levels between WT and *Dst*$^{dt\text{-}27J}$ DRGs at both P5 and P15 stages **(E-H)**, and no detectable differences are observed for kinesin heavy chain 5c (Kif5c) at the P15 stage **(I)**. Each lane represents DRG protein from a single n, statistical analysis by Student's *t*-test, ns $P > 0.05$.

Increased levels of lysosomal marker LAMP1 in *Dst*$^{dt\text{-}27J}$ sensory neurons

Previous work from our laboratory showed that autophagosomes accumulate in *Dst*$^{dt\text{-}Tg4}$ and *Dst*$^{dt\text{-}27J}$ sensory neurons (Ferrier et al., 2015). Though initially thought to be linked to decreased motor protein levels, it is now apparent that the major molecular motors involved in vesicle transport are present in adequate amounts. Considering axonal autophagosomes gain their motor proteins via endosomal fusion (Cheng et al., 2015a), forming a structure known as an amphisome, it is possible that there are fewer endosomes present to bestow motor activity to autophagosomes, or perhaps not enough endosomes maturing into lysosomes for autophagosomes to fuse with and digest their contents. Therefore, we aimed to investigate whether vesicles of the endolysosomal pathway are impacted by *Dst* loss-of-function. Immunoblot evaluation of early endosome and late endosome markers, Rab5 and Rab7 respectively, showed no difference in levels between wild type and *Dst*$^{dt\text{-}27J}$ P15 DRGs (Figure 4.3A, B). However, evaluation of the terminal lysosomal stage revealed significant increases in the LAMP1 lysosomal protein in both P5 and P15 *Dst*$^{dt\text{-}27J}$ DRGs (Figure 4.3C, D). Immunofluorescence analysis of P5 primary sensory neurons grown in culture for 5 d also confirmed increased levels of the LAMP1 protein in *Dst*$^{dt\text{-}27J}$ sensory neurons when normalized to DRG area (Figure 4.3E, F). An upward shift in LAMP1 intensity per cell area was identified in *Dst*$^{dt\text{-}27J}$ sensory neurons (Figure 4.3G), which lead us to evaluate LAMP1 signal based on sensory neuron size. Interestingly, we observed smaller sensory neurons do not show any difference in LAMP1 intensity (Figure 4.3I and K), but rather only medium-large size *Dst*$^{dt\text{-}27J}$ sensory neurons showed significantly higher LAMP1 levels compared to wild type (Figure 4.3H and J).

An increase in LAMP1 could stem from a number of sources including increased lysosomal biogenesis, impaired degradative capacity, or even a block in the pathway such as cargo acquisition or disassembly. Heightened lysosomal biogenesis was determined not to be responsible for the increase in LAMP1, as our evaluation of certain coordinated lysosome expression and regulation (CLEAR) genes did not show increase in expression of *Atp6v1*, *Ctsb*, *Hexa*, *Lyz2*, *Psap*, or *Lamp1* in P5 of P15 $Dst^{dt\text{-}27J}$ DRGs (Figure 4.3L, M). We did however observe a consistent down-regulation in *Atp6v1* across time points, along with reduced expression of *Hexa* and *Psap* by P15 in $Dst^{dt\text{-}27J}$ DRGs.

We next sought to determine how this increased LAMP1 signal in $Dst^{dt\text{-}27J}$ sensory neurons was linked to lysosome status, and we asked whether lysosomes are present in higher numbers or whether they are larger in size. To address this, we performed transmission electron microscopy (TEM) on whole DRG tissues from P15 wild type and $Dst^{dt\text{-}27J}$ mice to characterize quantity and morphology of lysosomes. Surprisingly, we did not observe any difference between genotypes in the number of dark, electron-dense vesicles that would traditionally be characterized as lysosomes (Figure 4.4A). Instead, we observed an abundance of large, single-membraned, empty vesicles scattered throughout the cytoplasm of P15 $Dst^{dt\text{-}27J}$ DRGs. Quantification indicated that these structures are present at significantly higher numbers in P15 $Dst^{dt\text{-}27J}$ DRGs at all spinal levels (cervical, thoracic, and lumbar; Figure 4.4B). TEM analysis of P5 DRGs however did not show any signs of these empty vesicles in $Dst^{dt\text{-}27J}$ DRGs, and few differences could be seen between wild type and $Dst^{dt\text{-}27J}$ at this stage (Figure 4.4C).

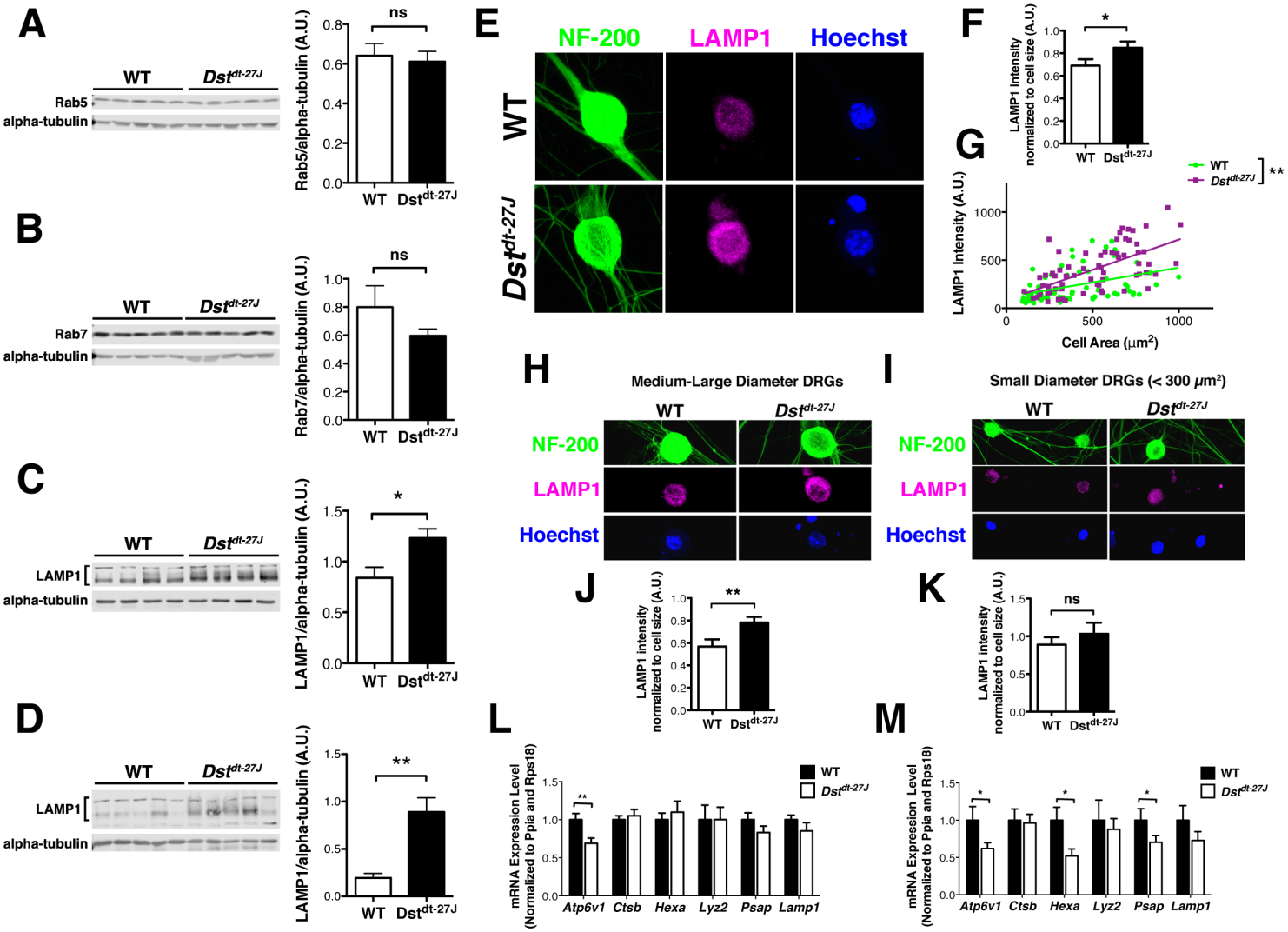


**Figure 4.3 Lysosomal protein LAMP1 is elevated in medium-large diameter *Dst*$^{dt\text{-}27J}$ DRGs.** Fluorescence immunoblot analysis of P15 DRGs reveals no detectable difference in levels of early or late endosome markers, Rab5 **(A)** and Rab7 **(B)**, respectively. Lysosome marker LAMP1 however is present at higher levels in P5 **(C)** and P15 **(D)** *Dst*$^{dt\text{-}27J}$ DRGs. Immunofluorescence staining of P5 sensory neurons cultured for 5 d further confirms increase LAMP1 signal intensity from *Dst*$^{dt\text{-}27J}$ sensory neurons **(E, F)**. Linear regression analysis also shows an upward shift in LAMP1 signal intensity per increased cell area in *Dst*$^{dt\text{-}27J}$ sensory neurons **(G)**, leading to separate analysis of small (> 300 μm$^2$) and medium-large area neurons. Significantly higher LAMP1 signal intensity was found to be restricted to medium-large area *Dst*$^{dt\text{-}27J}$ neurons **(H and**

**J)**, as no differences in LAMP1 intensity were seen in small area neurons **(I and K)**. qRT-PCR analysis of coordinated lysosome expression and regulation (CLEAR) genes *Atp6v1*, *Ctsb*, *Hexa*, *Lyz2*, *Psap*, *Lamp1* at P5 **(L)** and P15 **(M)** in WT and $Dst^{dt\text{-}27J}$ DRGs show no increased expression within $Dst^{dt\text{-}27J}$, suggesting lysosomal biogenesis is not increased. Instead, *Atp6v1* was found to be consistently down-regulated at P5 and P15 stages, while *Hexa* and *Psap* were down-regulated by P15 stage in $Dst^{dt\text{-}27J}$ DRGs (n = 4, statistical analyses by Student's *t*-test, ns $P > 0.05$, * $P < 0.05$, ** $P < 0.01$).

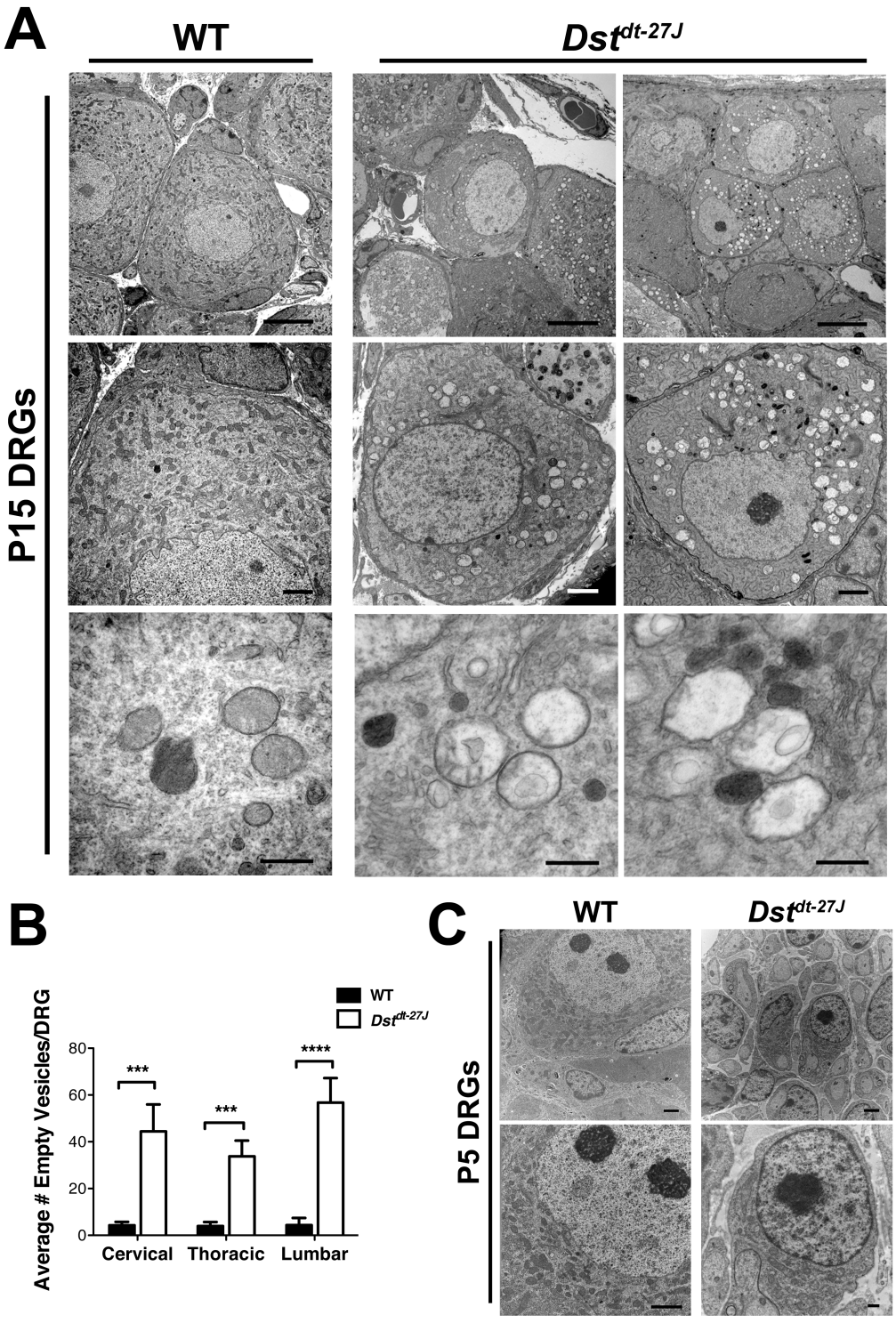


**Figure 4.4 A significant abundance of empty single-membrane vesicles is observed in phenotype stage (P15) *Dst*$^{dt\text{-}27J}$ DRGs, but is absent in pre-phenotype stage DRGs (P5). (A)** Electron micrographs of P15 *Dst*$^{dt\text{-}27J}$ DRG tissue reveal an accumulation of empty single-

membraned vesicles scattered throughout the cytoplasm of sensory neurons. Age matched wild type DRGs appear normal, with an absence of empty vesicles (top panel scale bar = 10 μm, middle panel scale bar = 2 μm, bottom panel scale bar = 500 nm). **(B)** Quantification of the empty vesicles from DRGs at cervical, thoracic, and lumbar levels shows a significantly higher number in $Dst^{dt\text{-}27J}$ as compared to wild type DRGs (n = 3; statistical analysis by Student's *t*-test, *** $P < 0.001$, **** $P < 0.0001$). **(C)** Electron micrographs from pre-phenotype (P5) stage mice show a lack of empty single-membraned vesicles in $Dst^{dt\text{-}27J}$ DRGs (n = 1; top panel scale bar = 2 μm, bottom panel WT scale bar = 2 μm, bottom panel $Dst^{dt\text{-}27J}$ scale bar = 500 nm).

## Discussion

The levels of motor proteins are unaltered in *Dst*$^{dt}$ DRGs

Although our analysis showed that transcript levels for molecular motors decreased, the motor proteins are present at appropriate levels as they are unchanged from wild type. This unusual pattern of reduced gene expression and steady protein levels could be associated with the long-lived nature of theses proteins (Brown et al., 2005), or might be linked to the reduced protein turnover in *Dst*$^{dt}$ sensory neurons (Ferrier et al., 2015). The vesicle trafficking defects observed in *Dst*$^{dt}$ sensory neurons are most likely a result of impaired motor protein recruitment to vesicles, which is compounded by microtubule instability in cases of complete Dst-a absence (i.e. *Dst*$^{dt\text{-}27J}$, and *Dst*$^{dt\text{-}tmEfu1}$ knockout mice) (Liu et al., 2003; Liu et al., 2007; Ryan et al., 2012b; Lynch-Godrei et al., 2018). Prior studies have characterized a reduction in Dync1i1 and Dctn1 within spinal cord and sciatic nerve endosomal fractions from *Dst* null mice (Liu et al., 2007), pointing to Dst-a involvement in retrograde motor recruitment to vesicles. The previous reports of normal mitochondrial transport in *Dst*$^{dt}$ sensory neurons (Pool et al., 2006; Liu et al., 2007) can also be explained by the differences between adaptor molecules involved in mitochondrial versus. vesicular transport, for which Dst-a is likely not integral. Our future work will be aimed at evaluating which motor proteins are impaired in their recruitment to endosomes, lysosomes, and autophagosomes within *Dst*$^{dt\text{-}27J}$ sensory neurons, as well as determining which Dst-a isoforms are critically responsible for vesicular motor protein recruitment.

The endolysosomal pathway is disrupted in *Dst*$^{dt\text{-}27J}$ sensory neurons

While endosomes appeared to be present in appropriate quantities within *Dst*$^{dt\text{-}27J}$ DRGs, we observed significantly higher levels of the lysosomal protein LAMP1 by immunoblot analysis

of P5 and P15 *Dst*$^{dt\text{-}27J}$ DRGs, and by immunofluorescence of P5 sensory neurons grown for 5 d. The highest LAMP1 signal was restricted to medium-large *Dst*$^{dt\text{-}27J}$ sensory neurons, which are the DRG cell types most vulnerable to *Dst* loss-of-function, and degenerate the quickest (Janota, 1972; al-Ali and al-Zuhair, 1989; Carlsten et al., 2001; Ferrier et al., 2014). This association could either be indicative of a pathological role involving accumulating lysosomes, or of a normal progression of cell death. Although evaluation of the CLEAR gene network indicates that lysosome biogenesis is not increased, it did reveal reduced transcript levels of *Atp6v1*, which encodes the cytosolic $V_1$ domain of the V-ATPase protein responsible for lowering the pH in lysosomes. Decreased levels of this protein could lead to defective acidification of lysosomes, and although this is not expected to impair autophagosome-lysosome fusion, it could impair degradation of luminal contents (Mauvezin and Neufeld, 2015). Previous work evaluating lysosomal hydrolase activity in *Dst*$^{dt}$ trigeminal nerve reported an increase in acid hydrolases at earlier stages, followed by a decline in later stages. It is possible this also occurs in *Dst*$^{dt}$ sensory neurons, though this has not yet been investigated. (Thornburg and Hanker, 1975) We have also seen from P5 *Dst*$^{dt\text{-}Tg4}$ sensory neurons in culture, autolysosome formation is not blocked, as many large autolysosomes containing undigested material are clearly visible (Ferrier et al., 2015). Though their rate of formation, clearance, and degradative capacity has yet to be investigated.

The striking accumulation of empty single-membraned vesicles by the P15 stage in *Dst*$^{dt\text{-}27J}$ mice is also under investigation, as we do not yet know the identity of these structures. Morphological studies, along with our current understanding of the state of autophagy within *Dst*$^{dt}$ sensory neurons would suggest that these structures are likely to be autolysosomes (Arakawa et al., 2017). Mature autolysosomes possess only a single outer membrane (as the

inner membrane is degraded upon fusion) (Parzych and Klionsky, 2014; Dikic and Elazar, 2018), are positive for both LAMP1 and LC3-II (Maday et al., 2012), and may appear empty in nature once their contents have been completely degraded, which is supported by our data from P15 $Dst^{dt\text{-}27J}$ DRGs. However, the perinuclear accumulation of these empty vesicles could be indicative of an issue in autolysosomal disassembly. In particular, the complete lack of these vesicles at the P5 stage, while widespread DRG cell death is occurring (Kothary et al., 1988), supports the hypothesis that their accumulation by P15 is related to a disruption in the autophagic process.

We have mounting evidence to suggest that autophagy is indeed disrupted, and not upregulated. The lack of upregulated CLEAR genes indicates that mTORC1 remains active in $Dst^{dt\text{-}27J}$ DRGs, and that the autolysosomal pathway is not upregulated (Menzies et al., 2017). This would instead point to autophagosome/autolysosome accumulation and reduced degradation. Our previous investigation of autophagosomal flux in $Dst^{dt\text{-}Tg4}$ sensory neurons also indicates a block in autophagosomal degradation (Mizushima and Yoshimori, 2007), though the precise location along with pathway had not been identified. Further examination of the autolysosomal pathway and determining the identity of the single-membraned empty vesicles seen in phenotype stage $Dst^{dt\text{-}27J}$ DRGs will help us to better understand the specific stage in the pathway impacted by Dst loss-of-function. This will in turn yield additional insights into the roles of Dst-a.

**Acknowledgements**

This project was funded by a grant from the Canadian Institutes of Health Research to RK (MOP-126085). ALG is supported by an Ontario Graduate Scholarship.

**Supplementary Material**

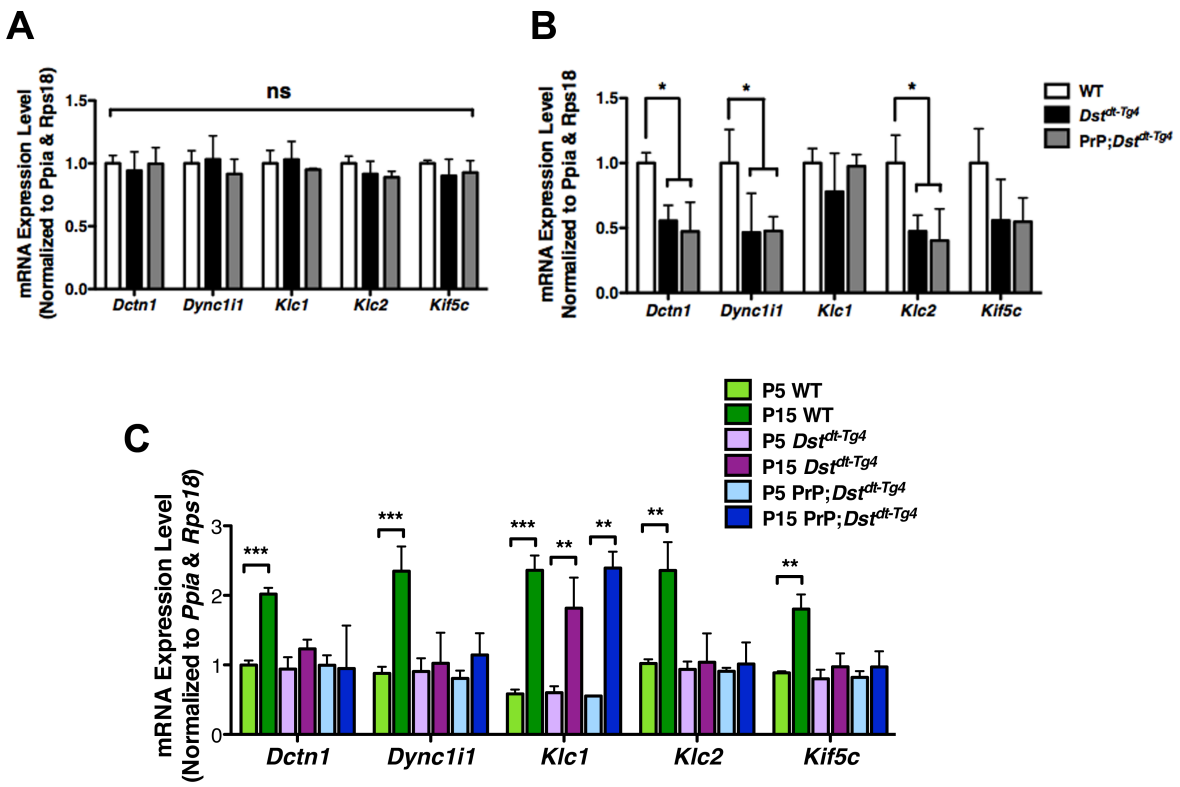


**Figure S4.1 Down-regulation of *Dctn1*, *Dync1i1*, and *Klc2* in DRGs from the *Dst*$^{dt\text{-}Tg4}$ mouse, and the PrP;*Dst*$^{dt\text{-}Tg4}$ rescue mouse are due to a failure to upregulate expression that occurs with development. (A)** qRT-PCR of P5 DRGs reveals no change in expression levels for any of the molecular motors analyzed. However, by P15 stage *Dst*$^{dt\text{-}Tg4}$ and Prp;*Dst*$^{dt\text{-}Tg4}$ DRGs show reduced levels of *Dctn1*, *Dync1i1*, and *Klc2* transcripts compared to wild type **(B)**. (n = 4, statistical analysis by Student's *t*-test). Age-wise comparison reveals that the observed down-regulation is caused by a failure to increase expression through development, as we can see that all targets show an increase in expression from P5 to P15 ages in WT DRGs **(C)**. (n = 4; statistical analysis by two-way ANOVA and Tukey *post-hoc* test, ns $P > 0.05$, * $P < 0.05$, ** $P < 0.01$, *** $P < 0.001$).

# Chapter 5:

# Characterization of gastrointestinal pathologies in the *dystonia musculorum* mouse model for hereditary sensory and autonomic neuropathy type VI

# Characterization of gastrointestinal pathologies in the *dystonia musculorum* mouse model for hereditary sensory and autonomic neuropathy type VI

Anisha Lynch-Godrei[1,2], Yves De Repentigny[1], Rebecca A. Yaworski[1], Sabrina Gagnon[1], James Butcher[3], Juliana Manoogian[3] Alain Stintzi[3], and Rashmi Kothary[1,2,3,4,5,*]

[1] Regenerative Medicine Program, Ottawa Hospital Research Institute, Ottawa, Canada, K1H 8L6;

[2] Department of Cellular and Molecular Medicine, Faculty of Medicine, University of Ottawa, Ottawa, Canada, K1H 8M5;

[3] Department of Biochemistry, Microbiology, and Immunology, Faculty of Medicine, University of Ottawa, Ottawa, Canada, K1H 8M5;

[4] Department of Medicine, University of Ottawa, Ottawa, Canada, K1H 8M5;

[5] Centre for Neuromuscular Disease, University of Ottawa, Canada, K1H 8M5

* Correspondence to: Rashmi Kothary, Ottawa Hospital Research Institute, 501 Smyth Road, ORCC 4406a, Ottawa, Ontario, K1H 8L6; Tel: (613) 737-8707; Fax: (613) 737-8803; Email: rkothary@ohri.ca

***Under revision by Neurogastroenterology and Motility.***

**Author Contributions:**

ALG performed the research (figures 5.1A-D, 5.2A-G, 5.3A-D, 5.4, 5.5A-G, 5.6A, 5.7A, and supplemental figures S5.1, S5.2), assisted by YDR (figures 5.1E, 5.3A-D, 5.7B-C), RAY (figure 5.5B) and SG. JB (figures 5.6B-E, and supplemental figure S5.3), JM, and AS performed the microbiome experiments and analysis. ALG designed the research study, analyzed the data, and wrote the paper with assistance and supervision from RK.

**Abstract**

Background: *Dystonia musculorum* (*Dst*$^{dt}$) is a murine disease caused by recessive mutations in the dystonin (*Dst*) gene. Loss of dorsal root ganglion (DRG) sensory neurons, ataxia and dystonic postures before death by postnatal day 18 (P18) are hallmark features. Recently we observed gas accumulation and discoloration in the small intestine and cecum in *Dst*$^{dt}$ mice by P15. The human disease resulting from dystonin loss of function, known as Hereditary Sensory and Autonomic Neuropathy type VI (HSAN-VI), has also been associated with gastrointestinal (GI) symptoms including chronic diarrhea and abdominal pain. As neuronal dystonin isoforms are expressed in the GI tract, we hypothesized that dystonin loss-of-function in *Dst*$^{dt\text{-}27J}$ enteric nervous system (ENS) neurons resulted in neurodegeneration associated with the GI abnormalities.

Methods: We characterized the nature of the GI abnormalities observed in *Dst*$^{dt}$ mice through histological analysis of the gut, assessing the ENS for signs of neurodegeneration, evaluation of GI motility and absorption, and by profiling the microbiome.

Key Results: Though gut histology, ENS viability, and GI absorption were normal, slowed GI motility, thinning of the colon mucous layer, and reduced microbial richness/evenness were apparent in *Dst*$^{dt\text{-}27J}$ mice by P15. Neurodegeneration of extrinsic ENS input was observed via analysis of the vagus nerve.

Conclusions & Inferences: *Dst*$^{dt\text{-}27J}$ GI defects are not linked to ENS neurodegeneration, but are likely a result of decreased autonomic control over the gut. Further characterization of HSAN-VI patient GI symptoms is necessary to determine potential treatments targeting symptom relief.

## Introduction

Hereditary sensory and autonomic neuropathy type VI (HSAN-VI) is a recessive genetic disease that results from mutations in the human dystonin gene (*DST*, also known as *BPAG1*; MIM# 113810). The disease was first classified in 2012 in three infants of the Ashkenazi Jewish population, who presented with severe joint contractures and numerous autonomic disturbances that ultimately lead to death before the age of two (Edvardson et al., 2012). Since then, at least 7 other cases have been identified in adult individuals presenting with milder symptoms including, joint abnormalities, skin ulcers, hypohydrosis/hyperhidrosis, sexual dysfunction, chronic diarrhea and abdominal pain (Cappuccio et al., 2017; Manganelli et al., 2017; Fortugno et al., 2018). The variability of symptoms and lifespan between patients can largely be attributed to differences in mutations, and the *DST* isoforms affected. The most severely affected infant patients possessed a homozygous frameshift mutation that disrupted the expression of all neuronal DST isoforms (Edvardson et al., 2012), while the adult HSAN-VI patients possess mutations that preserve expression of at least one DST isoform. Considering the potential for DST isoform compensation recently characterized in our laboratory, this may have significant biological effects on prolonging longevity (Lynch-Godrei et al., 2018).

The Dst protein is a large cytoskeletal-linker of the spectraplakin family of proteins (>600 kDa) (Roper et al., 2002; Jefferson et al., 2007; Atai et al., 2012; Suozzi et al., 2012). Differential expression of *Dst* gene produces neuronal (Dst-a), muscle (Dst-b), and epithelial (Dst-e) isoforms; whereby alternative splicing of the 5' exons in neuronal and muscle *Dst* yields 3 unique isoforms: Dst-a/b1, -a/b2, and -a/b3 (Leung et al., 2001; Ferrier et al., 2013). Just as with humans, a mouse disease known as *dystonia musculorum* ($Dst^{dt}$) results due to mutations in *Dst*. Initially, mutant mice are indistinguishable from their littermates until around postnatal day

10 when they begin to show signs of ataxia. This rapidly progresses to writhing and twisting of the trunk, and ultimately death by about postnatal day 17. Recently however, we discovered that mutant mice have noticeable differences in their gastrointestinal (GI) tracts, which are consistently present by postnatal day 15. This is characterized by a massive accumulation of gas causing severe distension of the small intestine and cecum, and is often accompanied by small intestine discoloration (dark brown-black color). As dystonin loss-of-function has its greatest impact on dorsal root ganglia (DRG) sensory neurons, causing numerous intracellular disruptions and rapid neurodegeneration (Bernier et al., 1995; Dalpé et al., 1998; Carlsten et al., 2001; Young and Kothary, 2008; Ryan et al., 2012b; Ryan et al., 2012c; Ferrier et al., 2015), we wondered whether the neurons of the enteric nervous system (ENS) were similarly vulnerable to cell death. This seemed a likely possibility given that 10-30% of the neurons in the ENS are intrinsic primary afferent neurons of sensory nature (Furness, 2012), and degeneration of these neurons could reasonably alter gastrointestinal homeostasis and cause the gastrointestinal tract (GIT) defects seen in *Dst*$^{dt}$ mice (Coulombe et al., 2014).

Here we set out to characterize *Dst*$^{dt}$ GIT pathologies, evaluate ENS viability, assess GIT function, and characterize the *Dst*$^{dt}$ gut microbiome to elucidate the underlying cause of the GIT abnormalities, which could help give insights into the GI symptoms experienced by HSAN-VI patients.

## Materials and Methods

*Animals:*

The *Dst*$^{dt\text{-}27J}$ mouse line arose by spontaneous mutation at the Jackson Laboratory. This mouse line is likely null for the *Dst-a* transcript, though if mRNA is present it may harbour a mutation (Pool et al., 2005). This mouse line is maintained in a stepped-down animal facility at the University of Ottawa. Genotyping was determined by PCR amplification of genomic tail DNA, as described previously (Lynch-Godrei and Kothary, 2016). All experimental protocols were approved by the University of Ottawa Animal Care Committee, and use of experimental mice followed the guidelines set by the Canadian Council on Animal Care, and the Animals for Research Act.

*RNA isolation & RT-PCR:*

RNA was isolated from RNA*later*™ (Invitrogen; USA) stored P15 GIT tissues, and P15 wild type nodose ganglion tissue using the RNeasy® Mini Kit (Qiagen; Netherlands), as per the manufacturer's protocol. Samples were reverse-transcribed with $RT^2$ First Strand cDNA synthesis kit (Qiagen; Netherlands) using 1 µg RNA. cDNA from GIT sections was further diluted to a 1 in 5 preparation using RNase-free water (Qiagen; Netherlands). Reaction mix and cycling parameters previously described (Lynch-Godrei and Kothary, 2016). Products were run in a 2% agarose gel containing RedSafe™ nucleic acid staining solution (Froggabio; Canada), and visualized under UV light.

*Histologic analysis:*

For hematoxylin and eosin (H&E) staining, whole GIT was extracted from P5 and P15 mice and fixed in formalin (Fisher Scientific; USA) at 4°C for 48 h. Samples were transferred to 70% ethanol and stored at 4°C until processing. For periodic acid Schiff (PAS) staining, samples were fixed in Carnoy's solution (Electron Microscopy Sciences; USA) for 3 h at 4°C, then transferred to 1X PBS and immediately processed. The University of Ottawa (Department of Pathology and Laboratory Medicine) embedded samples in paraffin wax and cut sections by microtome to a thickness of 4 μm (H&E), or 3 μm (PAS) and subsequently stained using a Leica ST5010 Autostainer XL combined with Leica CV5030 Glass Coverslipper (Concord, ON, Canada). Stained slides were scanned with a MIRAX MIDI digital slide scanner (Zeiss; Göttingen, Germany), or Aperio ScanScope slide scanner (Leica; Concord, Ontario, Canada). Images were acquired with 3DHISTECH Pannoramic Viewer 1.15.4 (Budapest, Hungary), or Aperio ImageScope (Leica; Concord, ON, Canada) software.

*Immunohistochemistry:*

P5 and P15 GIT cross-sections, and P15 skin transverse sections were prepared at a thickness of 4 μm as described above. Slides were deparaffinized in three 5 min washes of 100% HEMO-DE (Electron Microscopy Sciences, USA), and gradually rehydrated in 100%-95%-70%-50%-0% ethanol. Heat induced antigen retrieval step was performed using sodium citrate buffer at pH 6.0. Sections were permeabilized with 0.1% Triton X-100 (Sigma-Aldrich; USA) for 5 min, and then blocked with 10% goat serum (Fischer Scientific; USA) + 1% bovine serum albumin (Sigma-Aldrich; USA) and 0.01% Triton X-100 for 1 h. Blocking buffer was used for primary and secondary antibody dilutions. The following primary antibody dilutions were

applied for 1 h: anti-BPAG1 (1:50, Cosmo Bio CAC-NU-01-BP1; Japan), anti-HuC/D (1:400; Invitrogen A21271; USA), anti-cleaved caspase 3 (1:300, Cell Signaling 9664S; USA), and anti-glial fibrillary acidic protein (1:500, Invitrogen 13-0300; USA). Three 5 min washes in 1X PBS were done before applying the following secondary antibody dilutions for 1 h: Alexa Fluor 488 goat anti-rabbit (1:200, Invitrogen A-11034), Alexa Fluor 555 goat anti-rat (1:200, Invitrogen A-21434), and Alexa Fluor 647 goat anti-mouse (1:200, Invitrogen A32728). Hoechst (1:5000, Fisher Scientific 62249) was then applied for 5 min, followed by three 5 min washes in 1X PBS, and finally slides were mounted in DAKO fluorescent mounting medium (Dako S3023).

Whole mount staining of longitudinal layer myenteric plexus (LLMP) was performed on P15 mice. GIT segments measuring 50 mm were harvested from mice, cut longitudinally to expose the mucosa, and pinned to Sylgard 184 (Dow Corning; USA) coated plates. Samples were fixed overnight at 4°C with Zamboni fixative (Newcomer Supply; USA). Three 15 min washes with 1X PBS were performed at RT on a rotator. The mucosal layers and circular muscle layer were removed with forceps, and the remaining LLMP was transferred to a 24-well plate. LLMPs were blocked for 2 h in 10% goat serum plus 0.5% Triton X-100 in 1X PBS. Primary antibodies and concentrations described above were used here, though diluted in 3% goat serum plus 0.5% Triton X-100 in 1X PBS and incubated overnight at 4°C. Samples were washed three times in 1X PBS for 10 min on a rotator, and incubated in secondary antibody solution composed of 3% goat serum plus 0.5% Triton X-100 in 1X PBS, and Alexa Fluor 488 goat anti-mouse (1:200, Invitrogen A-11001), Alexa Fluor 555 goat anti-rat (1:200, Invitrogen A-21434). Hoechst (1:5000) was applied for 5 min, followed by three 10 min washes in 1X PBS, and finally slides were mounted in DAKO fluorescent mounting medium (Dako S3023).

Micrographs acquired using a Zeiss AxioObserver Z.1 inverted microscope with Axiocam 506 mono camera (Göttingen, Germany).

*Gastrointestinal transit:*

P15 mice were given GastroSense™750 (PerkinElmer®; USA) in 1X PBS by oral gavage at a dose of 0.125 nmol. At three hours post-gavage mice were sacrificed, and GI tracts were cut into segments (stomach, small intestine was measured and divided into 10 equal length segments, cecum, and colon divided into 3 equal segments). The Odyssey Imaging System (LI-COR Biosciences; Lincoln, NB, USA) was employed to measure fluorescence signal intensity in each GIT segment. Segment intensity was then normalized to the total signal detected per mouse.

Stool frequency was assessed by evaluating the number of stool pellets produced per half hour interval over 4.5 h. During testing, P15 mice were kept in individual beakers atop a heating block.

*Absorption analyses:*

Blood plasma was collected from P15 mice fasted 4 h, and blood serum was collected from P15 mice fasted 8 h. A single n constitutes pooled sampled from 2-3 mice in order to obtain sufficient volumes for analysis. Plasma was used for glucose, phosphorus, sodium, chloride, and albumin, while serum was used for magnesium, calcium, iron, and folate. All analyses were carried out by IDEXX Laboratories Canada (ON, Canada).

D-xylose assay (Chondrex, Inc.; WA, USA) was also performed in P15 mice by administering 1 mg/g body weight D-xylose in 1X PBS via oral gavage.(Ijaz et al., 1987) Blood

plasma was collected at 2 and 4 h post administration, and D-xylose concentrations determined according to manufacturer's protocol.

*Microbiome analysis:*

Breeding pairs and their pups were maintained on a 12 h light–dark cycle at 25°C. Stool samples were collected from pups of 3 heterozygous ($Dst^{dt\text{-}27J/+}$) breeding pairs. A total of 20 wild type, and 14 $Dst^{dt\text{-}27J}$ stool samples were collected. Pups were removed from their home cage at P15 to collect stool samples, which were subsequently snap frozen in liquid nitrogen and stored at -80°C.

Metagenomic DNA extraction from mouse stools, V6-16S rRNA gene library construction and sequencing was done as previously described (Mottawea et al., 2016). Briefly, metagenomic DNA was extracted using beads beating, extracted DNA normalized and the V6-16S rRNA gene PCR amplified. Sample amplicons were normalized by mass, pooled together, sized selected and quantified using a Agilent Bioanalyzer. The pooled library was subsequently templated and sequenced using an IonChef and Ion Torrent Proton sequencer using the manufacturer's recommended protocol. Raw sequencing reads were quality filtered and demultiplexed prior to operational taxonomic units (OTU) picking as previously described (Mottawea et al., 2016) and have been deposited at the NCBI Sequence Read Archive (http://www.ncbi.nlm.nih.gov/sra) under ascension PRJNA542920. QIIME 1.9.1 was used to identify OTU's using a closed reference strategy against the Greengenes 13.5 database and the data analyzed using phyloseq (Caporaso et al., 2010; McMurdie and Holmes, 2013). OTUs present in < 5% of the final sample dataset were removed and samples were rarefied to 200,000 reads prior to analysis. The final dataset consisted of microbiota profiles from 19 wild type and

13 *Dst*$^{dt\text{-}27J}$ mice. Differences in alpha diversities were assessed using Mann-Whitney tests and the factors impacting beta diversity clustering were accessed with the adonis function from vegan (Oksanen, 2016). Differentially abundant taxa and inferred functional gene content were assessed using Maaslin controlling for breeding pairs and littermates using the default parameters (Morgan et al., 2012; Langille et al., 2013). Features were considered significantly differentially abundant with a P value < 0.05 and where appropriate, after controlling for multiple hypothesis testing using the Benjamini and Hochberg approach.

*Transmission electron microscopy and toluidine blue staining:*

P15 mice were anesthetized and transcardially perfused with 5 ml 1X PBS followed by 10 ml Karnovsky's fixative (4% paraformaldehyde, 2% glutaraldehyde [Sigma-Aldrich, USA] and 0.1 M sodium cacodylate [Electron Microscopy Science, USA] in 1X PBS, pH 7.4). Segments of vagus nerve gastric branch (1 mm) were collected and kept in fixative until processed. Segments were washed in 0.1M sodium cacodylate buffer for 1 h, and again overnight. Samples were post-fixed with 1% $OsO_4$ (Electron Microscopy Science, USA) in 0.1M sodium cacodylate buffer for 1 h and subsequently dehydrated in an ascending concentration of ethanol. Nerve segments were infiltrated and embedded in spurr resin (Electron Microscopy Science, USA), and polymerized overnight at 70ºC. Ultrathin sections (80 nm) were collected onto 200-mesh copper grids and stained with 2% aqueous uranyl acetate (Electron Microscopy Science, USA) and Reynold's lead citrate. Specimens were examined by transmission electron microscopy at 4000X and 10,000X magnification (n = 2).

Semithin sections of 0.3 μm from resin embedded vagus nerves were mounted on glass slides and stained with 1% toluidine blue (Thermo Fisher Scientific, USA) and 2% borate in distilled water for light microscopic examination (20X magnification).

*Statistical analysis:*

Graphical data presented as mean ± SEM. Prism 5.0 GraphPad software was used for statistical analyses. Two-way comparisons were done by two-tailed Student's *t*-test. Multiple comparison tests done by one-way ANOVA, followed by Tukey's *post hoc* test. $P < 0.05$ was considered statistically significant (shown as *).

## Results

Anatomical and histological characterization of *Dst*$^{dt-27}$ gastrointestinal tract

The work presented here is primarily performed on the *Dst*$^{dt-27J}$ allele, where all neuronal isoforms of dystonin (Dst-a) are absent.(Pool et al., 2005) Inspection of P15 *Dst*$^{dt-27J}$ GIT gross morphology reveals a stark difference compared to wild type. The defining feature is a large accumulation of gas, causing severe distension of the small intestine and cecum (Figure 5.1A), while in some cases we also observe discoloration of the GIT, appearing brown-black throughout the small intestine (Figure 5.1A right panel). *Dst*$^{dt-27J}$ mice do not appear to have impaired feeding, as stomachs are similarly full by the point of sacrifice. Though, we do remark a significant reduction in total body weight of *Dst*$^{dt-27J}$ mice at P15 (Figure 5.1B), as well a shorter GIT length (Figure 5.1C) that is likely attributed to the smaller size of the mice.

As we suspected that the *Dst*$^{dt-27J}$ GIT abnormalities were linked to enteric nervous system defects, we first confirmed expression of the *Dst-a* isoforms at various points throughout the wild type GIT by reverse transcriptase polymerase chain reaction (RT-PCR). Indeed we do see expression of *Dst-a*, with *Dst-a3* being the predominant isoform expressed across all GIT levels, and *Dst-a1* and *-a2* mainly being expressed in esophagus, ileum, and colon (Figure 5.1D). We also ruled out the potential involvement of the epithelial isoform (Dst-e/BPAG1e) with relation to the GIT defects, as the presence of this isoform is confirmed in *Dst*$^{dt-27J}$ skin (Figure 5.1E), indicating that this isoform is not disrupted in *Dst*$^{dt-27J}$ mice (Seehusen et al., 2016). It should also be noted that BPAG1e is not expressed in the GIT (with exception of the esophagus), and is therefore not expected to be involved in this pathology (Sachsenberg-Studer et al., 2001; Giorda et al., 2004).

Histological analysis of P15 duodenum, jejunum, ileum, and colon by hematoxylin & eosin staining revealed no differences in villi length, villi width, crypt length, crypt width, smooth muscle thickness, or colon goblet cell number between $Dst^{dt\text{-}27J}$ and wild type mice (Figure 5.2A-G), with the exception of an increase in crypt width in $Dst^{dt\text{-}27J}$ jejunum.

We then assessed whether the GIT abnormalities could be observed before onset of the neurologic $Dst^{dt}$ phenotype. Examination of whole GIT from P5 $Dst^{dt\text{-}27J}$ and wild type mice did not reveal any major differences (Figure S5.1A). Histological differences were also not observed, indicating that the bioarchitecture of the GIT is consistently normal throughout the course of disease (Figure S5.1B).

Our findings at the P15 stage were also confirmed in the $Dst^{dt\text{-}Tg4}$ allele (no expression of *Dst-a1* and *-a2*), and the *PrP-Dst-a2/PrP-Dst-a2*;$Dst^{dt\text{-}Tg4}$ transgenic mouse model ($Dst^{dt\text{-}Tg4}$ mice exogenously expressing *Dst-a2* under the prion protein promoter) (Ferrier et al., 2014). Gross morphology at P15 is consistent with $Dst^{dt\text{-}27J}$ mice (Figure S5.2B). Expression of *Dst-a* isoforms predictably shows a lack of *Dst-a1* and *-a2* in $Dst^{dt\text{-}Tg4}$ GIT, as well as expression of *Dst-a3* at levels similar to wild type (Figure S5.2A).

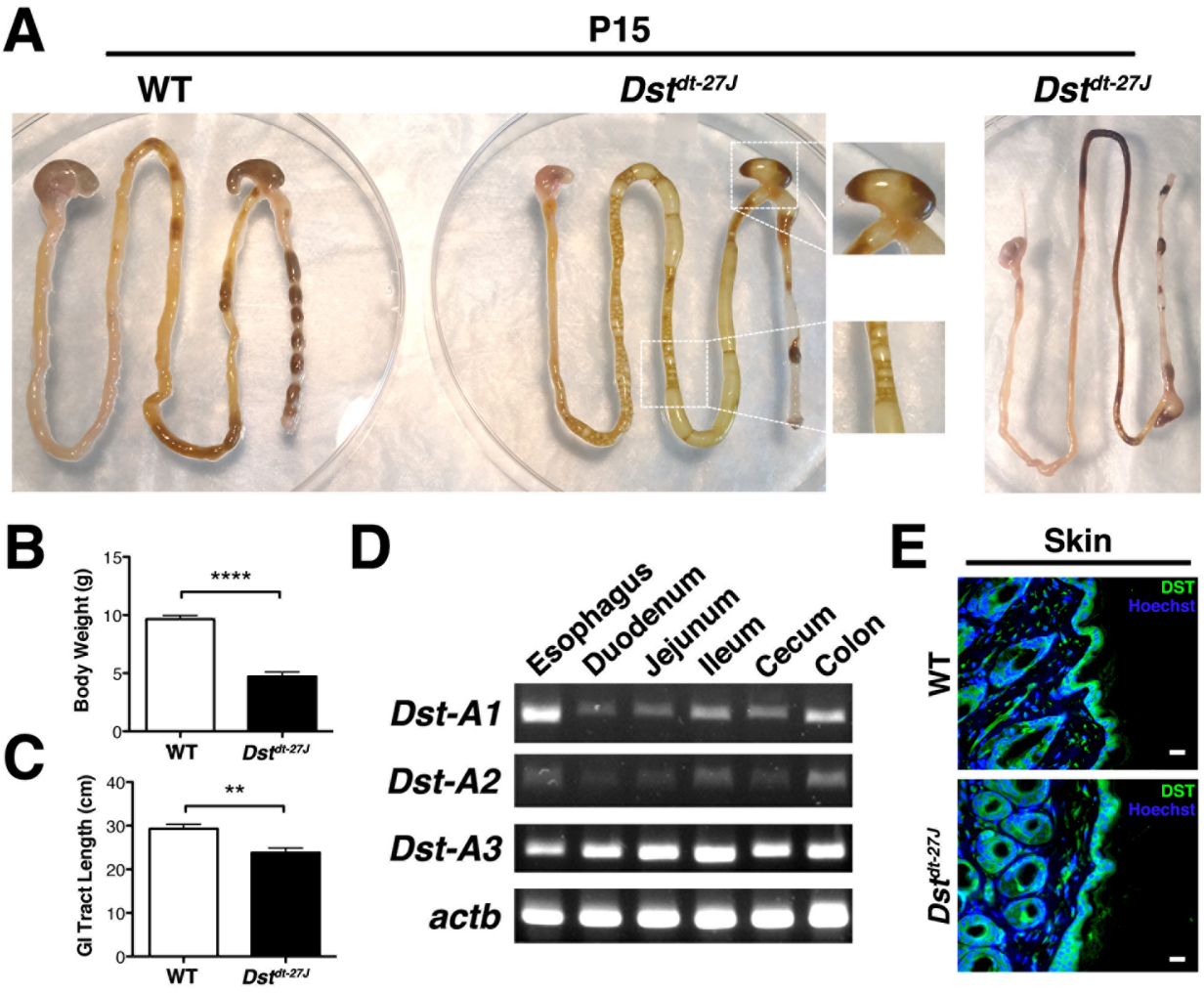


**Figure 5.1.** Examination of the gastrointestinal tract in phenotype-stage wild type and *Dst*$^{dt\text{-}27J}$ mice. **A)** Whole gut morphology is altered in P15 *Dst*$^{dt\text{-}27J}$ mice. The *Dst*$^{dt\text{-}27J}$ GI phenotype manifests as either a massive accumulation of gas causing intestinal distension (middle panel), or as an abnormal black-brown color through the distal small intestine and cecum. In both cases the appearance of fecal pellets in the colon is infrequent, and stool consistency is wet and loose. **B)** *Dst*$^{dt\text{-}27J}$ mice weigh significantly less than wild type at P15 (n = 8), and considering their smaller size their GI tract length is also significantly shorter **(C)**. (n = 7; ** - *P*-value < 0.01; **** *P*-value < 0.0001, graphical data represented as mean ± SEM, statistical analysis by two-tailed Student's *t*-test). **D)** RT-PCR for neuronal dystonin isoforms in P15 wild type mice confirms

expression of *Dst-a1*, *-a2*, and *-a3* throughout the GI tract, with actin (*actb*) serving as loading control. **E)** Immunofluorescence staining for DST in skin sections from P15 wild type and $Dst^{dt-27J}$ mice. DST is localized to the epidermal basal lamina in both genotypes, indicating that the epithelial isoform is not disrupted in $Dst^{dt-27J}$ mice (scale bar = 20 μm).

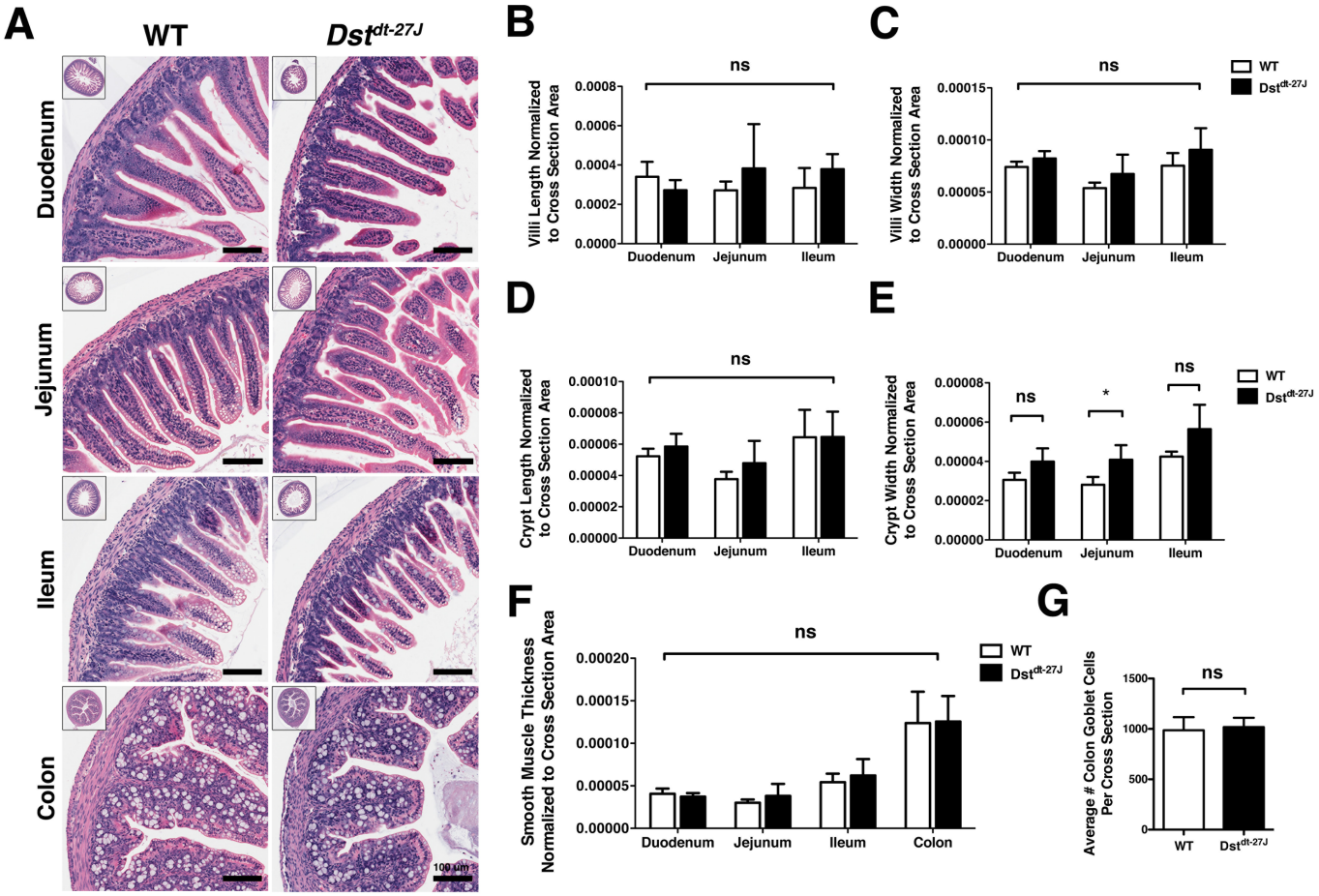


**Figure 5.2.** Intestinal morphology is not impaired in P15 *Dst*$^{dt\text{-}27J}$ mice. **A)** Hematoxylin and eosin stained duodenum, jejunum, ileum, and colon cross sections from wild type and *Dst*$^{dt\text{-}27J}$ mice (scale bar = 100 µm). Upper left hand corners also contain full cross section image at 5X magnification. Quantifications of **B)** villus length, **C)** villus width, **D)** crypt length, **E)** crypt width, and **F)** smooth muscle thickness all normalized to cross sectional area are represented. *Dst*$^{dt\text{-}27J}$ jejunum crypt length was found to be significantly increased compared to wild type, while no other comparisons were found to be statistically significant. **G)** Average number of colon goblet cells per cross sectional area was also assessed, revealing no difference between wild type and *Dst*$^{dt\text{-}27J}$ mice. (n = 4; ns - *P*-value > 0.05, * - *P*-value < 0.05; graphical data represented as mean ± SEM, statistical analysis by two-tailed Student's *t*-test).

Evaluation of enteric nervous system viability

Though we do not observe changes to the GIT at the histological level, this does not directly test the state of the ENS. Therefore we assessed submucosal and myenteric plexus neurons for signs of cell death by immunofluorescence staining for the neuronal marker HuC/D and the apoptotic marker cleaved caspase 3 (CC3). At the level of the duodenum, jejunum, ileum, and colon in P15 $Dst^{dt\text{-}27J}$ and wild type mice, we do not observe any co-localization of CC3 signal to neurons of either plexus (Figure 5.3A-D). Absence of neurodegeneration was also confirmed by FluoroJade C staining, where we did not observe any difference in staining patterns between wild type and $Dst^{dt\text{-}27J}$ small or large intestine sections (data not shown). This indicates that the ENS neurons are not actively undergoing cell death at the P15 stage. However, there still remains the possibility that the major cell death events occurred earlier or that there are just fewer neurons in $Dst^{dt\text{-}27J}$ ENS to begin with. To address, this we analyzed whole mount preparations of longitudinal layer myenteric plexus (LLMP) to determine number of neurons per ganglia. HuC/D positive neuronal cell bodies were counted and then normalized to ganglion size as determined by the glial fibrillary acidic protein (GFAP) positive area. For all GIT levels assessed, no significant difference in neuronal cell density per ganglion was detected between wild type and $Dst^{dt\text{-}27J}$ (Figure 5.4A-B). Since ENS neurons are present at appropriate numbers, and are not undergoing neurodegeneration, we confirm that ENS neurons are not vulnerable to cell death like DRG neurons.

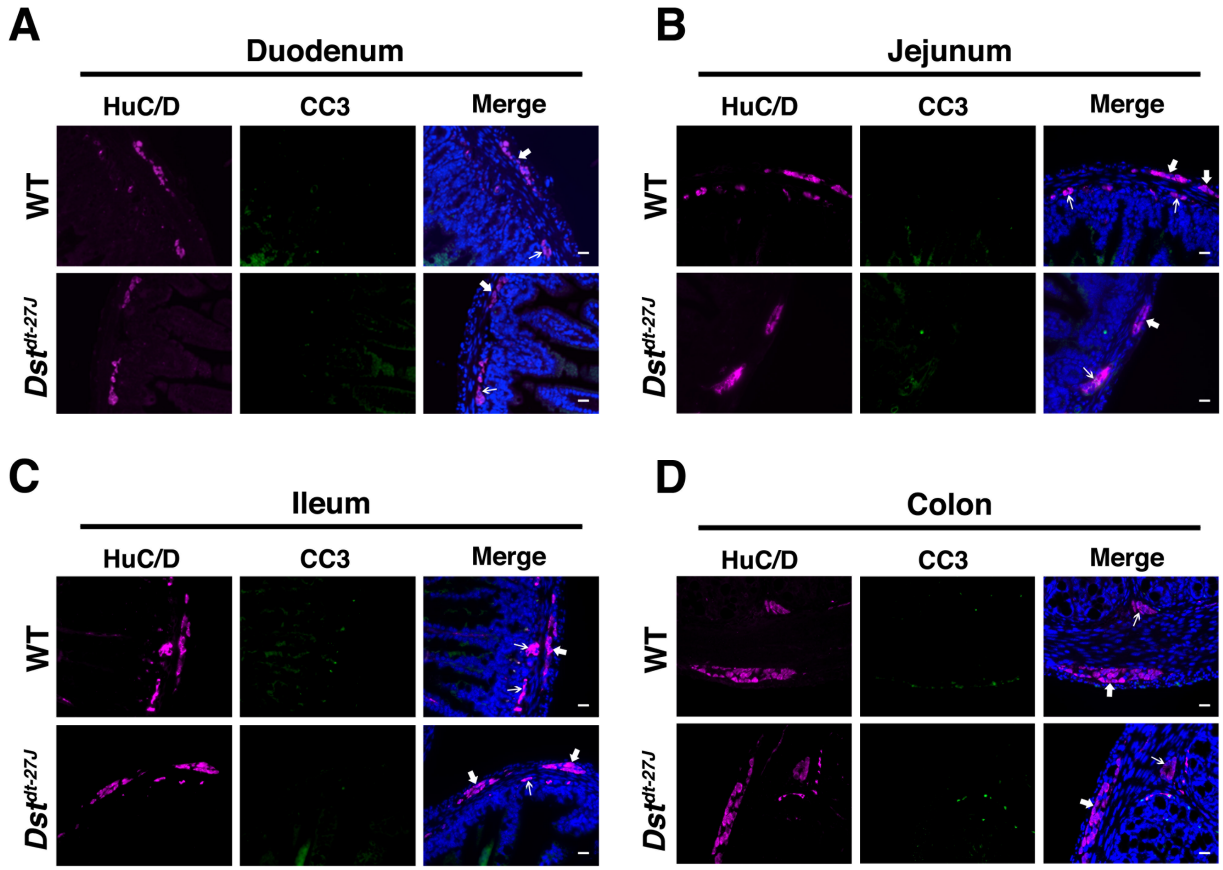


**Figure 5.3** Phenotype stage *Dst*$^{dt\text{-}27J}$ submucosal and myenteric plexus neurons are not undergoing apoptosis. Immunofluorescence micrographs of P15 wild type and *Dst*$^{dt\text{-}27J}$ duodenum **(A)**, jejunum **(B)**, ileum **(C)**, and colon **(D)** cross-sections. Neuronal marker HuC/D reveals ganglia from the myenteric plexus (thick arrows) and from the submucosal plexus (thin arrows). Micrographs were assessed for colocalization of the apoptotic marker cleaved caspase 3 (CC3) to neuronal cell bodies. In both wild type and *Dst*$^{dt\text{-}27J}$ sections, no CC3 signal was observed in either plexus. (n = 6; HuC/D - magenta, CC3 - green, Hoechst - blue; scale bar = 20 μm).

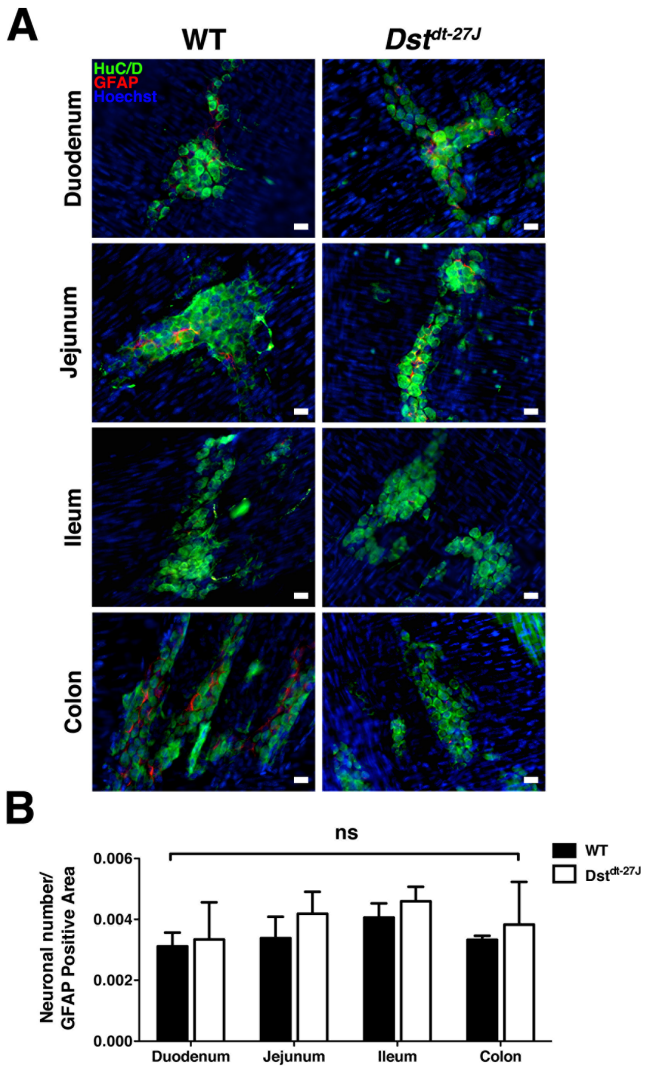


**Figure 5.4** Number of myenteric plexus neurons per ganglia is similar between P15 wild type and *Dst*$^{dt\text{-}27J}$ mice. **A)** Whole mount longitudinal layer myenteric plexus (LLMP) preparations were obtained from P15 wild type and *Dst*$^{dt\text{-}27J}$ mice. Neuronal cell bodies stained with HuC/D (green) were counted and normalized to the ganglion area as defined by the GFAP stained area (red; scale bar = 20 μm). **B)** Quantification of the average number of neurons per ganglia in the duodenum, jejunum, ileum, and colon shows no significant difference between wild type and *Dst*$^{dt\text{-}27J}$ (n = 4; ns - *P*-value > 0.05; graphical data represented as mean ± SEM, statistical analysis by two-tailed Student's *t*-test).

Assessing gastrointestinal function

Considering the striking GIT phenotype of *Dst*$^{dt}$ mice, we wondered whether this translated to defects in GI function, specifically absorption and motility. To assess GI transit we administered a fluorescent tracer, GastroSense™750, to P15 mice by oral gavage. After a three-hour period, GITs were removed and cut into pieces to determine the signal intensity per segment normalized to total signal intensity (Figure 5.5A). Subtle but significant increases in signal intensity were observed in the most posterior segment of small intestine (SI 10) and in the cecum of wild type mice. This difference represents faster intestinal transit in P15 wild type mice compared to *Dst*$^{dt\text{-}27J}$ mice.

Stool frequency was also assessed to evaluate stool consistency as well as to gauge colonic transit. Wild type mice initially show high stool production, with a significant increase compared to *Dst*$^{dt\text{-}27J}$ mice being observed at the 1 h time point (Figure 5.5B). Eventually wild type mice show a levelling around 0 stool pellets by 2.5 hours, likely as a result of the mice not actively feeding. Qualitative examination of the stool produced by both mice showed that *Dst*$^{dt\text{-}27J}$ mice produce very irregular, damp, black or orange-colored stool, which is consistent with signs of diarrhea in mice (although production is infrequent). In contrast, wild type mice produce firm, brown stools at a fairly frequent rate.

Absorption was also assessed by measuring plasma and serum concentrations of electrolytes/compounds that are dependent upon adequate GI absorption. Levels of phosphorus, sodium, chloride, magnesium, calcium, and glucose were similar between wild type and *Dst*$^{dt\text{-}27J}$ mice (Figure 5.5C). Plasma levels of albumin were significantly reduced in *Dst*$^{dt\text{-}27J}$ mice (Figure 5.5G), this however may be a result of liver or kidney defects rather than a GIT absorption issue. Serum levels of iron and folate were also assessed, as these are absorbed mainly by the

duodenum and jejunum, respectively; no significant differences are seen between wild type and *Dst*$^{dt\text{-}27J}$ mice for either (Figure 5.5D-E). As a final measure of intestinal absorption, P15 mice were given D-xylose by oral gavage and plasma samples were collected at 2 and 4 h post administration. No significant difference in D-xylose plasma concentration was detected between wild type and *Dst*$^{dt\text{-}27J}$ mice at either time point (Figure 5.5F). Ultimately these results indicate that GI absorption is normal in *Dst*$^{dt\text{-}27J}$ mice.

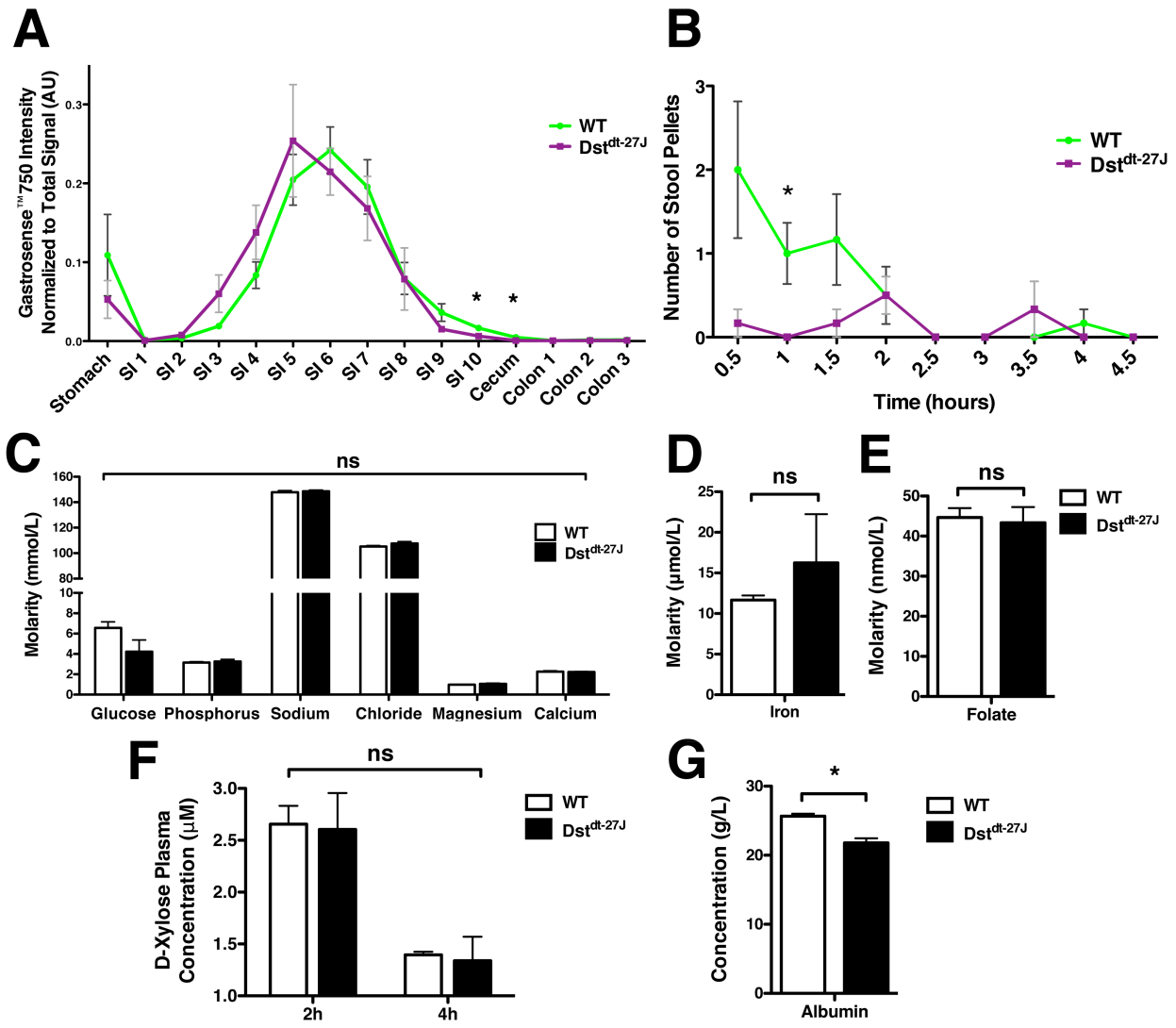


**Figure 5.5** *Dst*$^{dt\text{-}27J}$ GIT motility is mildly reduced, while absorption is normal. **A)** Relative intensity of the GastroSense™750 signal per GIT segment in P15 wild type and *Dst*$^{dt\text{-}27J}$ mice 3 h post administration. Wild type small intestine segment 10 (SI 10) and cecum had higher signal intensity compared to *Dst*$^{dt\text{-}27J}$ indicating faster GI motility (n = 7). **B)** Frequency of stool production was also assessed in P15 wild type and *Dst*$^{dt\text{-}27J}$ mice. Wild type mice initially produce more stool pellets more frequently than *Dst*$^{dt\text{-}27J}$, with a significant difference being observed at 1 h (n = 6). No significant differences were observed in circulating levels of glucose,

phosphorus, sodium, chloride, magnesium, calcium **(C)**, nor for iron **(D)**, or folate **(E)**. **F)** A D-xylose assay was also carried out to evaluate efficiency of GI absorption into blood plasma. Plasma levels of D-xylose at 2 h and 4 h post administration were not significantly different between wild type and $Dst^{dt\text{-}27J}$ mice (ns - *P*-value > 0.05). **G)** A small but significant decrease in serum albumin levels was detected in P15 $Dst^{dt\text{-}27J}$ mice compared to wild type (6 wild type mice used in all serum/plasma analyses, and number of $Dst^{dt\text{-}27J}$ mice used is as follows: 5 for glucose, phosphorus, sodium, chloride, and albumin, 4 used for magnesium, calcium, and iron, 3 used for folate analyses; * - *P*-value < 0.05; graphical data represented as mean ± SEM, statistical analysis by two-tailed Student's *t*-test).

Investigating the microbiome

The role of the mucous layer that sits atop the epithelium in the colon is two-fold in that it provides a layer of protection to the host, but also provides a supportive growth environment for the resident microbiota. At P5 we observe a thick healthy layer of mucous gel in both wild type and $Dst^{dt\text{-}27J}$ periodic acid Schiff (PAS) stained colon cross-sections (Figure 5.6A). However, by P15 the colon mucous layer in $Dst^{dt\text{-}27J}$ mice has been greatly reduced (thinned, and no visible striations; Figure 5.6A). We subsequently assessed the gut microbiota in $Dst^{dt\text{-}27J}$ mice. Stools were collected from wild type and $Dst^{dt\text{-}27J}$ mice at postnatal day 15 and metagenomic DNA extracted for 16S rRNA gene amplicon profiling to characterize the microbial communities within. This analysis revealed that the $Dst^{dt\text{-}27J}$ mice microbiotas were significantly reduced in both species richness (Figure 5.6B) and species diversity (Figure 5.6C). The wild type and $Dst^{dt\text{-}27J}$ microbiotas show a high degree of co-clustering when performing a principal co-ordinate analysis using the unweighted Unifrac distance (Figure 5.6D) suggesting that the differences between the genotypes are fairly minor when compared to other variables such as whether the mice were from the same breeding pair or whether the mice were litter mates (Supplemental Table 5.1). However, the $Dst^{dt\text{-}27J}$ microbiotas were more dispersed (Figure 5.6D) and further analysis revealed that wild type mice were significantly more similar to each other as compared to how similar $Dst^{dt\text{-}27J}$ mice were to each other (Figure 5.6E). Finally, we identified several taxa that were differentially abundant between the wild type and $Dst^{dt\text{-}27J}$ mice (Supplemental Table 5.2). In particular, several genera such as *Blautia, Prevotella* and *CF231* were enriched in the wild type mice while *Carnobacterium* and *Granulicatella* were enriched in the $Dst^{dt\text{-}27J}$ mice (Figure S5.3).

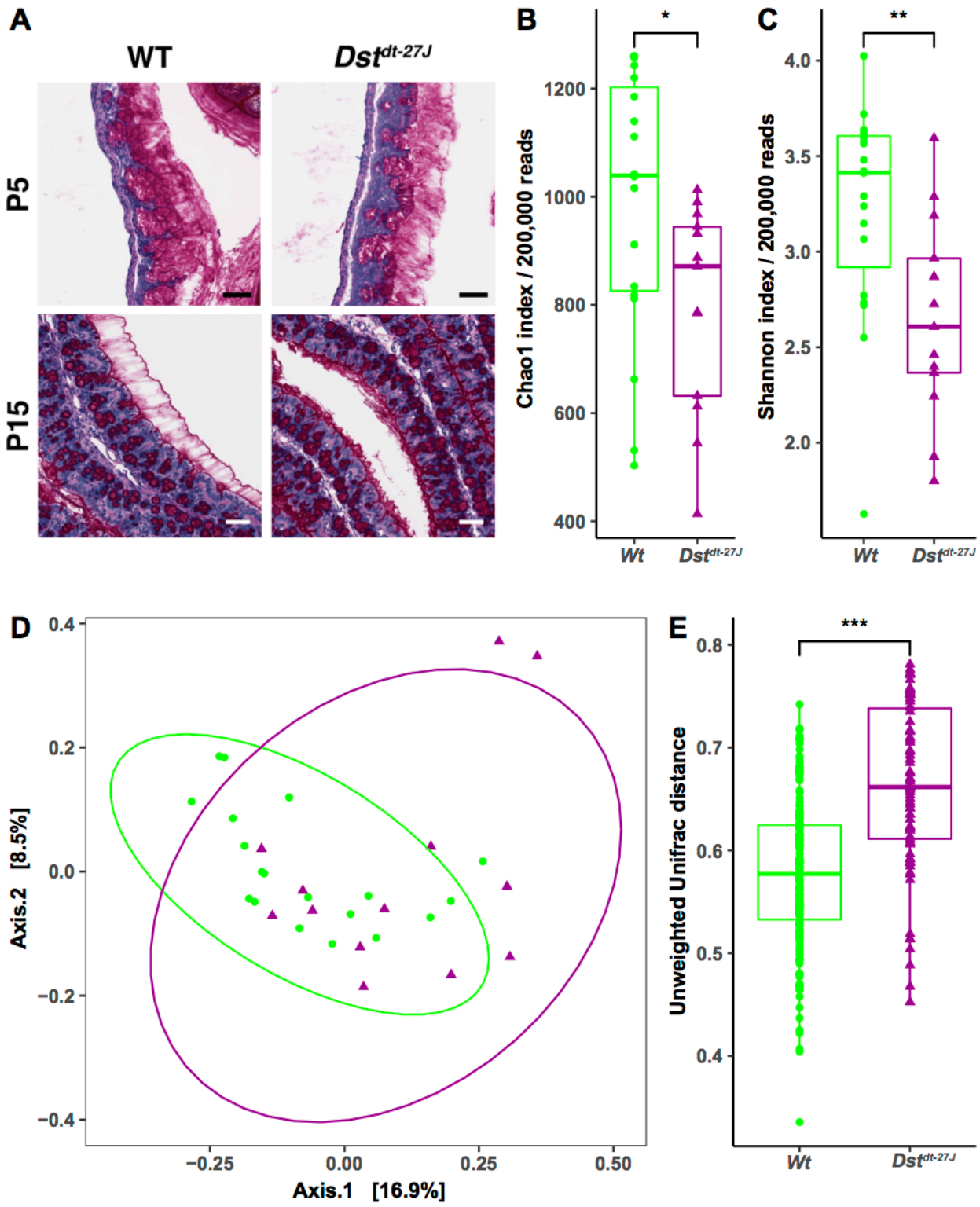


**Figure 5.6** *Dst*$^{dt\text{-}27J}$ mice show thinning of the colon mucous layer and a reduced microbial richness/evenness. **A)** Periodic acid Schiff staining of transverse colon sections from P5 and P15

wild type and *Dst*$^{dt\text{-}27J}$ mice. A thick mucous layer is observed in P5 *Dst*$^{dt\text{-}27J}$ colon, but by P15 its thickness has been greatly reduced compared to wild type (n = 3; scale bar = 50 μm). **B)** Chao1 index (richness) and **C)** Shannon index (evenness) as compared to wild type mice. **D)** *Dst*$^{dt\text{-}27J}$ mouse microbiotas do not separate from wild type using principal coordinate analysis with the unweighted Unifrac distance but are more dispersed from each other. D) The wild type mice microbiotas are more similar to each other than the *Dst*$^{dt\text{-}27J}$ microbiotas are to each other using the unweighted Unifrac distance. Wild type mice are denoted by green circles and *Dst*$^{dt\text{-}27J}$ by purple triangles in all panels. Boxplots represent in interquartile range with the line representing the median and the ellipses in D represent 95% confidence intervals. Statistical significance denoted by asterisks (* - *P*-value < 0.05; ** - *P*-value < 0.01; *** - *P*-value < 0.001).

Evaluating the role of the autonomic nervous system

As the integrity of the ENS was found to remain intact, we aimed to investigate higher order neural input as the possible cause of the *Dst*$^{dt}$ GI phenotype. The vagus nerve's enteric branch was selected for this analysis, as it is a major source of extrinsic input onto the ENS and could be clearly identified and extracted in the small P15 pups. Preliminary confirmation of *Dst-a* isoform expression in the vagus nerve nodose ganglion also lead us to believe that loss of function could lead to defects (Figure 5.7A). Since the average *Dst*$^{dt}$ mouse is significantly smaller than wild type (Figure 5.1B & Figure S5.2I), we size-matched wild type and *Dst*$^{dt\text{-}27J}$ mice for this analysis. Toluidine blue stained cross sections of the vagus nerve shows a reduction in diameter in *Dst*$^{dt\text{-}27J}$ mice (Figure 5.7B). Total number of axons present appears to be reduced, in addition to a reduction in size of the remaining axons. A closer look by transmission electron microscopy, we observe a higher proportion of amyelinated and hypomyelinated axons, and fewer unmyelinated axons in *Dst*$^{dt\text{-}27J}$ mice compared to wild type (Figure 5.7C). Taken together these findings indicate a high degree of neurodegeneration of the vagus nerve extrinsic input onto the ENS.

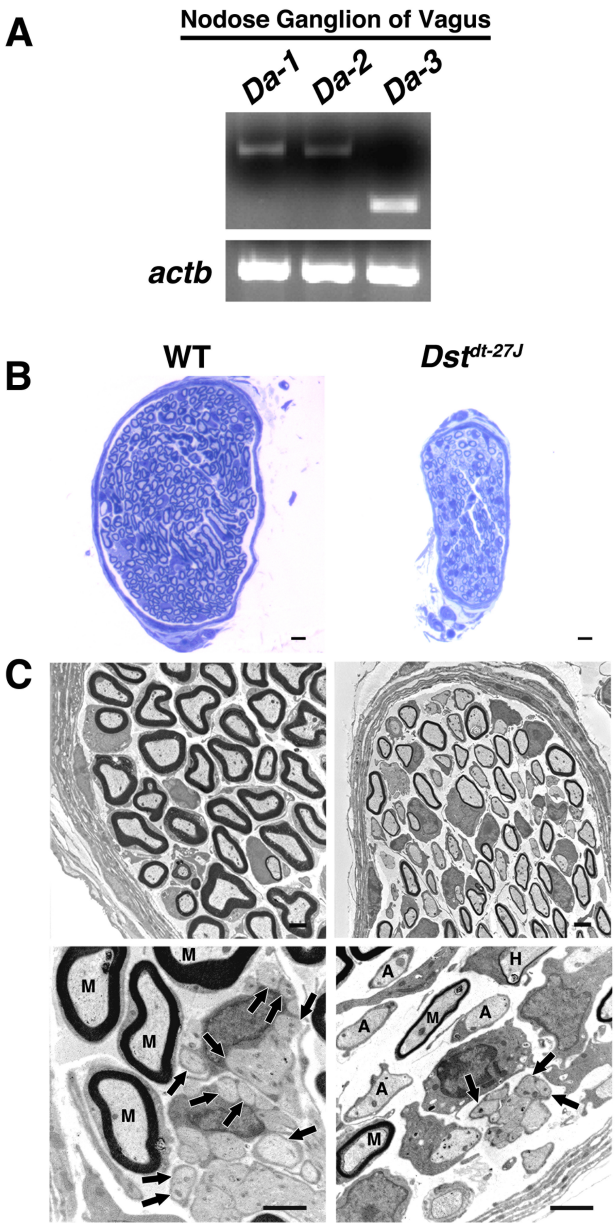


**Figure 5.7** Vagus nerve degeneration is evident in P15 *Dst*$^{dt\text{-}27J}$ mice. **A)** Neuronal dystonin transcript expression confirmed by RT-PCR in P15 wild type nodose ganglion, with actin (*actb*) as loading control. **B)** Toluidine blue staining of cross-sections of the enteric branch of the vagus nerve in wild type and size-matched *Dst*$^{dt\text{-}27J}$ mice. Vagus nerve in *Dst*$^{dt\text{-}27J}$ mice is much smaller in diameter and has far fewer myelinated axons present (n = 2; scale bar = 10 μm). **C)** Electron micrographs of vagus nerve enteric branch cross sections. Size-matched *Dst*$^{dt\text{-}27J}$ mice exhibit a

high degree of amyelinated and hypomyelinated axons, as well as far fewer unmyelinated axons compared to wild type (M - myelinated axons, A - amyelinated axons, H - hypomyelinated axons, black arrows - unmyelinated axons; n = 2; scale bar = 2 μm).

## Discussion

GI defects are often observed alongside neurodegenerative disease, though determining whether these pathologies are intrinsic to the gut or a consequence of higher order neural defects is not always clear (Marola et al., 2016; Poirier et al., 2016; Fang et al., 2017; Takamatsu et al., 2018). Likewise, HSAN-VI patients have GI symptoms without clear cause, and *Dst*$^{dt}$ mice have a distinct GI phenotype characterized by small intestinal gas accumulation and GIT discoloration. Since neuronal dystonin is expressed throughout the GIT, we aimed to investigate whether the GI abnormalities in *Dst*$^{dt}$ mice could be linked to ENS neurodegeneration due to dystonin loss-of-function. Interestingly, although *Dst*$^{dt}$ mice have a clear GIT phenotype/abnormality, this does not translate to histological defects. Structure of villi, crypts, and smooth muscle all appear to remain intact (as they are of appropriate dimensions considering the smaller size of *Dst*$^{dt}$ mice). Our results also indicate that *Dst*$^{dt\text{-}27J}$ myenteric plexus and submucosal plexus neurons remain intact as they are CC3 negative (Figure 5.3), and have similar FluoroJade C staining pattern as wild type (data not shown). We also assessed whether *Dst*$^{dt\text{-}27J}$ mice had an appropriate number of neurons per myenteric ganglion (thus accounting for neuronal loss prior to the P15 time point), and still no ENS differences were observed compared to wild type. Given this, we can conclude that ENS neurons are not immediately vulnerable to neurodegeneration upon dystonin loss-of-function like in *Dst*$^{dt}$ DRG sensory neurons and motor neurons (Kothary et al., 1988; Ichikawa et al., 2006; De Repentigny et al., 2011; Ferrier et al., 2014; Ferrier et al., 2015; Hossain et al., 2018). Our recent findings related to *Dst-a3* upregulation and compensation in dystonin-dependent tissues would also suggest that the lack of any increase in *Dst-a3* expression at any GIT level in *Dst*$^{dt\text{-}Tg4}$ mice might indicate that the enteric nervous system is not impacted by dystonin loss-of-function (Figure S5.2) (Lynch-Godrei

et al., 2018). It is likely that the ENS contains other compensatory spectraplakin proteins (e.g. Macf1) that make up for dystonin loss of function, which has been suggested for other cell types that express dystonin but do not exhibit defects or cell death (Bernier et al., 2000; Boyer et al., 2010; Kornfeld et al., 2016; Lynch-Godrei et al., 2018).

Nevertheless, *Dst*$^{dt\text{-}27J}$ mice do exhibit a small reduction in GI motility as well as a thinning of the mucous layer lining the colon. We believe that these effects are linked to dystonin loss-of-function impacting the extrinsic neural input on the ENS. Autonomic control over the GIT consists of the parasympathetic nervous system (PNS), which arises from the vagus nerve and lumbosacral spinal cord preganglionic neurons, as well as the sympathetic nervous system which arises from sympathetic chain ganglia and prevertebral ganglia including: the celiac ganglion, superior and inferior mesenteric ganglion, and the pelvic ganglion (Browning and Travagli, 2014). Any imbalance between SNS and PNS control over the GIT would likely result in altered function. Considering the young age of the mice, and their small size we were only able to extract the vagus nerve (gastric branch) for analysis. Having controlled for the small size of *Dst*$^{dt\text{-}27J}$ mice by size matching to wild type, we still observed major signs of axonal loss and demyelination, as well as a reduction in the overall diameter of the vagus nerve cross section (Figure 5.7B-C). This extensive level of neurodegeneration in *Dst*$^{dt\text{-}27J}$ vagus nerve is likely also a predictor for the state of other autonomic PNS and SNS centers. Although the GIT is capable of maintaining a functional state without central input, loss of the 'fine tuning' provided by higher control can impact GI function, especially immediately after neuronal loss as the GIT requires time to adjust (Browning and Travagli, 2014). Our results also suggest an autonomic imbalance favouring SNS input rather than PNS. Acetylcholine released by the PNS has roles in stimulating crypt goblet cell Muc2 secretion, as well as increasing peristalsis (Specian and

Neutra, 1980; Johansson et al., 2013; Birchenough et al., 2015). Thus, if PNS innervation to the GIT is impaired, as is seen by vagus nerve degeneration in *Dst*$^{dt\text{-}27J}$ mice, the expected downstream effects of this would include thinning of the colon mucous layers and slowed GI motility.

With respect to the colon mucous layer of *Dst*$^{dt\text{-}27J}$ mice, we observe a progressive thinning from P5 to P15. The mucous producing goblet cells are present throughout the colon in appropriate numbers (Figure 5.2G), indicating their abundance is not responsible for mucous layer thinning. Also, as far as we know, goblet cells do not express dystonin, thus it is unlikely that dystonin loss-of-function plays a role in Muc2 export to the luminal surface. The microbiome results also support the idea of a decrease in PNS activity. The external mucosal layer of the colon has a major role in supporting the microbiota environment and providing a source of nutrients (Johansson et al., 2013). The significant decrease in richness/evenness of the microbiota in *Dst*$^{dt\text{-}27J}$ mice could be a consequence of this mucosal layer thinning (i.e. fewer available nutrients and a less hospitable space for the microbiota to thrive). We believe that the loss of this supportive environment for the microbiota in the large intestine paired with the defective GI motility in *Dst*$^{dt\text{-}27J}$ mice may provide an opportunity for microbes to move anteriorly and abnormally colonize the small intestine. This can lead to small intestinal bacterial overgrowth (SIBO), which is often caused by gastric dysmotility and has such accompanying effects as excessive gas production causing bloating, abdominal distension, abdominal pain, and diarrhea (Dukowicz et al., 2007; de Lisle et al., 2010). This would help to explain the striking GI phenotype we observe in *Dst*$^{dt}$ mice, and also gives insights onto the potential causes of the GI symptoms experienced by HSAN-VI patients.

To date, 10 patients have been described with HSAN-VI, 7 of whom continue to live into adulthood and have reported a multitude of autonomic symptoms, including GI problems such as chronic diarrhea and abdominal pain (Edvardson et al., 2012; Cappuccio et al., 2017; Manganelli et al., 2017; Fortugno et al., 2018). Furthermore, only one patient has undergone comprehensive GI evaluation, whereby no GI abnormalities could be found that might explain her symptoms (Cappuccio et al., 2017). Although it is likely that the root cause of GIT symptoms in HSAN-VI patients is due to autonomic disturbances that are difficult to treat, we may still be able to treat the resulting symptoms and improve quality of life. Further evaluation of HSAN-VI patients and direct assessment for GI abnormalities and the potential presence of SIBO are necessary to determine appropriate therapeutic interventions.

**Acknowledgements**

This project was funded by grants from the Canadian Institutes of Health Research to RK (# MOP-126085), and to AS (#MOP-114872), and a grant from Genome Canada and the Ontario Genomics Institute to AS (#OGI-149). ALG is supported by an Ontario Graduate Scholarship.

**Supplementary Material**

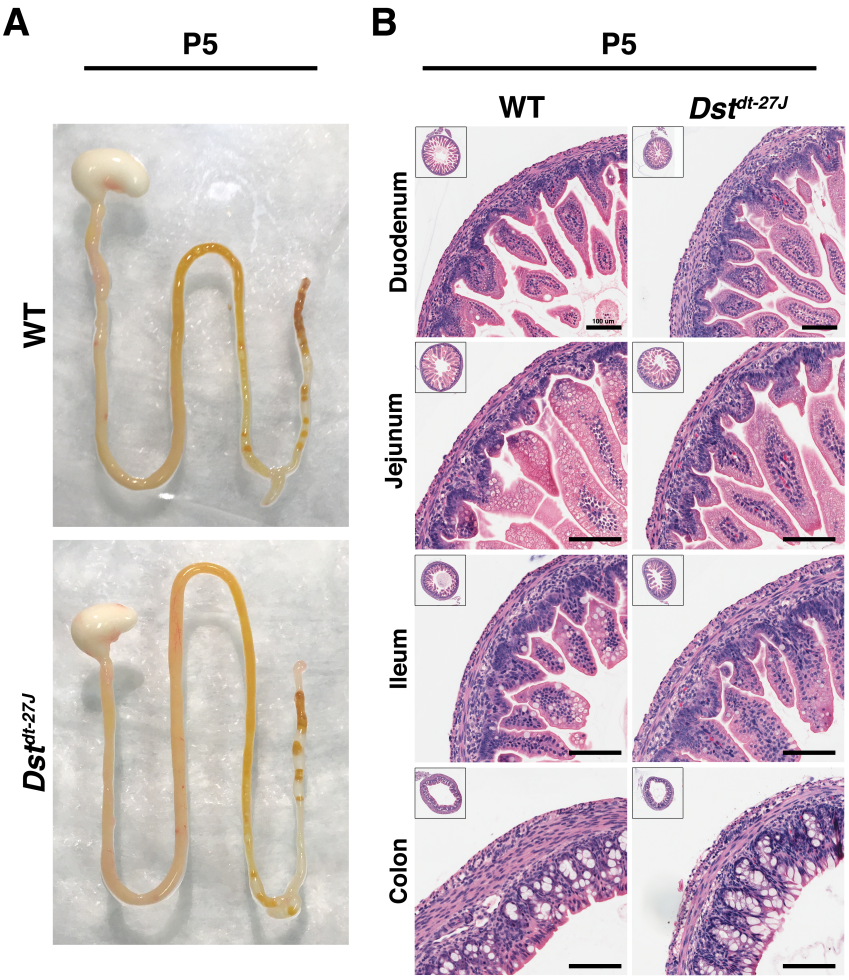


**Figure S5.1.** Pre-phenotype stage *Dst*$^{dt-27J}$ gut does not present with any abnormalities. **A)** *Dst*$^{dt-27J}$ whole gastrointestinal morphology does not appear to be different from wild type at the P5 stage. Normal coloring, and lack of gas accumulation are observed at this early stage. **B)** Hematoxylin and eosin staining of P5 duodenum, jejunum, ileum, and colon cross-sections from wild type and *Dst*$^{dt-27J}$ mice. Qualitative analysis did not reveal any major differences between the two (n = 4; scale bar = 100 μm).

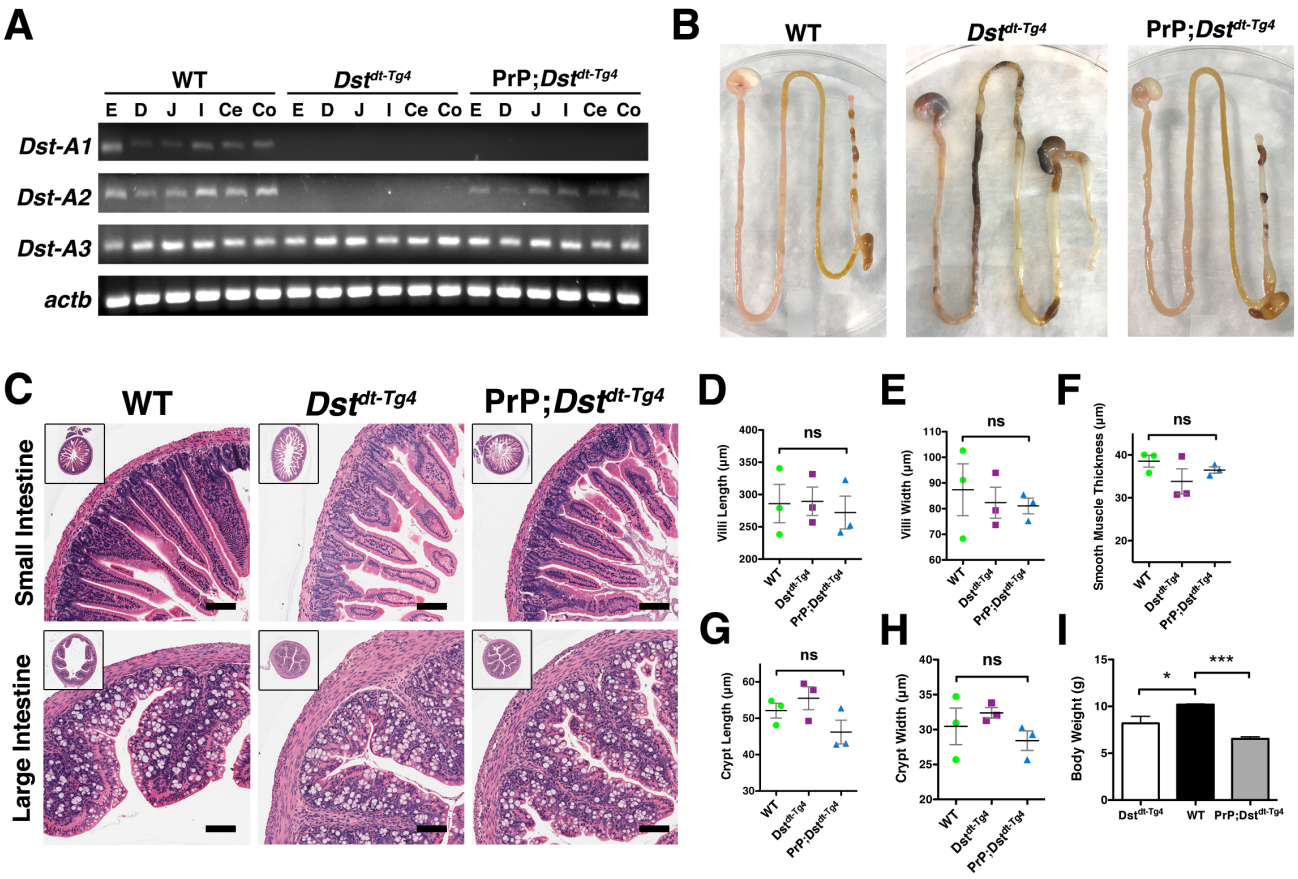


**Figure S2.** Gastrointestinal assessment of the *Dst*$^{dt\text{-}Tg4}$ allele, and the *PrP-Dst*$^{dt\text{-}Tg4}$ transgenic rescue mouse model. The *Dst*$^{dt\text{-}Tg4}$ mouse has disrupted expression of *Dst-a1* and *Dst-a2* isoforms but retains the *Dst-a3* isoform. The *PrP-Dst*$^{dt\text{-}Tg4}$ rescue mouse is the *Dst*$^{dt\text{-}Tg4}$ mouse exogenously expressing *Dst-a2*. By RT-PCR analysis in **A)** we can see that *Dst*$^{dt\text{-}Tg4}$ mice lack *Dst-a1* and *-a2* expression in the gut, while *PrP-Dst*$^{dt\text{-}Tg4}$ mice exhibit expression of *Dst-a2* though at much lower levels than wild type. Both *Dst*$^{dt\text{-}Tg4}$ and *PrP-Dst*$^{dt\text{-}Tg4}$ mice however appear to express *Dst-a3* at levels similar to wild type. Actin (*actb*) serves as a loading control. **B)** Gross morphology in P15 *Dst*$^{dt\text{-}Tg4}$ mice is highly similar to what we see in the *Dst*$^{dt\text{-}27J}$ allele (gas accumulation and discoloration). *PrP-Dst*$^{dt\text{-}Tg4}$ mice however do not show these abnormalities to the same extent, and appear much more similar to wild type. **C)** Hematoxylin and eosin staining of small intestine (duodenum), and large intestine (colon) cross-sections from

P15 wild type, *Dst*$^{dt\text{-}Tg4}$, and *PrP-Dst*$^{dt\text{-}Tg4}$ mice. Quantifications of villi length **(D)**, villi width **(E)**, smooth muscle thickness **(F)**, crypt length **(G)**, and crypt width **(H)** as measured from the cross-section micrographs (n = 4; scale bar = 100 μm; ns - *P*-value > 0.05, statistical analysis by two-tailed Student's *t*-test). **I)** *Dst*$^{dt\text{-}Tg4}$ and *PrP-Dst*$^{dt\text{-}Tg4}$ mice have significantly reduced body weights compared to wild type (* - *P*-value < 0.05, *** - *P*-value < 0.001; graphical data represented as mean ± SEM, statistical analysis by two-tailed Student's *t*-test).

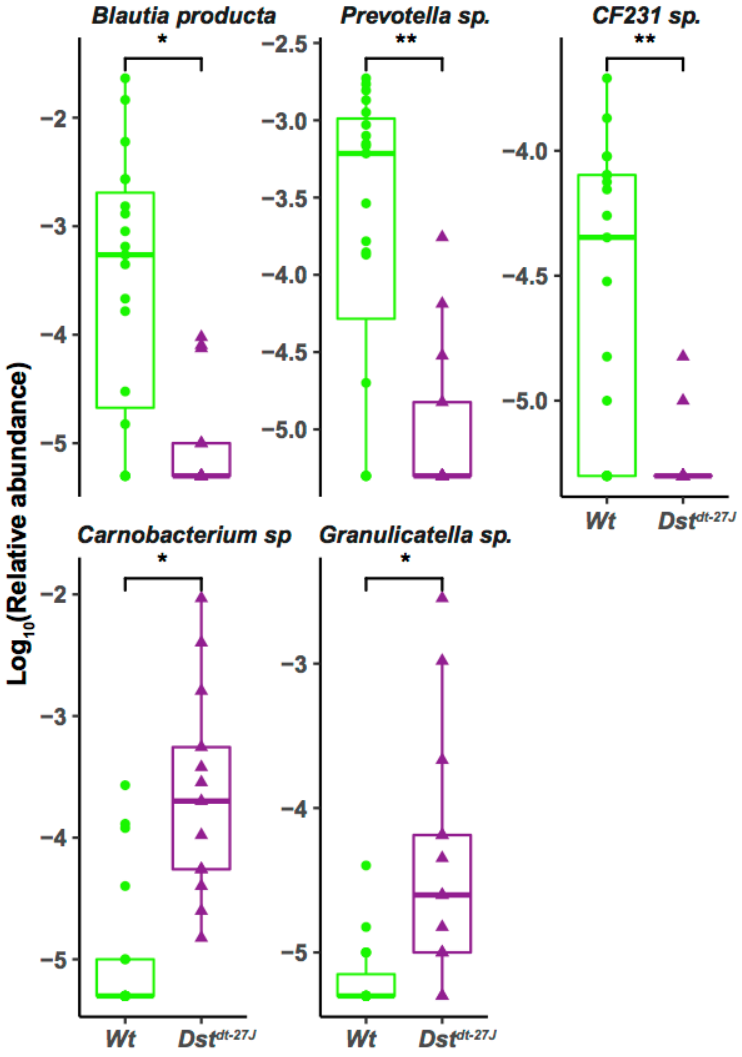


**Figure S5.3** Selected differentially abundant genera between wild type and *Dst*$^{dt\text{-}27J}$ mice. Wild type mice are denoted by green circles and *Dst*$^{dt\text{-}27J}$ by purple triangles in all panels. Boxplots represent in interquartile range with the line representing the median. Pseudocounts equal to a single read were added to zero values to allow for $Log_{10}$ plotting. Statistical significance denoted by asterisks (* - P-value < 0.05; ** - P-value < 0.01; *** - P-value < 0.001).

**Supplemental Table 5.1 Factors impacting mouse microbiota clustering.**

| | Bray-Curtis | | Weighted Unifrac | | Unweighted Unifrac | |
|---|---|---|---|---|---|---|
| **Covariate** | **R2** | **P-value** | **R2** | **P-value** | **R2** | **P-value** |
| **Genotype** | 0.0629 | 0.008 | 0.0510 | 0.104 | 0.0787 | 0.001 |
| **Breeding pair** | 0.1318 | 0.001 | 0.0723 | 0.199 | 0.1185 | 0.001 |
| **Litter mate** | 0.2600 | 0.001 | 0.2822 | 0.023 | 0.2332 | 0.001 |
| **Residuals** | 0.5463 | NA | 0.5939 | NA | 0.5697 | NA |

**Supplemental Table 5.2 Taxa identified as being differentially abundant between the mouse genotypes after controlling for breeding pair and littermate**

| Feature | Increased group | Coefficient | # of samples | # of non-zero samples | P-value | Q-value |
|---|---|---|---|---|---|---|
| Bacteria_k; Bacteroidetes_p; Bacteroidia_c; Bacteroidales_o; Paraprevotellaceae_f; Undefined_g | Wild type mice | 0.018379957 | 32 | 17 | 2.40E-06 | 4.00E-03 |
| Bacteria_k; Bacteroidetes_p; Bacteroidia_c; Bacteroidales_o; Paraprevotellaceae_f; Undefined_g; Undefined_s | Wild type mice | 0.018379957 | 32 | 17 | 2.40E-06 | 4.00E-03 |
| Bacteria_k; Firmicutes_p; Bacilli_c; Bacillales_o; Thermoactinomycetaceae_f | Wild type mice | 0.023134154 | 32 | 17 | 7.62E-06 | 4.00E-03 |
| Bacteria_k; Firmicutes_p; Bacilli_c; Bacillales_o; Thermoactinomycetaceae_f; Undefined_g | Wild type mice | 0.023134154 | 32 | 17 | 7.62E-06 | 4.00E-03 |
| Bacteria_k; Firmicutes_p; Bacilli_c; Bacillales_o; Thermoactinomycetaceae_f; Undefined_g; Undefined_s | Wild type mice | 0.023134154 | 32 | 17 | 7.62E-06 | 4.00E-03 |
| Bacteria_k; Bacteroidetes_p; Bacteroidia_c; Bacteroidales_o; Paraprevotellaceae_f; CF231_g | Wild type mice | 0.006184728 | 32 | 16 | 9.11E-06 | 4.00E-03 |
| Bacteria_k; Bacteroidetes_p; Bacteroidia_c; Bacteroidales_o; Paraprevotellaceae_f; CF231_g; Undefined_s | Wild type mice | 0.006184728 | 32 | 16 | 9.11E-06 | 4.00E-03 |
| Bacteria_k; Bacteroidetes_p; Bacteroidia_c; Bacteroidales_o; Paraprevotellaceae_f | Wild type mice | 0.018402137 | 32 | 20 | 1.25E-05 | 4.66E-03 |
| Bacteria_k; Bacteroidetes_p; Bacteroidia_c; Bacteroidales_o; Prevotellaceae_f; Prevotella_g; Undefined_s | Wild type mice | 0.021839293 | 32 | 21 | 1.32E-05 | 4.66E-03 |
| Bacteria_k; Bacteroidetes_p; Bacteroidia_c; Bacteroidales_o; Prevotellaceae_f | Wild type mice | 0.02132555 | 32 | 26 | 2.14E-05 | 5.74E-03 |
| Bacteria_k; Bacteroidetes_p; Bacteroidia_c; Bacteroidales_o; Prevotellaceae_f; Prevotella_g | Wild type mice | 0.020600555 | 32 | 23 | 4.67E-05 | 8.17E-03 |
| Bacteria_k; Bacteroidetes_p; Bacteroidia_c; Bacteroidales_o; Rikenellaceae_f; AF12_g | Wild type mice | 0.059176818 | 32 | 25 | 9.80E-05 | 1.23E-02 |
| Bacteria_k; Bacteroidetes_p; Bacteroidia_c; Bacteroidales_o; Rikenellaceae_f; AF12_g; Undefined_s | Wild type mice | 0.059176818 | 32 | 25 | 9.80E-05 | 1.23E-02 |
| Bacteria_k; Firmicutes_p; Bacilli_c; Bacillales_o; Bacillaceae_f; Oceanobacillus_g | *Dst*$^{dt\text{-}27J}$ mice | -0.002264282 | 32 | 11 | 1.43E-04 | 1.46E-02 |
| Bacteria_k; Firmicutes_p; Clostridia_c; Clostridiales_o; Lachnospiraceae_f; Blautia_g; producta_s | Wild type mice | 0.02022176 | 32 | 22 | 1.69E-04 | 1.46E-02 |
| Bacteria_k; Firmicutes_p; Bacilli_c; Lactobacillales_o; Undefined_f | *Dst*$^{dt\text{-}27J}$ mice | -0.003247455 | 32 | 15 | 2.88E-04 | 2.02E-02 |
| Bacteria_k; Firmicutes_p; Bacilli_c; Lactobacillales_o; Undefined_f; Undefined_g | *Dst*$^{dt\text{-}27J}$ mice | -0.003247455 | 32 | 15 | 2.88E-04 | 2.02E-02 |
| Bacteria_k; Firmicutes_p; Bacilli_c; Lactobacillales_o; Undefined_f; Undefined_g; Undefined_s | *Dst*$^{dt\text{-}27J}$ mice | -0.003247455 | 32 | 15 | 2.88E-04 | 2.02E-02 |
| Bacteria_k; Firmicutes_p; Bacilli_c; | *Dst*$^{dt\text{-}27J}$ mice | - | 32 | 20 | 3.47E- | 2.28E- |

| Feature | Increased group | Coefficient | # of samples | # of non-zero samples | P-value | Q-value |
|---|---|---|---|---|---|---|
| Lactobacillales_o; Carnobacteriaceae_f; Carnobacterium_g | | 0.008583114 | | | 04 | 02 |
| Bacteria_k; Firmicutes_p; Bacilli_c; Lactobacillales_o; Carnobacteriaceae_f; Carnobacterium_g; Undefined_s | *Dst*$^{dt\text{-}27J}$ mice | -0.008583114 | 32 | 20 | 3.47E-04 | 2.28E-02 |
| Bacteria_k; Firmicutes_p; Bacilli_c; Lactobacillales_o; Carnobacteriaceae_f; Granulicatella_g | *Dst*$^{dt\text{-}27J}$ mice | -0.003299845 | 32 | 20 | 3.70E-04 | 2.28E-02 |
| Bacteria_k; Firmicutes_p; Bacilli_c; Lactobacillales_o; Carnobacteriaceae_f; Granulicatella_g; Undefined_s | *Dst*$^{dt\text{-}27J}$ mice | -0.003299845 | 32 | 20 | 3.70E-04 | 2.28E-02 |
| Bacteria_k; Firmicutes_p; Bacilli_c; Bacillales_o; Bacillaceae_f; Oceanobacillus_g; oncorhynchi_s | *Dst*$^{dt\text{-}27J}$ mice | -0.001730234 | 32 | 10 | 3.82E-04 | 2.31E-02 |
| Bacteria_k; Firmicutes_p; Bacilli_c; Lactobacillales_o; Enterococcaceae_f; Vagococcus_g | *Dst*$^{dt\text{-}27J}$ mice | -0.001488214 | 32 | 8 | 7.43E-04 | 3.37E-02 |
| Bacteria_k; Firmicutes_p; Bacilli_c; Lactobacillales_o; Enterococcaceae_f; Vagococcus_g; Undefined_s | *Dst*$^{dt\text{-}27J}$ mice | -0.001488214 | 32 | 8 | 7.43E-04 | 3.37E-02 |

*Note: only significant taxa listed

# Chapter 6:

# General Discussion

**The emergence of HSAN-VI**

The human dystonin gene (*DST*, also known as bullous pemphigoid antigen 1 - *BPAG1*) consists of 496 kb located on the short arm of chromosome 6. The *DST* gene is fairly complex in that various tissue-specific promoters yield epithelial (dystonin-e/BPAG1e), neuronal (dystonin-a/BPAG1a), and muscle (dystonin-b/BPAG1b) specific isoforms, while alternative splicing of the neuronal and muscle isoforms further produce 3 unique proteins termed dystonin-a1/b1, dystonin-a2/b2, and dystonin-a3/b3 (Leung et al., 2001). As the dystonin proteins belong to the spectraplakin family of proteins (Suozzi et al., 2012; Kunzli et al., 2016), they function as cytoskeletal linkers responsible for maintaining structural integrity and mediating processes like intracellular trafficking (De Repentigny et al., 2003; Liu et al., 2003; Ryan et al., 2012b). Considering the large size of the human *DST* gene, it should be susceptible to mutations over time, which would eventually manifest to some observable phenotype. However, up until recently, the complete lack of any reported human cases had suggested that all *DST* mutations were likely embryonic lethal.

In 2004, the first instance of a *DST* gene disruption associated with a disease phenotype was described in a female child with a 6;15 chromosomal translocation (Giorda et al., 2004). The breakage point occurred toward the 3' end of *DST*, and was predicted to affect only dystonin-a and dystonin-b isoforms. The patient presented with esophageal atresia, and through development she would exhibit severe motor and mental retardation, non-progressive encephalopathy, and delayed visual maturation. Her second chromosome 6 however, was unaffected by the translocation and would still express full-length dystonin-a and dystonin-b transcripts. In an attempt to explain her clinical presentation, it was suggested that either

haploinsufficiency of *DST* was enough to cause pathology, or that truncated dystonin-a/b interrupted function of the full-length protein leading to manifestation of symptoms.

It was not until 2012 that the first homozygous mutations in the human *DST* gene were discovered to be associated with a severe phenotype that shared many features with a subset of genetic disorders termed Hereditary sensory and autonomic neuropathies (HSAN) (Axelrod, 2002; Axelrod and Gold-von Simson, 2007). Three infants from 2 consanguineous families from Ashkenazi Jewish background presented with dysautonomic symptoms, distal contractures, motionless open-mouthed facies, and severe psychomotor retardation (see Table 6.1 and 6.2) (Edvardson et al., 2012). Ultimately, all three patients would die around the age of two from cardio-pulmonary events, likely related to poor autonomic control. Also of note was that a second pregnancy for one of the families was aborted at 21 weeks due to signs of the same disease as its sibling. The underlying mutation in these patients was determined to be a frameshift occurring at Glu4955, which leads to the loss of 502 amino acids at the C-termini microtubule-binding domain. As this domain is common to all dystonin-a and dystonin-b splice variants, it effectively ablates expression of the predominant neural and muscle isoforms. Considering disease presentation shared many clinical features as HSAN-III (also named familial dysautonomia), though more severe, this newly identified disorder was termed HSAN-VI.

In 2017 we then learned that homozygous *DST* mutations do not exclusively produce a disease phenotype that is lethal in infancy, as two separate case studies would describe *DST* mutations in adolescent, and adult patients. Manganelli and colleagues identified three siblings from a non-consanguineous family from southern Italy as having two heterozygous compound mutations in the *DST* gene, which affected the expression of dystonin-a2 and -b2 isoforms (Manganelli et al., 2017). These patients exhibited impaired pain sensitivity and distal

ulcerations since infancy, weakness of intrinsic foot muscles, and a number of autonomic disturbances including heat intolerance, problems with sweating, pupillary abnormalities, chronic diarrhea, and sexual dysfunction (see Table 6.1 and 6.2). The second case report identifies a female patient with both skin and neuronal phenotype, which results from compound heterozygous mutations in *DST* affecting exon 7 (specific to dystonin-a1*,* and -a2), and exon 29 (common to dystonin-e, dystonin-a, and dystonin-b isoform) (Cappuccio et al., 2017). She presented with chronic diarrhea, iris heterochromia, bilateral cataracts, syringomyelia from D3-D8, bilateral sensorineural hearing loss, pain insensitivity, skin blistering, and behavioural problems such as avoidant/restrictive food intake disorder, obsessive compulsive disorder, and anxiety (see Table 6.1 and 6.2).

Most recently, in 2018 Fortugno and colleagues described three elderly siblings from an Italian family with biallelic *DST* mutations ablating dystonin-a2/b2 expression, also causing dystonin-a1/b1 and dystonin-a3/b3 haploinsufficiency (Fortugno et al., 2018). These patients recall experiencing dysautonomic symptoms in childhood, and between the ages of 20-40 they would present painless fractures, osteomyelitis, joint deformities, and diabetes mellitus type II (see Table 6.1 and 6.2).

It has only been over the last few years that we have observed the first human cases of *DST* mutation, leading to its classification as HSAN-VI, a lethal form of sensory neuropathy. Through the identification of adult patients with deleterious *DST* mutations, this definition would expand to categorize HSAN-VI as a spectrum disorder with severity being determined by which isoforms are affected. With a growing awareness of HSAN-VI, we can expect to observe the number of reported cases to increase in the coming years.

**Table 6.1 Genetic comparison of the various HSAN-VI patients**

| | Family Background | Mutation type | Exons | *DST* Isoforms Present | | | |
|---|---|---|---|---|---|---|---|
| | | | | ***DST-E*** | ***DST-A/B1*** | ***DST-A/B2*** | ***DST-A/B3*** |
| **Edvardson et al. (2012)** | Consanguineous Ashkenazi Jewish | Frameshift deletion: c.14865delA | 86 | + | - | - | - |
| **Manganelli et al. (2017)** | Non-Consanguineous southern Italian | Compound heterozygote: 1)c.687+1G>A 2) c.616C>T | 4 & 5 | + | + | - | + |
| **Cappuccio et al. (2017)** | Non-consanguineous | Compound heterozygote: 1)c.806C>T, 2)c.3886A>G | 7 & 29 | +/- | - | - | +/- |
| **Fortugno et al. (2018)** | Non-consanguineous Italian | Compound heterozygote: 1)c.608C>A 2)c.12988A>T | 4 & 70 | + | +/- | - | +/- |

+/- : haploinsufficient

**Table 6.2 Symptom comparison of the various HSAN-VI patients**

| | | Sex | Skin Defects | Bone/Joint Defects | Neurologic Symptoms | Dysautonomic Symptoms | Other | Cause of Death | Age of Onset |
|---|---|---|---|---|---|---|---|---|---|
| **Edvardson et al (2012)** | patient 1 | F | | | | | | cardio-pulmonary arrest | |
| | patient 2 | M | blotching | distal contractures | severe psychomotor retardation, absent deep tendon reflex | absent tearing, feeding and breathing difficulties | motionless, open mouth facies; early death (<2 y/o) | severe apneic episode | birth |
| | patient 3 | F | | | | | | cardio-pulmonary arrest | |
| | fetus 1 | N/A | N/A | bilateral club feet & hand clenching | N/A | N/A | aborted | N/A | N/A |
| **Manganelli et al (2017)** | patient 4 | M | | joint deformities, distal amputations | | hypohidrosis & heat intolerance, chronic diarrhea | | | |
| | patient 5 | M | distal ulcers | joint deformities, distal amputations | pain insensitivity, impaired touch & vibration sensitivity, altered deep tendon reflex | hypohidrosis & heat intolerance, chronic diarrhea, pupillary abnormalities, erectile dysfunction | weakness in intrinsic foot muscles | N/A | infancy |
| | patient 6 | M | | distal amputations | | hypohidrosis & heat intolerance, chronic diarrhea, pupillary abnormalities | | | |

| | | | | | | | | | |
|---|---|---|---|---|---|---|---|---|---|
| **Cappuccio et al (2017)** | patient 7 | F | recurrent blistering, peeling, ulcers, atrophic scars | osteoporosis | bilateral sensorineural hearing loss, pain insensitivity, headaches, behavioural disorders | chronic diarrhea, abdominal pain | iris heterochromia, cataract, syringomelia | N/A | 4 months |
| | patient 8 | M | | painless fractures, recurrent septic osteoarthritis, joint deformities, toe amputations | severe pain insensitivity, symmetric sensorineural hearing loss, altered deep tendon reflex | hyperhidrosis & heat intolerance, pupillary abnormalities, urinary incontinence | | | 37 y/o |
| **Fortugno et al (2018)** | patient 9 | M | ulcers | painless fractures, recurrent septic osteoarthritis, joint deformities, toe amputations | altered deep tendon reflex, reduced pain sensation | N/R | type II diabetes, general muscle weakness | N/A | N/R |
| | patient 10 | F | | painless bone fractures, osteomyelitis, toe amputations | severe pain insensitivity, altered deep tendon reflex | hypohidrosis & heat intolerance, xerophthalmia, xerostomia, vaginal dryness | | | child-hood |

N/R: not reported;
N/A: not applicable

**Discovery of neuronal dystonin isoforms**

Before the identification of the human disease HSAN-VI (Edvardson et al., 2012), the dystonin gene and its resulting protein had long since been studied in a murine model known as the *dystonia musculorum* (*Dst*$^{dt}$) mouse (Duchen et al., 1963, 1964; Duchen, 1976; Kothary et al., 1988; Brown et al., 1995b). In 1963, the *Dst*$^{dt}$ mouse that arose by spontaneous mutation was first described by Duchen and colleagues (Duchen et al., 1963, 1964). Severe ataxia and dystonic postures were the major phenotypic characteristics, which were also associated with significant sensory neuron degeneration. Although the underlying genetic mutation was not identified, the disease was predicted to be a result of autosomal recessive mutation. In 1995, two separate lines of work led to the identification of the *BPAG1*/*Dst* gene as causative for the *Dst*$^{dt}$ disease (Brown et al., 1995b; Guo et al., 1995). While studying the hemidesmosomal skin protein Bullous pemphigoid antigen 1 (BPAG1), generation of a BPAG1 knockout mouse unexpectedly produced the ataxic and dystonic phenotype associated with the *Dst*$^{dt}$ mouse (Guo et al., 1995). In parallel, definitive evidence came from cloning experiments identifying the gene that was disrupted by the insertion of an *hsp68-LacZ* transgene, which resulted in mice bearing the *Dst*$^{dt}$ phenotype (Kothary et al., 1988; Brown et al., 1995b). It was thus determined that the gene responsible for producing the BPAG1 skin protein was also responsible for producing the neuronal dystonin protein underlying *Dst*$^{dt}$ pathology.

Subsequent studies would later propose splice-variants of neuronal dystonin that were predicted to interact with intermediate filaments (termed BPAG1n), much like how the epithelial isoform dystonin-e interacts with keratin filaments in skin. It was hypothesized that loss of these BPAG1n isoforms was responsible for the neurological phenotype of the *Dst*$^{dt}$ mice (Yang et al., 1996). However, in 2001, a study evaluating BPAG1 isoform expression in mice found that

BPAG1n mRNA went completely undetected in neural tissue (Leung et al., 2001). This led to the discovery of the larger, more prominently expressed neuronal and muscle isoforms: dystonin-a and dystonin-b, respectively.

In the years to come, the neuronal and muscle specific splice variants would also be identified (see Table 6.3 for isoform summary). Elucidating the roles of the neuronal specific splice variants would become the focus, considering sensory neurons are the major cell type affected in *Dst*$^{dt}$ mice. However, the major challenge of studying dystonin and its various isoforms lies in the fact that the protein is remarkably large (dystonin-a = 615 kDa, dystonin-b = 834 kDa) and shares high amino acid sequence similarity between isoforms (Leung et al., 2001; Pool et al., 2005; Ferrier et al., 2013). This has made the development of Dst antibodies an incredibly arduous task, and as such there are currently no reliable isoform-specific antibodies available. Much of what we have learned about the functions of the individual isoforms has come from *in vitro* experiments utilizing siRNA knockdowns and fusion protein constructs, as well as *in vivo* examination of the *Dst*$^{dt}$ alleles that differ in the nature of their mutations and thus in the isoforms affected.

**What the *Dst*$^{dt}$ alleles can tell us about HSAN-VI heterogeneity**

By comparing the *DST* mutations identified in the individuals with HSAN-VI, the commonality amongst the cases is that dystonin-a2 is absent. From what we know through studies on *Dst*$^{dt}$ mice and through knockdown experiments on immortalized cells, dystonin-a2 is the most crucial isoform for neuronal functioning as its loss is associated with the most profound and lasting defects to intracellular pathways (Young and Kothary, 2008; Ryan et al., 2012b; Ryan et al., 2012c; Ferrier et al., 2013). We have also observed a moderate rescuing effect when

dystonin-a2 is partially restored to neurons in *Dst*$^{dt\text{-}Tg4}$ mice, which lack both dystonin-a1 and -a2. These mice have significantly longer lifespans, and show improvements in many pathways that are normally defective in *Dst*$^{dt\text{-}Tg4}$ mice (Ferrier et al., 2014). The results provided by *Dst*$^{dt}$ mouse experiments strongly suggest that dystonin-a2 is the major determinant for disease. Supportive evidence for this comes from the patients described by Manganelli and colleagues (Manganelli et al., 2017). The affected siblings have a milder form of HSAN-VI that continues into adulthood, and is associated with mutations impacting only the neuronal dystonin-a2 isoform (dystonin-b2 likely also affected, though muscle defects are not primary disease features). It therefore seems highly likely that disrupted expression of dystonin-a2 is both necessary, and sufficient to produce HSAN-VI. However, mutations affecting only dystonin-a1, or dystonin-a3 have not been described in humans or in *Dst*$^{dt}$ mouse models, and we therefore do not know to what extent these isoforms contribute to disease etiology. It may be that mutations in either of these isoforms do not result in any major clinical pathology, which could explain the absence in reported cases. Additionally, isoform compensation may be a mechanism that could be involved in masking these mutations, as we recently observed this phenomenon in *Dst*$^{dt\text{-}Tg4}$ mice (Chapter 3). As these mice retain dystonin-a3, we saw a significant upregulation of this isoform in neural tissues most affected by dystonin loss-of-function. This upregulation was associated with maintenance of microtubule stability in sensory neurons (a function previously unknown to this isoform), which was reversed upon loss of transcript overexpression (Lynch-Godrei et al., 2018). This pattern of upregulation is consistent with dystonin-a3 compensating for the loss of dystonin-a1 and -a2. Thus, it is reasonable to believe that each of the dystonin-a isoforms possesses the ability to modify its normal function and substitute for an absent or non-

functional isoform. Nevertheless, future work involving isoform specific knockouts is still needed to conclusively determine the role of each isoform in HSAN-VI pathogenesis.

Seeing as *DST* mutations can result in a milder form of HSAN-VI expanding into adulthood, HSAN-VI should be recognized as a spectrum disorder whereby severity of disease may be predicted based on the isoforms affected. Of interest, $Dst^{dt\text{-}27J}$ mice, which are completely null for all neuronal isoforms of dystonin, present with the most severe phenotype (ataxic affecting all limbs and dystonic postures) and have the shortest lifespan (Lynch-Godrei et al., 2018). This $Dst^{dt\text{-}27J}$ allele would most closely resemble the first group of very severe HSAN-VI patients identified by Edvardson and colleagues (Edvardson et al., 2012). The adolescent female described by Cappuccio and colleagues may be the most severe amongst the adult HSAN-VI patients (Cappuccio et al., 2017). Her genotype would most resemble $Dst^{dt\text{-}Tg4}$, or $Dst^{Gt(E182H05)Wrst}$ alleles as she lacks both dystonin-a1 and -a2 (Pool et al., 2005; Horie et al., 2014), but is haploinsufficient for dystonin-a3. Though her symptoms are not identical to the other adult HSAN-VI patients, her younger age may indicate that these symptoms have yet to develop. She does however have a number of unique symptoms including iris heterochromia, cataracts, syringomyelia from D3-D8, osteoporosis, headaches, and behavioral problems (anxiety, obsessive compulsive disorder, and avoidant/restrictive food intake disorder), suggesting the potential for dystonin-a1 and -a2. Retention of the dystonin-a3 isoform might also contribute to her longer lifespan compared to the dystonin-a null infants. She also experienced skin blistering, which was hypothesized to be a result of dystonin-e haploinsufficiency. However, considering the presence of skin ulceration and a lack of dystonin-e isoform involvement in the other adult HSAN-VI patients, it is likely that her skin blisters are a result of peripheral neuropathy leading to skin damage going unnoticed. Furthermore, heterozygous

*Dst*$^{tm1EFu}$ mice (dystonin knockouts) do not display skin symptoms and have intact hemidesmosomes at the dermo-epidermal junction (Guo et al., 1995). Thus far, the group of patients described by Manganelli and colleagues likely represent the mildest form of HSAN-VI as they only have dystonin-a2/b2 isoforms affected. With coming age, HSAN-VI patients may develop new symptoms indicating novel roles of dystonin isoforms that would never have been characterized in *Dst*$^{dt}$ mice due to limitations such as short lifespan and objective measures. As more individuals with *DST* mutations are identified, and as we continue our investigation of affected tissues and mechanisms in *Dst*$^{dt}$ mice, we hope to gain a better understanding of how each isoform contributes to disease.

**Table 6.3 Major isoforms of dystonin**

| | Tissue | | |
|---|---|---|---|
| | **Skin** | **Neuron** | **Muscle** |
| **Major isoforms** | dystonin-e/BPAG1e | dystonin-a1/BPAG1a1, dystonin-a2, BPAG1a2, dystonin-a3/BPAG1a3 | dystonin-b1BPAG1b1, dystonin-b2/BPAG1b2, dystonin-b3/BPAG1b3 |

## Conclusions

With the recent identification of adult patients with deleterious *DST* mutations, it has become clear that HSAN-VI can present on a spectrum based on which neuronal dystonin isoforms are impacted. Current evidence indicates that dystonin-a2 is the most important factor dictating development of HSAN-VI. Though to further advance our knowledge of what roles the other neuronal dystonin isoforms play in the development of HSAN-VI, if any, dystonin-a1 and -a3 should be independently assessed. As isoform compensation is a mechanism that potentially modulates disease presentation, expression levels of remaining isoforms should also be evaluated. Though many HSAN-VI symptoms have been accurately predicted by $Dst^{dt}$ mice, the short lifespan of these mice is a major limitation for addressing how dystonin loss-of-function impacts adult HSAN-VI patients. Also, considering the diverse expression pattern of dystonin-a across tissues, this suggests there are many more roles for the dystonin isoforms that have yet to be characterized. Further evaluation of these HSAN-VI patients, and identification of novel *DST* mutations will be pivotal in our understanding of the biological roles of the dystonin-a isoforms and how they relate to pathogenesis.

# Appendix

## A.1 Cytoskeletal Linker Protein Dystonin Is Not Critical to Terminal Oligodendrocyte Differentiation or CNS Myelination

Samantha F. Kornfeld[1,2,#], Anisha Lynch-Godrei[1,2,#], Sawyer R. Bonin[1], Sabrina Gibeault[1], Yves De Repentigny[1], Rashmi Kothary[1,2,3,4,*]

[1] Regenerative Medicine Program, Ottawa Hospital Research Institute, Ottawa, Canada, K1H 8L6;

[2] Department of Cellular and Molecular Medicine, Faculty of Medicine, University of Ottawa, Ottawa, Canada, K1H 8M5;

[3] Department of Medicine, University of Ottawa, Ottawa, Canada, K1H 8M5;

[4] Centre for Neuromuscular Disease, University of Ottawa, Canada, K1H 8M5

*To whom correspondence should be addressed at: Ottawa Hospital, 501 Smyth Road, ORCC 4406a, Ottawa, Ontario, K1H 8L6, Canada; Tel: (613) 737-8707; Fax: (613) 737-8803; Email: rkothary@ohri.ca

[#] These authors contributed equally to this work

***Published in PLoS One, 11(2): e0149201***

**Author Contributions**

Conceived and designed the experiments: SFK, ALG, RK. Performed the experiments: SFK, ALG, SRB, SG, YDR. Analyzed the data: SFK, ALG, SRB. Contributed reagents/materials/analysis tools: SFK, ALG, SRB, SG, YDR, RK. Wrote the paper: SFK, RK.

**Abstract**

Oligodendrocyte differentiation and central nervous system myelination require massive reorganization of the oligodendrocyte cytoskeleton. Loss of specific actin- and tubulin-organizing factors can lead to impaired morphological and/or molecular differentiation of oligodendrocytes, resulting in a subsequent loss of myelination. Dystonin is a cytoskeletal linker protein with both actin- and tubulin-binding domains. Loss of function of this protein results in a sensory neuropathy called Hereditary Sensory and Autonomic Neuropathy type VI in humans and *dystonia musculorum* in mice. This disease presents with severe ataxia, dystonic muscle and is ultimately fatal early in life. While loss of the neuronal isoforms of dystonin primarily leads to sensory neuron degeneration, it has also been shown that peripheral myelination is compromised due to intrinsic Schwann cell differentiation abnormalities. The role of this cytoskeletal linker in oligodendrocytes, however, remains unclear. We sought to determine the effects of the loss of neuronal dystonin on oligodendrocyte differentiation and central myelination. To address this, primary oligodendrocytes were isolated from a severe model of dystonia musculorum, $Dst^{dt\text{-}27J}$, and assessed for morphological and molecular differentiation capacity. No defects could be discerned in the differentiation of $Dst^{dt\text{-}27J}$ oligodendrocytes relative to oligodendrocytes from wild-type littermates. Survival was also compared between $Dst^{dt\text{-}27J}$ and wild-type oligodendrocytes, revealing no significant difference. Using a recently developed migration assay, we further analyzed the ability of primary oligodendrocyte progenitor cell motility, and found that $Dst^{dt\text{-}27J}$ oligodendrocyte progenitor cells were able to migrate normally. Finally, *in vivo* analysis of oligodendrocyte myelination was done in phenotype-stage optic nerve, cerebral cortex and spinal cord. The density of myelinated axons and g-ratios of $Dst^{dt\text{-}27J}$ optic nerves was normal, as was myelin basic protein expression in both cerebral cortex and spinal cord. Together

these data suggest that, unlike Schwann cells, oligodendrocytes do not have an intrinsic requirement for neuronal dystonin for differentiation and myelination.

## Introduction

Oligodendrocytes (OLs), the myelinating cells of the central nervous system (CNS), undergo complex morphological and molecular changes during differentiation and myelination. As oligodendrocyte progenitor cells (OPCs), they are migratory, mitotic cells with a relatively simple morphology. Upon interaction with appropriate environmental signals, OPCs exit the cell cycle and initiate differentiation to become increasingly branched, non-migratory, post-mitotic OLs. OL branches are able to contact and wrap their membrane around axons to produce the compact myelin necessary for saltatory conduction and trophic and metabolic axonal support (Nave, 2010; Lee et al., 2012; Simons et al., 2014). Contrary to the myelinating Schwann cells of the peripheral nervous system (PNS), which myelinate axons in a 1:1 ratio, a single oligodendrocyte can contact and myelinate many axons simultaneously (Pfeiffer et al., 1993; Poliak and Peles, 2003).

Requirements for the transition from OPC to OL are numerous and include both cell intrinsic and extrinsic factors. A major outcome of the initiation of differentiation is massive reorganization of the cytoskeleton into a progressively ramified arrangement. In OLs, this means promoting and maintaining the organization of microfilaments and microtubules, as intermediate filaments are absent from these cells (Baumann and Pham-Dinh, 2001; Bauer et al., 2009). Initial membrane protrusions are instigated by microfilament growth to form filopodia, which then expand to form thicker, microfilament- and microtubule-rich lamellipodia (Bauer et al., 2009). Multiple actin- and tubulin-organizing factors are necessary and essential to OL differentiation. A loss of OL morphological complexity is observed in the absence of actin-organizing factors Wiscott-Aldrich syndrome protein (N-WASP), WASP family verprolin-homologous protein 1 (WAVE1), focal adhesion kinase (FAK) and integrin-linked kinase (ILK) (Kim et al., 2006;

Bacon et al., 2007; Forrest et al., 2009; O'Meara et al., 2013), as well as tubulin-organizing factors tubulin polymerization promoting protein (TPPP/p25), 2',3'-cyclic-nucleotide 3'-phosphodiesterase (CNPase), Fyn kinase and tau (Klein et al., 2002; Lee et al., 2005; Lehotzky et al., 2010), amongst others. As morphological differentiation is a requirement for successful myelination to occur, it is clear that the capacity of an OL for cytoskeletal reorganization is critical to CNS function and health.

One cytoskeleton-organizing factor with an unclear role in OLs is the large cytoskeletal linker protein dystonin (Dst), which is a member of the plakin family (Ferrier et al., 2013). Tissue-specific isoforms of Dst are found in neural, muscle and epithelial compartments (Sawamura et al., 1991; Brown et al., 1995a; Leung et al., 2001; Okumura et al., 2002). *Dst* in neural tissue can be alternatively spliced to give rise to the three neuronal transcripts, Dst-a1, -a2 and -a3. The proteins encoded by these transcripts differ only in their N-terminal regions, which localize them regionally within the cell (Ferrier et al., 2013). In common between the neuronal isoforms are both an actin-binding and a microtubule-binding domain, conferring their function as cytoskeletal linkers (Leung et al., 2001; Ryan et al., 2012b). Loss of dystonin results in ultimately fatal peripheral neuropathies, namely hereditary sensory and autonomic neuropathy type VI (HSAN-VI) in humans and *dystonia musculorum* ($Dst^{dt}$) in mice, characterized by ataxia, dystonic muscle and sensory neuron degeneration (Brown et al., 1995b; Edvardson et al., 2012).

While pathology of sensory neurons is the major contributor to $Dst^{dt}$ pathogenesis, investigation has also been undertaken to assess the effects of neuronal *Dst* loss in myelinating glial cells. Two models of $Dst^{dt}$, $Dst^{dt\text{-}Tg4}$ (lacking Dst-a1 and -a2) and $Dst^{dt\text{-}27J}$ (lacking all neuronal isoforms), have peripheral myelination abnormalities that were attributable to intrinsic differentiation defects in Schwann cells (Bernier et al., 1998). Subsequently, CNS myelination

was explored in $Dst^{dt\text{-}Tg4}$ animals through analysis of optic nerve and spinal cord, and it was suggested that OLs are unable to myelinate normally in the absence of Dst (Saulnier et al., 2002); however, tools for comprehensive analysis of the character of these OLs were lacking at the time, leaving conclusions about the intrinsic role of neuronal Dst in OL differentiation and myelination somewhat ambiguous.

Here, we take advantage of a recently developed method for primary culture of mouse OLs (O'Meara et al., 2011b), as well as an assay to measure OL migratory capacity (O'Meara et al., 2016) to characterize the morphological and molecular differentiation of OLs from the more severe $Dst^{dt\text{-}27J}$ model of $Dst^{dt}$, which lacks all neuronal *Dst* isoforms. While we show that both OPCs and OLs do express all three neuronal isoforms of *Dst* endogenously, OLs isolated from $Dst^{dt\text{-}27J}$ animals do not show a deficiency in morphological or molecular maturity in vitro. Survival is not compromised in OLs lacking *Dst*, and OPC migration is unaffected. Further, contrary to previous observations made in the less severe $Dst^{dt\text{-}Tg4}$ model, we found no defects in myelin sheath thickness or MBP expression *in vivo*. Taken together, our *in vitro* and *in vivo* findings suggest that OLs do not possess a critical requirement for Dst in differentiation and myelination.

## Materials and Methods

### Animals

For qRT-PCR experiments, wild type Sprague-Dawley rats were obtained from Charles River. The mutant mouse line *Dst*$^{dt\text{-}27J}$ was used for all other experiments. This line arose from a spontaneous mutation in the *Dst* allele, which confers phenotype in a recessive manner. The mutant animals were first identified at the Jackson Laboratory, and were then characterized as expressing very low levels of neuronal *Dst* transcript levels relative to wild-type animals (Pool et al., 2005). The animals were sacrificed at P0-P1 for primary OL cell culture and at P15 for *in vivo* analyses. Genotypes were determined by PCR amplification of genomic tail DNA. The University of Ottawa Animal Care Committee approved all experimental protocols. The protocols conformed to or exceeded those defined in the Canadian Council on Animal Care's Guide to the Care and Use of Experimental Animals, and the Animals for Research Act.

### Cell culture

Primary rat OPC and OL cultures were generated from P2 cerebral cortex tissue as described previously (Chen et al., 2007). In brief, cortices were dissociated with 0.01% trypsin (Sigma) in the presence of 10 μg /mL DNase (Sigma). Mixed glial cultures were plated in DMEM (Wisent) containing 20% fetal bovine serum, 2% Glutamax (Gibco) and 0.5% penicillin/streptomycin (Gibco) on poly-L-lysine (PLL) coated filter cap flasks for 10 days at 37°C and 5% $CO_2$. Flasks were then shaken overnight at 220 rpm, and medium containing suspended OPCs was removed from the flasks. Contaminating glial cells were removed from suspension by differential adhesion. To obtain proliferating OPC cultures, OPCs were plated in SATO medium with 2% Glutamax, 0.1% bovine serum albumin (Sigma), 50 μg/mL apo-

transferrin (Sigma), 5 μg/mL insulin (Sigma), 30 nM sodium selenite (Sigma), 10 nM D-biotin (Sigma) and 10 nM hydrocortisone (Sigma) supplemented with 10 ng/mL PDGF-AA (Millipore) and 10 ng/mL bFGF (Millipore). To obtain differentiating OL cultures, OPCs were plated in SATO medium as above but supplemented with 5 μg/mL N-acetyl-L-cysteine (Sigma), 15 nM triiodothyronine (Sigma) and 10 ng/mL ciliary neurotrophic factor (CNTF; AbD Serotec).

Primary mouse OL cultures were generated from P0 cerebral cortex tissue as described previously (O'Meara et al., 2011b). Briefly, cortices were dissociated with papain, and mixed glial cultures were plated in DMEM containing 10% fetal bovine serum, 1% Glutamax, 5 μg/mL insulin and 0.33% penicillin/streptomycin on PLL-coated filter cap flasks for 6 days at 37°C and 8.5% $CO_2$. Medium was further supplemented with 5 μg/mL insulin and cultures were kept at 5% $CO_2$ for an additional 3–4 days. Cultures were then shaken overnight at 220 rpm, and enriched for OPCs by differential adhesion. The OPCs were then plated in differentiating SATO medium with 0.5% fetal bovine serum, 1% Glutamax, 5 μg/mL insulin, 50 μg/mL holo-transferrin (Sigma), 50 ng/mL CNTF and 0.33% penicillin/streptomycin on coverslips dual-coated with PLL and laminin (LN2) and kept at 37°C and 5% $CO_2$.

OPC migration assay

OPC aggregates were collected and plated as described previously (O'Meara et al., 2016). In brief, following shaking of the mixed glial cultures, medium containing suspended OLs was filtered through 0.45 μm mesh. The mesh was then inverted, and a pipet was used to wash medium back through the mesh to dislodge isolated OPC aggregates. These were collected in a dish, and a dissection microscope was used to identify and remove single aggregates to be plated on LN2 coated coverslips. The aggregates were placed in conditioned mixed glial culture

medium (containing insulin) collected from flasks prior to shaking. Cells were left to migrate for 4 and 24 hours prior to fixation. For quantification, concentric circles were overlaid placing the original OPC aggregate at the center. Rings were set at 50 μm increments from the aggregate for migration at 4 hours, and at 100 μm increments for 24 hours migration.

qRT-PCR

RNA was isolated from ~1.5 x 105 primary rat OPCs and OLs using the RNeasy Mini Kit (Qiagen). Samples were collected from proliferating OPCs 4 hours post-seeding in proliferation medium, and from a mixed population of pre-myelinating and myelinating OLs on day 1.5 post-seeding in differentiation medium. Samples were reverse-transcribed with $RT^2$ First Strand cDNA synthesis kit (Qiagen) using 120 ng total RNA. Relative expression of each of the three neuronal *Dst* transcripts in proliferating OPCs and differentiation OLs was determined by qRT-PCR. Briefly, each 25 μL reaction contained 5–12 μL total cDNA, 12.5 μL SsoFast EvaGreen Supermix (Bio-Rad), either 0.2 μL 10 μM forward + reverse primers for *Dst-a1*, 1 μL 10 μM forward + reverse primers for *Dst-a2* and *-a3* transcripts or 0.2 μL 10 μM forward + reverse primers for actin transcripts, and RNase-free water. All samples were amplified using the following protocol: 3 min at 95°C, followed by 40 cycles of 95°C for 10 sec, 60°C for 10 sec and 72°C for 30 sec. Runs were amplified using a Bio-Rad CFX96 and analyzed using qBase+ software. For each primer set, 4–6 biological replicates were analyzed (n = 5–6, n = 1 animal) and samples were run in technical quadruplicates. Technical replicates were used for analysis only when Cq values differed by 0.25 or less. The following primers were used for amplification: *Dst-a1* forward CTA CAT GTA CGT GGA GGA GCA (779 bp), *Dst-a2* forward GAG GGC TGT GCT TCG GAT AG (741 bp), *Dst-a3* forward GTC TCC AAG GAT GCA CCT AGG

GAT, *Dst-a1/a2/a3* reverse CAT CGT TTG CAC CAA TGC C, actin forward CCG TCA GGC AGC TCA TAG CTC TTC, and β-actin (*actb*) reverse CTG AAC CCT AAG GCC AAC CGT. Bands for each transcript were visualized by running qRT-PCR products in a 1% agarose gel containing RedSafe™ nucleic acid staining solution.

Immunofluorescence

All samples were fixed in 3% paraformaldehyde. Cells were fixed for 15 min at room temperature, while OPC aggregates were fixed overnight at 4°C. Following fixation, coverslips were washed with PBS, permeabilized for 5 min in 0.1% Triton-X (Sigma), and blocked for 1 hour in 10% goat serum. Cells stained for F-actin were additionally blocked with 0.1% bovine serum albumin (BSA) for 30 min, and incubated with 1:50 rhodamine-phalloidin (Life Technologies) in 0.1% BSA for 45 min at room temperature. Samples were incubated with primary antibody in 10% goat serum overnight at 4°C, at the following concentrations: NG2 1:250 (EMD Millipore), MAG 1:50 (EMD Millipore), MBP 1:100 (AbD Serotec), Olig2 clone 211.F1.1 1:50 (EMD Millipore), and cleaved-caspase 3 (CC3) 1:100 (Cell Signaling). Cells were again washed with PBS, and then incubated with secondary antibodies (Alexa-555, Alexa-488, Alexa-647; Invitrogen) at 1:200 in 10% goat serum for 2 hours at room temperature. All samples were counterstained with Hoechst and mounted in Dako fluorescent mounting medium. For maturation marker and CC3 analyses, n = 3 for both WT and $Dst^{dt\text{-}27J}$. For quantification of cells undergoing caspase-mediated apoptosis, the proportion of CC3+/Olig2+ cells out of all Olig2+ cells was calculated, to avoid quantification of any contaminating cells. Quantification was done for 20–30 photographs taken at 20X magnification from at least two separate coverslips.

Morphological analysis

Sholl analysis was used to quantify branching complexity of DD3 OLs by overlaying concentric circles at 30 μm increments from the cell body using ImageJ. Branch intersections were counted at each ring. Cells used for Sholl analysis were co-stained for F-actin to visualize branches and Olig2 to confirm OL identity. For DD6 OLs, total membrane area was measured by tracing total cell outline using ImageJ. Cells used for quantification of membrane area were co-stained with MAG and MBP to visualize both non-compact and compact myelin membrane. For both Sholl and membrane area analyses, n = 3 for WT and $Dst^{dt\text{-}27J}$. Sholl analysis was conducted for 30 cells per n, and membrane area was measured for 60 cells per n. Cells were deemed membrane positive when they showed any MBP stained region in which branches were no longer discernible but instead were replaced by flattened membrane sheet of any size. Membrane negative cells showed no MBP staining and no membrane sheets. The presence or absence of membrane was quantified for n = 3 for WT and $Dst^{dt\text{-}27J}$. For each n, 20– 30 photographs taken at 20X magnification were analyzed from at least two separate coverslips.

Western blotting

Cerebral cortex and spinal cord samples were collected from P15 WT and $Dst^{dt\text{-}27J}$ animals and flash-frozen in liquid nitrogen. Tissue from one animal was considered 1 n, and a total of n = 6 was collected. Protein was isolated by gently homogenizing tissue in 1X RIPA lysis buffer (Sigma) on ice. The lysate was centrifuged at 4°C at high speed to remove insoluble material. Samples were separated by SDS-PAGE in a 15% gel. Membranes were incubated in 1:1000 CNPase (Abcam), 1:1000 MOG (Abcam), 1:1000 MBP (AbD Serotec) and 1:50,000 alpha-tubulin (Cell Signaling) primary antibodies overnight at 4°C in Odyssey blocking buffer

(Li-Cor Biosciences). Membranes were washed in 1X TBS, then incubated with secondary antibody (IRDye 680RD and 800CW; Li-Cor Biosciences) at 1:10,000 in Odyssey blocking buffer for 1 hour at room temperature. Membranes were visualized and bands quantified using the Li-Cor Odyssey CLx Infrared Imaging System.

Transmission Electron Microscopy (TEM)

P15 WT and *Dst*$^{dt\text{-}27J}$ mice were anesthetized by $CO_2$ and transcardially perfused with 5 mL of phosphate-buffered saline (PBS) followed by 10 mL of Karnovsky's fixative (4% paraformaldehyde, 2% glutaraldehyde and 0.1 M sodium cacodylate in phosphate-buffered saline, pH 7.4). Optic nerves were collected and fixed overnight at 4°C in the same fixative. Following fixation, 1 mm segments were cut transversely from the mid-point of each nerve. Segments were subsequently washed twice in 0.1 M sodium cacodylate buffer for 1 hour and again overnight at room temperature. Segments were post-fixed with 1% osmium tetroxide in 0.1 M sodium cacodylate buffer for 1 hour at room temperature. These were washed twice in distilled water for 5 min, and then dehydrated twice for 20 min for each step in a graded series of ethanol from water through 30%-50%-70%-85%-95% ethanol. This was followed by two 30 min washes in 100% ethanol, two 15 min washes in 50% ethanol/50% acetone, and two 15 min washes in 100% acetone. Optic nerve segments were infiltrated in 30% spurr resin/acetone for 20 min and once overnight, then in 50% spurr resin/acetone for 6 hours, and finally in 100% spurr resin overnight. Segments remained in 100% spurr resin, which was changed twice a day for three days at room temperature. All infiltration steps were performed on a rotator. Specimens were embedded in fresh liquid spurr resin and then polymerized overnight at 70°C. Ultrathin sections (80 nm) of the optic nerve segments were collected onto 200-mesh copper grids and

dried overnight prior to staining. Ultrathin sections were stained with 2% aqueous uranyl acetate and Reynold's lead citrate. Sections were observed under a transmission electron microscope (Hitachi 7100).

Optic nerves were collected from n = 4 for both WT and *Dst*$^{dt\text{-}27J}$. Quantification of myelinated axons was done for 12 electron micrographs per n taken at 4000X. G-ratio was measured by calculating the diameter of the axon/diameter of the axon + myelin using ImageJ. For each n, 25 g-ratios were measured for a total of 100 measurements from both WT and *Dst*$^{dt\text{-}27J}$.

Toluidine blue staining

Semithin transverse sections (0.5 μm) of optic nerves were embedded in resin, mounted on glass slides, and stained with toluidine blue. Sections were scanned with a MIRAX MIDI (Zeiss) and viewed using Zeiss MIRAX viewer software. These samples were used for qualitative optic nerve assessment only.

Statistical analysis

All statistics were done using Prism 6 GraphPad software, with the exception of the qPCR data, which was analysed using qbase+ software (Biogazelle). All two-way comparisons were done using a two-tailed Student's *t*-test. Comparisons for qPCR data were done using one-way ANOVA followed by Tukey's post hoc test. Analysis of g-ratios by axon caliber was done by linear regression analysis. Data shown represent mean ± SEM with the exception of myelinated axon density and mean g-ratio, which represent mean ± SD.

## Results

OPCs and OLs endogenously express all neuronal *Dst* transcripts

Expression of neuronal dystonin in CNS tissue has previously been demonstrated by both RNA in situ hybridization and RT-PCR (Bernier et al., 1995; Dalpé et al., 1998; Saulnier et al., 2002). However, we wished to confirm expression of the three transcripts specifically in OLs. Using RNA extracted from primary proliferating OPCs and differentiating OLs we performed qRT-PCR for *Dst-a1*, *-a2*, and *-a3*. All three transcripts are expressed in proliferating OPCs, and in differentiating OLs (Appendix Figure 1.1). *Dst-a1* and *-a2* showed similar expression levels between OPCs and differentiating OLs, while *Dst-a3* showed significantly increased expression in differentiation OLs relative to proliferating OPCs.

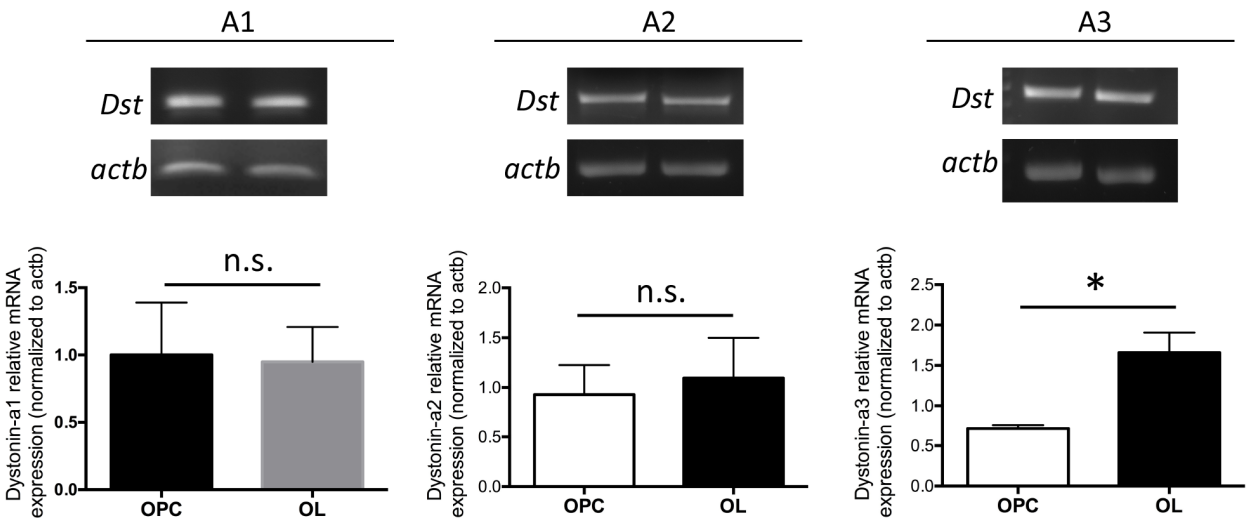


**Appendix Figure 1.1.** Proliferating OPCs and differentiating OLs express neuronal *Dst* transcripts. Top: Representative RT-PCR products from *Dst-a1*, *-a2* and *-a3* with *actb* loading control in primary proliferating OPCs (left lanes) and differentiating OLs (right lanes). Bottom: qRT-PCR analysis of *Dst-a1*, *-a2* and *-a3* expression in primary proliferating OPCs and differentiating OLs. n = 4–6; ΔΔCt, *Dst* normalized to *actb*. * - $P < 0.05$, n.s. - $P > 0.05$; two-tailed Student's *t*-test. Data represent mean ± SEM.

Loss of neuronal *Dst* does not affect morphological maturation *in vitro*

It has been illustrated in many instances that loss of cytoskeleton-interacting proteins bears a negative effect on OL differentiation and myelin membrane formation. Since Dst is able to directly interact with both microfilaments and microtubules, we first sought to determine whether loss of dystonin affects the morphological complexity of differentiating OLs. We isolated mixed glial cultures from $Dst^{dt\text{-}27J}$ mice and WT littermates, and then further isolated OPCs to produce purified cultures as described previously (O'Meara et al., 2011b). OPCs were allowed to differentiate on a mixed PLL/LN2 substrate for three days (DD3) or six days (DD6), representing intermediately differentiated or terminally differentiated time points, respectively. At DD3, Sholl analysis was used to assess complexity but revealed no significant differences in branch extension between $Dst^{dt\text{-}27J}$ and WT OLs (Appendix Figure 1.2A and 2B). OLs in the two conditions were also equally capable of producing membrane at this stage of differentiation, as evidenced by similar proportions of membrane-positive cells (Appendix Figure 1.2C). This was maintained at DD6, where again similar proportions of cells were capable of producing membrane (Appendix Figure 1.2F). Cell complexity was further assessed at DD6 by measuring membrane area, which again revealed no differences between $Dst^{dt\text{-}27J}$ and WT OLs (Appendix Figure 1.2D and 2E).

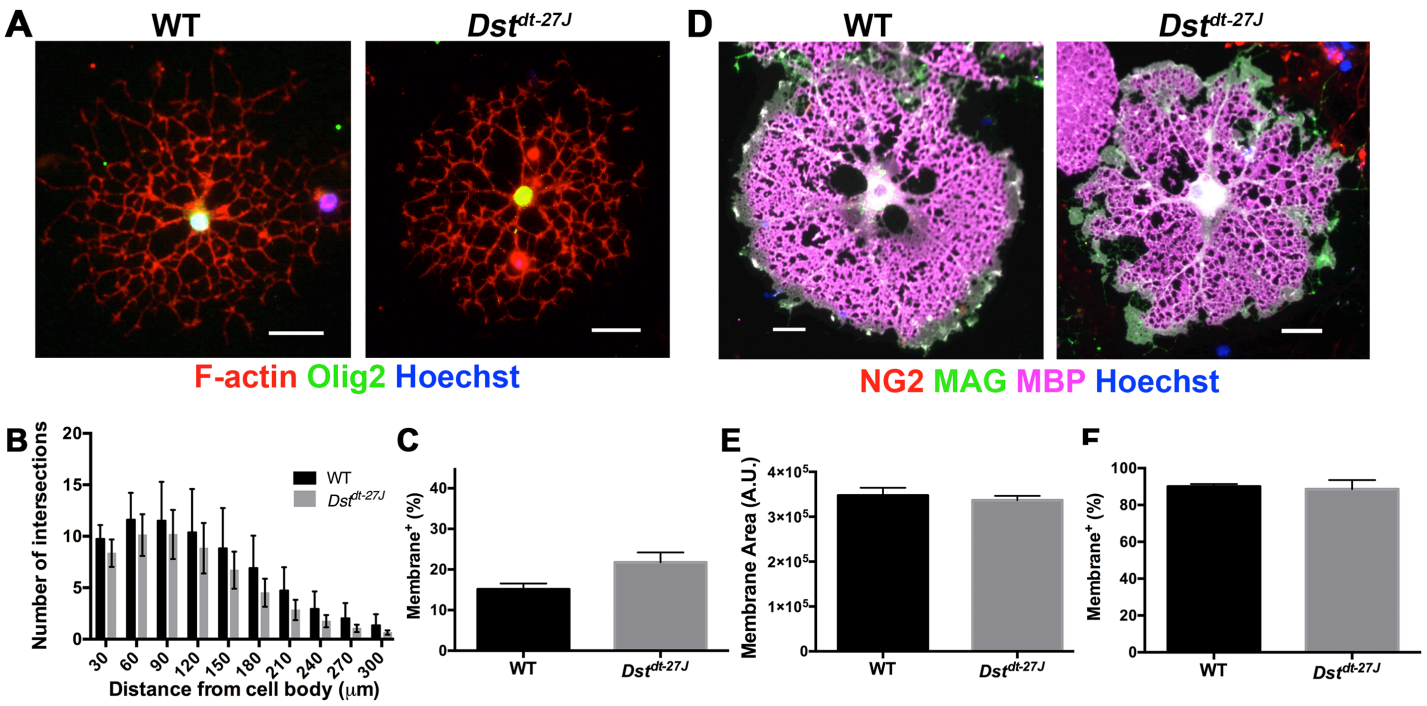


**Appendix Figure 1.2.** *Dst*$^{dt\text{-}27J}$ OLs exhibit normal morphological differentiation. **A)** Immunofluorescence micrographs of WT and *Dst*$^{dt\text{-}27J}$ showing branching at DD3. **B)** Sholl analysis of DD3 OLs. Rings were set at 30 μm increments for quantification of intersections. **C)** Quantification of the percentage of membrane positive OLs at DD3. **D)** Immunofluorescence micrographs of WT and *Dst*$^{dt\text{-}27J}$ total membrane production at DD6. **E)** Quantification of membrane area at DD6. **F)** Quantification of the percentage of membrane positive OLs at DD6. **B)**, **C)**, **E)**, **F)**: n = 3; all comparisons non-significant by two-tailed Student's *t*-test. Data represent mean ± SEM. Scale bars = 50 μm.

Loss of neuronal *Dst* does not affect molecular OL maturation *in vitro*

While OL morphological maturity is associated with increased branch complexity and eventual membrane formation, molecular maturity involves decreased expression of NG2 concurrent with increased expression first of myelin associated glycoprotein (MAG) followed by myelin basic protein (MBP). To determine whether $Dst^{dt\text{-}27J}$ OLs were able to follow a normal molecular differentiation time course, we assessed proportions of $NG2^{+}$ (OPC stage), $MAG^{+}/MBP^{-}$ (intermediate OL stage) and $MAG^{+}/MBP^{+}$ (terminal OL stage) cells at both DD3 and DD6. No significant differences were found in the presence of any of these markers at DD3 (Appendix Figure 1.3A and 3B) or DD6 (Appendix Figure 1.3C and 3D), indicating that OLs lacking *Dst* are able to follow a normal molecular differentiation pattern in vitro.

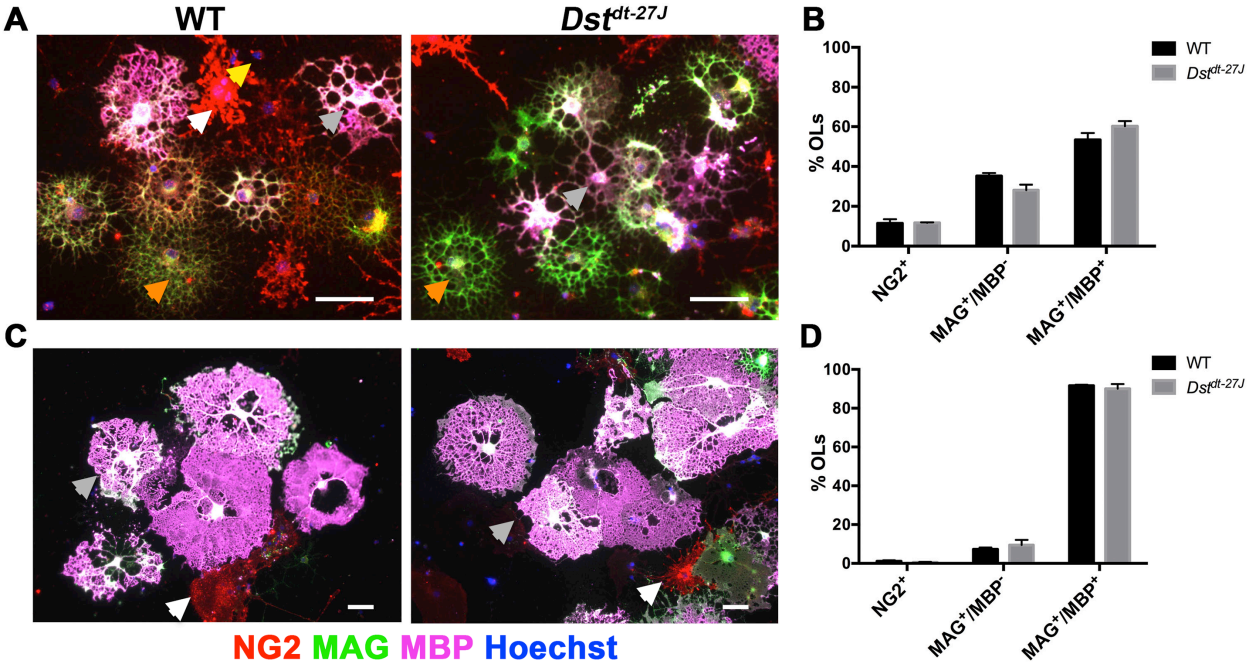


**Appendix Figure 1.3** *Dst*$^{dt\text{-}27J}$ OLs exhibit normal molecular differentiation. **A)** Immunofluorescence micrographs of WT and *Dst*$^{dt\text{-}27J}$ showing maturation marker expression at DD3. **B)** Quantification of the proportion of NG2$^{+}$, MAG$^{+}$/MBP$^{-}$, and MAG$^{+}$/MBP$^{+}$ OLs at DD3. **C)** Immunofluorescence micrographs of WT and *Dst*$^{dt\text{-}27J}$ showing maturation marker expression at DD6. **D)** Quantification of the proportion of NG2$^{+}$, MAG$^{+}$/MBP$^{-}$, and MAG$^{+}$/MBP$^{+}$ OLs at DD6. **B)**, **D)**: n = 3; all comparisons non-significant by two-tailed Student's *t*-test. Data represent mean ± SEM. Arrowheads: yellow = NG2$^{+}$, orange = MAG$^{+}$/MBP$^{-}$, grey = MAG$^{+}$/ MBP$^{+}$, white = contaminating cell. Scale bars = 50 µm.

Apoptosis is not induced in OLs in vitro in the absence of neuronal *Dst*

To ensure that the apparent health of *Dst*-deficient OLs was not isolated to a subpopulation of surviving cells, we assessed OL cultures at both DD3 and DD6 for apoptosis. Differentiating OLs were not undergoing significantly more apoptosis at either DD3 or DD6, as assessed by the presence of apoptotic marker cleaved-caspase 3 (CC3; Appendix Figure 1.4).

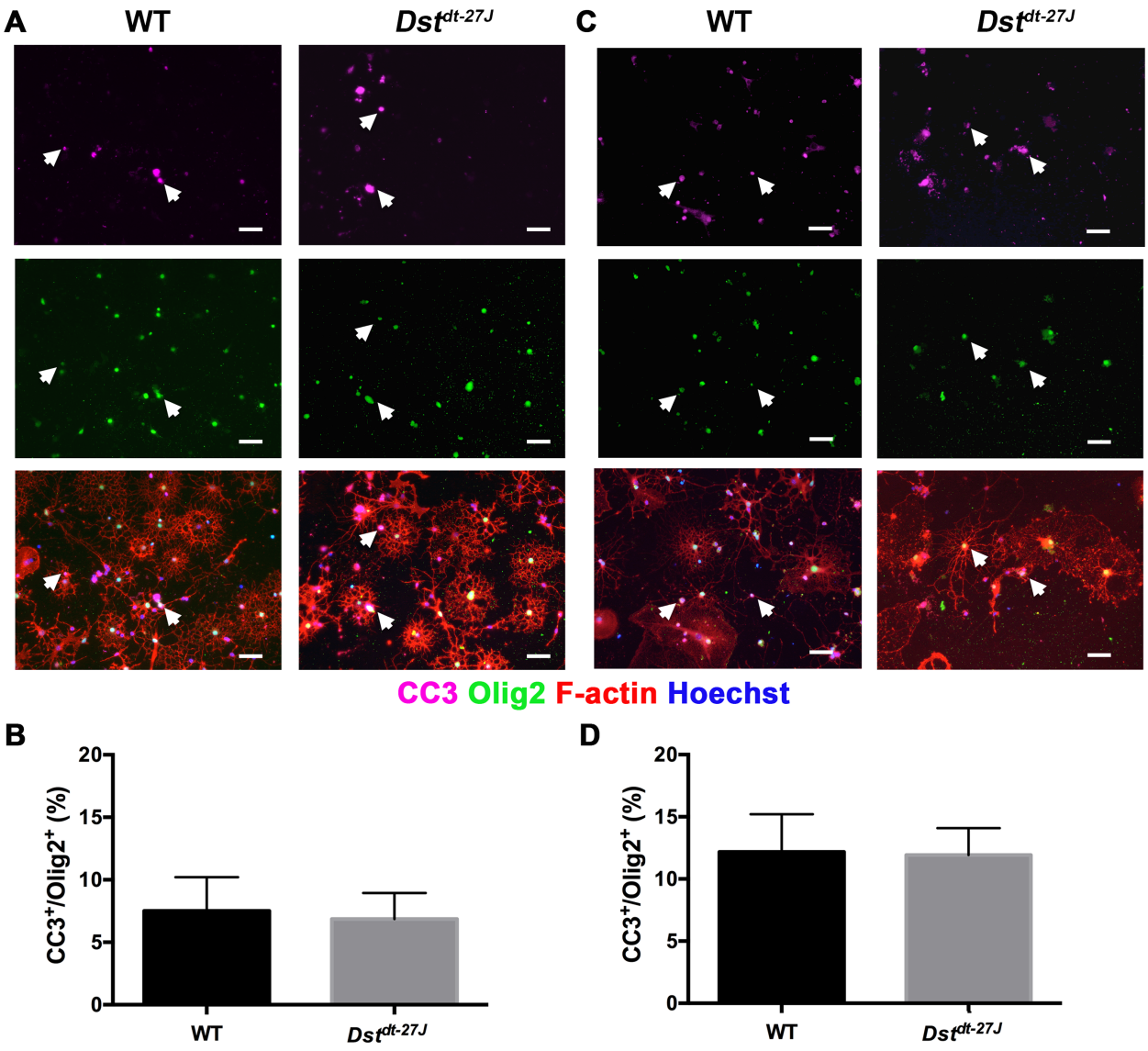


**Appendix Figure 1.4** Apoptosis is not increased in *Dst*$^{dt\text{-}27J}$ OLs. **A)** Immunofluorescence micrographs of WT and *Dst*$^{dt\text{-}27J}$ showing colocalization of nuclear CC3 and Olig2 in apoptotic OLs at DD3. **B)** Quantification of the proportion of CC3$^{+}$/Olig2$^{+}$ relative to total Olig2$^{+}$ OLs at DD3. **C)** Immunofluorescence micrographs of WT and *Dst*$^{dt\text{-}27J}$ showing colocalization of nuclear CC3 and Olig2 in apoptotic OLs at DD6. D. Quantification of the proportion of CC3$^{+}$/Olig2$^{+}$ relative to total Olig2$^{+}$ OLs at DD6. **A)**, **C)**: Arrowheads represent CC3$^{+}$/Olig2$^{+}$ OLs. **B)**, **D)**: n = 3; all comparisons non-significant by two-tailed Student's *t*-test. Data represent mean ± SEM. Scale bars = 50 µm.

OPCs lacking neuronal *Dst* migrate normally *in vitro*

While the effects of loss of neuronal Dst have been little investigated, loss of muscle dystonin has been found to impair migration in myoblasts (Poliakova et al., 2014). Since OPCs are also highly migratory cells, we sought to determine if their motility is affected by a lack of neuronal dystonin. Using a recently established method OPC aggregates were isolated from OPCs in suspension and plated on LN2 substrate (O'Meara et al., 2016). Aggregates of roughly equal size were selected and allowed to migrate for 4 or 24 hours. Migration was assessed by quantifying the proportion of total $NG2^+$ cells found at set distances from the original aggregate after 4 and 24 hours post-seeding. Migration ability was similar between $Dst^{dt\text{-}27J}$ OPCs and WT OPCs at both 4 hours and 24 hours (Appendix Figure 1.5).

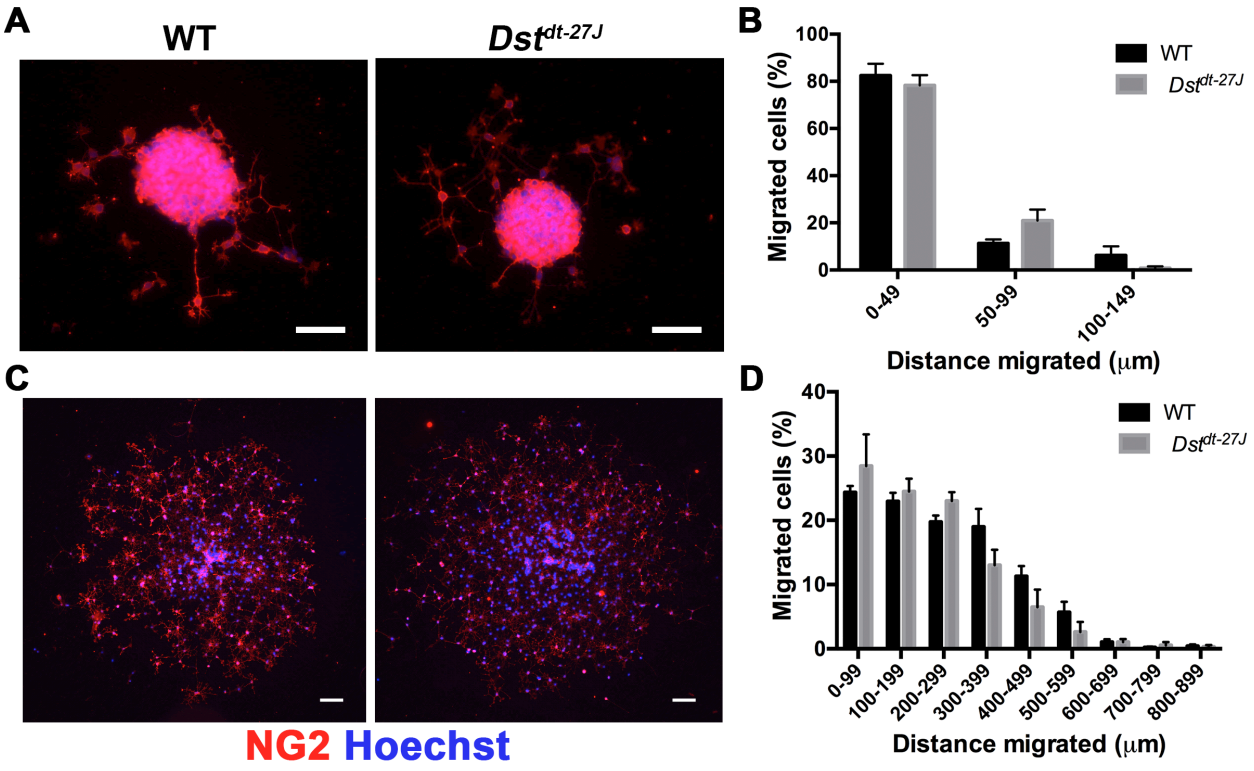


**Appendix Figure 1.5** Migration is normal in *Dst*$^{dt\text{-}27J}$ OPCs. **A)** Immunofluorescence micrographs of WT and *Dst*$^{dt\text{-}27J}$ of OPC aggregates 4 hours post-seeding. **B)** Quantification of the proportion of NG2$^{+}$ OPCs migrated at 4 hours within rings set at 50 μm increments from the aggregate. **C)** Immunofluorescence micrographs of WT and *Dst*$^{dt\text{-}27J}$ of OPC aggregate 24 hours post-seeding. **D)** Quantification of the proportion of NG2$^{+}$ OPCs migrated at 24 hours within rings set at 100 μm increments from the center of the aggregate. **B)**, **D)**: n = 3; all comparisons non-significant by two-tailed Student's *t*-test. Data represent mean ± SEM. Scale bars = 50 μm.

CNS myelination is normal in mice lacking neuronal *Dst*

*In vitro* analyses revealed no intrinsic differentiation or migration defects in OPCs/OLs lacking *Dst*; however, this does not preclude myelination deficiencies from occurring *in vivo*. Thus, we assessed myelination of the optic nerve in P15 $Dst^{dt\text{-}27J}$ mice along with WT littermates for comparison. In this model, P15 is end-stage phenotype, and all $Dst^{dt\text{-}27J}$ animals exhibited typical $Dst^{dt}$ symptoms of ataxia, hind-limb clasping and twisting of the trunk (Ferrier et al., 2013).

No obvious size difference or myelination defects could be observed on examination of toluidine blue-stained optic nerves (Appendix Figure 1.6A). A more detailed analysis was performed in optic nerves by transmission electron microscopy (TEM; Appendix Figure 1.6B). WT and $Dst^{dt\text{-}27J}$ optic nerves contained similar numbers of myelinated axons (Appendix Figure 1.6C). Further assessment of myelin sheath thickness by TEM revealed no overall difference in g-ratio between WT and $Dst^{dt\text{-}27J}$ optic nerves (Appendix Figure 1.6D), nor was there any shift in myelin distribution based on axon caliber (Appendix Figure 1.6E). Finally, assessment of myelination status was done outside of the optic nerve by quantifying CNPase, MOG and MBP levels in both cerebral cortex and spinal cord, also revealing no change in any of these markers of mature myelin between WT and $Dst^{dt\text{-}27J}$ (Appendix Figure 1.6F–6M).

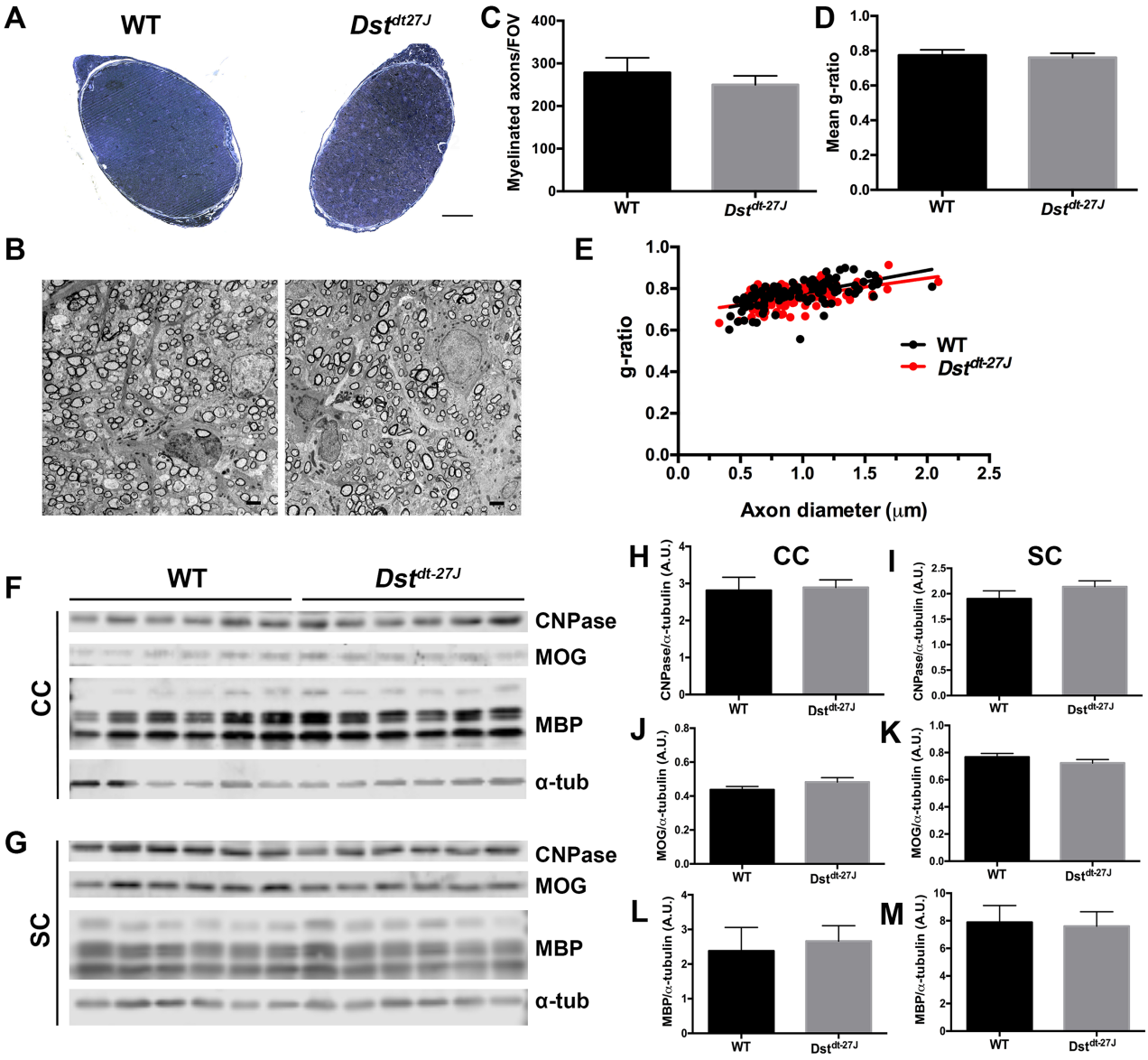


**Appendix Figure 1.6** Myelination occurs normally in vivo in *Dst*$^{dt\text{-}27J}$ animals. **A)** Light microscope images of transected toluidine blue-stained optic nerves from P15 WT and *Dst*$^{dt\text{-}27J}$ mice. **B)** Electron micrographs of transected optic nerves from P15 WT and *Dst*$^{dt\text{-}27J}$ mice. **C)** Quantification of the number of myelinated axons per field of view (FOV) in optic nerves from P15 WT and *Dst*$^{dt\text{-}27J}$ mice. **D)** Quantification of average g-ratio of all myelinated axons per FOV in optic nerves from P15 WT and *Dst*$^{dt\text{-}27J}$ mice. **E)** g-ratios plotted by axon caliber in optic nerves from P15 WT and *Dst*$^{dt\text{-}27J}$ mice. **F)**, **G)** Fluorescence Western blot analysis of CNPase,

MOG, MBP and α-tubulin (α-tub) from cerebral cortex (CC—top panels) and spinal cord (SC—bottom panels) from P15 WT and *Dst*$^{dt\text{-}27J}$ mice. Protein sizes—CNPase: 48 kDa; MOG: 27 kDa; MBP isoforms, from top to bottom: 21.5 kDa, 18.5 kDa, 17.0 kDa, 14.0 kDa. α-tub: 52 kDa. **H)**, **I)** Quantification of total CNPase normalized to α-tub (from blots pictured in **F**), **G**). **J**), **K)** Quantification of total MOG normalized to α-tub (from blots pictured in **F)**, **G**). **L)**, **M)** Quantification of total MBP normalized to α-tub (from blots pictured in **F)**, **G**). **C)**, **D)**: n = 4; **H) - M)**: n = 6; all comparisons non-significant by two-tailed Student's *t*-test. **C)**, **D)**: data represent mean ± SD. **H) - M)**: data represent mean ± SEM. **E)**: n = 100; data represent individual measurements, comparison non- significant by linear regression analysis. **A)**: scale bar = 50 μm. **B)**: scale bar = 2 μm.

**Discussion**

The loss of functional neuronal *Dst* isoforms results in a severe phenotype characterized by ataxia, dystonia and death (Brown et al., 1995b; Edvardson et al., 2012). While the phenotype is largely a consequence of sensory neuron degeneration, previous work has implicated myelinating cells in both the PNS and CNS as contributors to, if not instigators of, the $Dst^{dt}$ phenotype (Bernier et al., 1998; Saulnier et al., 2002). Specifically in the CNS, it has been argued that minor myelination pathologies are in fact early signs of OL-intrinsic defects in the CNS, and that further deterioration would occur if longevity of the animal model was not so limited (Saulnier et al., 2002). However, tools to investigate this hypothesis were wanting at the time. With our present study, we sought to clarify the effects of *Dst* loss on OLs using the severe $Dst^{dt\text{-}27J}$ model lacking all neuronal *Dst* isoforms. By employing methods to isolate and culture $Dst^{dt\text{-}27J}$ OPCs and OLs *in vitro*, we were able to divorce OLs from not only the short phenotypic lifespan of the animal model but also from the influence of $Dst^{dt\text{-}27J}$ neurons. This allowed us to observe OL-intrinsic behaviors in the absence of neuronal Dst.

Our results suggest that even lacking all three neuronal *Dst* isoforms, no intrinsic defects exist in OL differentiation at the morphological or molecular levels. This apparent regularity in OL behavior was not limited to a subpopulation of surviving healthy cells, as apoptosis was not increased in $Dst^{dt\text{-}27J}$. Further, *in vivo* analysis revealed no deficits in CNS myelination of axons or in myelin sheath thickness in optic nerve, and no loss of CNPase, MOG or MBP in spinal cord or cerebral cortex. These findings are dissimilar to what was previously found in the less severe $Dst^{dt\text{-}Tg4}$ model, which retains functional *Dst-a3* (Saulnier et al., 2002). While our results do not disqualify the existence of myelination defects in that model, it seems intuitive that if CNS myelination defects are indeed part of $Dst^{dt}$ pathology then the more severe model would exhibit

more severe CNS myelination problems. It must also be noted that while some qualitative *in vitro* analyses of OLs was undertaken in the initial study (revealing no obvious morphological defects in $Dst^{dt\text{-}Tg4}$ OLs) (Saulnier et al., 2002), the tools to isolate and culture primary mouse OLs were limited and thus restricted the ability for a more comprehensive analysis of intrinsic OL biology, as we have done here.

We must also acknowledge that while this study provides fairly detailed molecular and morphological analyses, these assessments were done at a single pre-myelinating time point and at a point where terminal differentiation is known to occur for these cells *in vitro*. Thus, it is possible that differences in morphological and/or molecular development may occur at time points prior to terminal differentiation, which we did not investigate. However, since terminal differentiation is achieved with equal success in both WT and $Dst^{dt\text{-}27J}$ OLs *in vitro* within the expected time line, any differences in their development prior to this point must be transient and are unlikely to affect their biological function as mature OLs. This is supported by our *in vivo* data, which reveal no defects in optic nerve myelination, cerebral cortex myelin protein expression or spinal cord myelin protein expression even at end-stage of the *dystonia musculorum* disease. Again, differences in developmental timing in OL maturation and myelination prior to this point cannot be ruled out *in vivo*, but if they do occur these too must be temporary as even end-stage $Dst^{dt\text{-}27J}$ animals exhibit myelin status and health that is indistinguishable from WT animals. While our study is primarily concerned with the biological relevance of the loss of *Dst* in OPCs and OLs, additional investigation would need to be undertaken to clarify whether any transient differences in differentiation dynamics arise when *Dst* is absent.

Interestingly, intrinsic differentiation and myelination defects do exist in Schwann cells in both the $Dst^{dt\text{-}Tg4}$ and $Dst^{dt\text{-}27J}$ models, and are more severe when all three neuronal isoforms are absent (Bernier et al., 1998). This was illustrated in *in vitro* primary cultures and *in vivo* transplant experiments in which $Dst^{dt\text{-}Tg4}$ and $Dst^{dt\text{-}27J}$ Schwann cells failed to differentiate or myelinate normally. While many similarities exist between Schwann cells and OLs—most obviously their function as producers of myelin—there are also many differences that may account for their apparent disparate requirement for neuronal *Dst*. First, intermediate filaments are present in Schwann cells and play a role in peripheral myelination, while OLs do not contain intermediate filaments (Baumann and Pham-Dinh, 2001; Bauer et al., 2009; Nave, 2010; Triolo et al., 2012). Dst can bind some intermediate filaments in addition to microfilaments and microtubules, and loss of *Dst* leads to disorganization of intermediate filaments α-internexin, neurofilament and peripherin in sensory neurons (Leung et al., 1999a; De Repentigny et al., 2011). A second key difference between OLs and Schwann cells is the production of a basement membrane. Following contact with an axon, Schwann cells surround their exterior layer with a basement membrane, the mechanical integrity of which is required for continued wrapping of the axon and subsequent myelin production (Bunge et al., 1989; Tsiper and Yurchenco, 2002). Further, OLs and Schwann cells express a different complement of integrins, transmembrane heterodimeric complexes that convey signals between the extracellular matrix and intracellular space largely to elicit cytoskeletal reorganization (O'Meara et al., 2011a; O'Meara et al., 2013; Pellegatta et al., 2013). It has been speculated that Dst may interact with some integrins to mediate cytoskeletal organization (Bernier et al., 1998; Saulnier et al., 2002). Thus it is possible that in Schwann cells, Dst is involved in any or all of intermediate filament organization,

basement membrane formation and mediation of signaling of specific integrin complexes—none of which are present in OLs.

Further explanation may exist for the seemingly disposable nature of neuronal Dst in OLs. In mammals, a second member of the spectraplakin exists: microtubule-actin crosslinking factor 1 (Macf1; variantly actin crosslinking family 7/Acf7). Two isoforms of Macf1 are preferentially expressed in CNS tissues with little expression in PNS tissues, and share significant homology with neuronal Dst (Bernier et al., 1996; Bernier et al., 2000). Macf1 can regulate cytoskeletal dynamics, and has both actin-binding and microtubule-binding domains, similar to Dst (Leung et al., 1999b; Bernier et al., 2000; Karakesisoglou et al., 2000). This raises the possibility that neuronal Dst does serve a function in the CNS, which may be compensated for by Macf1 if the former is lost. However, this idea was previously investigated in the $Dst^{dt\text{-}27J}$ model; no increase in Macf1 was observed in brain or spinal cord from $Dst^{dt}$ animals, as would be expected if additional Macf1 were required to fill a role normally played by Dst (Bernier et al., 2000). While this does not preclude a compensatory function for Macf1, it does suggest that—much like OLs and Schwann cells—Macf1 and neuronal Dst serve similar functions that are likely restricted to their respective nervous system compartments.

Finally, though the lack of Dst does not appear to be biologically relevant to the terminal differentiation of OLs during developmental myelination, it may be required for remyelination following a demyelinating injury. In the healthy CNS, any damage to mature myelin that may occur can be repaired by the differentiation of resident OPCs into new myelinating OLs, which subsequently ensheathe denuded areas of an axon. Though this process is believed to largely mimic the processes of developmental myelination—the so-called recapitulation hypothesis (Franklin and Hinks, 1999; Fancy et al., 2011) – the final product of remyelination includes both

thinner sheaths and shorter internodes than expected. This raises the possibility that different mechanisms are involved in remyelination than in developmental myelination, and this remains an important open question in OL biology. Interestingly, it has also been noted that in some instances of CNS demyelination, remyelination is carried out not by OLs but by Schwann cells (Zawadzka et al., 2010). These Schwann cells are not emigrated from the peripheral nervous system, but surprisingly arise from CNS glial progenitors in specific circumstances when the injury results not only in demyelination but also in depletion of astrocytes at the injury cite (Zawadzka et al., 2010; Monteiro de Castro et al., 2015). The expression of dystonin has not been investigated in the context of remyelination. Future work should include the use of remyelination models applied to $Dst^{dt}$ animals—such as organotypic brain slice culture—to explore the role of neuronal *Dst* in this important process, particularly when Schwann cells are implicated in CNS recovery from demyelination.

## Conclusions

Here, comprehensive *in vitro* and *in vivo* analyses were performed to better understand the role of neuronal *Dst* in OLs using the $Dst^{dt\text{-}27J}$ animal model. Our results revealed that even in the absence of all three isoforms of *Dst*, OLs are able to differentiate normally both morphologically and molecularly. Survival of OLs lacking *Dst* is not compromised, nor is migration of OPCs. *In vivo* assessment of optic nerve myelination at disease end-stage showed normal density of myelinated axons and myelin thickness in optic nerve, as well as normal expression levels of CNPase, MOG and MBP in both spinal cord and cerebral cortex in animals with *dystonia musculorum*. While we cannot rule out the occurrence of transient differences in OL maturity or that other cellular processes may be affected in OPCs and OLs in the absence of

*Dst*, these data suggest that neuronal *Dst* is not essential for proper terminal OL differentiation or functional myelin development in the CNS.

**Supplementary Material**

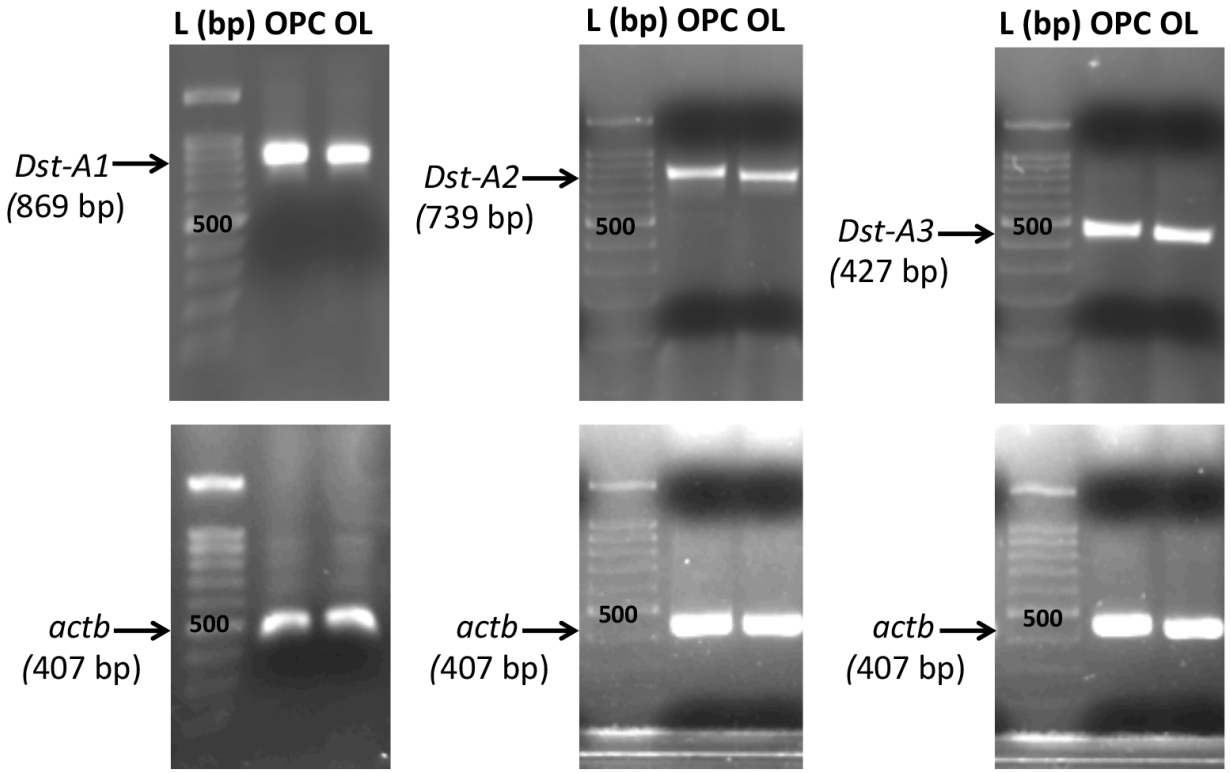


**Appendix Figure S1.1** Proliferating OPCs and differentiating OLs express neuronal *Dst* transcripts. Whole-gel view of RT-PCR *Dst-a1*, *-a2* and *-a3* with *actb* loading control in primary proliferating OPCs and differentiating OLs. L = ladder; bp = base pairs.

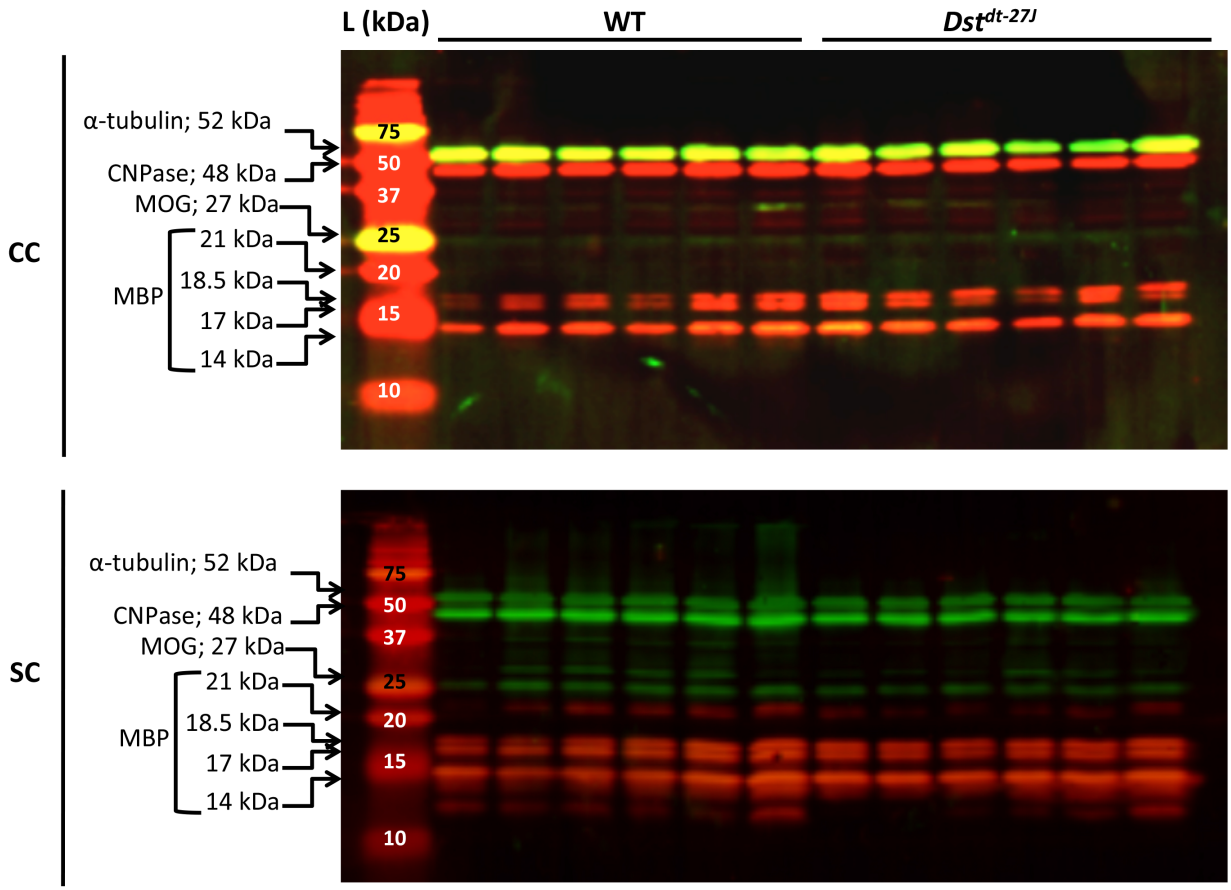


**Appendix Figure S1.2** CNPase, MOG, and MBP expression is unchanged in *Dst*$^{dt\text{-}27J}$ cerebral cortex and spinal cord. Whole-membrane view of all CNPase, MOG, and MBP isoforms, as well as α- tubulin (green) in cerebral cortex (CC) and spinal cord (SC) from P15 wild type (WT) and *Dst*$^{dt\text{-}27J}$ mice. L = ladder; kDa = kilodaltons.

## References:


al-Ali SY, al-Zuhair AG (1989) Fine structural study of the spinal cord and spinal ganglia in mice afflicted with a hereditary sensory neuropathy, dystonia musculorum. J Submicrosc Cytol Pathol 21:737-748.

Alper JD, Decker F, Agana B, Howard J (2014) The motility of axonemal dynein is regulated by the tubulin code. Biophys J 107:2872-2880.

Aplin A, Jasionowski T, Tuttle DL, Lenk SE, Dunn WA, Jr. (1992) Cytoskeletal elements are required for the formation and maturation of autophagic vacuoles. J Cell Physiol 152:458-466.

Arakawa S, Tsujioka M, Yoshida T, Tajima-Sakurai H, Nishida Y, Matsuoka Y, Yoshino I, Tsujimoto Y, Shimizu S (2017) Role of Atg5-dependent cell death in the embryonic development of Bax/Bak double-knockout mice. Cell Death Differ 24:1598-1608.

Atai NA, Ryan SD, Kothary R, Breakefield XO, Nery FC (2012) Untethering the nuclear envelope and cytoskeleton: biologically distinct dystonias arising from a common cellular dysfunction. Int J Cell Biol 2012:634214.

Axelrod FB (2002) Hereditary sensory and autonomic neuropathies. Familial dysautonomia and other HSANs. Clin Auton Res 12 Suppl 1:I2-14.

Axelrod FB, Gold-von Simson G (2007) Hereditary sensory and autonomic neuropathies: types II, III, and IV. Orphanet J Rare Dis 2:39.

Bacon C, Lakics V, Machesky L, Rumsby M (2007) N-WASP regulates extension of filopodia and processes by oligodendrocyte progenitors, oligodendrocytes, and Schwann cells-implications for axon ensheathment at myelination. Glia 55:844-858.

Batlevi Y, Martin DN, Pandey UB, Simon CR, Powers CM, Taylor JP, Baehrecke EH (2010) Dynein light chain 1 is required for autophagy, protein clearance, and cell death in Drosophila. Proc Natl Acad Sci U S A 107:742-747.

Bauer NG, Richter-Landsberg C, Ffrench-Constant C (2009) Role of the oligodendroglial cytoskeleton in differentiation and myelination. Glia 57:1691-1705.

Baumann N, Pham-Dinh D (2001) Biology of oligodendrocyte and myelin in the mammalian central nervous system. Physiol Rev 81:871-927.

Bernier G, Kothary R (1998) Prenatal onset of axonopathy in Dystonia musculorum mice. Dev Genet 22:160-168.

Bernier G, Mathieu M, De Repentigny Y, Vidal SM, Kothary R (1996) Cloning and characterization of mouse ACF7, a novel member of the dystonin subfamily of actin binding proteins. Genomics 38:19-29.

Bernier G, De Repentigny Y, Mathieu M, David S, Kothary R (1998) Dystonin is an essential component of the Schwann cell cytoskeleton at the time of myelination. Development 125:2135-2148.

Bernier G, Brown A, Dalpe G, De Repentigny Y, Mathieu M, Kothary R (1995) Dystonin expression in the developing nervous system predominates in the neurons that degenerate in dystonia musculorum mutant mice. Mol Cell Neurosci 6:509-520.

Bernier G, Pool M, Kilcup M, Alfoldi J, De Repentigny Y, Kothary R (2000) Acf7 (MACF) is an actin and microtubule linker protein whose expression predominates in neural, muscle, and lung development. Dev Dyn 219:216-225.

Bhanot K, Young KG, Kothary R (2011) MAP1B and clathrin are novel interacting partners of the giant cyto-linker dystonin. J Proteome Res 10:5118-5127.

Birchenough GM, Johansson ME, Gustafsson JK, Bergstrom JH, Hansson GC (2015) New developments in goblet cell mucus secretion and function. Mucosal Immunol 8:712-719.

Bjorkoy G, Lamark T, Brech A, Outzen H, Perander M, Overvatn A, Stenmark H, Johansen T (2005) p62/SQSTM1 forms protein aggregates degraded by autophagy and has a protective effect on huntingtin-induced cell death. J Cell Biol 171:603-614.

Boyer JG, Bhanot K, Kothary R, Boudreau-Lariviere C (2010) Hearts of dystonia musculorum mice display normal morphological and histological features but show signs of cardiac stress. PLoS One 5:e9465.

Brown A, Dalpe G, Mathieu M, Kothary R (1995a) Cloning and characterization of the neural isoforms of human dystonin. Genomics 29:777-780.

Brown A, Bernier G, Mathieu M, Rossant J, Kothary R (1995b) The mouse dystonia musculorum gene is a neural isoform of bullous pemphigoid antigen 1. Nat Genet 10:301-306.

Brown A, Copeland NG, Gilbert DJ, Jenkins NA, Rossant J, Kothary R (1994) The genomic structure of an insertional mutation in the dystonia musculorum locus. Genomics 20:371-376.

Brown CL, Maier KC, Stauber T, Ginkel LM, Wordeman L, Vernos I, Schroer TA (2005) Kinesin-2 is a motor for late endosomes and lysosomes. Traffic 6:1114-1124.

Browning KN, Travagli RA (2014) Central nervous system control of gastrointestinal motility and secretion and modulation of gastrointestinal functions. Compr Physiol 4:1339-1368.

Bult C, Blake J, Smith C, Kadin J, Richardson J (2019) Mouse Genome Database (MGD). In: Nucleic Acids Res., (D1): D801-D806 Edition. Bar Harbor, Maine: The Jackson Laboratory.

Bunge RP, Bunge MB, Bates M (1989) Movements of the Schwann cell nucleus implicate progression of the inner (axon-related) Schwann cell process during myelination. J Cell Biol 109:273-284.

Caporaso JG et al. (2010) QIIME allows analysis of high-throughput community sequencing data. Nature Methods 7:335.

Cappuccio G, Pinelli M, Torella A, Alagia M, Auricchio R, Staiano A, Nigro V, Tudp, Brunetti-Pierri N (2017) Expanding the phenotype of DST-related disorder: A case report suggesting a genotype/phenotype correlation. Am J Med Genet A 173:2743-2746.

Carlsten JA, Kothary R, Wright DE (2001) Glial cell line-derived neurotrophic factor-responsive and neurotrophin-3-responsive neurons require the cytoskeletal linker protein dystonin for postnatal survival. J Comp Neurol 432:155-168.

Chen Y, Balasubramaniyan V, Peng J, Hurlock EC, Tallquist M, Li J, Lu QR (2007) Isolation and culture of rat and mouse oligodendrocyte precursor cells. Nat Protoc 2:1044-1051.

Cheng XT, Zhou B, Lin MY, Cai Q, Sheng ZH (2015a) Axonal autophagosomes recruit dynein for retrograde transport through fusion with late endosomes. J Cell Biol 209:377-386.

Cheng XT, Zhou B, Lin MY, Cai Q, Sheng ZH (2015b) Axonal autophagosomes use the ride-on service for retrograde transport toward the soma. Autophagy 11:1434-1436.

Coulombe J, Gamage P, Gray MT, Zhang M, Tang MY, Woulfe J, Saffrey MJ, Gray DA (2014) Loss of UCHL1 promotes age-related degenerative changes in the enteric nervous system. Front Aging Neurosci 6:129.

Dalpé G, Leclerc N, Vallee A, Messer A, Mathieu M, De Repentigny Y, Kothary R (1998) Dystonin is essential for maintaining neuronal cytoskeleton organization. Mol Cell Neurosci 10:243-257.

de Lisle RC, Sewell R, Meldi L (2010) Enteric circular muscle dysfunction in the cystic fibrosis mouse small intestine. Neurogastroenterol Motil 22:341-e387.

De Repentigny Y, Deschenes-Furry J, Jasmin BJ, Kothary R (2003) Impaired fast axonal transport in neurons of the sciatic nerves from dystonia musculorum mice. J Neurochem 86:564-571.

De Repentigny Y, Ferrier A, Ryan SD, Sato T, Kothary R (2011) Motor unit abnormalities in Dystonia musculorum mice. PLoS One 6:e21093.

Denton D, Kumar S (2019) Autophagy-dependent cell death. Cell Death Differ 26:605-616.

Dikic I, Elazar Z (2018) Mechanism and medical implications of mammalian autophagy. Nat Rev Mol Cell Biol 19:349-364.

Dompierre JP, Godin JD, Charrin BC, Cordelieres FP, King SJ, Humbert S, Saudou F (2007) Histone deacetylase 6 inhibition compensates for the transport deficit in Huntington's disease by increasing tubulin acetylation. J Neurosci 27:3571-3583.

Duchen LW (1976) Dystonia musculorum--an inherited disease of the nervous system in the mouse. Adv Neurol 14:353-365.

Duchen LW, Strich SJ, Falconer DS (1963) Dystonia musculorum. A hereditary neuropathy of mice affecting mainly sensory pathways. The Journal of Physiology 165:7-9.

Duchen LW, Strich SJ, Falconer DS (1964) Clinical and Pathological Studies of an Hereditary Neuropathy in Mice (Dystonia Musculorum). Brain 87:367-378.

Dukowicz AC, Lacy BE, Levine GM (2007) Small intestinal bacterial overgrowth: a comprehensive review. Gastroenterology & hepatology 3:112-122.

Edvardson S, Cinnamon Y, Jalas C, Shaag A, Maayan C, Axelrod FB, Elpeleg O (2012) Hereditary sensory autonomic neuropathy caused by a mutation in dystonin. Ann Neurol 71:569-572.

Fancy SP, Chan JR, Baranzini SE, Franklin RJ, Rowitch DH (2011) Myelin regeneration: a recapitulation of development? Annu Rev Neurosci 34:21-43.

Fang T, Jozsa F, Al-Chalabi A (2017) Nonmotor Symptoms in Amyotrophic Lateral Sclerosis: A Systematic Review. Int Rev Neurobiol 134:1409-1441.

Fernyhough P, Calcutt NA (2010) Abnormal calcium homeostasis in peripheral neuropathies. Cell Calcium 47:130-139.

Ferrier A, Boyer JG, Kothary R (2013) Cellular and molecular biology of neuronal dystonin. Int Rev Cell Mol Biol 300:85-120.

Ferrier A, De Repentigny Y, Lynch-Godrei A, Gibeault S, Eid W, Kuo D, Zha X, Kothary R (2015) Disruption in the autophagic process underlies the sensory neuropathy in dystonia musculorum mice. Autophagy 11:1025-1036.

Ferrier A, Sato T, De Repentigny Y, Gibeault S, Bhanot K, O'Meara RW, Lynch-Godrei A, Kornfeld SF, Young KG, Kothary R (2014) Transgenic expression of neuronal dystonin isoform 2 partially rescues the disease phenotype of the dystonia musculorum mouse model of hereditary sensory autonomic neuropathy VI. Hum Mol Genet 23:2694-2710.

Forrest AD, Beggs HE, Reichardt LF, Dupree JL, Colello RJ, Fuss B (2009) Focal adhesion kinase (FAK): A regulator of CNS myelination. J Neurosci Res 87:3456-3464.

Fortugno P, Angelucci F, Cestra G, Camerota L, Ferraro AS, Cordisco S, Uccioli L, Castiglia D, De Angelis B, Kurth I, Kornak U, Brancati F (2018) Recessive mutations in the neuronal isoforms of DST, encoding dystonin, lead to abnormal actin cytoskeleton organization and HSAN type VI. Hum Mutat.

Franklin RJ, Hinks GL (1999) Understanding CNS remyelination: clues from developmental and regeneration biology. J Neurosci Res 58:207-213.

Fukushima N, Furuta D, Hidaka Y, Moriyama R, Tsujiuchi T (2009) Post-translational modifications of tubulin in the nervous system. J Neurochem 109:683-693.

Furness JB (2012) The enteric nervous system and neurogastroenterology. Nat Rev Gastroenterol Hepatol 9:286-294.

Furness JB, Callaghan BP, Rivera LR, Cho H-J (2014) The Enteric Nervous System and Gastrointestinal Innervation: Integrated Local and Central Control. In: Microbial Endocrinology: The Microbiota-Gut-Brain Axis in Health and Disease (Lyte M, Cryan JF, eds), pp 39-71. New York, NY: Springer New York.

Geeraert C, Ratier A, Pfisterer SG, Perdiz D, Cantaloube I, Rouault A, Pattingre S, Proikas-Cezanne T, Codogno P, Pous C (2010) Starvation-induced hyperacetylation of tubulin is required for the stimulation of autophagy by nutrient deprivation. J Biol Chem 285:24184-24194.

Giorda R, Cerritello A, Bonaglia MC, Bova S, Lanzi G, Repetti E, Giglio S, Baschirotto C, Pramparo T, Avolio L, Bragheri R, Maraschio P, Zuffardi O (2004) Selective disruption of muscle and brain-specific BPAG1 isoforms in a girl with a 6;15 translocation, cognitive and motor delay, and tracheo-oesophageal atresia. J Med Genet 41:e71.

Guo L, Degenstein L, Dowling J, Yu QC, Wollmann R, Perman B, Fuchs E (1995) Gene targeting of BPAG1: abnormalities in mechanical strength and cell migration in stratified epithelia and neurologic degeneration. Cell 81:233-243.

Hammond JW, Cai D, Verhey KJ (2008) Tubulin modifications and their cellular functions. Curr Opin Cell Biol 20:71-76.

Hara T, Nakamura K, Matsui M, Yamamoto A, Nakahara Y, Suzuki-Migishima R, Yokoyama M, Mishima K, Saito I, Okano H, Mizushima N (2006) Suppression of basal autophagy in neural cells causes neurodegenerative disease in mice. Nature 441:885-889.

He C, Klionsky DJ (2009) Regulation mechanisms and signaling pathways of autophagy. Annu Rev Genet 43:67-93.

Hopkinson SB, Jones JCR (2000) The N Terminus of the Transmembrane Protein BP180 Interacts with the N-terminal Domain of BP230, Thereby Mediating Keratin Cytoskeleton Anchorage to the Cell Surface at the Site of the Hemidesmosome. Molecular Biology of the Cell 11:277-286.

Horie M, Watanabe K, Bepari AK, Nashimoto J, Araki K, Sano H, Chiken S, Nambu A, Ono K, Ikenaka K, Kakita A, Yamamura K, Takebayashi H (2014) Disruption of actin-binding domain-containing Dystonin protein causes dystonia musculorum in mice. Eur J Neurosci 40:3458-3471.

Hossain MI, Horie M, Yoshioka N, Kurose M, Yamamura K, Takebayashi H (2018) Motoneuron degeneration in the trigeminal motor nucleus innervating the masseter muscle in Dystonia musculorum mice. Neurochem Int 119:159-170.

Hoyer-Hansen M, Jaattela M (2007) Connecting endoplasmic reticulum stress to autophagy by unfolded protein response and calcium. Cell Death Differ 14:1576-1582.

Ichikawa H, De Repentigny Y, Kothary R, Sugimoto T (2006) The survival of vagal and glossopharyngeal sensory neurons is dependent upon dystonin. Neuroscience 137:531-536.

Ijaz MK, Sabara MI, Frenchick PJ, Babiuk LA (1987) Assessment of intestinal damage in rotavirus infected neonatal mice by a D-xylose absorption test. J Virol Methods 18:153-157.

Ikenaka K, Kawai K, Katsuno M, Huang Z, Jiang YM, Iguchi Y, Kobayashi K, Kimata T, Waza M, Tanaka F, Mori I, Sobue G (2013) dnc-1/dynactin 1 knockdown disrupts transport of autophagosomes and induces motor neuron degeneration. PLoS One 8:e54511.

Jahreiss L, Menzies FM, Rubinsztein DC (2008) The itinerary of autophagosomes: from peripheral formation to kiss-and-run fusion with lysosomes. Traffic 9:574-587.

Janke C, Kneussel M (2010) Tubulin post-translational modifications: encoding functions on the neuronal microtubule cytoskeleton. Trends Neurosci 33:362-372.

Janota I (1972) Ultrastructural studies of an hereditary sensory neuropathy in mice (dystonia musculorum). Brain 95:529-536.

Jefferson JJ, Leung CL, Liem RK (2006) Dissecting the sequence specific functions of alternative N-terminal isoforms of mouse bullous pemphigoid antigen 1. Exp Cell Res 312:2712-2725.

Jefferson JJ, Ciatto C, Shapiro L, Liem RK (2007) Structural analysis of the plakin domain of bullous pemphigoid antigen1 (BPAG1) suggests that plakins are members of the spectrin superfamily. J Mol Biol 366:244-257.

Johansen T, Lamark T (2011) Selective autophagy mediated by autophagic adapter proteins. Autophagy 7:279-296.

Johansson ME, Sjovall H, Hansson GC (2013) The gastrointestinal mucus system in health and disease. Nat Rev Gastroenterol Hepatol 10:352-361.

Karakesisoglou I, Yang Y, Fuchs E (2000) An epidermal plakin that integrates actin and microtubule networks at cellular junctions. J Cell Biol 149:195-208.

Kim HJ, DiBernardo AB, Sloane JA, Rasband MN, Solomon D, Kosaras B, Kwak SP, Vartanian TK (2006) WAVE1 is required for oligodendrocyte morphogenesis and normal CNS myelination. J Neurosci 26:5849-5859.

Kimura S, Noda T, Yoshimori T (2008) Dynein-dependent movement of autophagosomes mediates efficient encounters with lysosomes. Cell Struct Funct 33:109-122.

Klein C, Kramer EM, Cardine AM, Schraven B, Brandt R, Trotter J (2002) Process outgrowth of oligodendrocytes is promoted by interaction of fyn kinase with the cytoskeletal protein tau. J Neurosci 22:698-707.

Klionsky DJ et al. (2008) Guidelines for the use and interpretation of assays for monitoring autophagy in higher eukaryotes. Autophagy 4:151-175.

Köchl R, Hu XW, Chan EY, Tooze SA (2006) Microtubules facilitate autophagosome formation and fusion of autophagosomes with endosomes. Traffic 7:129-145.

Komatsu M, Waguri S, Chiba T, Murata S, Iwata J, Tanida I, Ueno T, Koike M, Uchiyama Y, Kominami E, Tanaka K (2006) Loss of autophagy in the central nervous system causes neurodegeneration in mice. Nature 441:880-884.

Kornfeld SF, Lynch-Godrei A, Bonin SR, Gibeault S, De Repentigny Y, Kothary R (2016) Cytoskeletal Linker Protein Dystonin Is Not Critical to Terminal Oligodendrocyte Differentiation or CNS Myelination. PLoS One 11:e0149201.

Kothary R, Clapoff S, Brown A, Campbell R, Peterson A, Rossant J (1988) A transgene containing lacZ inserted into the dystonia locus is expressed in neural tube. Nature 335:435-437.

Kunzli K, Favre B, Chofflon M, Borradori L (2016) One gene but different proteins and diseases: the complexity of dystonin and bullous pemphigoid antigen 1. Exp Dermatol 25:10-16.

Langille MGI, Zaneveld J, Caporaso JG, McDonald D, Knights D, Reyes JA, Clemente JC, Burkepile DE, Vega Thurber RL, Knight R, Beiko RG, Huttenhower C (2013) Predictive functional profiling of microbial communities using 16S rRNA marker gene sequences. Nature Biotechnology 31:814.

Lee J, Gravel M, Zhang R, Thibault P, Braun PE (2005) Process outgrowth in oligodendrocytes is mediated by CNP, a novel microtubule assembly myelin protein. J Cell Biol 170:661-673.

Lee Y, Morrison BM, Li Y, Lengacher S, Farah MH, Hoffman PN, Liu Y, Tsingalia A, Jin L, Zhang PW, Pellerin L, Magistretti PJ, Rothstein JD (2012) Oligodendroglia metabolically support axons and contribute to neurodegeneration. Nature 487:443-448.

Lehotzky A, Lau P, Tokesi N, Muja N, Hudson LD, Ovadi J (2010) Tubulin polymerization-promoting protein (TPPP/p25) is critical for oligodendrocyte differentiation. Glia 58:157-168.

Leung CL, Sun D, Liem RK (1999a) The intermediate filament protein peripherin is the specific interaction partner of mouse BPAG1-n (dystonin) in neurons. J Cell Biol 144:435-446.

Leung CL, Zheng M, Prater SM, Liem RK (2001) The BPAG1 locus: Alternative splicing produces multiple isoforms with distinct cytoskeletal linker domains, including predominant isoforms in neurons and muscles. J Cell Biol 154:691-697.

Leung CL, Sun D, Zheng M, Knowles DR, Liem RK (1999b) Microtubule actin cross-linking factor (MACF): a hybrid of dystonin and dystrophin that can interact with the actin and microtubule cytoskeletons. J Cell Biol 147:1275-1286.

Levine B, Kroemer G (2008) Autophagy in the pathogenesis of disease. Cell 132:27-42.

Liu JJ, Ding J, Wu C, Bhagavatula P, Cui B, Chu S, Mobley WC, Yang Y (2007) Retrolinkin, a membrane protein, plays an important role in retrograde axonal transport. Proc Natl Acad Sci U S A 104:2223-2228.

Liu JJ, Ding J, Kowal AS, Nardine T, Allen E, Delcroix JD, Wu C, Mobley W, Fuchs E, Yang Y (2003) BPAG1n4 is essential for retrograde axonal transport in sensory neurons. J Cell Biol 163:223-229.

Lynch-Godrei A, Kothary R (2016) Functional and Genetic Analysis of Neuronal Isoforms of BPAG1. Methods Enzymol 569:355-372.

Lynch-Godrei A, De Repentigny Y, Gagnon S, Trung MT, Kothary R (2018) Dystonin-A3 upregulation is responsible for maintenance of tubulin acetylation in a less severe dystonia musculorum mouse model for hereditary sensory and autonomic neuropathy type VI. Hum Mol Genet 27:3598-3611.

Maday S, Holzbaur EL (2014) Autophagosome biogenesis in primary neurons follows an ordered and spatially regulated pathway. Dev Cell 30:71-85.

Maday S, Wallace KE, Holzbaur EL (2012) Autophagosomes initiate distally and mature during transport toward the cell soma in primary neurons. J Cell Biol 196:407-417.

Manganelli F, Parisi S, Nolano M, Tao F, Paladino S, Pisciotta C, Tozza S, Nesti C, Rebelo AP, Provitera V, Santorelli FM, Shy ME, Russo T, Zuchner S, Santoro L (2017) Novel mutations in dystonin provide clues to the pathomechanisms of HSAN-VI. Neurology 88:2132-2140.

Marchbank K, Waters S, Roberts RG, Solomon E, Whitehouse CA (2012) MAP1B Interaction with the FW Domain of the Autophagic Receptor Nbr1 Facilitates Its Association to the Microtubule Network. Int J Cell Biol 2012:208014.

Marola S, Ferrarese A, Gibin E, Capobianco M, Bertolotto A, Enrico S, Solej M, Martino V, Destefano I, Nano M (2016) Anal sphincter dysfunction in multiple sclerosis: an observation manometric study. Open Med (Wars) 11:509-517.

Mauvezin C, Neufeld TP (2015) Bafilomycin A1 disrupts autophagic flux by inhibiting both V-ATPase-dependent acidification and Ca-P60A/SERCA-dependent autophagosome-lysosome fusion. Autophagy 11:1437-1438.

McMurdie PJ, Holmes S (2013) phyloseq: An R Package for Reproducible Interactive Analysis and Graphics of Microbiome Census Data. PLOS ONE 8:e61217.

Menzies FM et al. (2017) Autophagy and Neurodegeneration: Pathogenic Mechanisms and Therapeutic Opportunities. Neuron 93:1015-1034.

Mizushima N (2007) Autophagy: process and function. Genes Dev 21:2861-2873.

Mizushima N, Yoshimori T (2007) How to interpret LC3 immunoblotting. Autophagy 3:542-545.

Monastyrska I, Rieter E, Klionsky DJ, Reggiori F (2009) Multiple roles of the cytoskeleton in autophagy. Biol Rev Camb Philos Soc 84:431-448.

Monteiro de Castro G, Deja NA, Ma D, Zhao C, Franklin RJ (2015) Astrocyte Activation via Stat3 Signaling Determines the Balance of Oligodendrocyte versus Schwann Cell Remyelination. Am J Pathol 185:2431-2440.

Morgan XC, Tickle TL, Sokol H, Gevers D, Devaney KL, Ward DV, Reyes JA, Shah SA, LeLeiko N, Snapper SB, Bousvaros A, Korzenik J, Sands BE, Xavier RJ, Huttenhower C (2012) Dysfunction of the intestinal microbiome in inflammatory bowel disease and treatment. Genome Biology 13:R79.

Mottawea W, Chiang C-K, Mühlbauer M, Starr AE, Butcher J, Abujamel T, Deeke SA, Brandel A, Zhou H, Shokralla S, Hajibabaei M, Singleton R, Benchimol EI, Jobin C, Mack DR, Figeys D, Stintzi A (2016) Altered intestinal microbiota–host mitochondria crosstalk in new onset Crohn's disease. Nature Communications 7:13419.

Mueller S, Klaus-Kovtun V, Stanley JR (1989) A 230-kD basic protein is the major bullous pemphigoid antigen. J Invest Dermatol 92:33-38.

Mutasim DF, Takahashi Y, Labib RS, Anhalt GJ, Patel HP, Diaz LA (1985) A Pool of Bullous Pemphigoid Antigen(s) Is Intracellular and Associated with the Basal Cell Cytoskeleton-Hemidesmosome Complex. Journal of Investigative Dermatology 84:47-53.

Nave KA (2010) Myelination and the trophic support of long axons. Nat Rev Neurosci 11:275-283.

O'Meara RW, Michalski JP, Kothary R (2011a) Integrin signaling in oligodendrocytes and its importance in CNS myelination. J Signal Transduct 2011:354091.

O'Meara RW, Ryan SD, Colognato H, Kothary R (2011b) Derivation of enriched oligodendrocyte cultures and oligodendrocyte/neuron myelinating co-cultures from post-natal murine tissues. J Vis Exp.

O'Meara RW, Cummings SE, Michalski JP, Kothary R (2016) A new in vitro mouse oligodendrocyte precursor cell migration assay reveals a role for integrin-linked kinase in cell motility. BMC Neurosci 17:7.

O'Meara RW, Michalski JP, Anderson C, Bhanot K, Rippstein P, Kothary R (2013) Integrin-linked kinase regulates process extension in oligodendrocytes via control of actin cytoskeletal dynamics. J Neurosci 33:9781-9793.

Ogier-Denis E, Houri JJ, Bauvy C, Codogno P (1996) Guanine nucleotide exchange on heterotrimeric Gi3 protein controls autophagic sequestration in HT-29 cells. J Biol Chem 271:28593-28600.

Oksanen JB, FG; Kindt, R; Legendre, P; Minchin, PR; O'Hara, RB; Simpson, GL; Solymos, P; Stevens, MHH; Wagner H (2016) Vegan: Community Ecology Package. R Package. Version 24-1.

Okumura M, Yamakawa H, Ohara O, Owaribe K (2002) Novel alternative splicings of BPAG1 (bullous pemphigoid antigen 1) including the domain structure closely related to MACF (microtubule actin cross-linking factor). J Biol Chem 277:6682-6687.

Pankiv S, Clausen TH, Lamark T, Brech A, Bruun JA, Outzen H, Overvatn A, Bjorkoy G, Johansen T (2007) p62/SQSTM1 binds directly to Atg8/LC3 to facilitate degradation of ubiquitinated protein aggregates by autophagy. J Biol Chem 282:24131-24145.

Parzych KR, Klionsky DJ (2014) An overview of autophagy: morphology, mechanism, and regulation. Antioxid Redox Signal 20:460-473.

Pattingre S, Petiot A, Codogno P (2004) Analyses of Galpha-interacting protein and activator of G-protein-signaling-3 functions in macroautophagy. Methods Enzymol 390:17-31.

Pellegatta M, De Arcangelis A, D'Urso A, Nodari A, Zambroni D, Ghidinelli M, Matafora V, Williamson C, Georges-Labouesse E, Kreidberg J, Mayer U, McKee KK, Yurchenco PD, Quattrini A, Wrabetz L, Feltri ML (2013) alpha6beta1 and alpha7beta1 integrins are required in Schwann cells to sort axons. J Neurosci 33:17995-18007.

Pfeiffer SE, Warrington AE, Bansal R (1993) The oligodendrocyte and its many cellular processes. Trends Cell Biol 3:191-197.

Poirier A-A, Aubé B, Côté M, Morin N, Di Paolo T, Soulet D (2016) Gastrointestinal Dysfunctions in Parkinson's Disease: Symptoms and Treatments. Parkinson's Disease 2016:23.

Poliak S, Peles E (2003) The local differentiation of myelinated axons at nodes of Ranvier. Nat Rev Neurosci 4:968-980.

Poliakova K, Adebola A, Leung CL, Favre B, Liem RK, Schepens I, Borradori L (2014) BPAG1a and b associate with EB1 and EB3 and modulate vesicular transport, Golgi apparatus structure, and cell migration in C2.7 myoblasts. PLoS One 9:e107535.

Pool M, Rippstein P, McBride H, Kothary R (2006) Trafficking of macromolecules and organelles in cultured Dystonia musculorum sensory neurons is normal. J Comp Neurol 494:549-558.

Pool M, Boudreau Lariviere C, Bernier G, Young KG, Kothary R (2005) Genetic alterations at the Bpag1 locus in dt mice and their impact on transcript expression. Mamm Genome 16:909-917.

Prokop A, Beaven R, Qu Y, Sanchez-Soriano N (2013) Using fly genetics to dissect the cytoskeletal machinery of neurons during axonal growth and maintenance. J Cell Sci 126:2331-2341.

Ravikumar B, Acevedo-Arozena A, Imarisio S, Berger Z, Vacher C, O'Kane CJ, Brown SD, Rubinsztein DC (2005) Dynein mutations impair autophagic clearance of aggregate-prone proteins. Nat Genet 37:771-776.

Reed NA, Cai D, Blasius TL, Jih GT, Meyhofer E, Gaertig J, Verhey KJ (2006) Microtubule acetylation promotes kinesin-1 binding and transport. Curr Biol 16:2166-2172.

Roper K, Gregory SL, Brown NH (2002) The 'spectraplakins': cytoskeletal giants with characteristics of both spectrin and plakin families. J Cell Sci 115:4215-4225.

Rotthier A, Baets J, Timmerman V, Janssens K (2012) Mechanisms of disease in hereditary sensory and autonomic neuropathies. Nature Reviews Neurology 8:73.

Ryan SD, Ferrier A, Kothary R (2012a) A novel role for the cytoskeletal linker protein dystonin in the maintenance of microtubule stability and the regulation of ER-Golgi transport. Bioarchitecture 2:2-5.

Ryan SD, Bhanot K, Ferrier A, De Repentigny Y, Chu A, Blais A, Kothary R (2012b) Microtubule stability, Golgi organization, and transport flux require dystonin-a2-MAP1B interaction. J Cell Biol 196:727-742.

Ryan SD, Ferrier A, Sato T, O'Meara RW, De Repentigny Y, Jiang SX, Hou ST, Kothary R (2012c) Neuronal dystonin isoform 2 is a mediator of endoplasmic reticulum structure and function. Mol Biol Cell 23:553-566.

Sachsenberg-Studer EM, Runne U, Wehrmann T, Wolter M, Kriener S, Engels K, Elshorst-Schmidt T, Kaufmann R, Borradori L (2001) Bullous colon lesions in a patient with bullous pemphigoid. Gastrointest Endosc 54:104-108.

Saulnier R, De Repentigny Y, Yong VW, Kothary R (2002) Alterations in myelination in the central nervous system of dystonia musculorum mice. J Neurosci Res 69:233-242.

Sawamura D, Li K, Chu ML, Uitto J (1991) Human bullous pemphigoid antigen (BPAG1). Amino acid sequences deduced from cloned cDNAs predict biologically important peptide segments and protein domains. J Biol Chem 266:17784-17790.

Seehusen F, Kiel K, Jottini S, Wohlsein P, Habierski A, Seibel K, Vogel T, Urlaub H, Kollmar M, Baumgartner W, Teichmann U (2016) Axonopathy in the Central Nervous System Is the Hallmark of Mice with a Novel Intragenic Null Mutation of Dystonin. Genetics 204:191-203.

Simons M, Misgeld T, Kerschensteiner M (2014) A unified cell biological perspective on axon-myelin injury. J Cell Biol 206:335-345.

Sotelo C, Guenet JL (1988) Pathologic changes in the CNS of dystonia musculorum mutant mouse: an animal model for human spinocerebellar ataxia. Neuroscience 27:403-424.

Specian RD, Neutra MR (1980) Mechanism of rapid mucus secretion in goblet cells stimulated by acetylcholine. J Cell Biol 85:626-640.

Suozzi KC, Wu X, Fuchs E (2012) Spectraplakins: master orchestrators of cytoskeletal dynamics. J Cell Biol 197:465-475.

Takamatsu Y, Fujita M, Ho GJ, Wada R, Sugama S, Takenouchi T, Waragai M, Masliah E, Hashimoto M (2018) Motor and Nonmotor Symptoms of Parkinson's Disease: Antagonistic Pleiotropy Phenomena Derived from alpha-Synuclein Evolvability? Parkinsons Dis 2018:5789424.

Thornburg LP, Hanker JS (1975) Lysosomal hydrolases in the trigeminal ganglion of mice afflicted with an hereditary sensory neuropathy (dystonia musculorum). Acta Neuropathol 32:91-101.

Triolo D, Dina G, Taveggia C, Vaccari I, Porrello E, Rivellini C, Domi T, La Marca R, Cerri F, Bolino A, Quattrini A, Previtali SC (2012) Vimentin regulates peripheral nerve myelination. Development 139:1359-1367.

Tseng KW, Peng ML, Wen YC, Liu KJ, Chien CL (2011) Neuronal degeneration in autonomic nervous system of Dystonia musculorum mice. J Biomed Sci 18:9.

Tsiper MV, Yurchenco PD (2002) Laminin assembles into separate basement membrane and fibrillar matrices in Schwann cells. J Cell Sci 115:1005-1015.

Wang K, Klionsky DJ (2011) Mitochondria removal by autophagy. Autophagy 7:297-300.

Wang QJ, Ding Y, Kohtz DS, Mizushima N, Cristea IM, Rout MP, Chait BT, Zhong Y, Heintz N, Yue Z (2006) Induction of autophagy in axonal dystrophy and degeneration. J Neurosci 26:8057-8068.

Wloga D, Gaertig J (2010) Post-translational modifications of microtubules. J Cell Sci 123:3447-3455.

Wong E, Cuervo AM (2010) Autophagy gone awry in neurodegenerative diseases. Nat Neurosci 13:805-811.

Xie R, Nguyen S, McKeehan WL, Liu L (2010) Acetylated microtubules are required for fusion of autophagosomes with lysosomes. BMC Cell Biol 11:89.

Xie R, Nguyen S, McKeehan K, Wang F, McKeehan WL, Liu L (2011) Microtubule-associated protein 1S (MAP1S) bridges autophagic components with microtubules and mitochondria to affect autophagosomal biogenesis and degradation. J Biol Chem 286:10367-10377.

Yang Y, Dowling J, Yu QC, Kouklis P, Cleveland DW, Fuchs E (1996) An essential cytoskeletal linker protein connecting actin microfilaments to intermediate filaments. Cell 86:655-665.

Yang Y, Bauer C, Strasser G, Wollman R, Julien JP, Fuchs E (1999) Integrators of the cytoskeleton that stabilize microtubules. Cell 98:229-238.

Yang Z, Klionsky DJ (2010) Eaten alive: a history of macroautophagy. Nat Cell Biol 12:814-822.

Yorimitsu T, Nair U, Yang Z, Klionsky DJ (2006) Endoplasmic reticulum stress triggers autophagy. J Biol Chem 281:30299-30304.

Young KG, Kothary R (2008) Dystonin/Bpag1 is a necessary endoplasmic reticulum/nuclear envelope protein in sensory neurons. Exp Cell Res 314:2750-2761.

Young KG, Pinheiro B, Kothary R (2006) A Bpag1 isoform involved in cytoskeletal organization surrounding the nucleus. Exp Cell Res 312:121-134.

Zawadzka M, Rivers LE, Fancy SP, Zhao C, Tripathi R, Jamen F, Young K, Goncharevich A, Pohl H, Rizzi M, Rowitch DH, Kessaris N, Suter U, Richardson WD, Franklin RJ (2010)

CNS-resident glial progenitor/stem cells produce Schwann cells as well as oligodendrocytes during repair of CNS demyelination. Cell Stem Cell 6:578-590.